NOAA Project
Report

Construction of Five Additional Tsunami Inundation Maps for the Gulf of Mexico

and

A Probabilistic Methodology for Hazard Assessment Generated by Submarine Landslides in the Gulf of Mexico

Final Report to the
National Tsunami Hazard Mitigation Program (NTHMP)
in Completion of Project Awards
NA12NWS4670014
and
NA13NWS4670018

Authors

Juan J Horrillo	Texas A&M University at Galveston
Alyssa Pampell-Manis	Texas A&M University at Galveston
Bert Sweetman	Texas A&M University at Galveston
Collaborators:	
Chayne Sparagowski	Coastal Bend Council of Governments NTHMP Mitigation and Education Subcommittee
Lisha Parambath	Texas A&M University
Yoshinori Shigihara	Defense Academy of Japan

Under the guidance of
NTHMP Mapping and Modeling Subcommittee

National Tsunami Hazard Mitigation Program

National Oceanic and Atmospheric Administration

Ocean Engineering
Texas A&M University at Galveston
Galveston, Texas, 77553

November 2015

Contents

List of Figures

List of Tables

Executive Summary

This project focuses on the development of five (5) tsunami inundation maps for communities in the Gulf of Mexico (GOM) that will provide guidance to state emergency managers for tsunami hazard mitigation and warning purposes (NTHMP Award #NA12NWS4670014, Construction of Five Additional Tsunami Inundation Maps for the Gulf of Mexico). The communities covered in this report are: South Padre Island, TX, Galveston, TX, Mobile, AL, Panama City, FL, and Tampa, FL. Consequently, a detailed tsunami hazard assessment in terms of inundation maps is presented for the selected communities. In addition, a pilot study analyzing the probability of tsunami inundation for the northwest GOM is completed for South Padre Island, TX (NTHMP Award #NA13NWS4670018, A Probabilistic Methodology for Hazard Assessment Generated by Submarine Landslide in the Gulf of Mexico).

Potential tsunami sources for the GOM are local submarine landslides, which have been examined in the past by the Atlantic and Gulf of Mexico Tsunami Hazard Assessment Group (ten Brink et al., 2009). In their findings, they stated that submarine landslides in the GOM are considered a potential tsunami hazard. However, the probability of tsunamis generated by large landslides is low. This probability of occurrence is related to ancient (historical) massive landslides which were probably active prior to 7,000 years ago when large quantities of sediments were emptied into the Gulf of Mexico. Nowadays, sediment continues to empty into the Gulf of Mexico mainly from the Mississippi River. This sediment supply contributes to slope steepening and the increase of fluid pore pressure in sediments, which may lead to further landslide activity and hence, the reason for this study in determining the potential tsunami hazard and its effects in the Gulf of Mexico. In addition to the historical sources (3 in total), a probabilistic approach was implemented to fill gaps along the continental shelf between the historical landslide sources by adding synthetic landslide sources (4 in total) to cover the entire northern part of the GOM. Our probabilistic approach confirmed a recurrence period of major landslide events of around 8000 years, consistent with recent findings (Geist et al., 2013). These probabilistic tsunami sources are used as the maximum credible event that could happen in a region according to the local bathymetry, seafloor slope, and sediment information. These probabilistic maximum credible events together with the historical sources (seven sources in total) are then used to develop the inundation maps for five selected communities along the GOM. In order to estimate the extent and magnitude of the tsunami inundation caused by these submarine landslide sources, 3D and 2D numerical models were coupled following research advancement in tsunami energy transfer mechanisms. The 3D model, TSUNAMI3D, was used for the tsunami generation to determine the initial dynamic wave or source and passed as an input to the 2D non-hydrostatic model, NEOWAVE, to determine the tsunami wave propagation and the detailed runup and inundation extent in each of the selected communities. Tsunami flooding inland-extent, maximum inundation depth, maximum inundation elevation and maximum momentum flux and direction were determined within the inundation-prone areas of the five selected communities. Additionally, the probability of inundation above certain threshold levels was determined in a pilot study for South Padre Island, TX, giving the annual exceedance rates considering all seven landslide tsunami sources. Although the recurrence of destructive tsunami events are verified

to be quite low, our work-study has confirmed that submarine landslide events with similar characteristics to the ones determined here have indeed the potential to cause severe flooding and damage to GOM coastal communities. This work result is intended to provide guidance to local emergency managers to help with managing urban growth, evacuation planning, and public education with the vision to mitigate potential tsunami hazards in the GOM. .

1 Introduction

1.1 Background

Gulf of Mexico (GOM) coasts were included in the U.S. Tsunami Warning System in January 2005. The main purpose of the warning system is local emergency management's capability to act in response to warnings. To plan for the warning response, emergency managers must understand what specific areas within their jurisdictions are threatened by tsunamis. Coastal hazard areas susceptible to be inundated by tsunami events can be determined by historical events, by modeling potential tsunami events (worst case scenario), or by using a probabilistic approach to determine the period of recurrence or chances to exceed a certain threshold. As the GOM coastal regions have no significant recent historic tsunamis records, numerical modeling and probabilistic methodologies for source identification must be used to determine these coastal hazard zones.

Potential tsunami sources for the GOM are local submarine landslides and possibly earthquakes along the Caribbean plate boundary faults. However, preliminary modeling of potential tsunami sources outside the GOM by Knight (2006) indicated a very low threat and this type of tsunamigenic event may not pose a hazard to the GOM coastal communities. Nevertheless, ancient submarine landslides within the GOM basin may have generated tsunamis, as examined by ten Brink et al. (2009). In their findings, they stated that submarine landslides in the GOM are considered a potential tsunami hazard for the following reasons:

- Some dated submarine landslides in the GOM have a post-glacial age
- Large landslides in the GOM have been found in the submarine canyons and fan provinces extending from present Mississippi and other former large rivers that emptied into the GOM. These large submarine landslides were probably active before 7500 years ago
- Recent suggestions from seismic records of small-scale energetic submarine landslides in the GOM indicate that there is a probability of recurrence (Dellinger and Blum, 2009).

Therefore, this study aims to verify if an event of such tsunamigenic characteristics might certainly be a threat to GOM communities and, if so, what would be its effect in terms of inundation for GOM coastal regions.

This work determines all elements necessary to develop five (5) additional tsunami inundation maps that will provide guidance to state emergency managers to help optimize evacuation plans and real-time tsunami warnings for communities on the GOM coastline.

The development of these 5 tsunami inundation maps is based on the three (3) identified ancient (historical) events of local submarine landslides as described by ten Brink et al. (2009) and which lie along the northern continental shelf break of the GOM. In addition, four (4) more tsunami submarine landslide sources were determined by using a probabilistic approach following the general idea addressed in Maretzki et al. (2007), but improving on a Monte Carlo Simulation method by incorporating a Cholesky decomposition approach to determine correlated random values for important submarine landslide parameters. This method enables us to capture much better the relationships and trends seen in the observational data while also allowing for natural variability and uncertainty of these parameters. The four additional probabilistic sources are used to fill the gaps between the historical ones to mostly cover the northern GOM continental shelf break. The 7 submarine landslide sources are used to generate the tsunami maps for the 5 communities selected; the selected communities are listed below in clockwise order along the US GOM's coastline; see also Figure 1.

- South Padre Island, TX
- Galveston, TX
- Mobile, AL
- Panama City, FL
- Tampa, FL

These communities or geography regions were selected according to a preliminary study aiming to determine vulnerable areas based on the impact caused by the identified historical/ancient landslide events and the probabilistic ones, see Sections 3 and 4 for more details. The selection of the regions were also based on the proximity of submarine landslide sources, tsunami energy focusing, affected population or infrastructure, and the quality of existing local bathymetric and topographic data (availability of high-resolution Digital Elevation Models (DEMs)). Tsunami flooding inland-extent, maximum inundation depth, maximum of maximums inundation depth (across all sources), and maximum momentum flux and its direction were determined within the hazard areas of these selected communities. Additionally, a pilot study was completed for South Padre Island, TX analyzing the probability of tsunami inundation. We determined inundation that is exceeded for 500, 2500, 5000, and 10,000 year return periods, as well as annual probabilities that inundation will exceed 0m, 2m (∼6.6ft), 4m (∼13.1ft), and 6m (∼19.7ft).

1.2 Regional and Historical Context

South Padre Island

The South Padre Island community is located at the south part of Padre Island in southern Texas. Padre Island is a long sand-barrier island extending some ∼ 210 km (∼ 130 miles) along the coast of south Texas. The north end is just east of Corpus Christi (at 27° 37′ N, 97° 14′ W), and the south end is opposite Port Isabel (at 26° 5′ N, 97° 8′ W). The island is

separated from the mainland by the Laguna Madre and connected to the mainland at each end by causeways. It is divided by the dredged Port Mansfield Channel, which provides shipping access to the Gulf Intracoastal Waterway and to Port Mansfield from the Gulf of Mexico. The Island has a strong belt of dunes 3.0 to 7.0 m (10 to 23 ft) high which run along the Gulf side of the island. Nowhere is the island more than three miles ($\sim$ 4.8 km) wide.

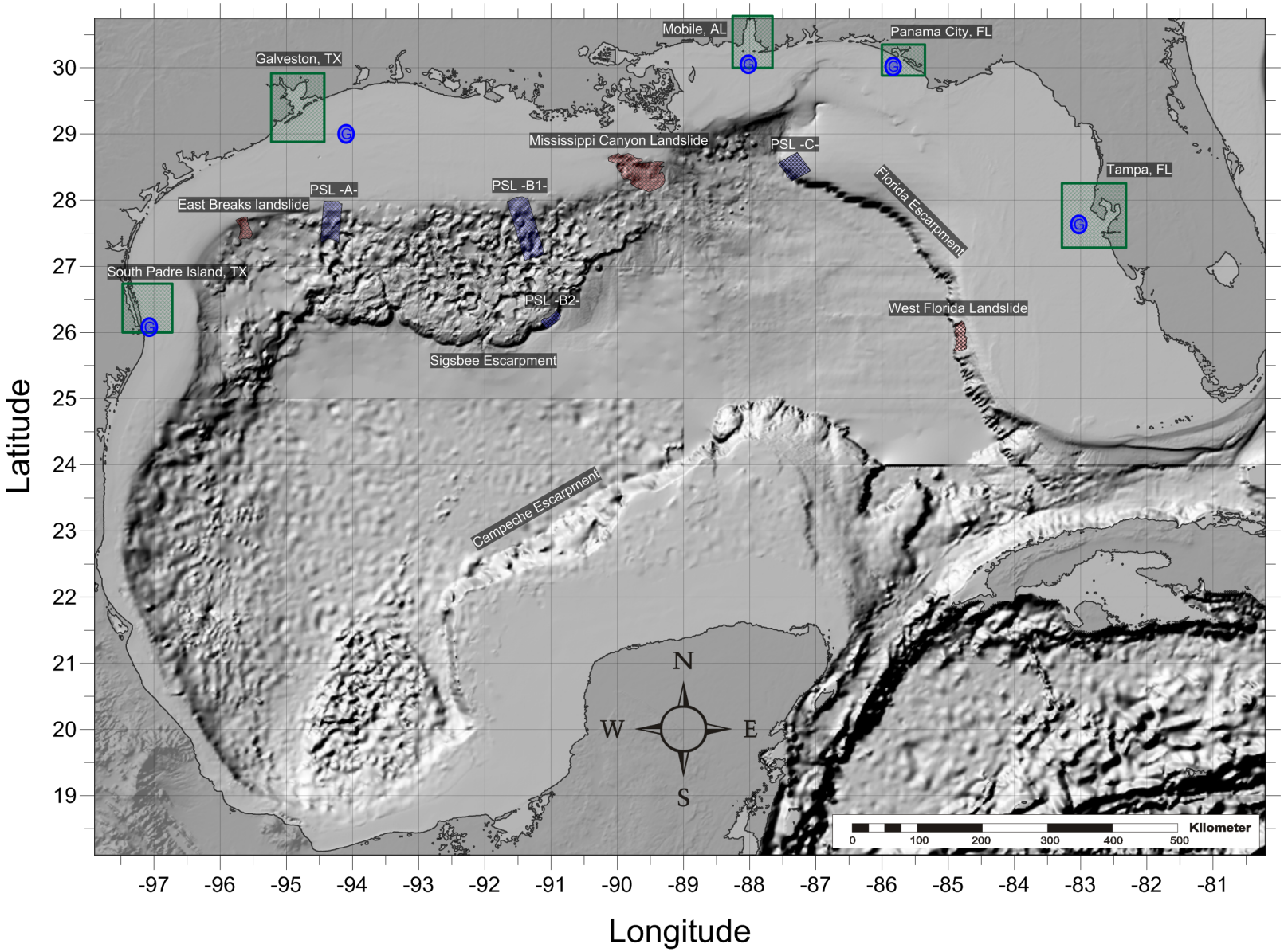

Figure 1: Selected communities or geography regions along the US GOM's coastline where tsunami maps were developed. Green hatched rectangles are communities selected; red hatched areas are historical landslide sources; blue hatched areas are Probabilistic Submarine Landslide (PSL) sources; blue dots are locations of numerical wave gauges.

The island was formed by the slow, ongoing process of sea erosion and deposition. The island is divided into three distinct areas: north, central, and south. The north is devoted to residential, water-oriented, recreational development. The central portion became Padre Island National Seashore in 1962, which is in its natural state except at Malaquite Beach. The south part has been developing rapidly since the 1970s as a resort area; the town of South Padre Island was incorporated in 1973 at the southern tip of the island. All of Padre Island is susceptible to tropical storm damage. Between 1900 and 1979 eleven tropical storms struck the island, an average of one every 7.1 years. Historically, developments have been hard to maintain against storm surge, flooding, and wind and wave erosion.

In September 1967, Hurricane Beulah caused extensive damage to the town of South Padre Island. An estimated storm tide of $8 - 14$ ft swept through South Padre Island, Port Isabel, and Boca Chica; tides were measured as high as 18 ft along the Cameron/Willacy County line south of Port Mansfield (Dunn, 2010).

On 23 July 2008, Hurricane Dolly made landfall on the island as a Category 1 storm, also causing extensive damage to the town. Some buildings were extensively damaged and had to be gutted due to the damage. In September 2008, Hurricane Ike caused moderate damage but severe erosion on the South Padre Island beaches, which recovered in time for the 2009 summer season. Recently, in July 2010, the island received heavy rains from Hurricane Alex, but the storm left the island generally undamaged.

As of the census of 2010, the population of South Padre Island was $2,837$ people. The population density was $1,343$ people per square mile ($519/$ km^2). In March, the island is a popular resort area to many tourists. Tens of thousands of tourists come to the island to enjoy the warm temperatures South Padre Island offers (Art Leatherwood, 2010).

Galveston, TX

Galveston Island is a long narrow strip of sand and shell that runs parallel to the shore, separated by channels and bays from the mainland. The island has been formed by deposits of sand and shell piled up by ocean waves and long-shore currents. The barrier formation lies along the Texas Gulf Coast margin, about ~ 80.5 km (~ 50 miles) southeast of Houston. The island is about ~ 43.5 km (~ 27 miles) long and no more than ~ 4.8 km (~ 3 miles) wide at its widest point. It is separated from the mainland by the Galveston Bay and the West Bays and connected to the mainland by the Galveston Causeway (Interstate 45) and the San Luis Pass bridge at the southwest end. The far northeast end of the island is separated from the Bolivar Peninsula by Bolivar Roads, which provides the entrance to Galveston Bay and the Houston Ship Channel. There are two major communities on Galveston Island: Jamaica Beach and the City of Galveston. The City of Galveston is one of the leading tourist destinations in Texas.

Several hurricanes have inflicted damage on the settled communities during the summer and fall seasons. However, the City of Galveston has a strong man-made storm protection seawall of 4.6 m ($15 - 16$ ft) high. This seawall was built after the infamous Galveston Hurricane of 1900, which hit the island as a Category 4 hurricane with wind speeds in excess of 135 mph (~ 217 km/h) and inundated the city with a storm surge of 15 ft (~ 4.6 m), exceeding the highest elevation in Galveston of only 8.7 ft (~ 2.7m) above sea level. The

most deadly natural disaster to hit the U.S. in recorded history, the storm killed 6,000-8,000 people. The seawall was subsequently built to protect the city from future hurricanes. This structure has successfully achieved its main objective of protecting the city from devastating storm events. Though the seawall provide some shielding, the bay and channel shorelines still face significant danger from storm surge. Hurricane Ike, in 2008, caused severe flooding of more than 3.5 m ($\sim$ 12 ft) of water in The Strand historical district and almost the entire city; the flooding mainly came from the bay side or channels. Dune systems in the unprotected areas on the barrier island are on the order of $\sim$ 2.0 to $\sim$ 3.0 m ($\sim$ 6.5 to $\sim$ 10 ft) high.

An estimated $\sim$ 6 million tourists visited the City of Galveston in 2013. With a population of fewer than 60,000 permanent residents, the City of Galveston hosts several festivities in which the number of visitors in one single day can exceed its own population. Throughout the year, the Port of Galveston serves as a passenger cruise ship terminal for cruise ships operating in the Caribbean, some of them with capacity of more than 4,000 passengers. The Lone Star Rally (in December) attracts over 450,000 motorcycle enthusiasts during a period of four days. The Mardi Gras festivities (February or March) span two weekends with more than 200,000 visitors during that period (Angelou Economics, 2008).

Mobile, AL

The city of Mobile is situated at the head of Mobile Bay on the bay's western shore. On the Eastern Shore of the bay are found several small communities, including Spanish Fort, Daphne, Fairhope, Point Clear, and Bon Secour. The cities of Gulf Shores and Dauphin lie just outside of the bay, on the Fort Morgan peninsula and Dauphin Island respectively. The head of the bay is crossed by two major thoroughfares, the Bayway and the Causeway. These two bridges serve as the primary connections between the city of Mobile and the Eastern Shore. Mobile is recognized as a prime port location as its port is one of the largest deepwater ports in the United States. Mobile also hosts huge shipyard companies and many private firms to support the maritime industry (Waterborne Commerce Statistics, 2010).

Dauphin Island is the larger community more exposed to direct flooding, i.e., a tsunami event. The island's eastern end helps to define the mouth of Mobile Bay. On this eastern tip is Fort Gaines which faces Fort Morgan sitting across the inlet to Mobile Bay, on Mobile Point. The eastern wider portion of the island (2 km), is shaded by thick pine trees, but the narrow, western part of the island features scrub growth and few trees. The island is connected to the mainland by the Gordon Persons Bridge. Dauphin Island is home to several historic sites and beaches which attract tourism, and fishing is a popular activity in the waters around the island too.

In late September of 1906, a hurricane made landfall just west of Mobile as a Category 2, producing a storm surge in excess of 3 m (10 ft) from Jackson County, MS, to the westernmost Florida peninsula. In Mobile, high water was reported nearly 10 ft (3 m) above mean tide level. On 17 August 1969, Hurricane Camille crossed the Mississippi coast as a Category 5 (the strongest known land-falling hurricane in recorded history), with landfall winds estimated at 175 mph (280 km/h) on the Mississippi coast. The entire barrier island chain of Mississippi and 70% of Dauphin Island were inundated by the high storm surge of

Hurricane Camille (U.S. Army Corps of Engineers, 1970). On 2 September 1985, Hurricane Elena (Category 3), hit Dauphin Island hard with steady winds of over 100 mph ($\sim$ 160 km/h) and a storm surge of up to 2.44 m (8 ft). In 1997, Hurricane Danny also caused extensive flooding on the east end of Dauphin Island. On 16 September 2004, Hurricane Ivan (Category 3), with winds around 120 mph ($\sim$ 200 km/h) at landfall site, moved inland near Gulf Shores along the Fort Morgan Peninsula. On 29 August 2005, Hurricane Katrina (Category 3) made landfall with wind speeds estimated around 120 mph (200 km/h) and a storm surge that reached 3.66 m (12 ft) at the USS Alabama along I-10 in Mobile.

As of the 2010 census, the number of inhabitants in Dauphin Island was 1238.

Panama City, FL

Settled along St. Andrews Bay and the Gulf of Mexico, Panama City is a hub that clasps military service people and tourists. The region hosts major Air Force and Navy facilities, the Tyndall Air Force Base to the east and the Naval Coastal Systems Center to the west. Panama City Beach, on the barrier located west of Panama City, faces the GOM to the west and the Grand Lagoons to the east. Its beaches attract tourists year-round and especially during spring break.

In September, 1975, Hurricane Eloise caused severe beach erosion in Bay County, resulting in extensive structural damage in the beach area. The metro areas of Pensacola and Panama City were hit hard in 1995 by Hurricane Opal, which packed winds of 125 mph (200 km/h). Recently, on 29 March 2014, Panama City Beach experienced a strong squall that generated a meteotsunami with a measured wave height at tide gauges of 1.20 m ($\sim$ 4 ft), damaging the beach infrastructure (Vilibić et al., 2014).

As of the 2010 census, Panama City had a population of 12,018. However, during the busiest spring break period between March 1 and April 15, the population can swell to $150,000 - 250,000$.

Tampa, FL

Tampa is part of the metropolitan area most commonly referred to as the Tampa Bay Area, located on the west central coast of Florida. The bay is a natural harbor that connects to the GOM, comprising Hillsboro Bay, McKay Bay, Old Tampa Bay, Middle Tampa Bay, and Lower Tampa Bay. The bay is home to several important ports (Port Tampa Bay, Port Manatee, and Port of St. Peterburg), shipyards, cargo/building/oil industry facilities, cruise ship terminals, and a Coast Guard Station. The most important port is Port Tampa Bay (the largest port in Florida). This port is located on Hillsboro and McKay Bays deep inside Tampa Bay. However, communities most exposed to direct tsunami flooding are those facing the GOM. These communities are connected to the mainland by several important relatively small bridges: Belleair, 5^{th} Ave. on 688, Park Blvd., Tom Stuart Causeway, Treasure Island Causeway, Corey Causeway, 35^{th} Ave. Bridge, and Pinella Bayway. The main bridges crossing Tampa Bay are: Sunshine Skyway Bridge, which spans Lower Tampa Bay from Bradenton on the south to St. Petersburg on the north (part of $I - 275$ & US 19); Gandy Bridge, spanning Old Tampa Bay from Tampa on the east to St. Petersburg on the west (part

of U.S. Route 92); Howard Frankland Bridge, which spans the middle of Old Tampa Bay from Tampa on the east to St. Petersburg on the west (part of $I-275$); Courtney Campbell Causeway, spanning northern Old Tampa Bay from Tampa on the east to Clearwater on the west (part of Florida State Road 60); Bayside Bridge, which runs almost parallel to the western shore of Old Tampa Bay from Largo on the south to Clearwater on the north; Oldsmar Bridge, which stretches from Safety Harbor on the west to Oldsmar on the east, near the northernmost point of Old Tampa Bay 22^{nd}; and Street Causeway, spanning the mouth of McKay Bay near Port Tampa Bay (part of U.S. Route 41).

In 23 October 1921, the Tampa Bay region was hit by a strong hurricane. The hurricane brought sustained winds of 75 mph (119 km/h) and a storm tide of 10.5 ft ($\sim$ 3 m). In Punta Gorda, a water gauge recorded a tide 7 ft (2.5 m) above normal. Tides $5-6$ ft ($1.5-2$ m) above normal were also reported in St. Petersburg and Punta Rassa. The hurricane also brought a storm surge of $10-12$ ft ($3-3.5$ m) to Tampa Bay (Ballingurd, D., 2006). In Tampa, much of the city was flooded, and three people were killed in drowning incidents and by flying debris.

As of 2014, Tampa-St. Petersburg-Clearwater Metro Area's population was 2,793,814 people, Sperling's BestPlaces `http://www.bestplaces.net/`

1.3 Submarine Landslide Hazard in the Gulf of Mexico

Of particular interest to this work is the tsunami hazard potential within the GOM and threats to the region's coastal communities as well as the large-scale shipping and natural oil resource exploration and production industries. While the GOM is certainly at lower risk for tsunami hazards than other U.S. coastal areas, investigations carried out by the U.S. Geological Survey (USGS) and the National Tsunami Hazard Mitigation Program (NTHMP) (ten Brink et al., 2009) revealed that three small tsunami events occurred within the GOM in the 20th century. The first, in October 1918, was a small indeterminate-amplitude tsunami wave generated by a seismic event west of Puerto Rico and detected by a Galveston, TX tide gauge station. The second occurred on 2 May 1922, when a 0.64 m (2.1 ft) amplitude wave was recorded at a Galveston tide gauge station. The third event resulted in seismic seiche waves originating from the 27 March 1964 Gulf of Alaska earthquake, and 0.18 m (0.6 ft) amplitude waves were recorded at a Freeport, TX tide gauge station. Thus, as reported by ten Brink et al. (2009), local submarine landslides in the GOM are considered to be the primary potential source of tsunami generation in the GOM.

Submarine landslides can, in general, occur in confined water bodies, near island formations, and along continental slopes. Tsunami generation by these slides depends on the geological characteristics of the sloping sediment and the triggering mechanism affecting the region. Common mechanisms to initiate an underwater landslide and the ensuing tsunami are earthquakes, overpressure due to rapid deposition of soil sediments, presence of weak soil layers, wave loading on the sea-bottom by storms or hurricanes, build-up of excess pore water pressure, gas hydrate dissociation by change of temperature or pressure, groundwater seepage, and slope oversteepening (Hampton and Locat, 1996; Locat and Lee, 2002; Mason et al., 2006). In the GOM, earthquakes are likely the primary triggering mechanism for submarine landslides. Several recent moderate-sized earthquakes in the GOM, including a

M5.3 earthquake that occurred 10 February 2006 (Dellinger and Blum, 2009) and a M5.9 earthquake on 10 September 2006 (significantly large for this region), indicate potential for modern slope failure triggered by seismic activity.

Tsunamis generated by submarine landslide events are distinctly different from those generated by earthquakes. Because of the smaller spatial scale of landslides as compared to fault slip sources, waves from submarine landslide sources are generated in a more radial direction than those from earthquakes and exhibit shorter wavelengths and stronger dispersion. Additionally, the longer time scales and large vertical displacements of the landslide source motion lead to more nonlinear behavior in wave generation as compared to earthquakes. Landslide tsunami can also produce much more localized damage than those generated by earthquakes. Their threat to life and property has been increasingly realized over the past century. In 1929 in Grand Banks, an earthquake-induced underwater landslide produced tsunami waves of $3 - 8$ m ($10 - 26$ ft) which killed 28 people along the coast of Newfoundland (Cranford, 2000). The 1964 Alaska earthquake generated multiple local submarine landslides, including one near old Valdez which produced waves $4.5 - 7.6$ m ($15 - 25$ ft) high (some localized up to 12 m (39 ft) (Brown, 1964) and resulted in 33 deaths at old Valdez - more than those caused by the earthquake at any other location. Even greater devastation was seen with the 1998 Papua New Guinea landslide tsunami, which produced waves up to 15 m (49 ft) high, took over 2200 lives, and destroyed three villages (Tappin et al., 2008).

Although a massive underwater landslide in the GOM is considered a potential hazard, the probability of such an event is quite low (Dunbar and Weaver, 2008). The probability of occurrence is related to large ancient landslides which were probably active prior to 7,000 years ago when large quantities of sediments were emptied into the GOM (ten Brink et al., 2009). However, sediments continue to empty into the GOM mainly from the Mississippi River. This sediment supply contributes to slope steepening and the increase of excess pore water pressure in the underlying soils, which may lead to slope instabilities and landslide activity. In addition, the unique geometry of the GOM makes even unlikely tsunami events potentially hazardous to the entire Gulf Coast. Waves tend to refract along continental slopes and shelf breaks, and given the curved structure of the GOM shelf and the concave shape of the coastline, any outgoing propagating wave could potentially affect the coast immediately adjacent to the landslide source as well as the opposite coast. Thus, while offshore the eastern and western U.S. coasts the primary threat from a local submarine landslide source is the backgoing tsunami wave, affecting a localized region in the opposite direction of slide motion, in the GOM both backgoing and outgoing waves from an submarine landslide event are a potential inundation threat to coastal communities a greater distance apart than their counterparts on the eastern or western U.S. coasts.

1.4 Probabilistic Maximum Credible Event in the Gulf of Mexico

Given the lack of significant historical tsunami events in the GOM, the degree of landslide tsunami hazard in the GOM and for U.S. Gulf Coast states is not well understood. Therefore, determining the potential impact of these events on coastal communities depends on reliable numerical landslide tsunami models to determine tsunami generation behavior and inundation threat. One of the main challenges to accurate and efficient submarine landslide

tsunami modeling is source determination. The three large-scale ancient submarine landslides with tsunamigenic potential recognized by ten Brink et al. (2009) represent worst-case tsunami scenarios affecting GOM coasts in the past. However, these events occurred more than 7,000 years ago, and without more data on recent events to help characterize tsunamigenic submarine landslide activity within the GOM, a deterministic approach to mapping regions of increased landslide tsunami hazard potential within the GOM is not possible. It is therefore necessary to develop nondeterministic methods to more accurately determine risk and regions of enhanced hazard for the GOM. Numerical modeling of submarine landslide tsunami generation is too computationally intensive to allow for a full-scale probabilistic assessment involving multiple submarine landslide scenarios across the entire GOM. Therefore, we implement a Monte Carlo Simulation (MCS) methodology to determine trial submarine landslide scenarios and calculate the probability of failure and tsunami generation. Previous studies by Maretzki et al. (2007) and Grilli et al. (2009) used a similar MCS approach to assess landslide tsunami hazard along the east coast of the United States, and work by Shigihara and Horrillo (2014) applied the techniques of Maretzki et al. (2007) and Grilli et al. (2009) to the unique bathymetry of the GoM. However, while those studies determined potential slope failure based on independent distributions of landslide location and dimension parameters, we find strong correlations between certain dimension parameters based on previous submarine landslide events, specifically the values for area, volume, and length. These correlations suggest a unique importance of these variables to overall submarine landslide behavior. Therefore, we implement a matrix correlation method for these critical submarine landslide parameters based on the Cholesky decomposition method, which allows us to incorporate both the uncertainty in the parameter values as well as the natural correlations seen in observational submarine landslide data within our MCS method. We assess submarine landslide potential along four transects drawn across the GOM continental slope based on these correlated distributions. Once a trial landslide location/depth and configuration is determined, its probability of failing and producing a tsunami is calculated based on the sediment parameters and seismic loading for that region. Those submarine landslide scenarios which produce the largest tsunami amplitude and have the highest probability (shortest return period) are deemed the most extreme or maximum credible event scenarios for each individual transect. The annual probability of these maximum credible scenarios are determined by the joint probability of failure with the annual probability of the triggering earthquake. Thus, we are able to associate an estimated return period to these probabilistic sources and provide a comparison to the ages of the three identified ancient sources. Details of the probabilistic methodology are given in Section 3.

2 Description of the Models

For the development of maps of inundation produced by landslide-generated tsunamis, a common approach is to combine a 3D Navier Stokes (NS) model for the landslide-induced waves with a 2D depth-integrated non-hydrostatic or Boussinesq model for the wave propagation and runup (coupled model). The 3D NS model determines the wave kinematics and the free surface configuration caused by the landslide (the initial tsunami wave source),

which are then input as the initial condition (hot start) to the more numerically efficient 2D non-hydrostatic model for the calculation of wave propagation and detailed runup.

The 3D NS numerical model used here, TSUNAMI3D, is based on the Computational Fluid Dynamics (CFD) model originally developed at Los Alamos National Laboratory (LANL) during the 1970's and follows the early work done by Hirt and Nichols (1981). It solves transient fluid flow with free surface boundaries based on the concept of the fractional Volume of Fluid (VOF) method using an Eulerian mesh of rectangular cells of variable size. The fluid equations solved are the finite difference approximation of the full NS equations and the incompressibility condition, which results from the continuity equation when the density is constant. The basic mode of operation is for a single fluid phase having multiple free surfaces. However, TSUNAMI3D also can be used for calculations involving two fluid phases separated by a sharp or diffusive interface, for instance, water and landslide material. In either case, both fluids are considered incompressible and treated as Newtonian. Internal obstacles, e.g. topography, walls, etc., are defined by blocking out fully or partially any desired combination of cells in the domain. It is well known that full 3D NS numerical models are highly computationally intensive and require a considerable amount of computer resources. Therefore, TSUNAMI3D has been simplified to overcome as much as possible the computational burden of 3D NS tsunami simulations. The simplification is derived from the large aspect ratio (horizontal/vertical scale) of the tsunami wave and the selected computational cell size required to construct an efficient 3D grid. The large aspect ratio of the tsunami wave requires also a large numerical grid aspect ratio to reduce runtime and memory usage. However, the grid aspect ratio should be smaller than the aspect ratio of the tsunami wave to simplify the fluid surface reconstruction. The standard VOF algorithm, the donor-acceptor technique of Hirt and Nichols (1981), has been simplified to account for this large cell aspect ratio. The pressure term is split into two components, hydrostatic and non-hydrostatic. Although TSUNAMI3D has the capability of variable grids (1D telescoping), it does not comprise the nesting capability (2D telescoping) which is needed for detailed inundation solutions on coastal regions. The interested reader is referred to Horrillo (2006); Horrillo et al. (2013) for more detailed information about the 3D NS model.

The 2D depth-integrated and non-hydrostatic model NEOWAVE is built on the nonlinear shallow-water equations with a non-hydrostatic pressure term to describe weakly dispersive waves. This approach is equivalent to existing models based on the classical Boussinesq equations. The model features a momentum-conserved advection scheme that enables the modeling of breaking waves without the aid of analytical solutions for bore approximation or empirical equations for energy dissipation. An upwind scheme extrapolates the free-surface elevation instead of the flow depth to provide the flux in the momentum and continuity equations. This scheme apparently improves the model stability which is essential for computation of energetic breaking waves and complex runups. The pressure term is split into hydrostatic and non-hydrostatic components, and the vertical velocity is introduced in response to the non-hydrostatic pressure through the three-dimensional continuity equation. The interested reader is referred to Yamazaki et al. (2008) to obtain more detailed information about the 2D depth-integrated/non-hydrostatic model.

Both models, TSUNAMI3D and NEOWAVE, have shown very good agreement with the benchmark cases provided by the National Tsunami Hazard Mitigation Program (NTHMP)

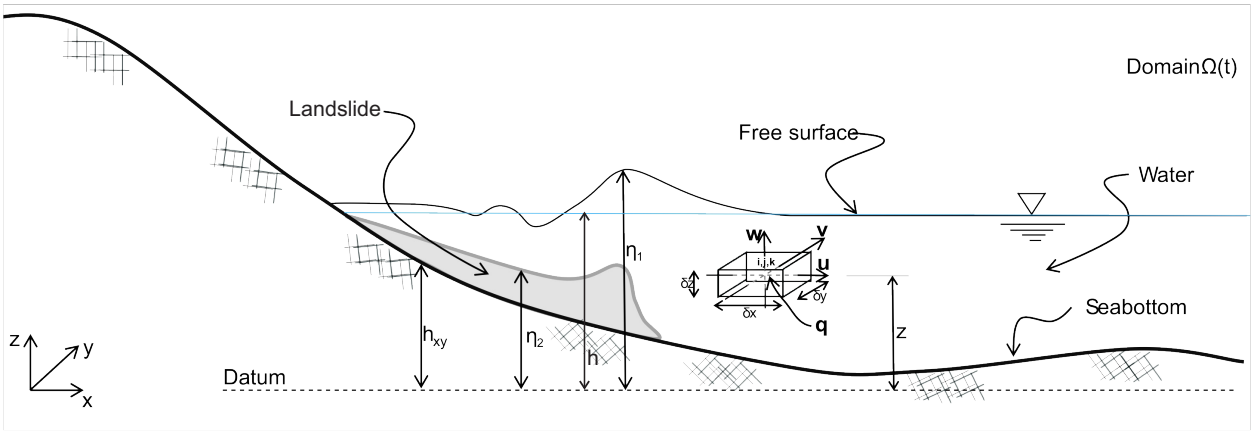

Figure 2: Sketch of model domain and variables for 3D NS model TSUNAMI3D.

for tsunami model validation and verification, report OAR-PMEL-135 (Synolakis et al., 2007). Results of the validation and verification of these models can be also found in the NTHMP's Workshop Proceedings (NTHMP, 2012).

2.1 3D NS Model's Governing Equations (TSUNAMI3D)

A schematic of the domain and variables used in TSUNAMI3D is given in Figure 2. The governing equations to describe the flow of two incompressible Newtonian fluids (*e.g.*, water and landslide) are the incompressibility condition of the continuity equation,

$$\frac{\partial u_i}{\partial x_i} = 0, \quad i = 1, 2, 3 \tag{1}$$

and the nonconservative equation of momentum given by:

$$\frac{\partial u_i}{\partial t} + u_j \frac{\partial u_i}{\partial x_j} = -\frac{1}{\rho_{1,2}} \left(\frac{\partial p}{\partial x_i} + \frac{\partial q}{\partial x_i} \right) + \frac{\partial}{\partial x_j} \left[\frac{\mu_{1,2}}{\rho_{1,2}} \left(\frac{\partial u_i}{\partial x_j} + \frac{\partial u_j}{\partial x_i} \right) \right] + g_i, \quad i, j = 1, 2, 3 \tag{2}$$

where $\mathbf{u} = [u(x, y, z, t),\ v(x, y, z, t),\ w(x, y, z, t)]$ are the velocity components along the coordinate axes $\mathbf{x} = [x, y, z]$ at time t. Here, the given subscripts $1, 2$ indicate physical parameters or variables corresponding to the water and landslide phases, i.e. $\rho_1(x, y, t)$ and $\rho_2(x, y, t)$ are the density of the water and landslide material respectively. The water and landslide phases are considered as Newtonian fluid, therefore, the kinematic viscosity μ_1/ρ_1 and μ_2/ρ_2 can be adjusted for internal friction,, Here μ_1 and μ_2 are the molecular viscosity of the water and landslide material respectively, thus, the landslide friction term in Equation 2 factored by μ_2/ρ_2 can be adjusted according to a constitutive model for landslide rheology, e.g. Bingham model, which is not implemented in this study. The acceleration due to gravity is represented by $\mathbf{g} = [0, 0, -g]$. The total pressure in each phase, $p_{tot} = p + q$, is divided into the hydrostatic pressure p and the dynamic or non-hydrostatic pressure q.

In the water domain the hydrostatic pressure is given by

$$p = \rho_1 g(\eta_1 - z) \tag{3}$$

such that $\partial p/\partial z = -\rho_1 g$. Here, z is the elevation measured from the vertical datum to the cell center and η_1 is the water free surface elevation measured from the vertical datum as well.

For the landslide phase, the total pressure $p_{tot} = p + q$, is determined by the hydrostatic pressure as

$$p = g[\rho_1(\eta_1 - \eta_2) + \rho_2(\eta_2 - z)] \tag{4}$$

and the dynamic pressure q. Here η_2 is the landslide free surface elevation measured from the vertical datum. The landslide material is also considered as a Newtonian fluid, with kinematic viscosity, μ_2/ρ_2 for internal friction.

Both water and landslide surface elevations, η_1 and η_2, are traced using the simplified VOF method based on the scalar function F and the donor-acceptor algorithm of Hirt and Nichols (1981). The method is based on the so-called fraction function F, in which F is defined as the fraction of fluid in the control volume cell (namely, volume of a computational grid cell). F is a discontinuous function, its value varies from 0 to 1 depending of the fluid interface location. Basically, when the cell is empty, with no fluid inside. the value of F is zero; when the cell is full, $F = 1$; therefore, when the fluid's interface is within the cell, then $0 < F < 1$. Details of the simplified VOF method can be also found in Horrillo et al. (2013).

For the discretization of the computational domain, the model uses an Eulerian variable mesh of rectangular cells with large aspect ratio. The governing equations are solved by using the standard explicit finite difference scheme starting with field variables such as $\mathbf{u}$, q and $\eta_{1,2}$ known at time $t = 0$. The governing equations are solved by discretizing the field variables spatially and temporally in the domain to obtain new field variables at any required time. All variables are treated explicitly with the exception of the non-hydrostatic pressure field q, which is implicitly determined (Casulli and Stelling, 1998). Non-linear terms are approximated by using an up-wind down-wind approach up to the third order (Horrillo et al., 2013). The hydrodynamic pressure field q is calculated through the Poisson's equation by using the incomplete Choleski conjugated gradient method to solve the resulting linear system of equations.

The friction term in the momentum equation can be adjusted to mimic the internal friction within the fluid body, i.e. the viscosity coefficient. This coefficient has been chosen to give the best possible agreement with the reference data.

2.2 2D Non-hydrostatic Model's Governing Equations (NEOWAVE)

The governing equations for the depth-integrated, non-hydrostatic NEOWAVE model (Kowalik et al., 2005; Yamazaki et al., 2008), are derived from the incompressible Navier-Stokes equation and the incompressibility condition of the continuity equation in a spherical coordinates system in which λ is the longitude, ϕ is the latitude, and z denotes the normal distance from the still water level (SWL). The resulting momentum equations along λ, ϕ, z directions are:

$$\frac{\partial U}{\partial t}+\frac{U}{R\cos\phi}\frac{\partial U}{\partial \lambda}+\frac{V}{R}\frac{\partial U}{\partial \phi}-\left(2\Omega+\frac{U}{R\cos\phi}\right)V\sin\phi = -\frac{g}{R\cos\phi}\frac{\partial \zeta}{\partial \lambda}-\frac{1}{2}\frac{1}{R\cos\phi}\frac{\partial Q}{\partial \lambda} -\frac{1}{2}\frac{Q}{DR\cos\phi}\frac{\partial(\zeta-h_b+\eta_{co})}{\partial \lambda}-n^2\frac{g}{D^{1/3}}\frac{U\sqrt{U^2+V^2}}{D} \tag{5}$$

$$\frac{\partial V}{\partial t}+\frac{U}{R\cos\phi}\frac{\partial V}{\partial \lambda}+\frac{V}{R}\frac{\partial V}{\partial \phi}+\left(2\Omega+\frac{U}{R\cos\phi}\right)U\sin\phi = -\frac{g}{R}\frac{\partial \zeta}{\partial \phi}-\frac{1}{2}\frac{1}{R}\frac{\partial Q}{\partial \phi} -\frac{1}{2}\frac{Q}{DR}\frac{\partial(\zeta-h_b+\eta_{co})}{\partial \phi}-n^2\frac{g}{D^{1/3}}\frac{V\sqrt{U^2+V^2}}{D} \tag{6}$$

$$\frac{\partial W}{\partial t}=\frac{Q}{D} \tag{7}$$

and the continuity equation reads

$$\frac{\partial(\zeta-\eta_{co})}{\partial t}+\frac{1}{R\cos\phi}\frac{\partial(UD)}{\partial \lambda}+\frac{1}{R\cos\phi}\frac{\partial(VD\cos\phi)}{\partial \phi}=0 \tag{8}$$

where U, V and W are depth-averaged velocity components in the λ, ϕ and z directions respectively. The variable t is the time, ζ is the free surface elevation from the SWL, R is the earth's radius, Ω is the earth's angular velocity, ρ is the water density, Q is the non-hydrostatic pressure, g is the gravitational acceleration and n is the Manning's coefficient for the sea-bottom friction. The vertical velocity W is assumed to have a linear distribution along the water column, therefore the vertical velocity component W is simply the average value of the vertical velocity at the free surface and the seafloor. The total depth is defined as $D=\zeta+(h_b-\eta_{co})$, where h_b is the water depth (from SWL to seafloor) and η_{co} is the seafloor co-seismic deformation (η_{co} is not considered in this study). A detailed discussion of NEOWAVE numerical scheme, solution and capability is found in Yamazaki et al. (2008).

2.3 3D-2D Coupling Process

One critical step in the coupling process of the two models is to determine the right moment of transferring the 3D model's wave and water kinematic (u,v and w) and free surface (η_1) field to the 2D non-hydrostatic model. The right time of transferring is controlled by the 3D domain size, and the total energy on the water induced by the submarine landslide. The 3D domain must be large enough to fully develop the generated waves without leaving the domain boundaries, and the wave energy should reach a maximum indicating that the generated waves are fully or mostly developed. If the domain size-energy considerations have been fulfilled, then the 3D field information or variables (u,v,w and η_1) are converted to two

dimensions by a simple column-wise depth averaging and inputted as the initial condition (hot start) to the 2D non-hydrostatic numerical model. For more detail about the coupling process between the two models the reader is referred to López-Venegas et al. (2014).

2.4 Energy Considerations

The generated waves are determined to have been fully developed when the total (potential plus kinetic) wave energy reaches a maximum. Energy in the system (3D domain) is determined at each phase (water and landslide) from the equations of classical mechanics by integrating each control volume or computational cell energy over the entire domain. The potential energy of the deformed water surface is measured in terms of $\eta_1 - h$, the free surface elevation from the SWL (see Figure 2). The wave's potential energy per unit horizontal area is given by

$$E_{P_{Water}} = \frac{1}{2}\rho_1 g(\eta_1 - h)^2. \tag{9}$$

The water or wave's kinetic energy is a function of the square of the velocity:

$$E_{K_{Water}} = \frac{1}{2}m_1(u^2 + v^2 + w^2) \tag{10}$$

where m_1 is the mass of the water fraction (F) in the control volume.

The energy of the landslide material can be calculated in a similar manner. The potential energy of the landslide material is measured in terms of the submerged sediment density $\rho_2 - \rho_1$ and the distance of the landslide surface η_2 from the vertical datum. The landslide potential energy per unit horizontal area is then given by

$$E_{P_{Slide}} = \frac{1}{2}(\rho_2 - \rho_1)g(\eta_2 - h_{xy})(h_{xy} + \eta_2) \tag{11}$$

where h_{xy} is the height of the seafloor from the vertical datum (see Figure 2 for reference). The landslide kinetic energy equation is again similar to that of the water:

$$E_{K_{Slide}} = \frac{1}{2}m_2(u^2 + v^2 + w^2) \tag{12}$$

with m_2 the mass of the fraction (F) of the landslide material in the control volume. Assuming a still water condition at $t = 0$, all energies are zero except for the potential energy of the landslide ($E_{P_{Slide}}(0)$), which has a value based on the landslide's location with respect to the reference vertical datum. At any time t, the change in landslide potential energy $E_{P_{Slide}}(0) - E_{P_{Slide}}(t)$ gives the amount of energy released into the system at that time.

Similar energy analysis was performed by Abadie et al. (2012) using a 2D numerical model for a landslide tsunami and by Sue et al. (2006) using a block slide experimental setup. Abadie et al. (2012) calculated potential and kinetic energy of the water/wave ahead of the landslide by integrating the energies from the tip of the landslide to the boundary of the computational domain. Sue et al. (2006) used data measurements to calculate potential and kinetic energy of the block landslide as well as the potential energy of the resulting wave,

thereby relating the energy of the landslide to the energy transferred to the wave. Here, we are able to perform a more comprehensive 3D energy analysis as the potential and kinetic energy of the wave and landslide can be easily calculated separately in time by integrating the respective energies from each computational cell, depending on the cell's fractional amount of water and/or landslide material. This allows a more complete view of the complex energy behavior in landslide motion, tsunamigenesis, and physical/numerical losses.

3 Probabilistic Submarine Landslides

Through a Monte Carlo Simulation (MCS) methodology, we have identified four probabilistic submarine landslides to be used as potential tsunami sources in addition to the three ancient sources for use in our inundation mapping efforts. (Full details of the probabilistic assessment are given in A. Pampell-Manis et al. (*J. Geophys. Res. Oceans*, under review). We assess SMF potential along four transects drawn across the GOM continental slope based on these correlated distributions. Once a trial landslide location/depth and configuration is determined,the factor of safety for slope stability is calculated based on the location and size of the landslide, sediment properties, and the local Peak Horizontal ground Acceleration (PHA) to determine if that configuration will fail. For those landslides that fail, a maximum tsunami amplitude η is calculated based on a semi-empirical formula for maximum tsunami depression determined by Grilli and Watts (2005) and Watts et al. (2005). A failure is considered to be tsunamigenic only if the maximum tsunami amplitude η for that event is greater than a certain threshold value η_{th}, which here is taken to be 0.02 m, or 2 cm. Other threshold values were tested, though it was found that smaller values of η_{th} did not significantly affect the resulting landslide parameter distributions. For some transects, the smaller threshold value resulted in slightly smaller landslide dimensions, though not significantly so, and for the purposes of providing a conservative (overly-cautious) estimate of worst-case scenario tsunami events, the larger threshold of 2cm was deemed more appropriate.

The probability of a tsunamigenic SMF is determined as the joint probability of the earthquake occurrence and the probability of slope failure producing a tsunami. Those SMF scenarios which produce the largest tsunami amplitude and have the highest probability (shortest return period) are deemed the most extreme probabilistic events for each individual transect, and the important landslide parameters (i.e. volume, area, length, width, depth, etc.) of these events are averaged to determine a probabilistic maximum credible scenario for each transect. The maximum credible event for each transect is used as a Probabilistic Submarine Landslide (PSL) source for the GOM, giving us four probabilistic sources in addition to the three ancient sources.

3.1 Methodology

Our MCS model depends on statistical distributions for GOM submarine landslide parameters, obtained from 25 landslides analyzed in McAdoo et al. (2000) as well as three ancient landslides described in ten Brink et al. (2009). The submarine landslide location and geometry data used here is given in Table 1. According to McAdoo et al. (2000), the GOM

contains the largest (in both area and volume) SMF footprints across all U.S. continental margins, and the GOM also features the widest range in magnitude of SMF area. The largest slides occur near the Mississippi Canyon in bathymetrically low regions of the deep-sea fan province, while the smallest failures are found within the salt provinces McAdoo et al. (2000); ten Brink et al. (2009). This suggests that different landslide behavior could be expected in regions of different bathymetric smoothness/regularity.

Information on sediment properties for the GOM comes from publicly available data of the Deep Sea Drilling Project (DSDP, 1966-1983), Ocean Drilling Program (ODP, 1985-2003), and Integrated Ocean Drilling Program (IODP, 2003-2013). Locations where deep (>100 m below the sea floor) sediment data exists are used to construct transects across the GOM continental slope. Specifically, in this study, sediment data is obtained from IODP Leg 308 Site 1319A in the northwest GOM, DSDP Leg 96 Site 619 in the north central GOM, and ODP Leg 100 Site 625B in the northeast. We thus draw three transects across the GOM continental slope through these drilling sites. These transects and the locations of the drilling sites are shown in Figure 3. Transects are labeled as Transect A through site IODP 308-1319A, Transect B through site DSDP 96-619, and Transect C through site ODP 100-625B. The bathymetry profile along each of these transects is shown in Figure 4. Transects A and B exhibit very irregular bathymetry due to movement of salt and overlying sediments in this province. However, we note that the first approximately 120 km of Transect B is highly irregular, while from approximately 150 km on the transect displays a smoother, more regular profile with a very clear slope increase defining the Sigsbee Escarpment. Due to the differences in submarine landslide size seen in different bathymetric regions McAdoo et al. (2000); ten Brink et al. (2009), we expect these two regions of Transect B to show different behavior in terms of landslide potential. Therefore, Transect B is subsequently partitioned into two sections: Transect B1 from the beginning to roughly 120 km, and Transect B2 from approximately 150 km to the end of the transect. Transect C lies across the northern part of the West Florida Slope carbonate platform and clearly exhibits very smooth and regular bathymetry with the well-defined steep slope of the Florida Escarpment.

The sediment properties obtained from the drilling site data are bulk density, ρ_S, and undrained shear strength, su. While some variability in sediment properties along each transect is expected, our data is limited to the drilling site locations, prompting us to assume the data from each drilling site to be valid along the entirety of its respective transect. This seems to be a reasonable first order approximation assuming the variability would have a minimal effect on MCS calculations.

Within the MCS routine, one million sets of random values are chosen for depth, area, volume, and length based on their distributions. Depth is normally distributed, while area, volume, and length are lognormally distributed. These parameters are selected as essential based on the necessity of determining a location and size for the trial landslide. Clearly, depth is essential to determining a trial landslide location along the transect. In addition, area, volume, and length are chosen as the critical size parameters based on trends seen in the data. Submarine landslide volume and area are very well-correlated, as shown by McAdoo et al. (2000) for slides off the west, east, and GOM coastal regions of the United States and by ten Brink et al. (2006) for slides off the north coast of Puerto Rico. Specifically for the past GOM SMF events used here, volume and area have a strong correlation coefficient of

Table 1: Measured data from previously identified submarine landslides in the GOM McAdoo et al. (2000), including the three ancient landslides East Breaks, Mississippi Canyon, and West Florida ten Brink et al. (2009). Landslide "Type" refers to either blocky (B), slump (S) or translational/disintigrative (T), as defined in McAdoo et al. (2000). Landslide numbers 26-28 are the ancient landslides East Breaks (EB), Mississippi Canyon (MC), and West Florida (WF). Values of N/A in the table indicate no data for that parameter is available.

Landslide Number	Lat (deg)	Lon (deg)	Type	Area (km^2)	Depth at Headscarp (m)	Length (km)	Width (km)	W/L	Headscarp Thickness (m)	T/L	Volume (km^3)	Adjacent Seafloor Slope (deg)	Failed Slope (deg)
1	26.25	-93	T	452	-1918	48.43	9.33	0.19	60	0.001	13.56	1.1	1
2	27.42	-92.49	S	44	-1423	9.43	4.67	0.50	140	0.015	3.08	2.1	5.8
3	27.39	-92.37	T	29	-1469	7.91	3.67	0.46	111.7	0.014	1.62	3	3.3
4	27.4	-92.27	S	62	-1356	9.97	6.22	0.62	148.3	0.015	4.60	3.1	4.9
5	27.3	-92.19	T	48	-1301	9.53	5.04	0.53	75	0.008	1.80	5.5	4.3
6	26.67	-92.26	T	52	-2024	13.60	3.82	0.28	200	0.015	5.20	5	2.8
7	26.67	-92.19	B	15	-1874	3.28	4.57	1.39	160	0.049	1.20	11.5	7.5
8	26.28	-92.14	T	15	-2053	13.91	1.08	0.08	110	0.008	0.83	1.1	2.5
9	26.36	-91.98	T	10.3	-2019	5.84	1.77	0.30	203.3	0.035	1.05	6	5.1
10	26.74	-91.61	T	1156	-2150	69.20	16.71	0.24	263.3	0.004	152.19	N/A	0.9
11	27.29	-91.41	B	9.6	-1757	5.44	1.77	0.32	160	0.029	0.77	12	8.6
12	27.11	-91.41	T	34	-1733	13.34	2.55	0.19	60	0.004	1.02	2.5	2.1
13	27.94	-91.32	B	143	-1076	11.80	12.12	1.03	176.3	0.015	12.61	5	6
14	26.21	-91.19	T	28	-2399	6.21	4.51	0.73	191.7	0.031	2.68	5.1	7.2
15	27.79	-91.18	B	42	-1332	6.69	6.28	0.94	172.5	0.026	3.62	8.1	3.2
16	28.03	-90.95	T	70	-910	4.76	14.71	3.09	146.7	0.031	5.13	3.1	4.4
17	26.51	-90.88	T	148	-2262	12.86	11.51	0.90	315	0.024	23.31	7.5	10.9
18	26.72	-90.72	T	55	-2395	6.84	8.04	1.18	255	0.037	7.01	9.9	8.1
19	27.9	-90.54	T	40	-1091	3.64	10.98	3.01	161.3	0.044	3.23	4.4	4.5
20	27.57	-90.24	T	748	-1404	42.48	17.61	0.41	55	0.001	20.57	1	0.9
21	27.46	-90.04	T	5509	-2328	180.91	30.45	0.17	53.8	0.0003	148.19	1.3	1.1
22	28.01	-89.42	T	1394	-2228	75.31	18.51	0.25	73.8	0.001	51.44	1.6	0.9
23	29.1	-88.93	T	2913	-1136	126.54	23.02	0.18	48.3	0.0004	70.35	2	1
24	29.95	-87.64	T	2460	-1414	90.23	27.27	0.30	97.5	0.001	119.93	1.3	1
25	30.87	-87.02	T	1098	-121	85.75	12.80	0.15	60	0.0007	32.94	1.9	1.9
26 (EB)	27.71	-94.69	T	519	-150	39.02	13.3	0.34	160	0.004	21.95	1.1	N/A
27 (MC)	28.51	-89.78	T	3687	-250	145.16	25.4	0.17	300	0.002	425	1	N/A
28 (WF)	26.09	-84.75	T	647	-800	18.97	34.1	1.80	150	0.008	16.2	5.8	N/A

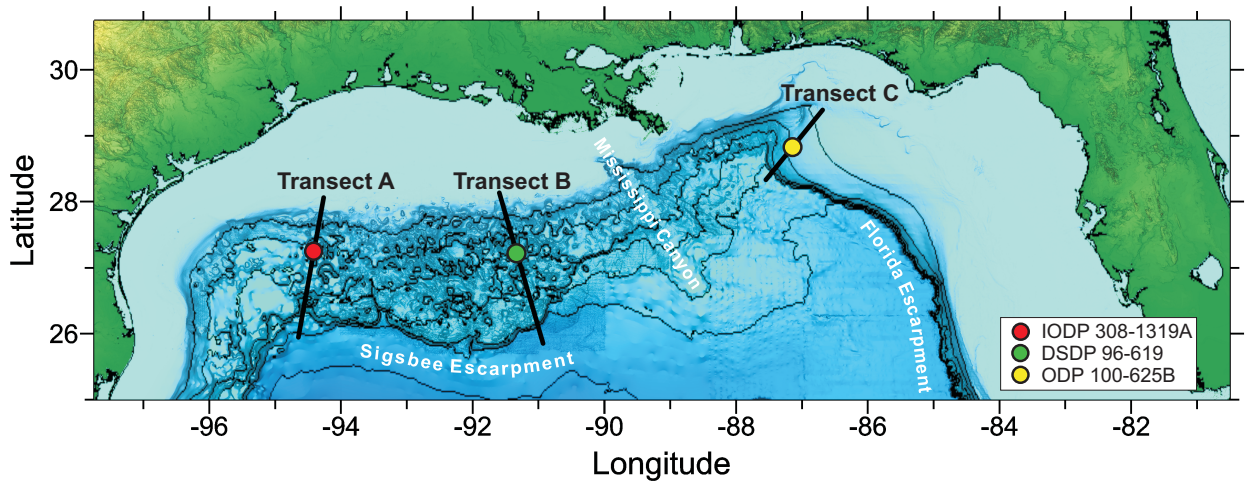

Figure 3: Locations of GOM sediment data used from the IODP (red circle), DSDP (green circle), and ODP (yellow circle) drilling surveys and transects (black lines) used in this study. Bathymetry contours are at 500 m levels. Bathymetric features are indicated for reference.

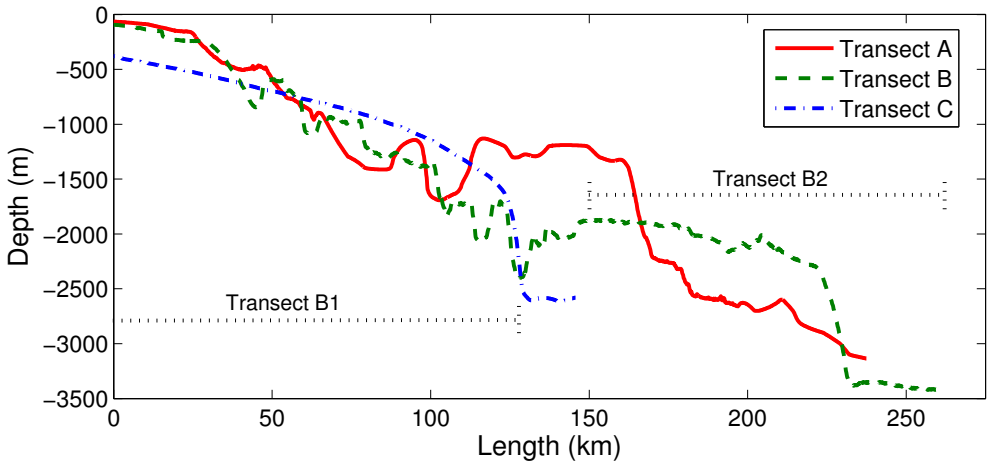

Figure 4: Bathymetry profiles for Transects A (solid), B (dashed line), and C (dot-dashed) across the GOM continental slope. Dotted black lines show extents of Transects B1 and B2 split from Transect B.

ρ=0.9572 (based on the associated normal distributions of the lognormal volume and area). In addition, we find that length is also well-correlated with both volume and area of GOM landslides, as seen in Figure 5. The correlation coefficients for these parameters are 0.9331 for length and area, and 0.8698 for length and volume.

These evident mutual-correlations led us to incorporate these trends within our MCS technique. In this way, our MCS methodology deviates from those of Maretzki et al. (2007), Grilli et al. (2009), and Shigihara and Horrillo (2014), where landslide dimensions of volume, length, and thickness are determined as random values drawn independently from their re-

spective distributions. In our MCS method, in order to maintain the obvious relationships we see from the significant correlation coefficients, we implement a Cholesky decomposition of the covariance matrix for area, volume, and length, based on the outline given in Thomopoulos (2012). Through this approach, the individual variables still follow their respective independent distributions, yet are allowed to vary based on their mutual correlations.

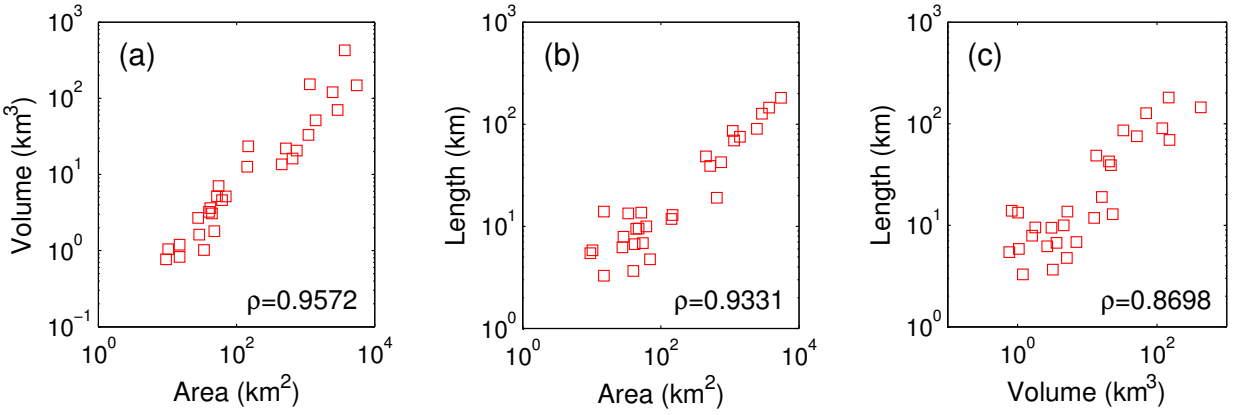

Figure 5: Data correlations from GOM observational submarine landslide data for (a) volume and area, (b) length and area, and (c) length and volume. Correlation coefficients ρ are also shown.

This approach is as follows. Since area (A), volume (V), and length (L) follow lognormal distributions, the natural logarithm of these variables are normally distributed. The associated normal distributions for area, volume, and length have means of μ_A, μ_V, and μ_L, respectively. The Cholesky decomposition of the covariance matrix Σ for the associated multivariate normal distribution is given by

$$\Sigma = CC^T, \tag{13}$$

with C a lower triangular matrix. Then, from a set of random normal variables $u_i \sim N(0,1)$, correlated normal variables X, Y, and Z can be determined by

$$\begin{bmatrix} X \\ Y \\ Z \end{bmatrix} = C \begin{bmatrix} u_1 \\ u_2 \\ u_3 \end{bmatrix} + \begin{bmatrix} \mu_A \\ \mu_V \\ \mu_L \end{bmatrix} \tag{14}$$

Then, the correlated lognormal variables A, V, and L are found from

$$\begin{bmatrix} A \\ V \\ L \end{bmatrix} = exp([X, Y, Z]^T) \tag{15}$$

Width (W) of the landslide is then calculated simply as $W = A/L$. Likewise, slide thickness (T) is determined as $T = 2V/A$.

Table 2 details the distributions and the values used in the MCS model, as determined from McAdoo et al. (2000) and ten Brink et al. (2009). The values μ and σ are the mean and standard deviation, respectively, of the normal distribution or, in the case of a lognormal distribution, they correspond to the parameters of the distribution (i.e. the mean and standard deviation of the natural logarithm of the distribution). Note that while distributions are indicated for Width and Width/Length, these are for informational purposes only; only the distributions for depth, area, volume, and length are used to determine random landslide parameters within the MCS model. Certain constraints were imposed on the range of some landslide dimensions in the MCS model in order to maintain physically relevant trial landslides, based on the ranges seen in the observational data (see Table 1) McAdoo et al. (2000); ten Brink et al. (2009). These constraints are given in the "MCS Constraints" column. The range of depths allowed in the MCS model varies across transects depending on the actual bathymetry so that failures can only occur at depths within the depth range of the individual transect. The value of "N/A" for volume indicates that no limitations were set for the volume a trial landslide could have. Values for area, length, and width were allowed to extend outside the range of those seen in the data in order to allow for variability from previous measurements, but maximum values were restricted to two standard deviations from the mean of the associated normal distributions. These maximum values correspond to a cumulative probability of approximately 0.977. This constraint was imposed in order to allow landslides larger than those which occurred previously while excluding those which may become unreasonably large with respect to the size of the GOM itself. Length is additionally limited for each transect in that the landslide length from the headscarp location cannot go beyond the end of the transect. The constraints for width/length are taken approximately from the data range in order to prevent unnaturally long and narrow failures and, likewise, those which are excessively wide.

Table 2: Distributions and range of values used for landslide location and size in the MCS model. Parameters μ and σ are the mean and standard deviation, respectively, in the case of a normal distribution, while for a lognormal distribution, they correspond to the parameters of the distribution, i.e. the mean and standard deviation of the logarithm of the distribution.

Parameter	Distribution	μ	σ	MCS Constraints
Depth (m)	normal	1513.32	661.76	varies
Area (km^2)	lognormal	5.03	1.95	$0 - 7659.5$
Volume (km^3)	lognormal	2.21	1.78	N/A
Length (km)	lognormal	2.92	1.22	$0 - 210.73$
Width (km)	lognormal	2.12	0.928	$0 - 53.28$
Width/Length	lognormal	-0.796	0.932	$0.07 - 2.9$

Once the landslide dimensions are selected, we perform a slope stability analysis to determine if the trial landslide will fail. The factor of safety of the trial landslide is calculated based on the infinite slope method for translational failures, assuming large-scale slides with $L >> T$; this method is reasonable for the GOM given the observed data and relatively mild slopes.The available sediment data indicates that sediments at the sites considered here are mostly fine-grained cohesive soils consisting of predominantly silty clay, which under

dynamic earthquake loading would be expected to exhibit undrained failures (Morgenstern, 1967). Thus, the factor of safety FS for a cohesive, translational slide is given considering a total stress analysis relating sediment undrained shear strength su to the shear stress τ, which combines the downslope gravity force with a pseudo-static horizontal component for earthquake loading Morgenstern (1967); ten Brink et al. (2009):

$$FS = \frac{su}{\tau} = \frac{su}{Tg((\rho_S - \rho_W)\sin\beta\cos\beta + k\rho_S\cos^2\beta} \tag{16}$$

where g is the gravitational acceleration constant; ρ_S and ρ_W are the densities of the landslide sediment and water, respectively; β is the failed slope angle; and k is the seismic coefficient, defined as $k = PHA/g$. A trial landslide is considered a failure event if $FS < 1$, that is, when the shear stress on the slip surface exceeds the shear strength of the sediment.

Since an SMF is assumed to be triggered by an earthquake in this model, following Grilli et al. (2009), the probability of a tsunamigenic SMF, P_{SMF}, is calculated as the joint probability of exceedance of the earthquake, P_{PHA}, with the probability that that earthquake causes a calculated trial landslide to fail and produce a tsunami wave, P_f, so that

$$P_{SMF} = P_{PHA}P_f \tag{17}$$

where $P_{PHA} = 1/\lambda$ and $P_f = n/N$, with n the number of tsunamigenic failures for a certain earthquake return period λ and N the total number of trial landslides generated by the MCS model for a given transect (here, $N = 1,000,000$). The resulting return period of the tsunamigenic SMF is given by $\lambda_{SMF} = 1/P_{SMF}$. In our model, the period of return λ is increased incrementally from 10 years to 10,000 years for each trial landslide to determine the minimum earthquake return period and PHA (if any) that will cause that configuration to fail based on the calculated FS. By the nature of FS, any larger PHA, and therefore larger return period, will induce a failure as well.

3.2 Probabilistic Submarine Landslide Results

Figure 6 shows example results for Transect A of volume versus area, length versus area, and length versus volume for tsunamigenic failures calculated by the MCS model (blue circles) as compared to observational data (red squares). Overall sizes of tsunamigenic failures generated by the MCS routine are consistent across the transects, although smaller SMFs are possible in Transect C as compared with the others. We find that implementing the Cholesky decomposition approach for random correlated variables within the MCS model results in values that encompass the historical data very well while still exhibiting variability that would be expected in nature. In cases where the observational data lies outside the model results, the MCS results are restricted due to either the constraints imposed within the MCS model as discussed above or to the limitation that the maximum return period of 10,000 years that can be accurately estimated by the MCS model; any configurations which result in a return period greater than 10,000 years are excluded. Additionally, since data for previous SMF events were combined to determine the governing distributions, not considering local bathymetric influences, the large observed slides which lie outside of the

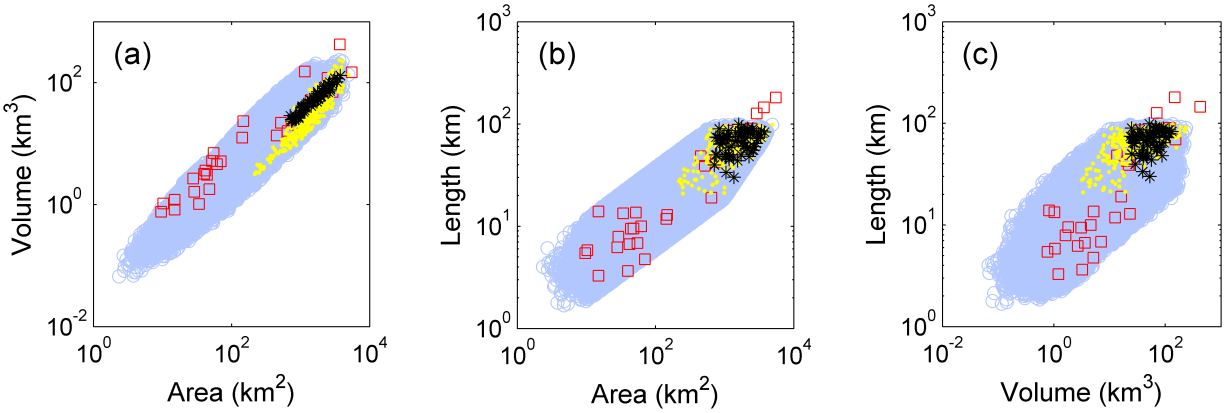

Figure 6: MCS parameter results for Transect A for (a) volume versus area, (b) length versus area, and (c) length versus volume. Blue circles are the tsunamigenic MCS model results ($\eta \geq 0.02$ m). Red squares are observational data (same as in Figure 5). Yellow dots correspond to the extreme tsunami amplitude η_{max} events. Black stars indicate the subset of extreme events with return periods in the first 100 years $\lambda_{S_{100}}$.

MCS model results for a given transect may be physically unrealistic for that region due to the local bathymetry.

The maximum credible landslide for each transect is defined here as the failure that produces the largest maximum tsunami amplitude and that occurs with the highest rate of recurrence or highest probability. Since several different landslide configurations may fail for a given λ, leading to multiple events with the same return period λ_{SMF} but with different tsunami amplitudes, we identify the extreme value of tsunami amplitude, η_{max}, for each λ_{SMF}. The η_{max} event which has the highest rate of recurrence, or shortest return period, will describe the maximum credible event. The smallest SMF return periods calculated from the joint probability are on the order of thousands of years, so probabilities are small, and negligible change in probability is seen as the return period is varied by a few hundred years. In an effort to determine a single probabilistic source for each transect, all events with essentially the same probability are considered collectively. Thus, the η_{max} extreme value events with return periods that fall into the first 100 years from the minimum calculated return period for a specific transect are considered representative of the highest-probability SMF event for that transect; this 100-year return period range is termed $\lambda_{S_{100}}$. For example, if the minimum return period for a transect is calculated to be 1000 years, all η_{max} events for that transect with a return period less than or equal to 1100 years are collected as a set of extreme events with probability 0.001. Table 3 shows the range of minimum return periods $\lambda_{S_{100}}$ as well as the range of earthquake return periods λ required to trigger these tsunamigenic failures for each transect. In Figure 6, the η_{max} extreme value events which initiate the maximum tsunami amplitudes for Transect A are indicated by yellow dots. The set of η_{max} events with return periods in $\lambda_{S_{100}}$ (the most likely extreme events) are indicated by black stars.

The probabilistic maximum credible event (PMCE) for a transect is then determined by

Table 3: Minimum return period range $\lambda_{S_{100}}$ for tsunamigenic SMFs generated by the MCS method, with number of events with return periods in that range, and the corresponding return period range of the triggering earthquake, λ.

Transect	A	B1	B2	C
# of events	64	34	2	4
$\lambda_{S_{100}}$ (yrs)	$7700 - 7800$	$5400 - 5500$	$4700 - 4800$	$550 - 650$
λ (yrs)	$3940 - 4570$	$3460 - 3790$	$340 - 350$	$130 - 160$

Table 4: Mean values of landslide location and dimension from all extreme-amplitude (η_{max}) tsunami events with return periods in $\lambda_{S_{100}}$. These values are used to create the probabilistic submarine landslide (PSL) sources in the 3D model.

Probabilistic Submarine Landslide Source	A	B1	B2	C
Depth (m)	85	130	2323	1098
Area (km^2)	1686	3118	282	1529
Volume (km^3)	57	69	45	315
Length (km)	68	96	13	34
Width (km)	25	32	22	46
Thickness (m)	67	44	323	404
η (m)	61	36	3.0	19

calculating mean values for location (depth) and dimension (area, volume, length, width, and thickness) from all of that transect's η_{max} events with a return period in $\lambda_{S_{100}}$. These PMCE landslide scenarios determine the four probabilistic submarine landslides (PSLs) we use as landslide tsunami sources in the GOM, and are named based on the name of the transect (A, B1, B2, C) they originate from: PSL-A, PSL-B1, PSL-B2, and PSL-C, for each respective transect. The mean dimensions for each PSL are given in Table 4. These mean dimensions are used to create the PSLs that are used as tsunami sources in the 3D model.

4 Numerical Domains and Tsunami Sources

Numerical simulations using a 3D model were carried out to determine initial tsunami wave amplitudes (initial tsunami source) generated by massive runoff of submarine landslide sediments along shelf breaks and escarpments in the northern part of the GOM. In total, seven (7) massive landslide configurations were created assuming an unstable (gravity-driven) sediment deposit condition. Three (3) of these massive sediment configurations are obtained from the geological footprint of historical events (ten Brink et al., 2009). The other four (4) massive landslide sediment configurations were obtained by a probabilistic methodology based on previous work by Maretzki et al. (2007); Grilli et al. (2009), and Shigihara and Horrillo (2014), see also Section 3. After the intial tsunami wave was generated, a 2D model was used to model tsunami amplitude throughout the GOM and inundation for specific communities. Using the 2D model, maximum tsunami wave amplitude, energy focusing, and arrival time in the entire GOM basin were determined using a coarser grid resolution of 1 arcminute = 60 arcseconds = ~ 1.8 km, which is depicted in Table 5 and Figure 7. This set of numerical simulations facilitated the selection of five (5) communities most at-risk and for which to develop the first set of detailed tsunami inundation maps. For the selection of a particular community and to obtain detailed tsunami inundation results, several factors were considered: 1) the proximity to the submarine landslide generation region; 2) the tsunami energy focusing or maximum surface elevation obtained using the coarser resolution GOM basin depicted in Table 5 and Figure 7; 3) the availability and quality of existing local bathymetry/topography or high-resolution Digital Elevation Model (DEM) data to use for detailed runup and inundation extent in that region; and 4) the community size in terms of the affected population and/or regional infrastructure.

Table 5: Coordinate limits for the entire GOM domain with grid resolution of 60 arcseconds (1 arcminute) to obtain maximum wave amplitude and arrival time of the first tsunami positive wave, see also Figure 7

Entire Gulf of Mexico 2D Domain (Resolution 60 arcseconds)	
Longitude	$97.9°W$ - $80.20°W$
Latitude	$18.10°N$ - $30.75°N$
$dx = dy$	1 arcminute = 60 arcseconds $=\sim 1.8$ km
Maximum Water Depth	$7,243$ m
dt	2.0 seconds
# of Cells in the x, y-directions	1063×760
Total # of Cells	$807,880$

The five (5) communities selected for detailed tsunami inundation modeling are: South Padre Island, TX; Galveston, TX; Mobile, AL; Panama City, FL; and Tampa, FL. For the detailed tsunami runup and inundation extent of the five selected communities, a finer grid resolution of 15 arcseconds was used for the northern part of the GOM. The 15 arcsecond resolution grid encompasses the northern part of the GOM as depicted in Table 6 and Figure 8. The northern GOM domain is referenced as the main domain which propagates

and transfers the tsunami signal to the finer domains through grid nesting, indicated by red rectangles along the northern coastline of the GOM in Figure 8.

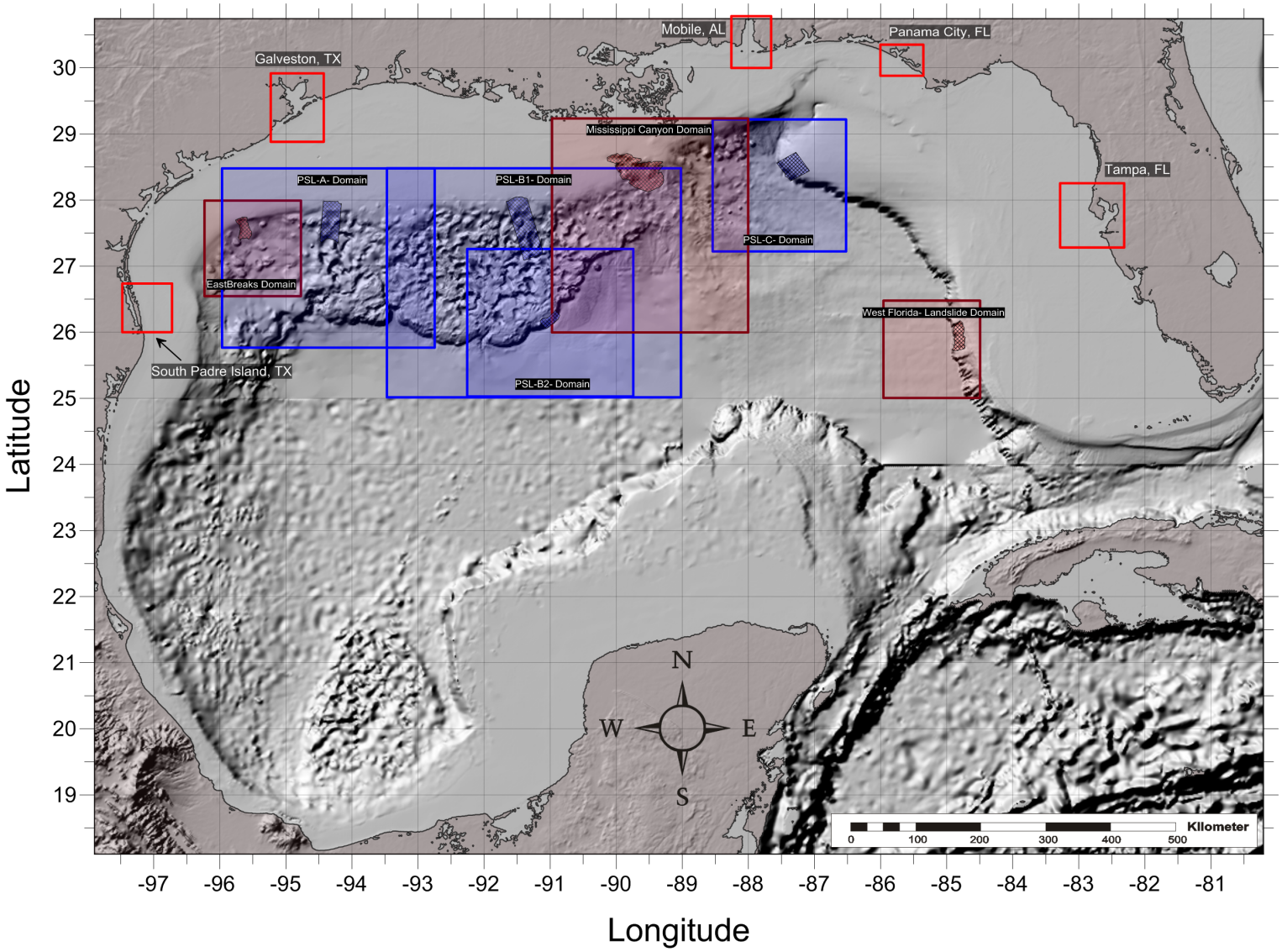

Figure 7: Calculation domains and bathymetry to obtain tsunami maximum wave amplitude, energy focusing and arrival time in the entire GOM. Red filled rectangles: 3D domains for historical submarine landslide calculations; hatched red region inside 3D domains: historical submarine landslides; blue filled rectangles: 3D domains for probabilistic submarine landslide calculations; hatched blue region inside 3D domains: probabilistic submarine landslides. Red rectangles along coastline indicate regions where tsunami inundation maps have been developed.

Table 6: Coordinate limits for the 2D northern GOM domain with grid resolution of 15 arcseconds to obtain detailed calculation of maximum wave amplitude, wave propagation, and runup on coastal regions, see also Figure 8

Northern Gulf of Mexico 2D Domain (Resolution 15 arcseconds)	
Longitude	$97.75°W$ - $80.50°W$
Latitude	$25.00°N$ - $30.75°N$
$dx = dy$	15 arcseconds $=\sim 460$ m
Maximum Water Depth	$3,706$ m
dt	0.5 second
# of Cells in the x, y-directions	4141×1381
Total # of Cells	$5'718,721$

It is important to clarify that tsunami generated by submarine landslides are expected to be stronger in the vicinity of the generation area due to the fact that the generated outgoing wave falls in the intermediate water wave regime as it propagates into deeper water, losing considerably most of its energy, contrary to the side- and back-going propagating waves which fall in the shallow water wave regime. In addition to being used to obtain detailed tsunami runup and inundation depth/extent for the five selected communities by the nesting process, the northern GOM domain better produces the overall details of the maximum tsunami wave amplitude and tsunami energy focusing than the larger 1 arcminute domain. In Figure 8, 3D tsunami wave calculation domains are indicated by filled rectangles. The red filled rectangles indicate computational domains where the geological footprint of historical landslide events (ten Brink et al., 2009) has been used to determine the initial dynamic tsunami wave or initial source caused by a given submarine landslide configuration, depicted by a red hatched region inside the computational domain. Blue filled rectangles indicate computational domains where the initial dynamic tsunami wave is determined by synthetic submarine landslide configurations created using the probabilistic approach (see Section 3) and depicted by the blue hatched interior region. One important step in the process of coupling the 3D model results (the initial dynamic tsunami wave) with the 2D model to compute the detailed wave propagation, runup, and inundation extent, is to determine the right moment to transfer the 3D tsunami field information or variables (velocity field, u, v, w and sealevel, η). The right time to transfer the information from the 3D to the 2D model is determined by the total energy of the water transferred by the submarine landslide to the water (see Sections 2.3-2.4). The 3D domain must be large enough to fully develop the generated waves before they leave the domain boundaries, and the wave energy should reach a maximum value, indicating that the generated waves had been fully or mostly developed. If the domain size-energy considerations have been fulfilled (which is obtained by trial and error), then the 3D field information is converted to 2D by simple column-wise depth averaging and input as the dynamic initial condition (hot start) into the 2D non-hydrostatic numerical model for calculation of detailed runup and inundation extent.

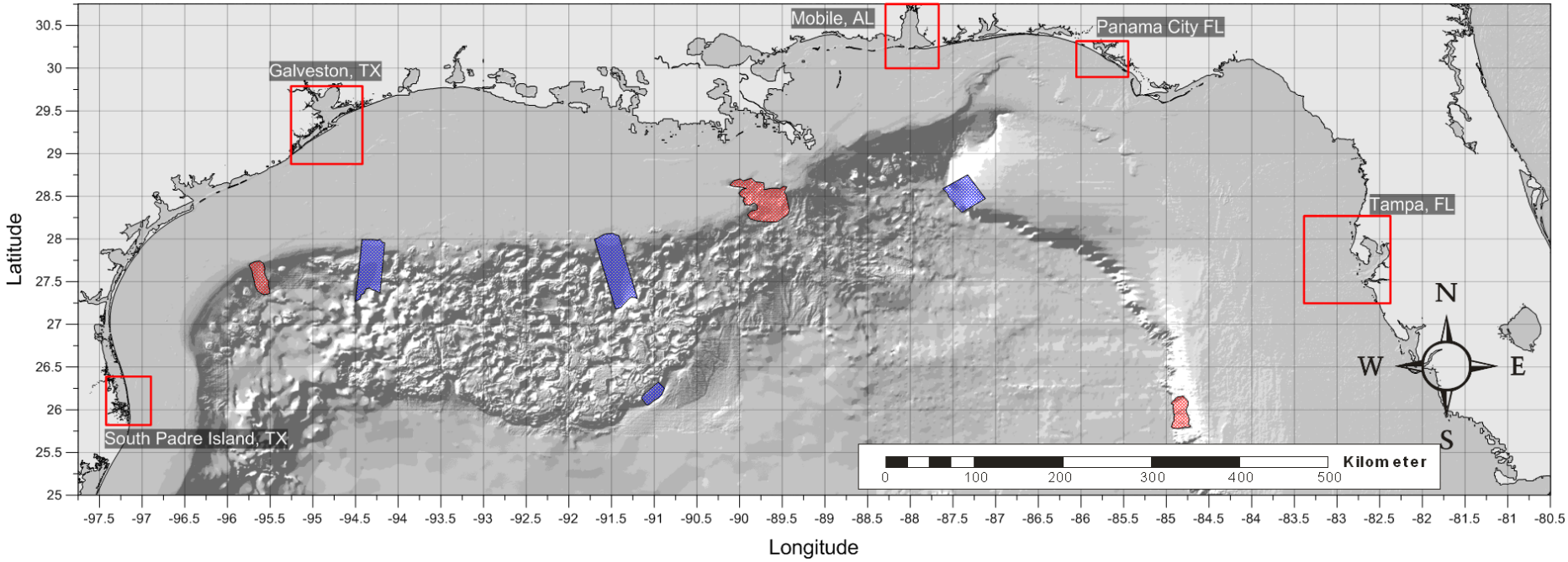

Figure 8: Northern GOM domain and bathymetry to obtain detailed tsunami runup and inundation extent at the five selected communities. Hatched red regions: historical submarine landslides; hatched blue regions: probabilistic submarine landslides. Red rectangles along coastline indicate regions where tsunami inundation maps have been developed.

Tables 8 to 20 summarize coordinate limits of the 3D calculation domain for each landslide event and other important information including: spatial resolution, time step size, domain maximum water depth, number of computational cells, and time at which the 3D model is stopped, which corresponds to the elapsed time of landslide deformation from the onset of sediment failure to the time of maximum potential energy transferred from the landslide to the water. The elapsed time of the landslide deformation is determined by the 3D domain size and the total energy of the water induced by the submarine landslide to obtain the initial dynamic tsunami surface deformation, as discussed above and in Sections 2.3-2.4.

Figures 9, 13, 17, 21, 25, 29, and 33, together with Tables 7 to 19, respectively, depict some important characteristics of the submarine landslides used in this work. The figures portray the 3D model domain limits for each of the submarine landslides and indicate the location and the pre-failure landslide configuration. The tables present general information on the submarine landslides and important characteristics required for the numerical calculations of the initial dynamic surface deformation. Two values for volume are given for the probabilistic landslides in tables 9, 11, 13, and 17: Probabilistic Average Volume and 3D Model Volume; this is because landslide configurations obtained from the probabilistic approach are carved out from the actual bathymetry using the probabilistic average dimensions, i.e. length, width, and headscarp thickness (excavation depth) to obtain the 3D numerical model volumes. The model volume quantities differ from the probabilistic average volume in some places due to the amount of seafloor irregularity present in that region.

4.1 Eastbreaks Submarine Landslide General Information

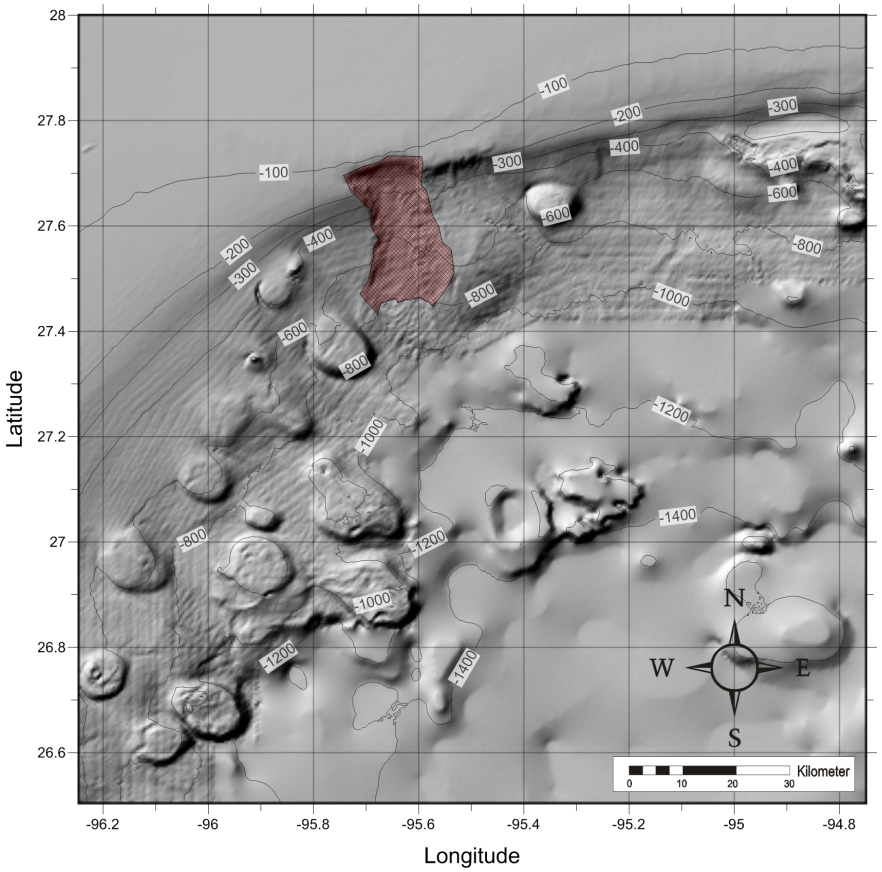

Figure 9: EastBreaks submarine landslide location, excavation limits, and surrounding bathymetry (in meters).

Table 7: Eastbreak Submarine Landslide general information

Geologic Setting	Shelf break edge
Post Failure Sedimentation:	Canyon appears to be partially filled (predominantly failure deposits with some post-failure sedimentation)
Age:	10000 - 25000 years
Maximum Credible Single Event:	Maximum: Volume: 21.95 km^3 Area: 519.52 km^2
Other Reported Volumes:	50 - 60 km^3
Excavation Depth:	$\sim$ 160 m (shelf to base of headwall scarp)
Run-out Distance:	91 km from end of the excavation and 130 km from headwall based on GLORIA mapping effort
Other Reported Run-out Distance:	160 km
3D Numerical Model volume	26.7 km^3

Figure 10 depicts tsunami arrival time of the East Breaks Submarine Landslide scenario for the entire GOM (one arcminute resolution). Figure 11 shows maximum tsunami wave amplitude using the same lower spatial resolution (one arcminute) to obtain on a global scale the energy focusing mechanisms along the continental shelf and the effect of predominant bathymetric features of the GOM like shelf break slopes, submarine escarpments, and submarine canyons. In Figure 12, maximum tsunami wave amplitude is depicted using a higher spatial resolution (15 arcseconds) to obtain more detailed information of wave behavior as waves propagate over those GOM bathymetric features.

Table 8: Coordinate limits for the EastBreaks Submarine Landslide Domain to obtain initial dynamic tsunami wave source

EastBreaks Submarine Landslide 3D Domain (Resolution 15 arcseconds)	
Longitude	$96.25°W$ - $94.75°W$
Latitude	$26.50°N$ - $28.00°N$
$dx = dy$ and dz	15 arcsec and variable $1 - 10$ m
Max. Water Depth	$1,703$ m
dt (variable)	≤ 0.50 sec
# of Cells in the x, y, z-direction	$361 \times 361 \times 350$
Total # of Cells	$45,612,350$
Elapsed time of landslide deformation	960 sec (16 min)

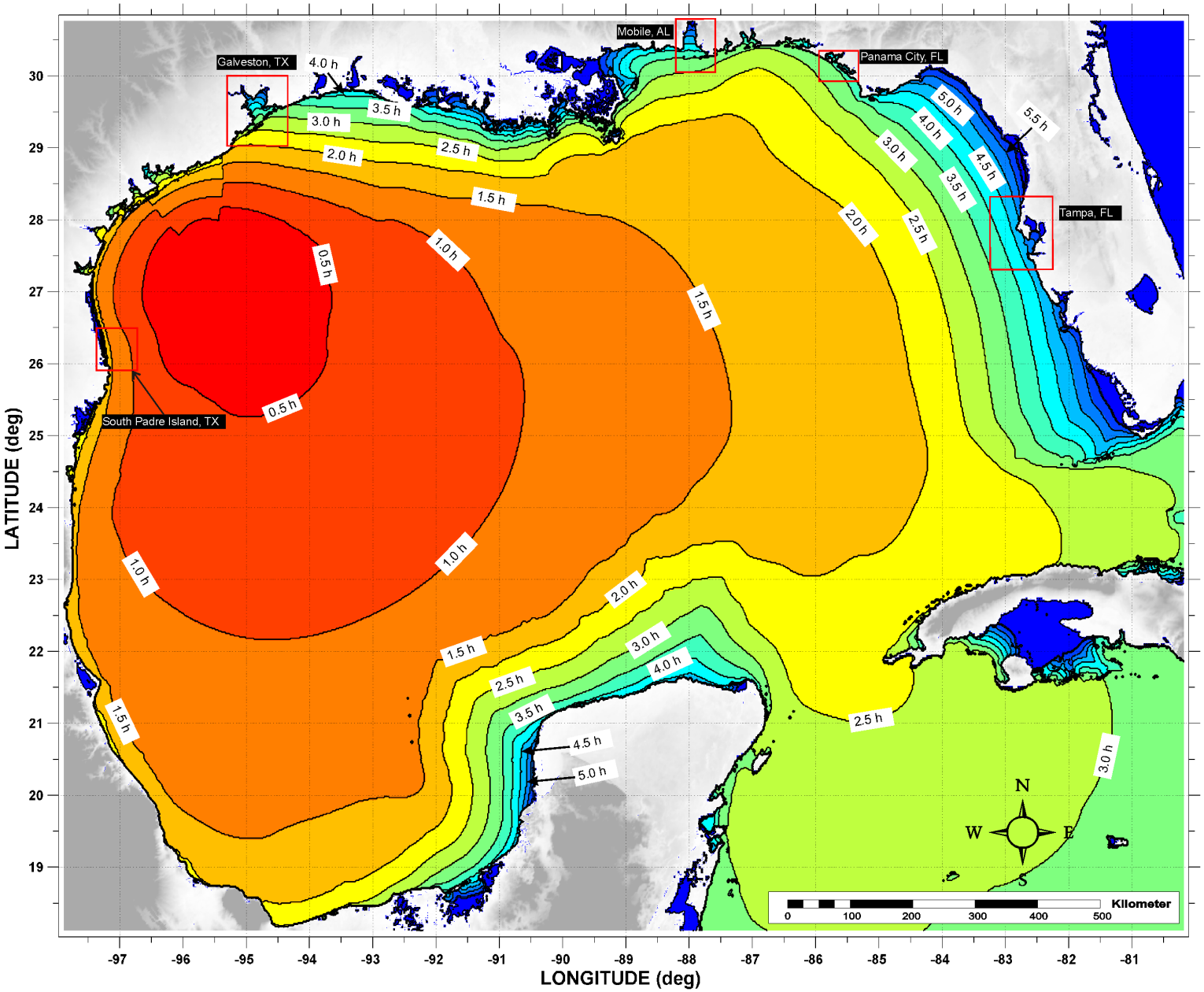

Figure 10: Tsunami arrival time for the East Breaks Submarine Landslide scenario. Red rectangles indicate regions where tsunami inundation maps have been developed.

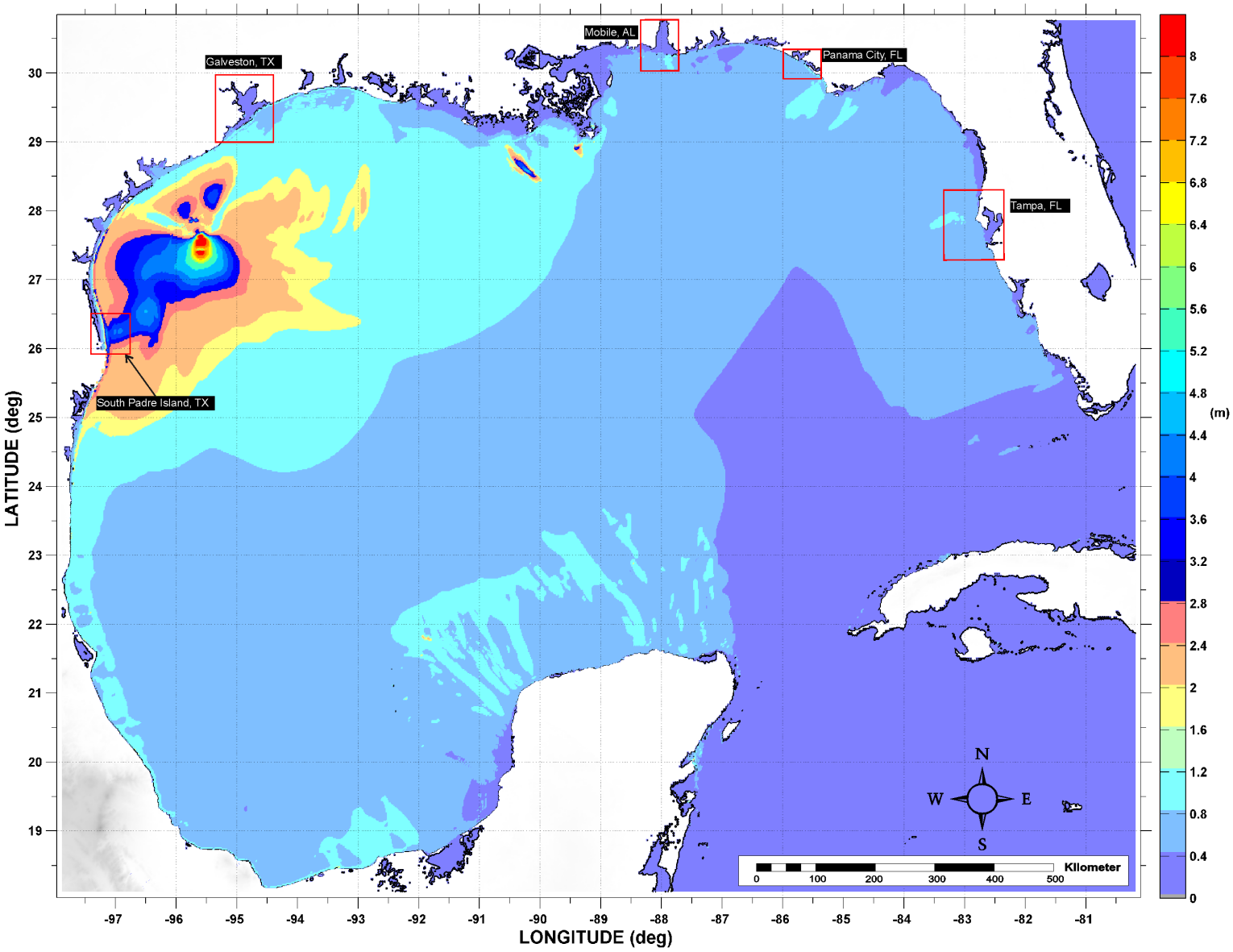

Figure 11: Maximum tsunami wave amplitude (one arcminute resolution) for the East Breaks Submarine Landslide scenario. Red rectangles indicate regions where tsunami inundation maps have been developed.

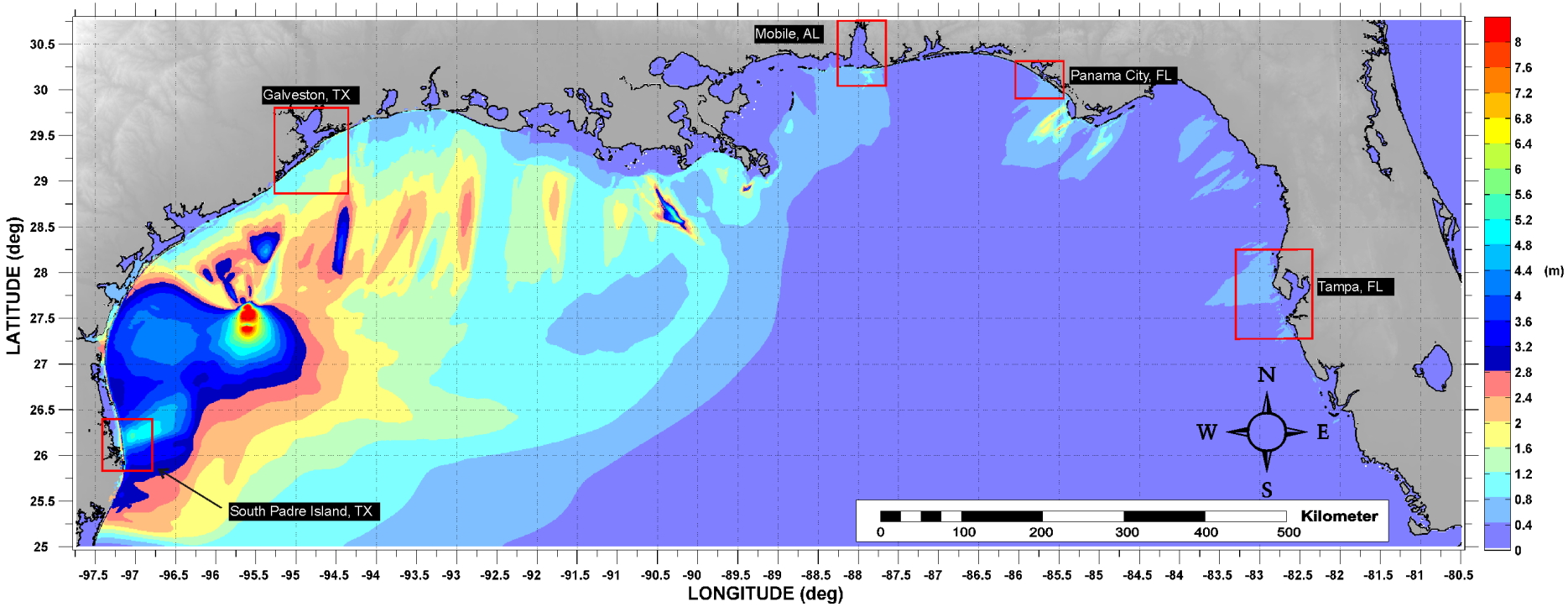

Figure 12: Maximum tsunami wave amplitude (15 arcsecond resolution) for the East Breaks Submarine Landslide scenario. Red rectangles indicate regions where tsunami inundation maps have been developed.

4.2 Probabilistic Submarine Landslide A (PSL-A) General Information

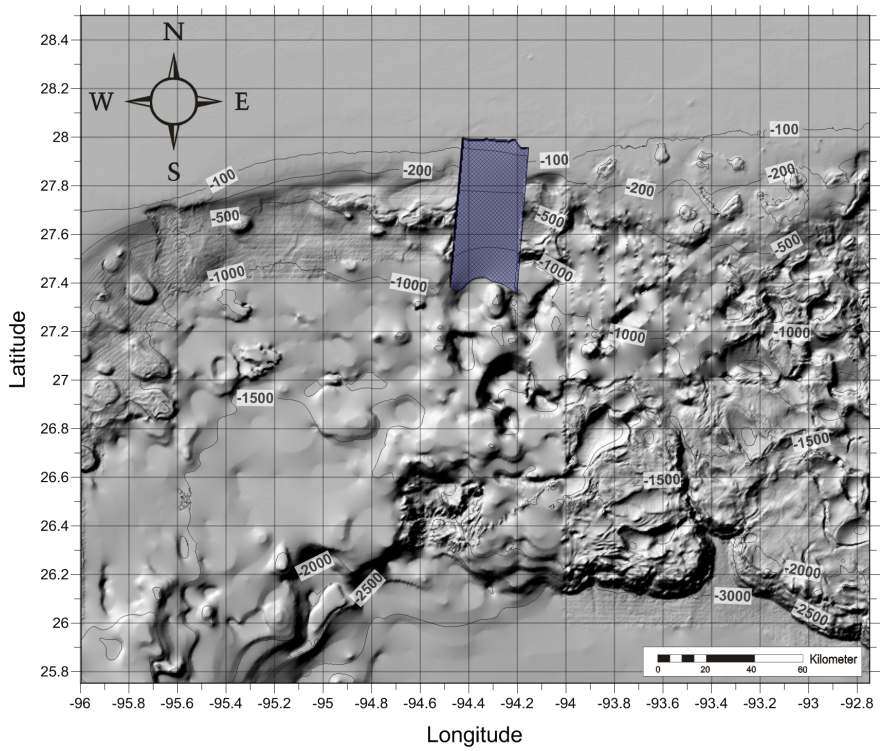

Figure 13: Probabilistic Submarine Landslide -A- location, excavation limits, and surrounding bathymetry (in meters).

Table 9: Probabilistic Submarine Landslide A

Geologic Setting	Shelf break edge
Predominant Sediment	Clay
Trigger Mechanism / Recurrence	Earthquake / $3,940 - 4,570$ years
Type of Sediment Failure	Translational
Probabilistic Tsunami Recurrence	$7,700 - 7,800$ years
Probabilistic Avg: Volume	~ 57 km^3
Area	$\sim 1,686$ km^2
Excavation: Headscarp Thickness	~ 67 m
Length	~ 68 km
Width	~ 25 km
3D Model Volume	58 km^3

Figure 14 depicts tsunami arrival time of the Probabilistic Submarine Landslide A (PSL-A) scenario (one arcminute resolution) for the entire GOM. Figure 15 shows maximum tsunami wave amplitude using the same lower spatial resolution (one arcminute) to obtain on a global scale the energy focusing mechanisms along the continental shelf and the effect of predominant bathymetric features of the GOM like shelf break slopes, submarine escarpments, and submarine canyons. In Figure 16, maximum tsunami wave amplitude is depicted using a higher spatial resolution (15 arcseconds) to obtain more detailed information of wave behavior as waves propagate over those GOM bathymetric features.

Table 10: Coordinate limits for the PSL-A Submarine Landslide Domain to obtain initial dynamic tsunami wave source

PSL-A Submarine Landslide 3D Domain (Resolution 15 arcseconds)	
Longitude	$96.00°W$ - $92.75°W$
Latitude	$25.75°N$ - $28.50°N$
$dx = dy$ and dz	15 arcsec and $1 - 34$ m
Max. Water Depth	$3,340$ m
dt (variable)	≤ 0.75 sec
# of Cells in the x, y, z-direction	$781 \times 661 \times 200$
Total # of Cells	$103,248,200$
Elapsed time of landslide deformation	1500 sec (25 min)

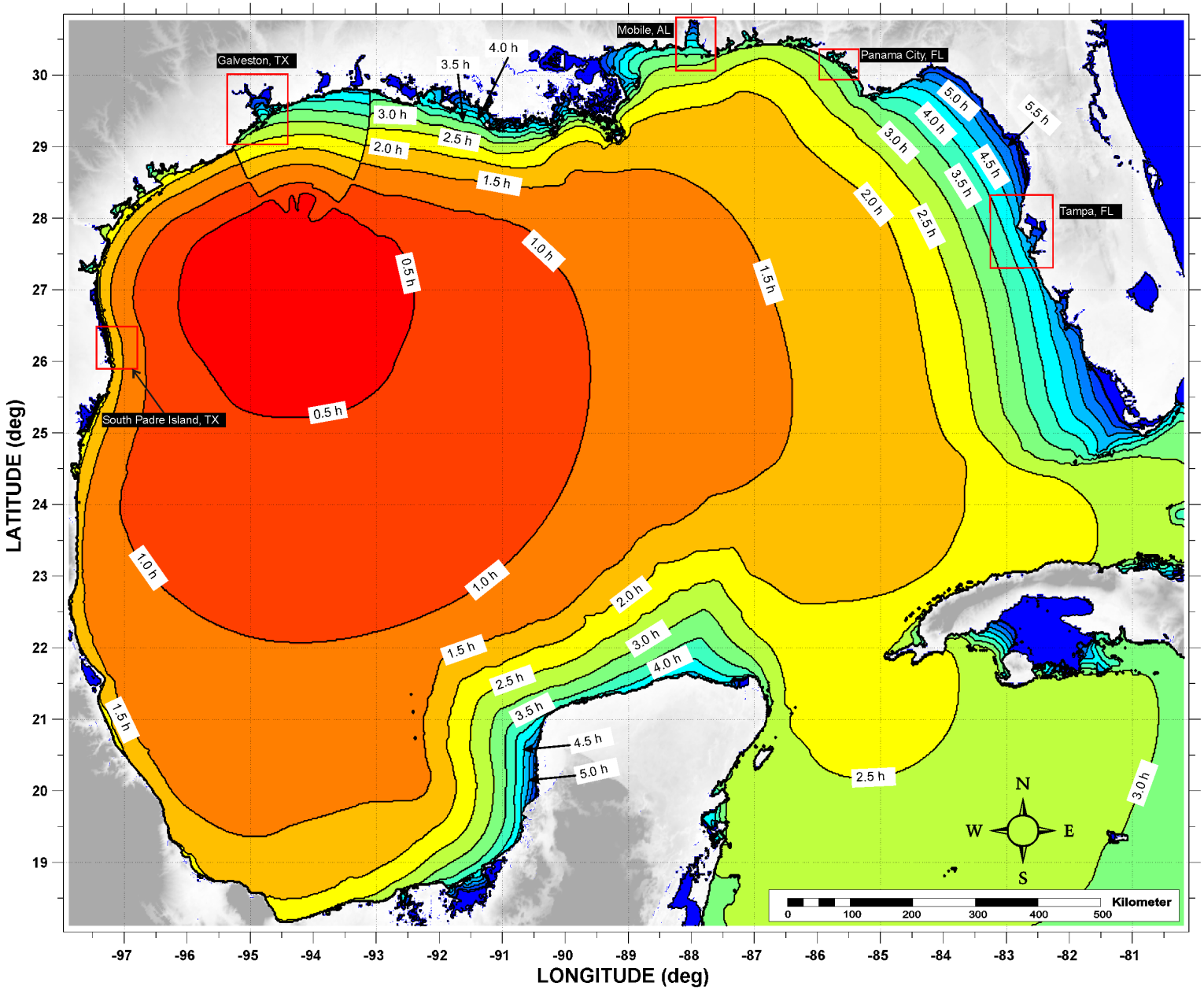

Figure 14: Tsunami arrival time for the Probabilistic Submarine Landslide -A- (PSL-A) scenario. Red rectangles indicate regions where tsunami inundation maps have been developed.

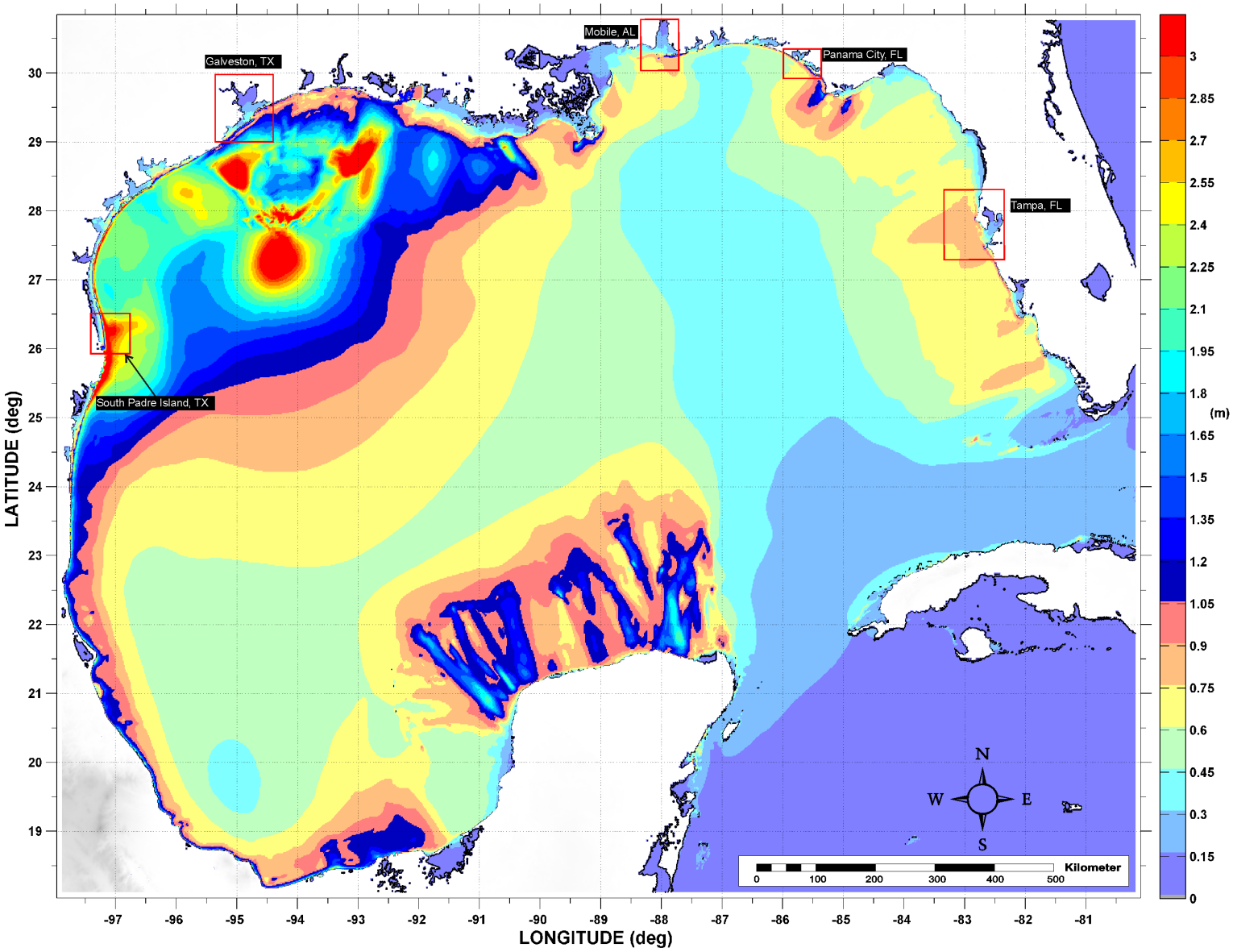

Figure 15: Maximum tsunami wave amplitude (one arcminute resolution) for the Probabilistic Submarine Landslide -A- (PSL-A) scenario. Red rectangles indicate regions where tsunami inundation maps had been developed.

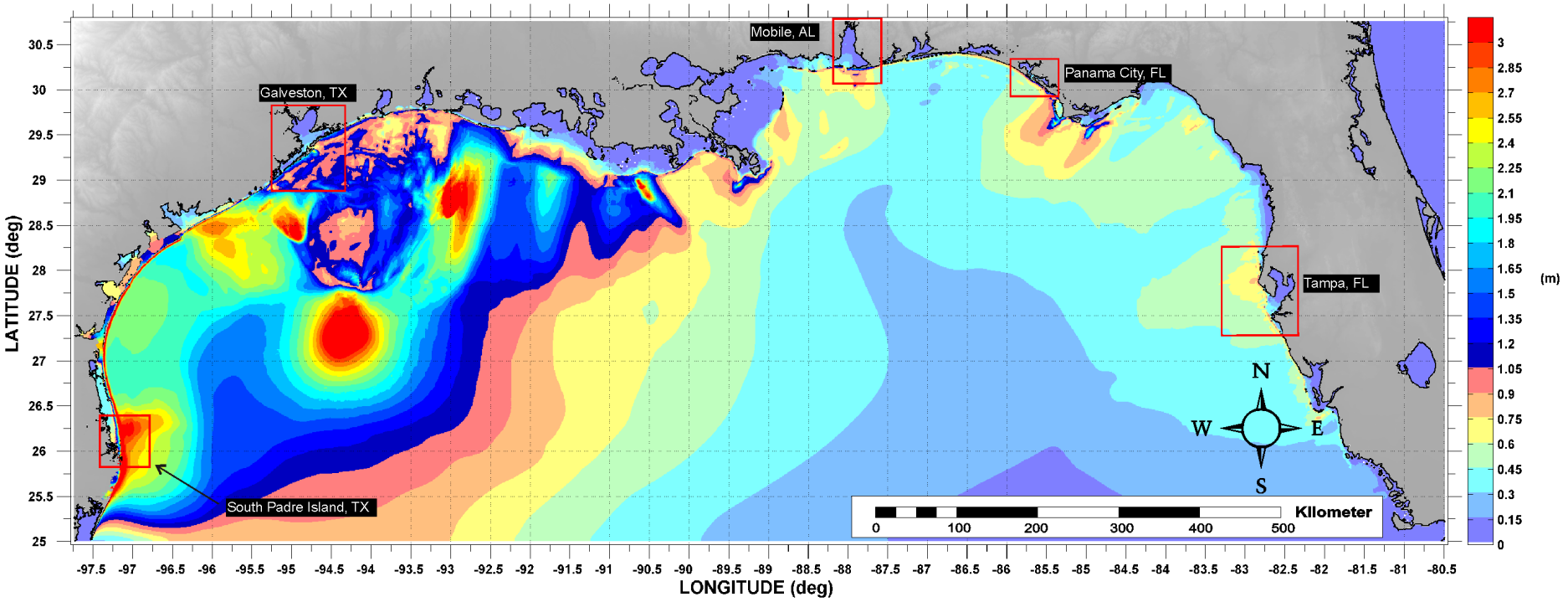

Figure 16: Maximum tsunami wave amplitude (15 arcsecond resolution) for the Probabilistic Submarine Landslide -A- (PSL-A) scenario. Red rectangles indicate regions where tsunami inundation maps have been developed.

4.3 Probabilistic Submarine Landslide B1 (PSL-B1) General Information

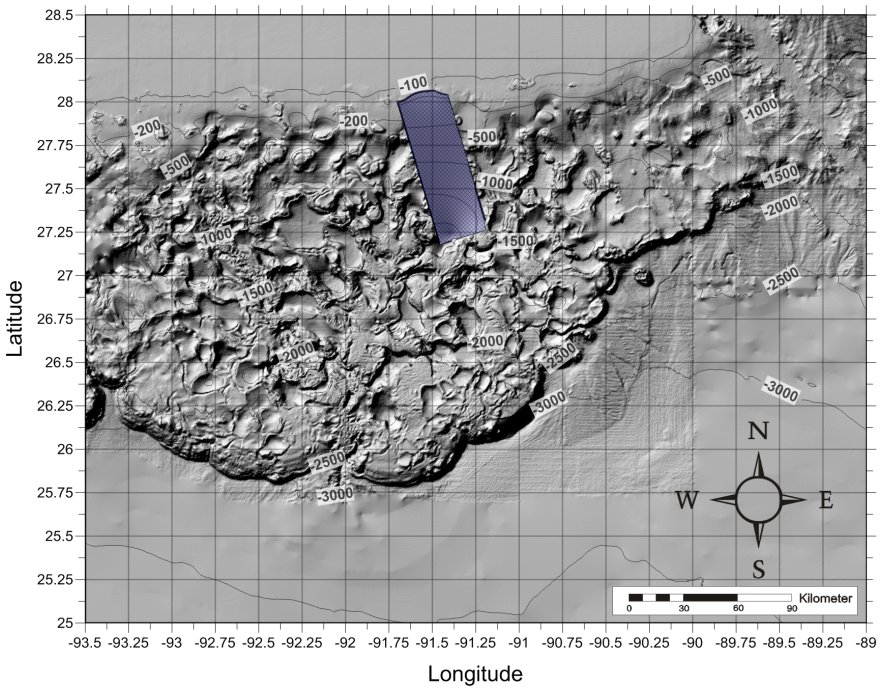

Figure 17: Probabilistic Submarine Landslide -B1- location, excavation limits, and surrounding bathymetry (in meters).

Table 11: Probabilistic Submarine Landslide B1

Geologic Setting	Shelf break edge
Predominant Sediment	Clay
Trigger Mechanism / Recurrence	Earthquake / $3,460 - 3,790$ years
Type of Sediment Failure	Translational
Probabilistic Tsunami Recurrence	$5,400 - 5,500$ years
Probabilistic Avg: Volume	69 km^3
Area	3118 km^2
Excavation: Headscarp Thickness	$\sim$ 44 m
Length	$\sim$ 96 km
Width	$\sim$ 32 km
3D Model Volume	57.3 km^3

Figure 18 depicts tsunami arrival time of the Probabilistic Submarine Landslide B1 (PSL-B1) scenario (one arcminute resolution) for the entire GOM. Figure 19 shows maximum tsunami wave amplitude using the same lower spatial resolution (one arcminute) to obtain on a global scale the energy focusing mechanisms along the continental shelf and the effect of predominant bathymetric features of the GOM like shelf break slopes, submarine escarpments, and submarine canyons. In Figure 20, maximum tsunami wave amplitude is depicted using a higher spatial resolution (15 arcseconds) to obtain more detailed information of wave behavior as waves propagate over those GOM bathymetric features.

Table 12: Coordinate limits for the PSL-B1 Submarine Landslide Domain to obtain initial dynamic tsunami wave source

PSL-B1 Submarine Landslide 3D Domain (Resolution 15 arcseconds)	
Longitude	$93.50°W$ - $89.00°W$
Latitude	$25.00°N$ - $28.50°N$
$dx = dy$ and dz	15 arcsec and $1 - 37$ m
Max. Water Depth	$3,658$ m
dt (variable)	≤ 0.72 sec
# of Cells in the x, y, z-direction	$1,081 \times 841 \times 200$
Total # of Cells	$181,824,200$
Elapsed time of landslide deformation	1800 sec (30 min)

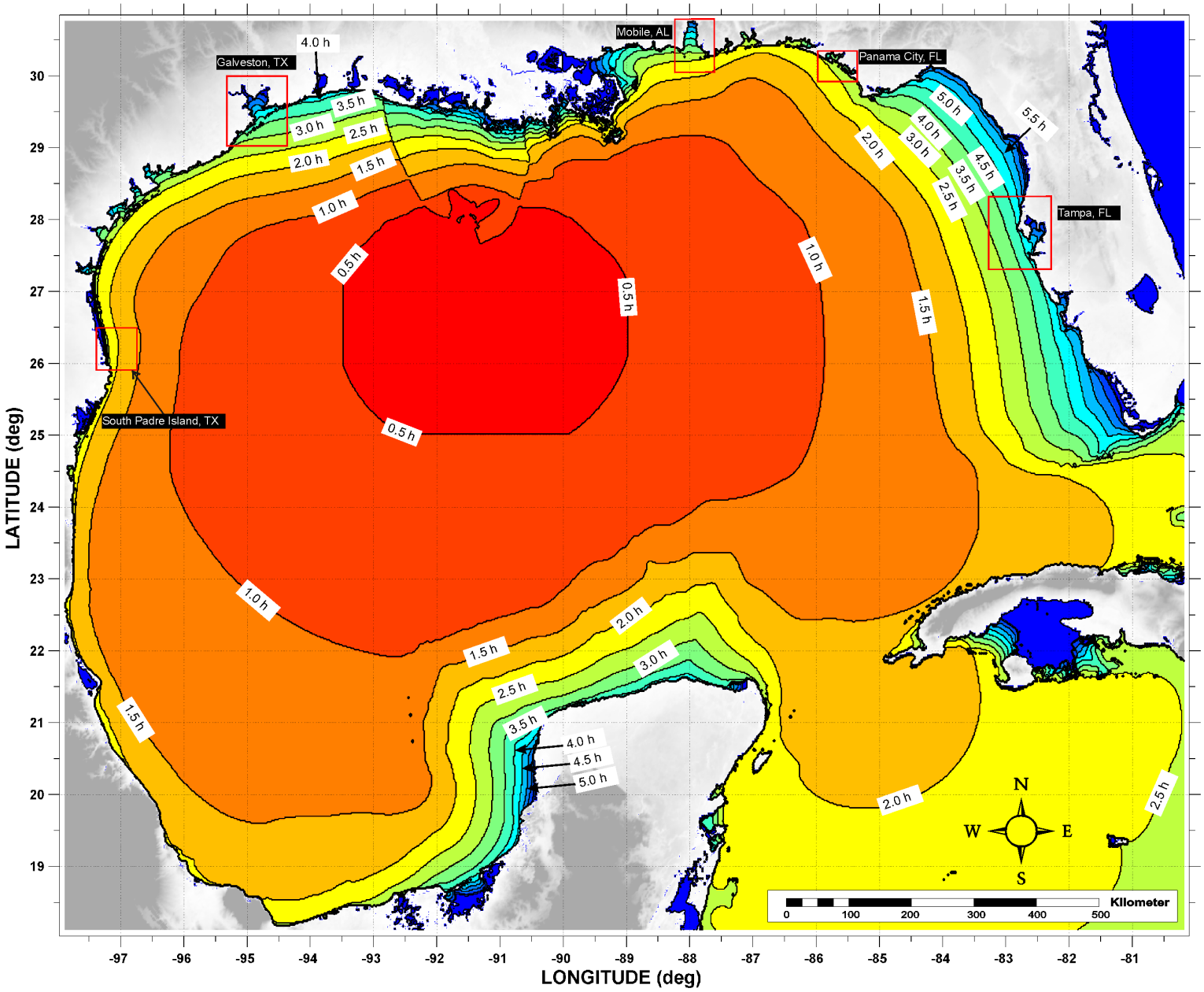

Figure 18: Tsunami arrival time for the Probabilistic Submarine Landslide -B1- (PSL-B1) scenario. Red rectangles indicate regions where tsunami inundation maps have been developed.

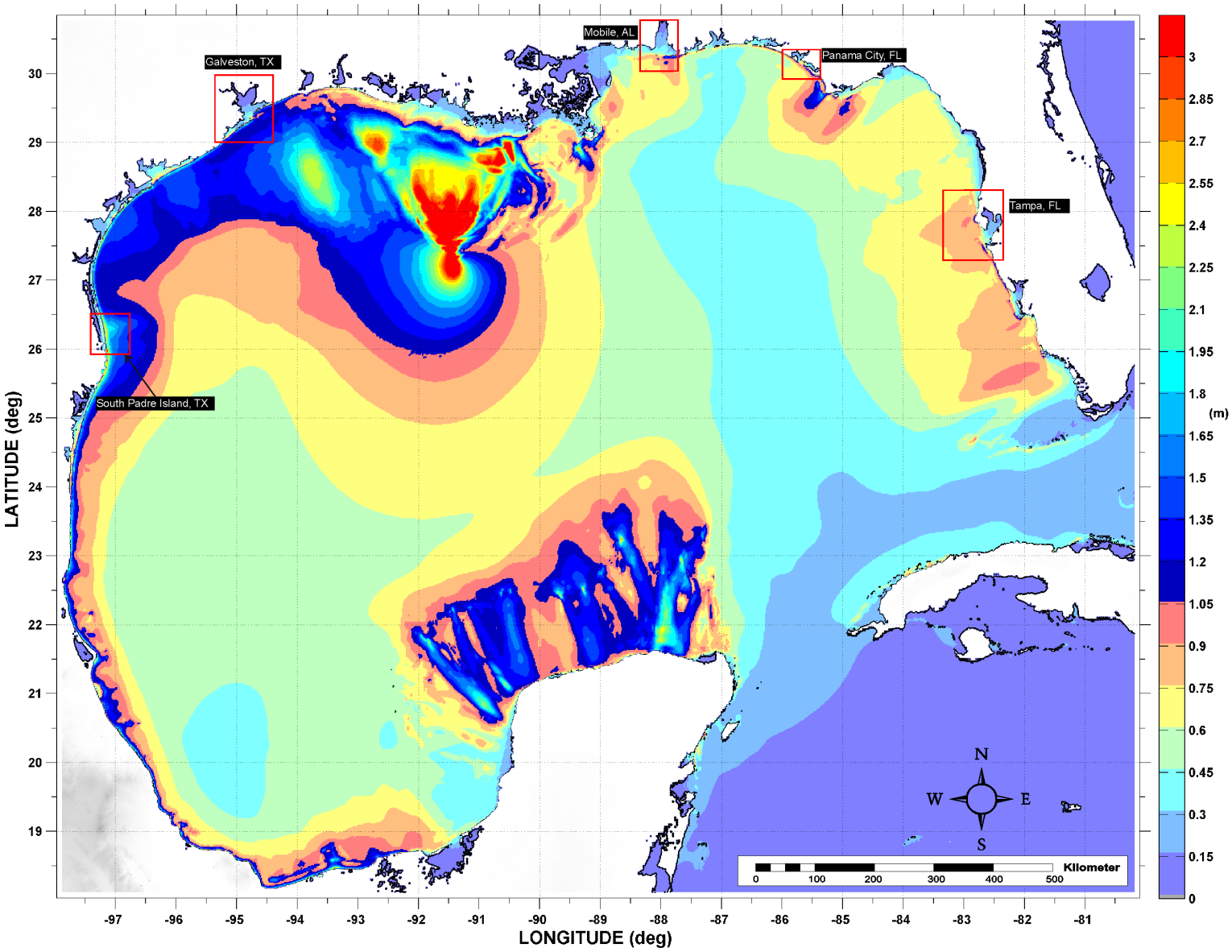

Figure 19: Maximum tsunami wave amplitude (one arcminute resolution) for the Probabilistic Submarine Landslide -B1- (PSL-B1) scenario. Red rectangles indicate regions where tsunami inundation maps have been developed.

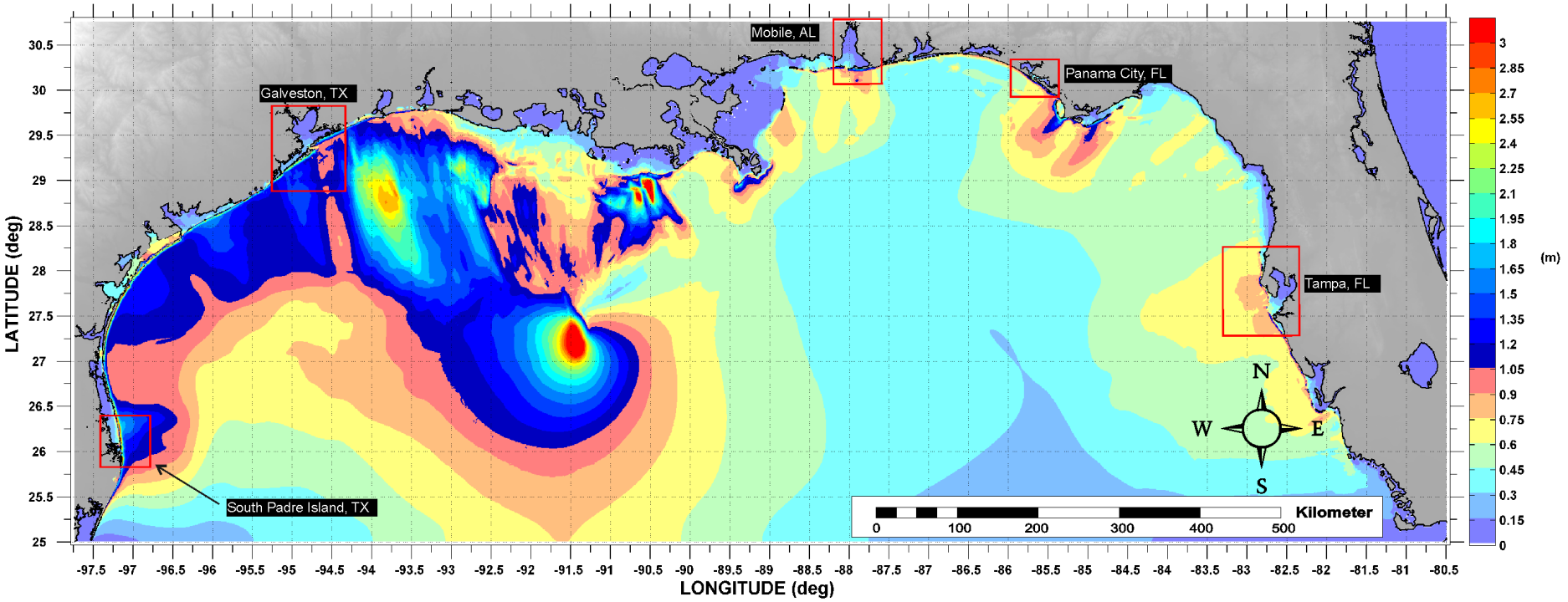

Figure 20: Maximum tsunami wave amplitude (15 arcsecond resolution) for the Probabilistic Submarine Landslide -B1- (PSL-B1) scenario. Red rectangles indicate regions where tsunami inundation maps have been developed.

4.4 Probabilistic Submarine Landslide B2 (PSL-B2) General Information

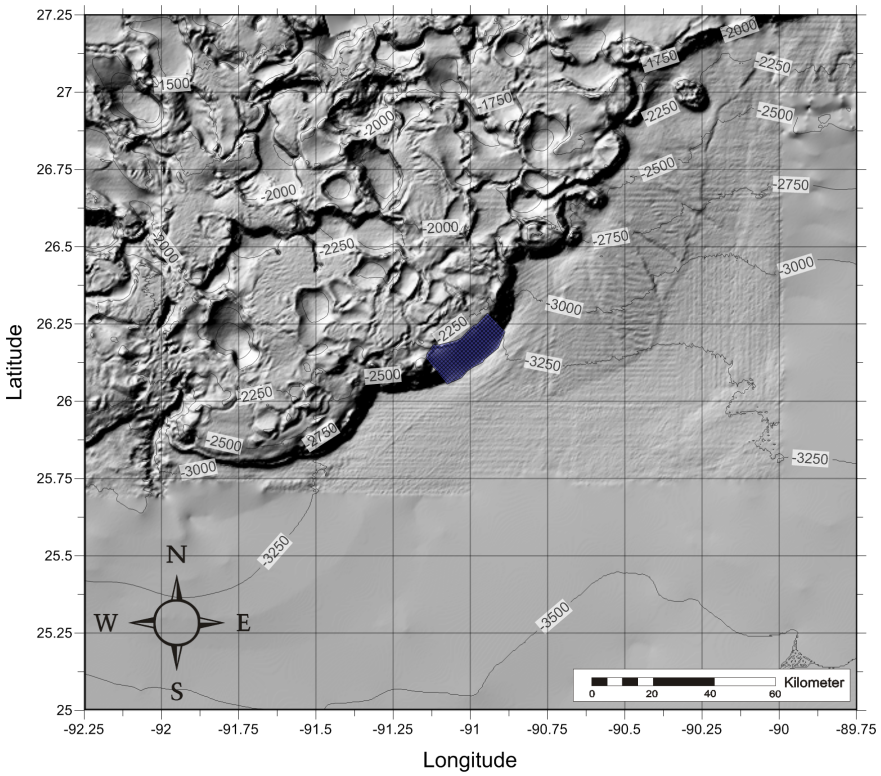

Figure 21: Probabilistic Submarine Landslide -B2- location, excavation limits, and surrounding bathymetry (in meters).

Table 13: Probabilistic Submarine Landslide B2

Geologic Setting	Escarpment-edge
Predominant Sediment	Clay
Trigger Mechanism / Recurrence	Earthquake /$340 - 350$ years
Type of Sediment Failure	Translational
Probabilistic Tsunami Recurrence:	$4,700 - 4,800$ years
Probabilistic Avg: Volume	45 km^3
Area	282 km^2
Excavation: Headscarp Thickness	$\sim$ 323 m
Length	$\sim$ 13 km
Width	$\sim$ 22 km
3D Model Volume	68 km^3

Figure 22 depicts tsunami arrival time of the Probabilistic Submarine Landslide B2 (PSL-B2) scenario (one arcminute resolution) for the entire GOM. Figure 23 shows maximum tsunami wave amplitude using the same lower spatial resolution (one arcminute) to obtain on a global scale the energy focusing mechanisms along the continental shelf and the effect of predominant bathymetric features of the GOM like shelf break slopes, submarine escarpments, and submarine canyons. In Figure 24, maximum tsunami wave amplitude is depicted using a higher spatial resolution (15 arcseconds) to obtain more detailed information of wave behavior as waves propagate over those GOM bathymetric features.

Table 14: Coordinate limits for the PSL-B2 Submarine Landslide Domain to obtain initial dynamic tsunami wave source

PSL-B2 Submarine Landslide 3D Domain (Resolution 15 arcseconds)	
Longitude	$92.25°W$ - $89.75°W$
Latitude	$25.00°N$ - $27.25°N$
$dx = dy$ and dz	15 arcsec and $1 - 37$ m
Max. Water Depth	$3,607$ m
dt (variable)	≤ 0.8 sec
# of Cells in the x, y, z-direction	$601 \times 541 \times 200$
Total # of Cells	$65,028,200$
Elapsed time of landslide deformation	480 sec (8 min)

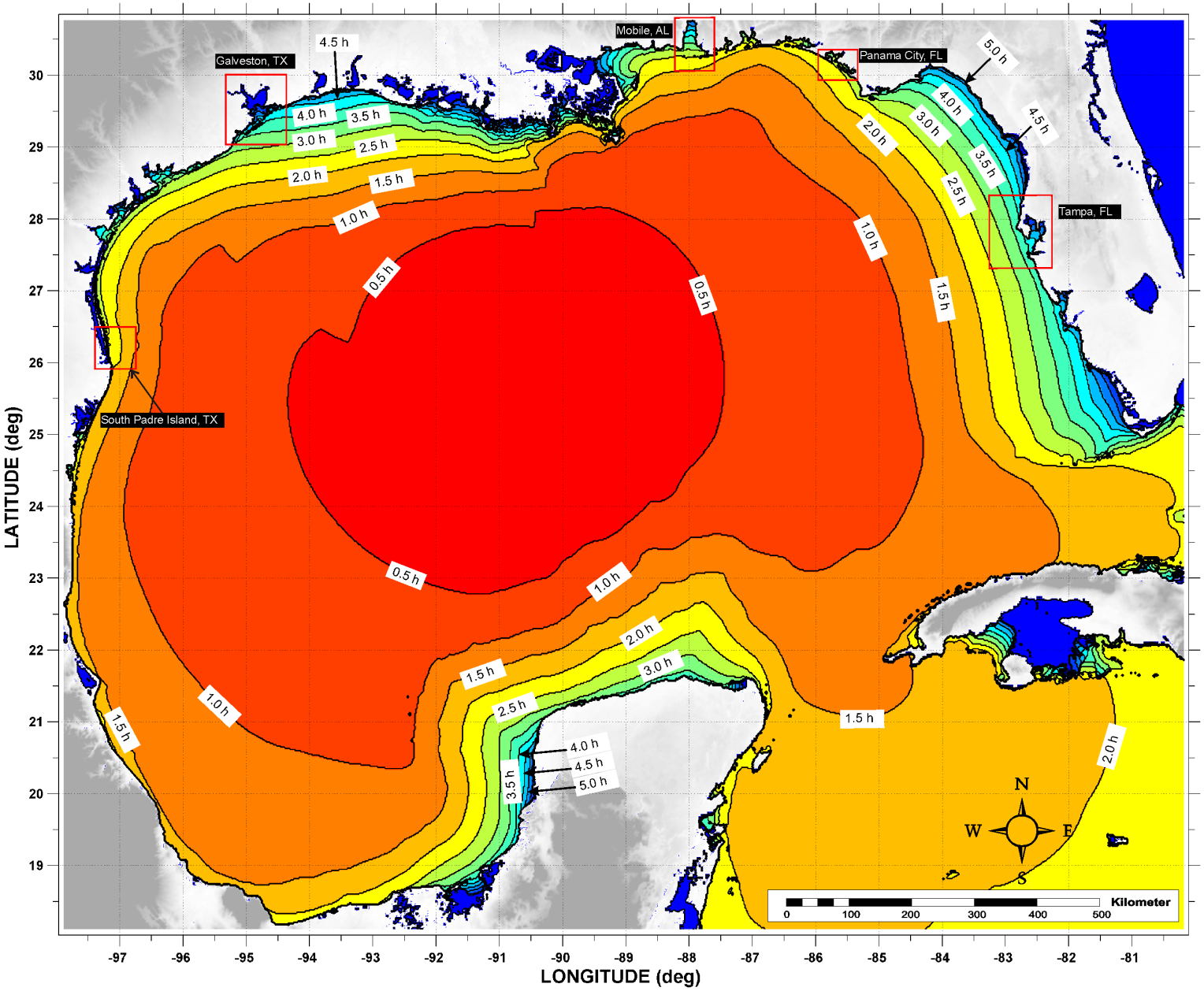

Figure 22: Tsunami arrival time for the Probabilistic Submarine Landslide -B2- (PSL-B2) scenario. Red rectangles indicate regions where tsunami inundation maps have been developed.

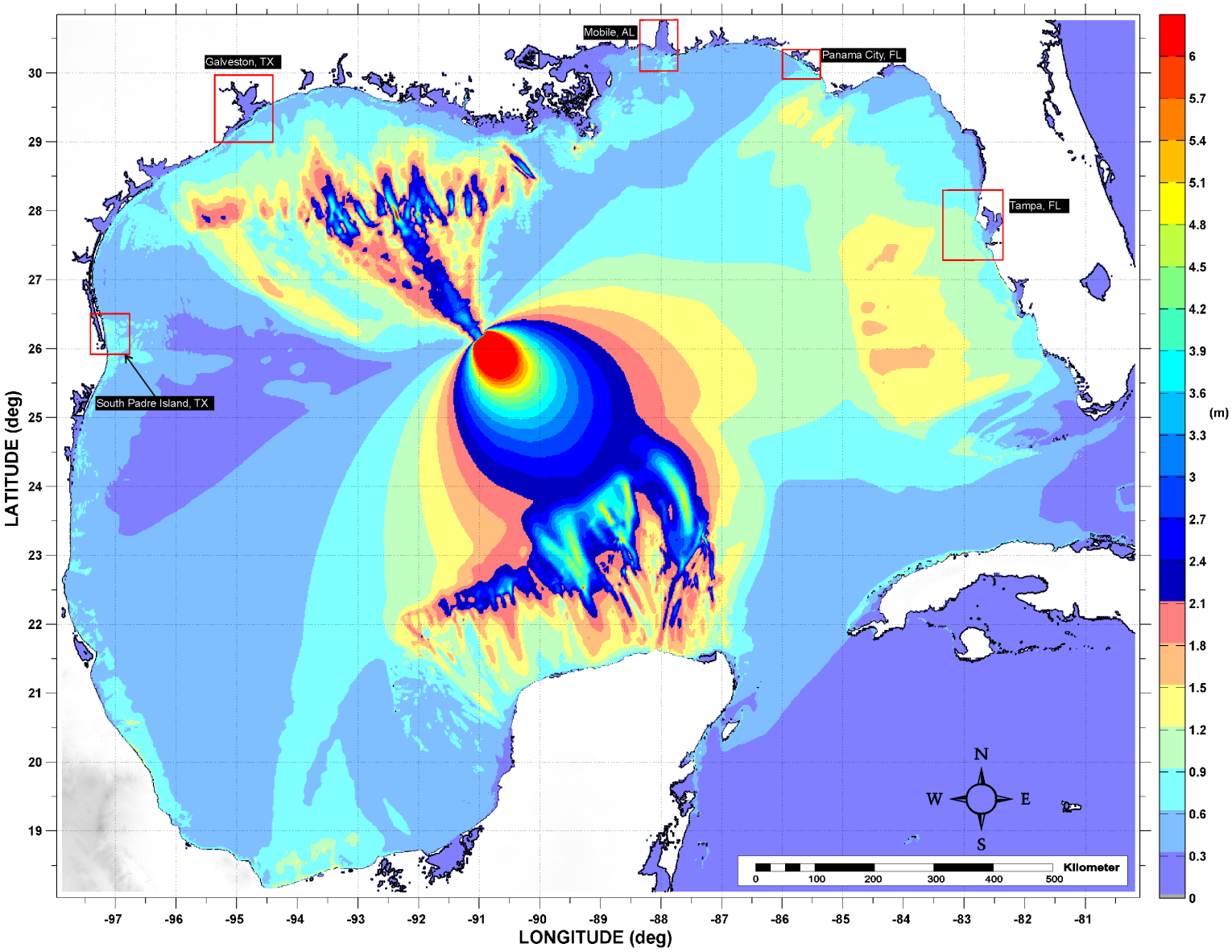

Figure 23: Maximum tsunami wave amplitude (one arcminute resolution) for the Probabilistic Submarine Landslide -B2- (PSL-B2) scenario. Red rectangles indicate regions where tsunami inundation maps have been developed.

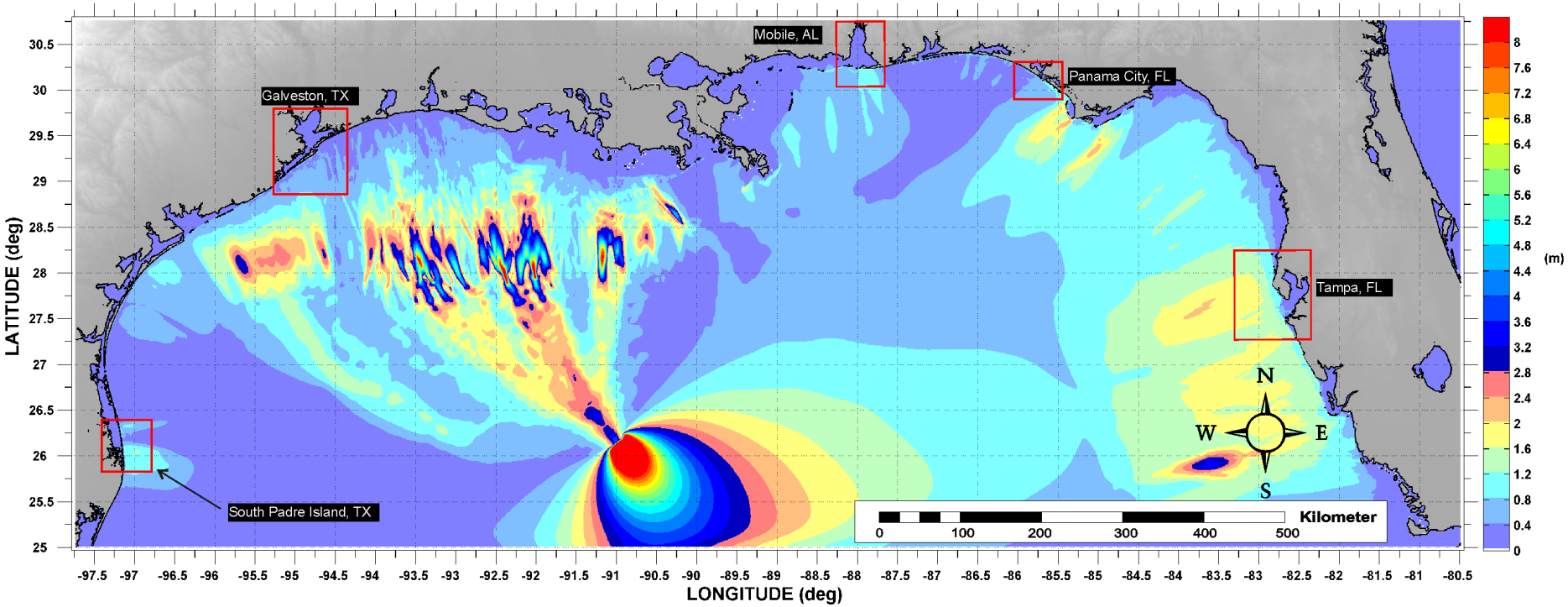

Figure 24: Maximum tsunami wave amplitude (15 arcsecond resolution) for the Probabilistic Submarine Landslide -B2- (PSL-B2) scenario. Red rectangles indicate regions where tsunami inundation maps have been developed.

4.5 Mississippi Canyon Submarine Landslide General Information

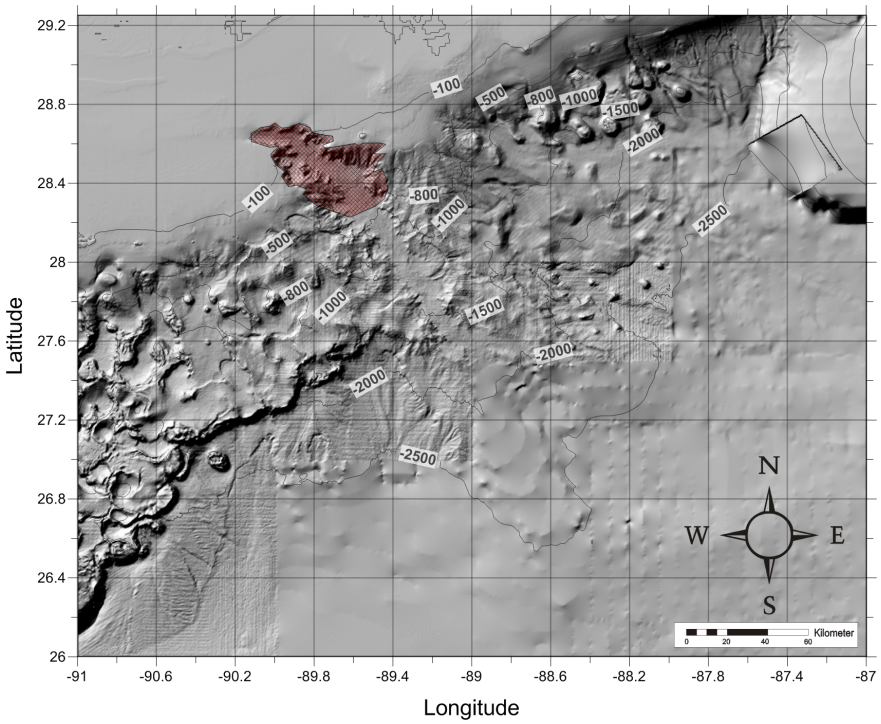

Figure 25: Mississippi Canyon submarine landslide location, excavation limits and surrounding bathymetry (in meters).

Table 15: Mississippi Canyon Submarine Landslide

Geologic Setting	Shelf-edge delta and fan system
Post Failure Sedimentation:	Canyon appears to be partially filled (failure deposits or post-failure sedimentation)
Age:	7500 - 11000 years
Maximum Credible Single Event:	Maximum: Volume: 425.54 km^3 Area: 3687.26 km^2
Other Reported Volumes:	1750km^3, 1500 - 2000 km^3
Excavation Depth:	$\sim$ 300 m (in the upper canyon)
Run-out Distance:	297 km from toe of the excavation area and 442 km from the headwall scarp
3D Model volume	425 km^3

Figure 26 depicts tsunami arrival time of the Mississippi Canyon Submarine Landslide scenario (one arcminute resolution) for the entire GOM. Figure 27 shows maximum tsunami wave amplitude using the same lower spatial resolution (one arcminute) to obtain on a global scale the energy focusing mechanisms along the continental shelf and the effect of predominant bathymetric features of the GOM like shelf break slopes, submarine escarpments, and submarine canyons. In Figure 28, maximum tsunami wave amplitude is depicted using a higher spatial resolution (15 arcseconds) to obtain more detailed information of wave behavior as waves propagate over those GOM bathymetric features.

Table 16: Coordinate limits for the Mississippi Canyon Submarine Landslide Domain to obtain initial dynamic tsunami wave source

Mississippi Canyon Submarine Landslide 3D Domain (Resolution 15 arcseconds)	
Longitude	$91.00°W$ - $87.00°W$
Latitude	$26.00°N$ - $29.25°N$
$dx = dy$ and dz	15 arcsec and $1 - 30$ m
Max. Water Depth	$3,389$ m
dt (variable)	≤ 0.5 sec
# of Cells in the x, y, z-direction	$961 \times 781 \times 233$
Total # of Cells	$174,876,053$
Elapsed time of landslide deformation	1861 sec (~ 31 min)

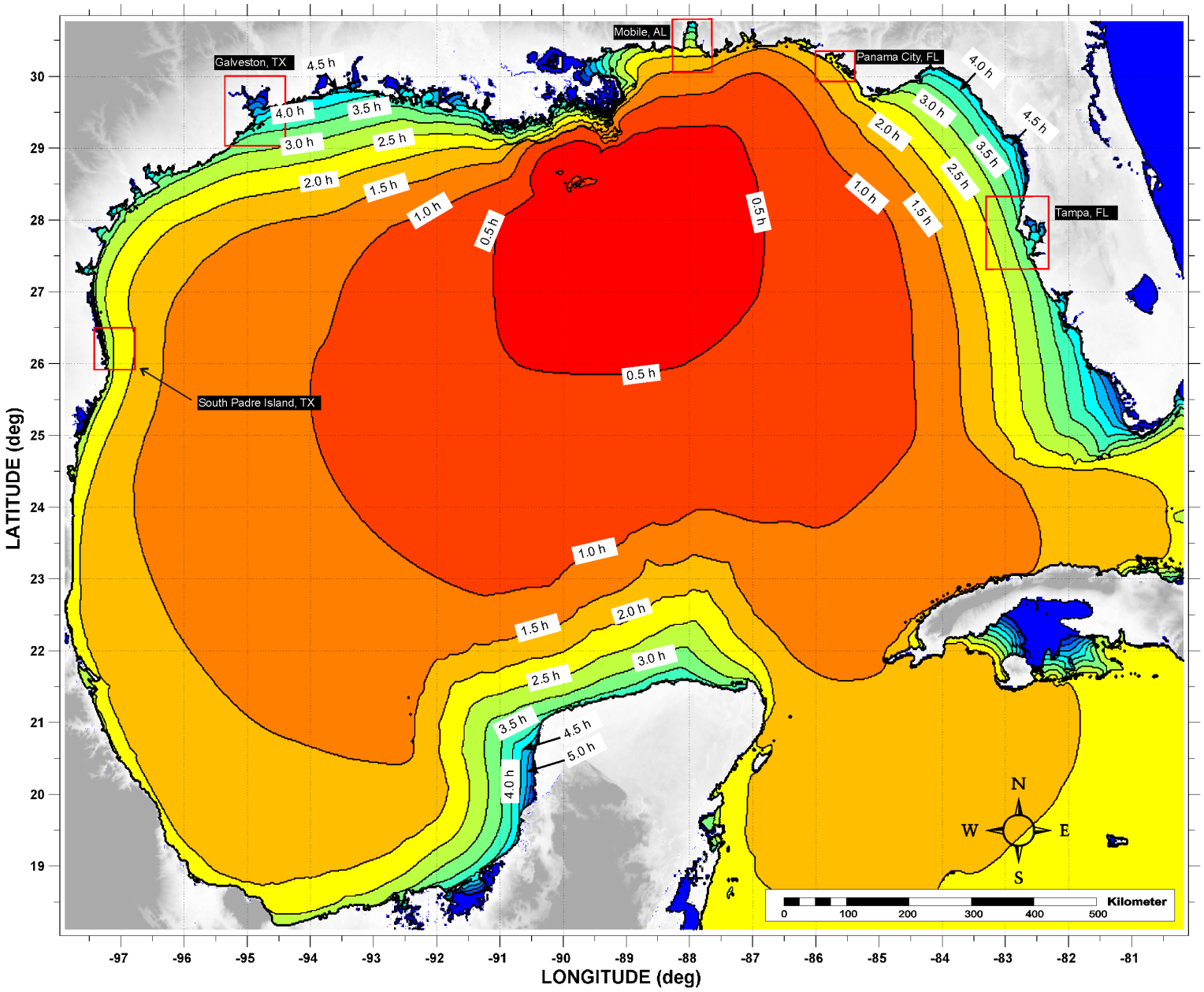

Figure 26: Tsunami arrival time for the Mississippi Canyon Submarine Landslide scenario. Red rectangles indicate regions where tsunami inundation maps have been developed.

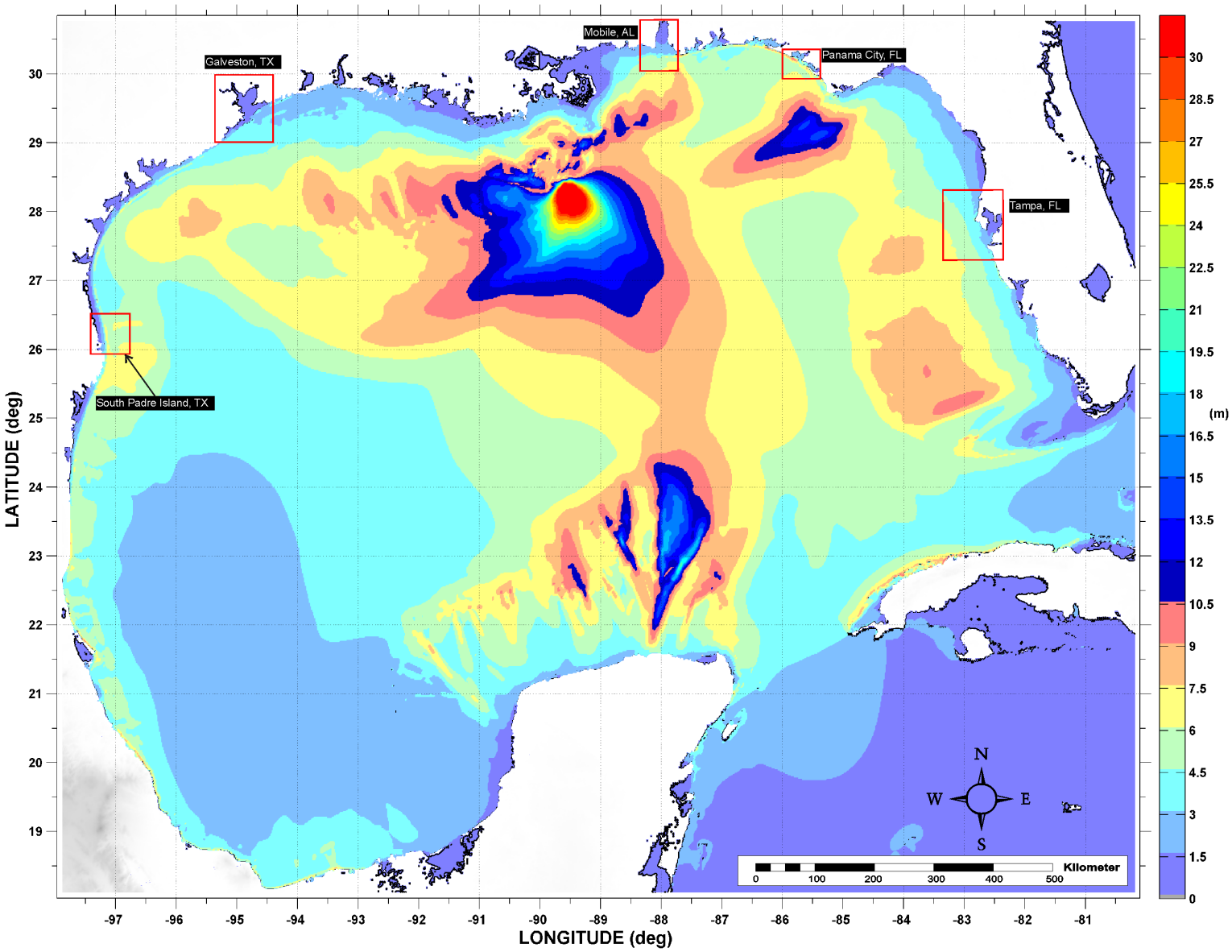

Figure 27: Maximum tsunami wave amplitude (one arcminute resolution) for the Mississippi Canyon Submarine Landslide scenario. Red rectangles indicate regions where tsunami inundation maps have been developed.

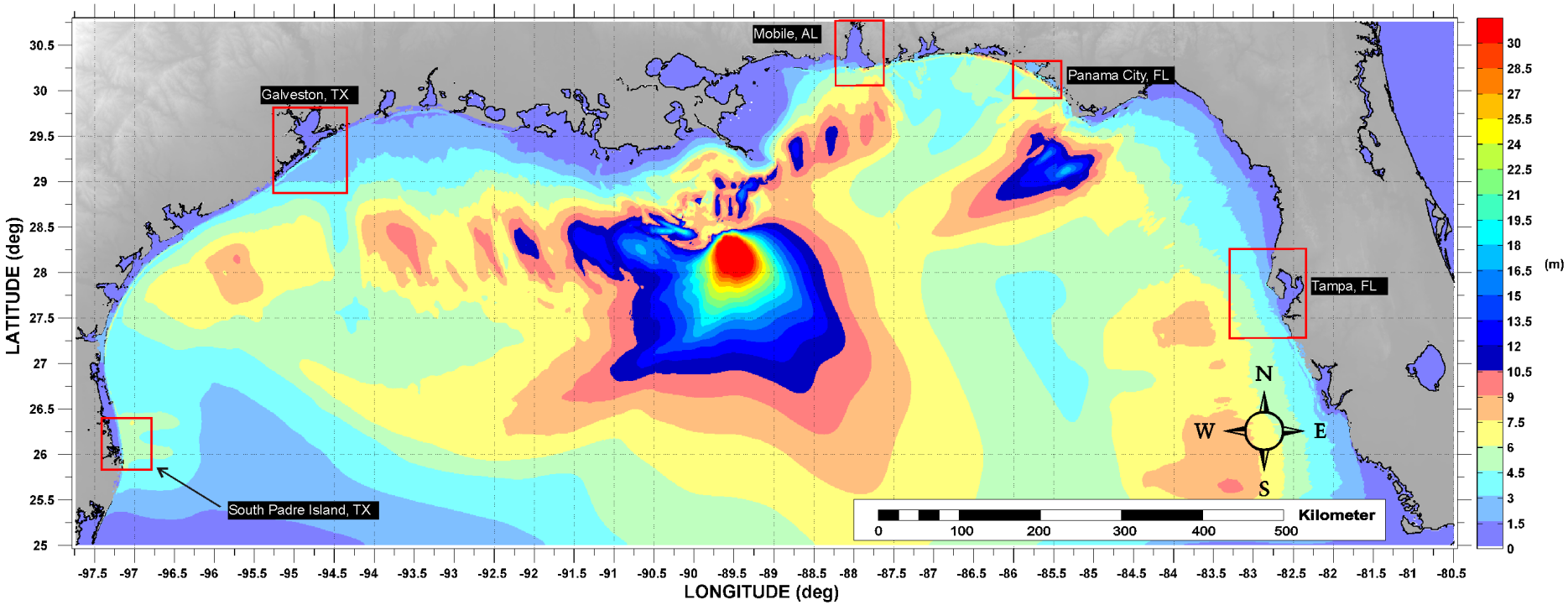

Figure 28: Maximum tsunami wave amplitude (15 arcsecond resolution) for the Mississippi Canyon Submarine Landslide scenario. Red rectangles indicate regions where tsunami inundation maps have been developed.

4.6 Probabilistic Submarine Landslide C (PSL-C) General Information

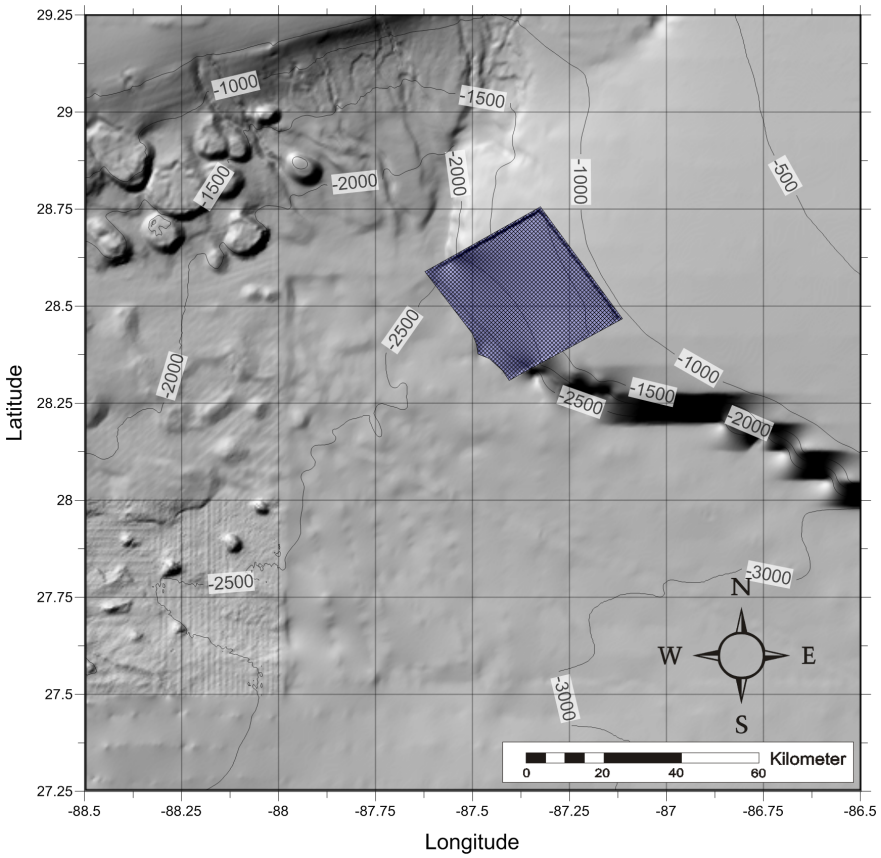

Figure 29: Probabilistic Submarine Landslide -C- location, excavation limits, and surrounding bathymetry (in meters).

Table 17: Probabilistic Submarine Landslide C

Geologic Setting	Shelf-slope
Predominant Sediment	Clay
Trigger Mechanism / Recurrence	Earthquake / $130 - 160$ years
Type of Sediment Failure	Translational
Probabilistic Tsunami Recurrence	$550 - 650$ years
Probabilistic Avg: Volume	315 km^3
Area	$1,529$ km^2
Excavation: Headscarp Thickness	~ 404 m
Length	~ 34 km
Width	~ 46 km
3D Model Volume	357 km^3

Figure 30 depicts tsunami arrival time of the Probabilistic Submarine Landslide C (PSL-C) scenario (one arcminute resolution) for the entire GOM. Figure 31 shows maximum tsunami wave amplitude using the same lower spatial resolution (one arcminute) to obtain on a global scale the energy focusing mechanisms along the continental shelf and the effect of predominant bathymetric features of the GOM like shelf break slopes, submarine escarpments, and submarine canyons. In Figure 32, maximum tsunami wave amplitude is depicted using a higher spatial resolution (15 arcseconds) to obtain more detailed information of wave behavior as waves propagate over those GOM bathymetric features.

Table 18: Coordinate limits for the PSL-C Submarine Landslide Domain to obtain initial dynamic tsunami wave source

PSL-C Submarine Landslide 3D Domain (Resolution 15 arcseconds)	
Longitude	$88.50°W$ - $86.50°W$
Latitude	$27.25°N$ - $29.25°N$
$dx = dy$ and dz	15 arcsec and $1 - 16$ m
Max. Water Depth	$3,158$ m
dt (variable)	≤ 0.5 sec
# of Cells in the x, y, z-direction	$481 \times 481 \times 405$
Total # of Cells	$93,701,250$
Elapsed time of landslide deformation	600 sec (10 min)

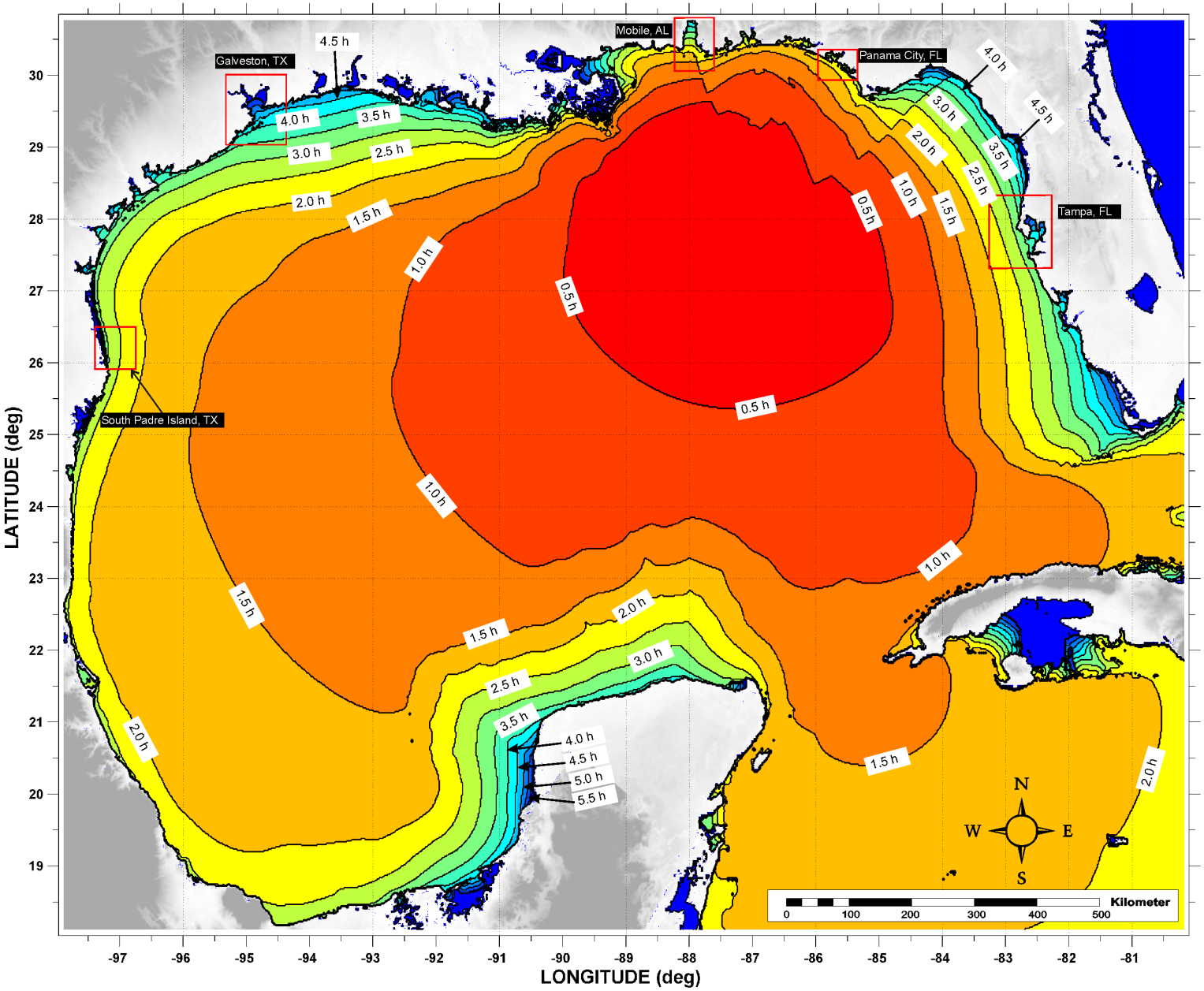

Figure 30: Tsunami arrival time for the Probabilistic Submarine Landslide -C- (PSL-C) scenario. Red rectangles indicate regions where tsunami inundation maps have been develop.

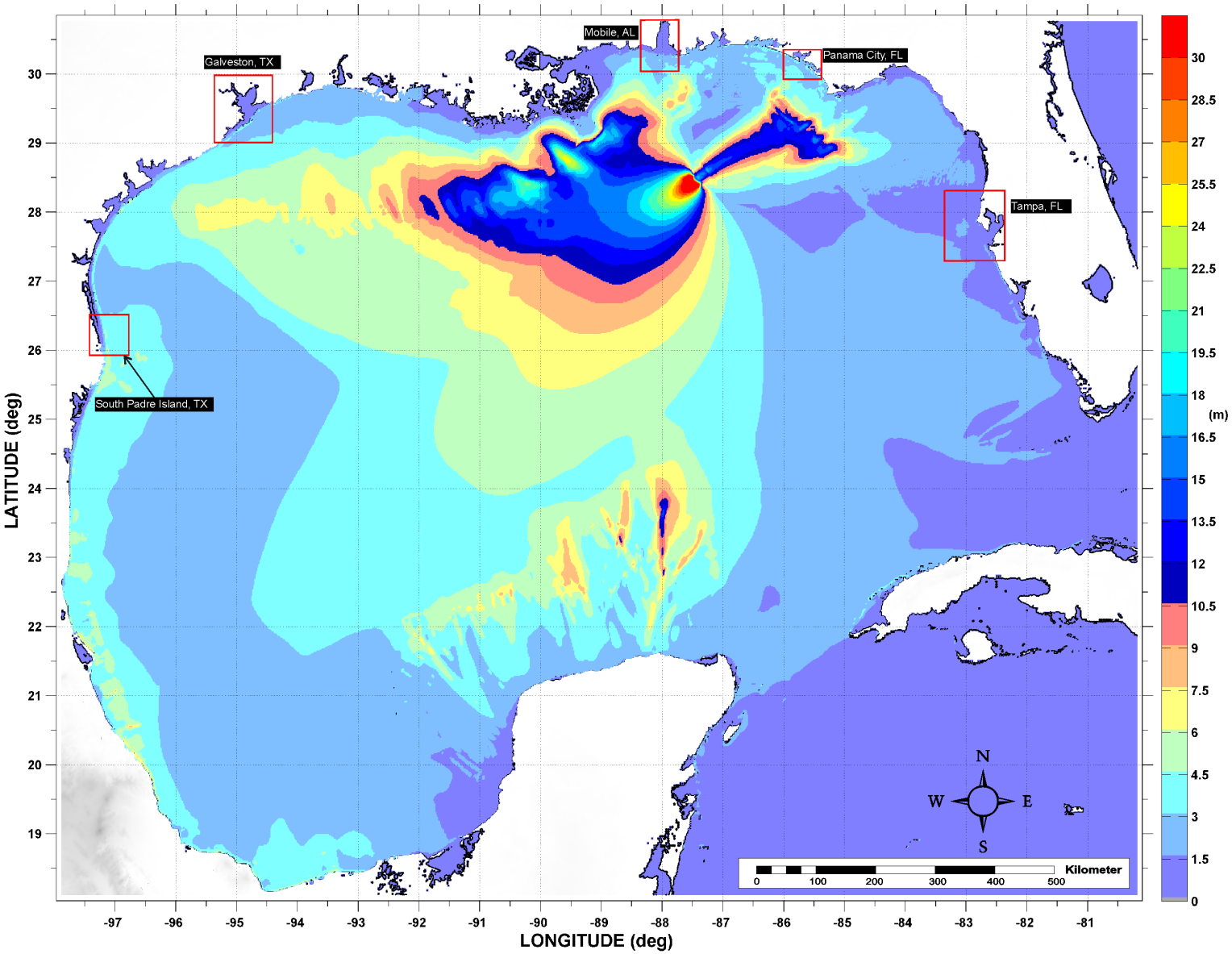

Figure 31: Maximum tsunami wave amplitude (one arcminute resolution) for the Probabilistic Submarine Landslide -C- (PSL-C) scenario. Red rectangles indicate regions where tsunami inundation maps have been developed.

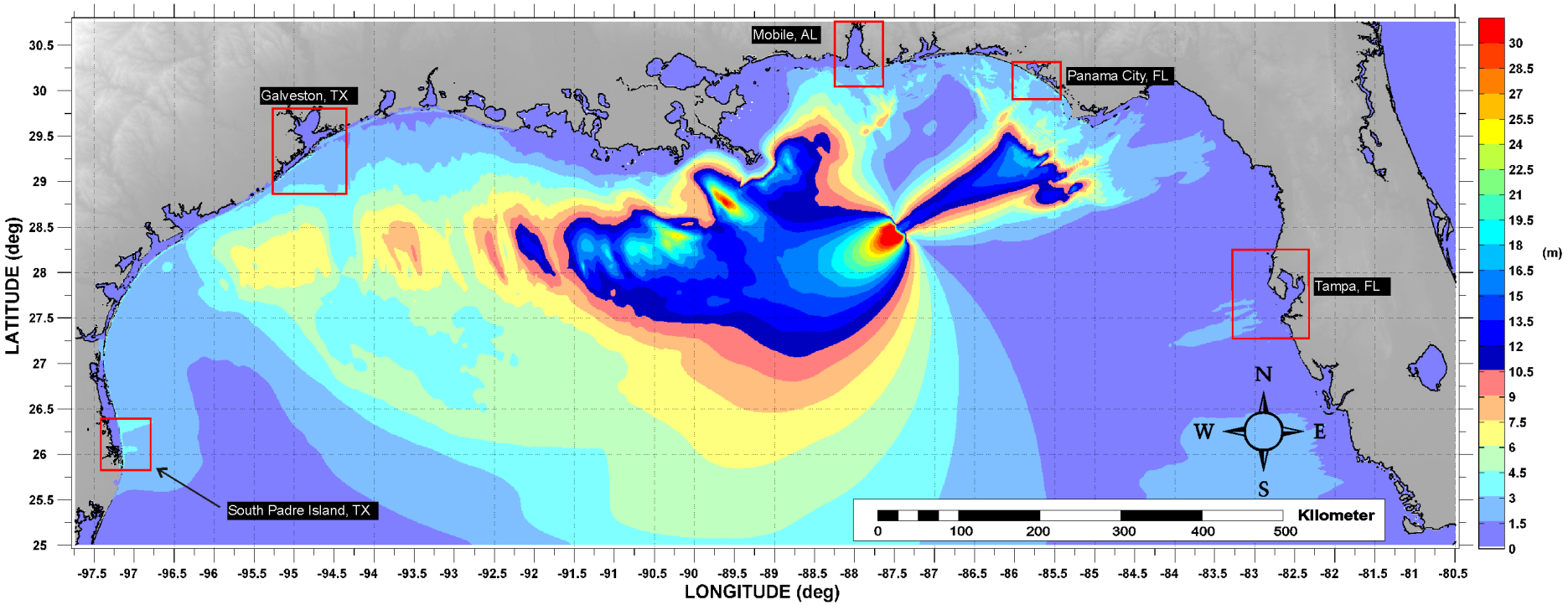

Figure 32: Maximum tsunami wave amplitude (15 arcsecond resolution) for the Probabilistic Submarine Landslide -C- (PSL-C) scenario. Red rectangles indicate regions where tsunami inundation maps have been developed.

4.7 West Florida Submarine Landslide General Information

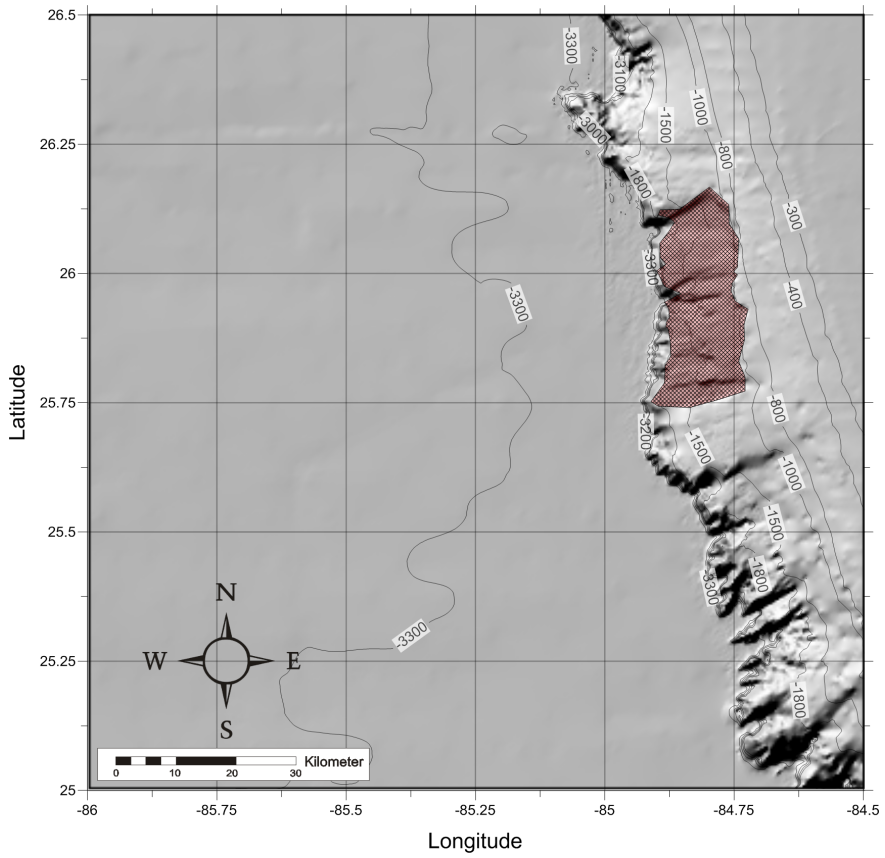

Figure 33: West Florida submarine landslide location, excavation limits and surrounding bathymetry (in meters).

Table 19: West Florida Submarine Landslide

Geologic Setting	Edge of a carbonate platform
Post Failure Sedimentation:	None visible on multi-beam images or on available high-resolution seismic profiles
Age:	Early Holocene or older ($>$ 10000) years
Maximum Credible Single Event:	Maximum Volume: 16.2 km^3 Area: 647.57 km^2
Excavation Depth:	$\sim$ 150 m
Run-out Distance:	Uncertain. The landslide deposit is at the base of the Florida Escarpment buried under younger Mississippi fan deposits
3D Model volume	18.4 km^3

Figure 34 depicts tsunami arrival time for the West Florida Submarine Landslide scenario (one arcminute resolution) for the entire GOM. Figure 35 shows maximum tsunami wave amplitude using the same lower spatial resolution (one arcminute) to obtain on a global scale the energy focusing mechanisms along the continental shelf and the effect of predominant bathymetric features of the GOM like shelf break slopes, submarine escarpments, and submarine canyons. In Figure 36, maximum tsunami wave amplitude is depicted using a higher spatial resolution (15 arcseconds) to obtain more detailed information of wave behavior as waves propagate over those GOM bathymetric features.

Table 20: Coordinate limits for the West Florida Submarine Landslide Domain to obtain initial dynamic tsunami wave source

West Florida Submarine Landslide 3D Domain (Resolution 15 arcseconds)	
Longitude	$86.00°W$ - $84.50°W$
Latitude	$25.00°N$ - $26.50°N$
$dx = dy$ and dz	15 arcsec and $1 - 29$ m
Max. Water Depth	$3,437$ m
dt (variable)	≤ 0.10 sec.
# of Cells in the x, y, z-direction	$361 \times 361 \times 240$
Total # of Cells	$31,277,040$
Elapsed time of landslide deformation	300 sec (5 min)

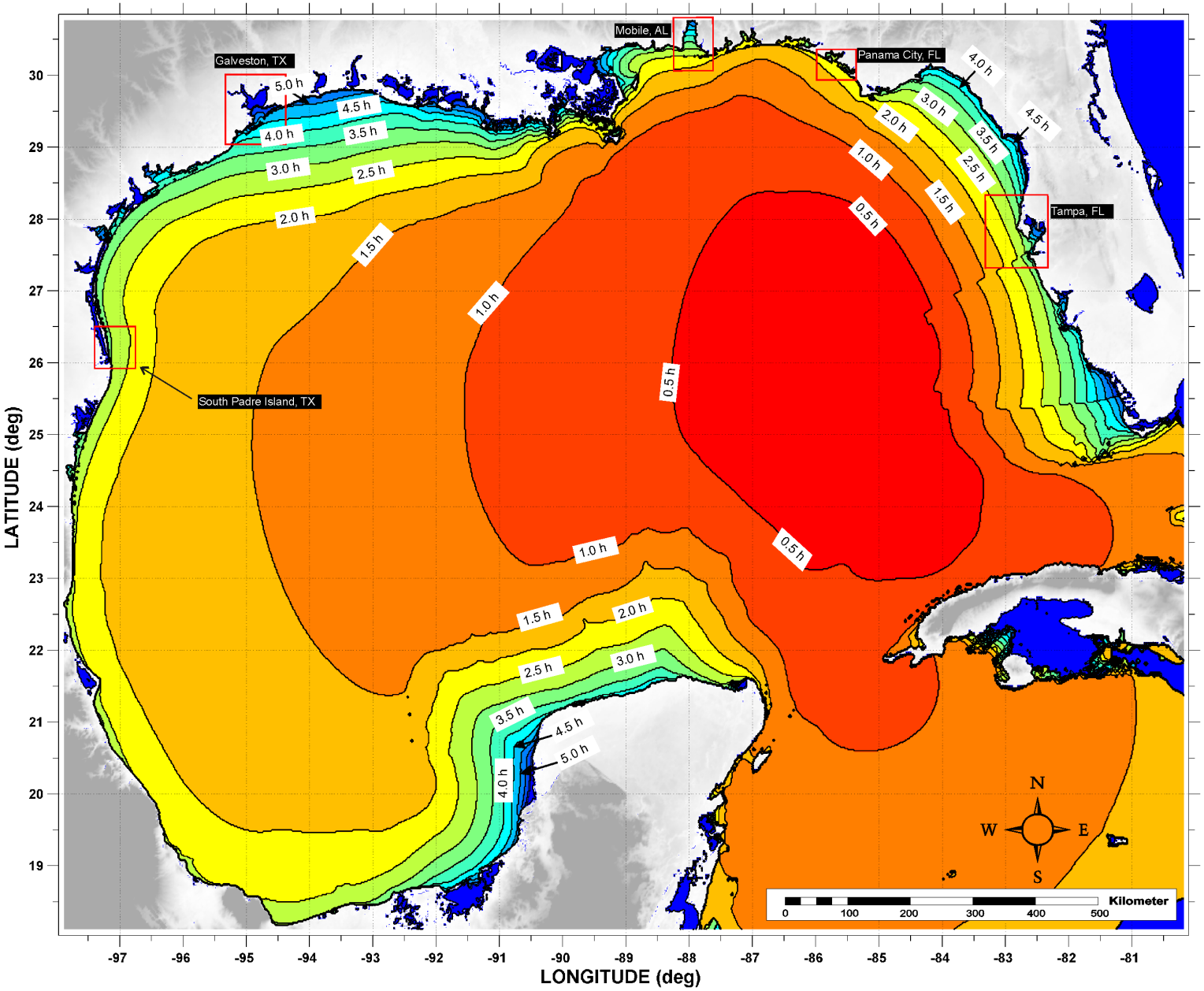

Figure 34: Tsunami arrival time for the West Florida Submarine Landslide scenario. Red rectangles indicate regions where tsunami inundation maps had been developed.

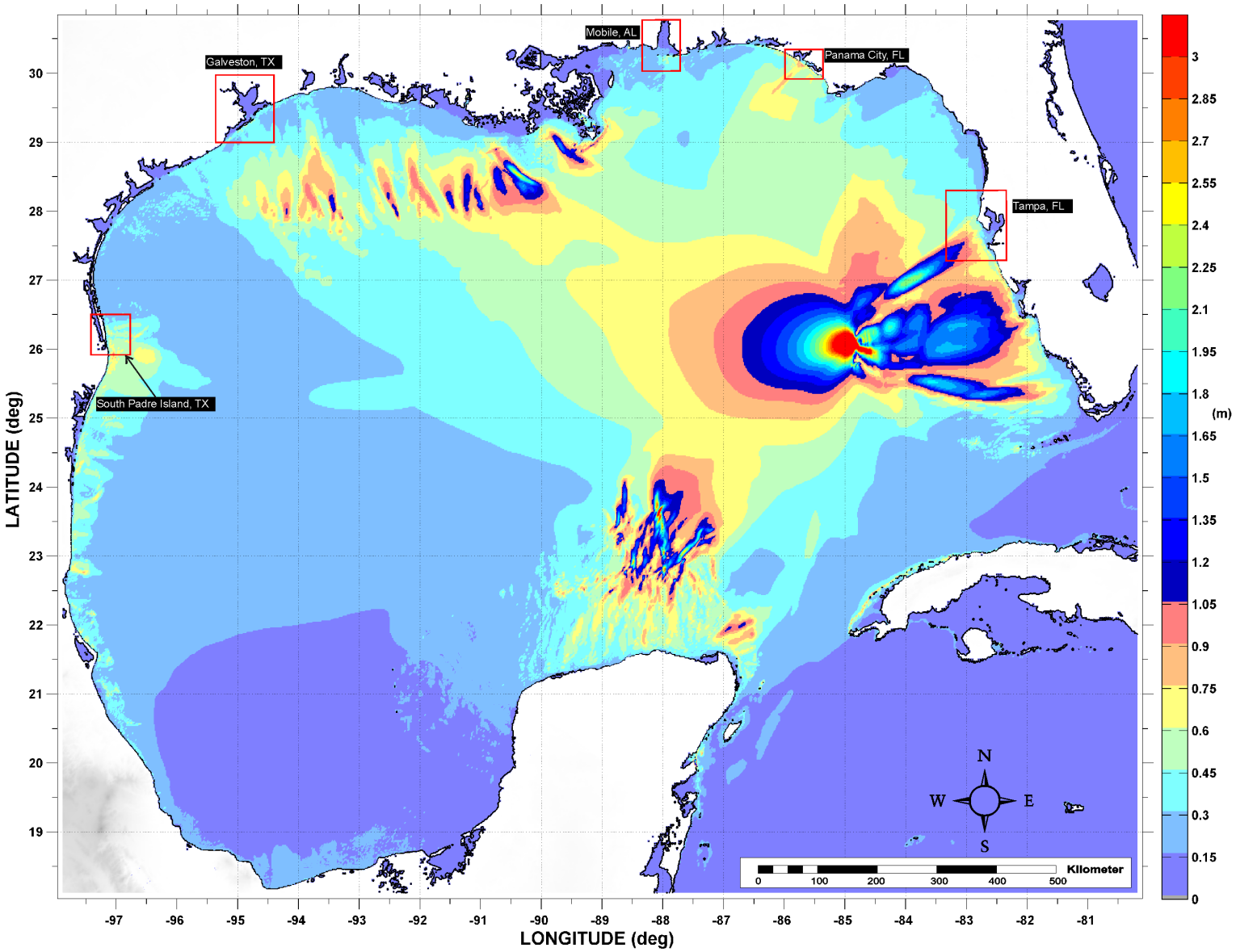

Figure 35: Maximum tsunami wave amplitude (one arcminute resolution) for the West Florida Submarine Landslide scenario. Red rectangles indicate regions where tsunami inundation maps have been developed.

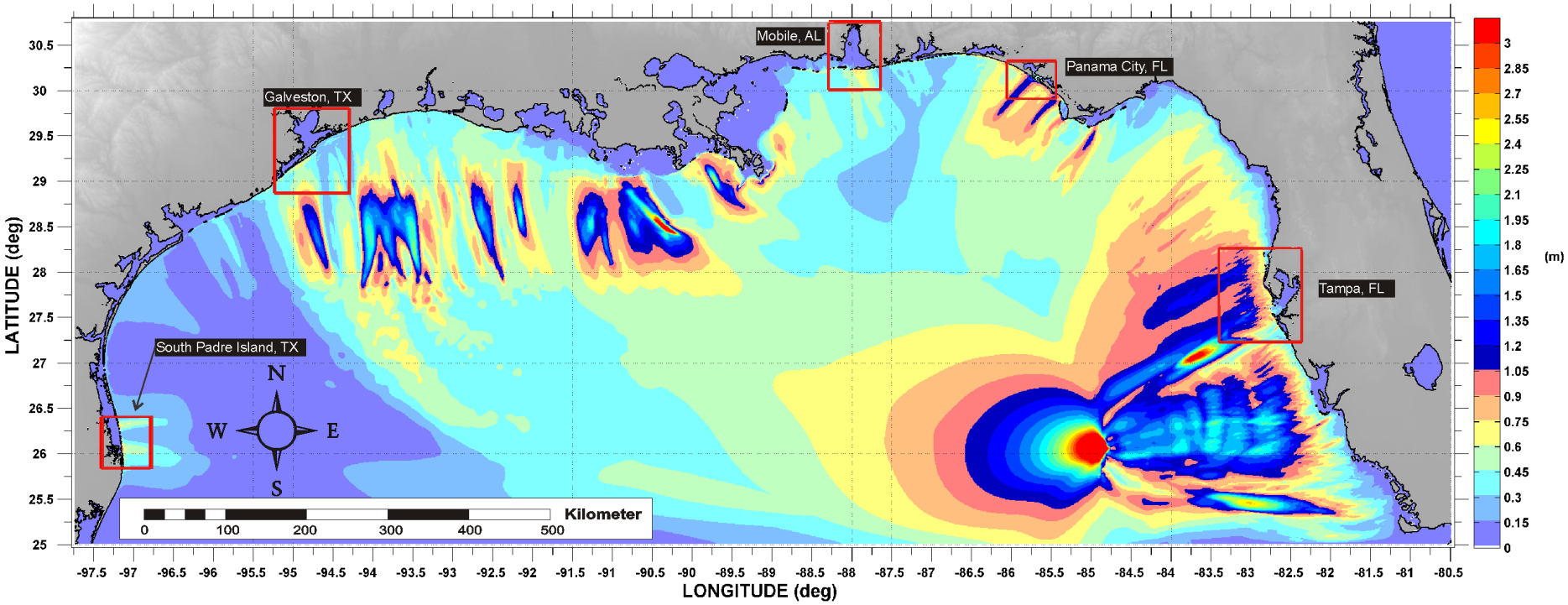

Figure 36: Maximum tsunami wave amplitude (15 arcsecond resolution) for West Florida Submarine Landslide scenario. Red rectangles indicate regions where tsunami inundation maps have been developed.

5 Tsunami Maps

5.1 South Padre Island, TX

South Padre Island, TX
Amplitude and Arrival Time of Maximum Tsunami Wave Recorded at Numerical Wave Gauge

Table 21: Maximum tsunami wave amplitude and corresponding arrival time after landslide failure at South Padre Island, TX numerical wave gauge: 26°4'34.96"N, 97°5'3.13"W (Figure 1), approximate water depth 20m. *The two values for wave amplitude and arrival time given for the West Florida landslide correspond to the first positive wave, which was not the maximum amplitude wave, and the third positive wave, which produced the absolute maximum wave amplitude recorded at this gauge.

Tsunami Source	Maximum Wave Amplitude (m)	Arrival Time After Landslide Failure (hr)
East Breaks	4.14	1.5
PSL-A	2.88	1.8
PSL-B1	1.31	2.2
PSL-B2	0.82	2.1
Mississippi Canyon	4.67	2.6
PSL-C	2.96	2.7
West Florida*	0.11, 0.67	2.9, 3.1

South Padre Island, TX
East Breaks Submarine Landslide
Maximum Inundation Depth

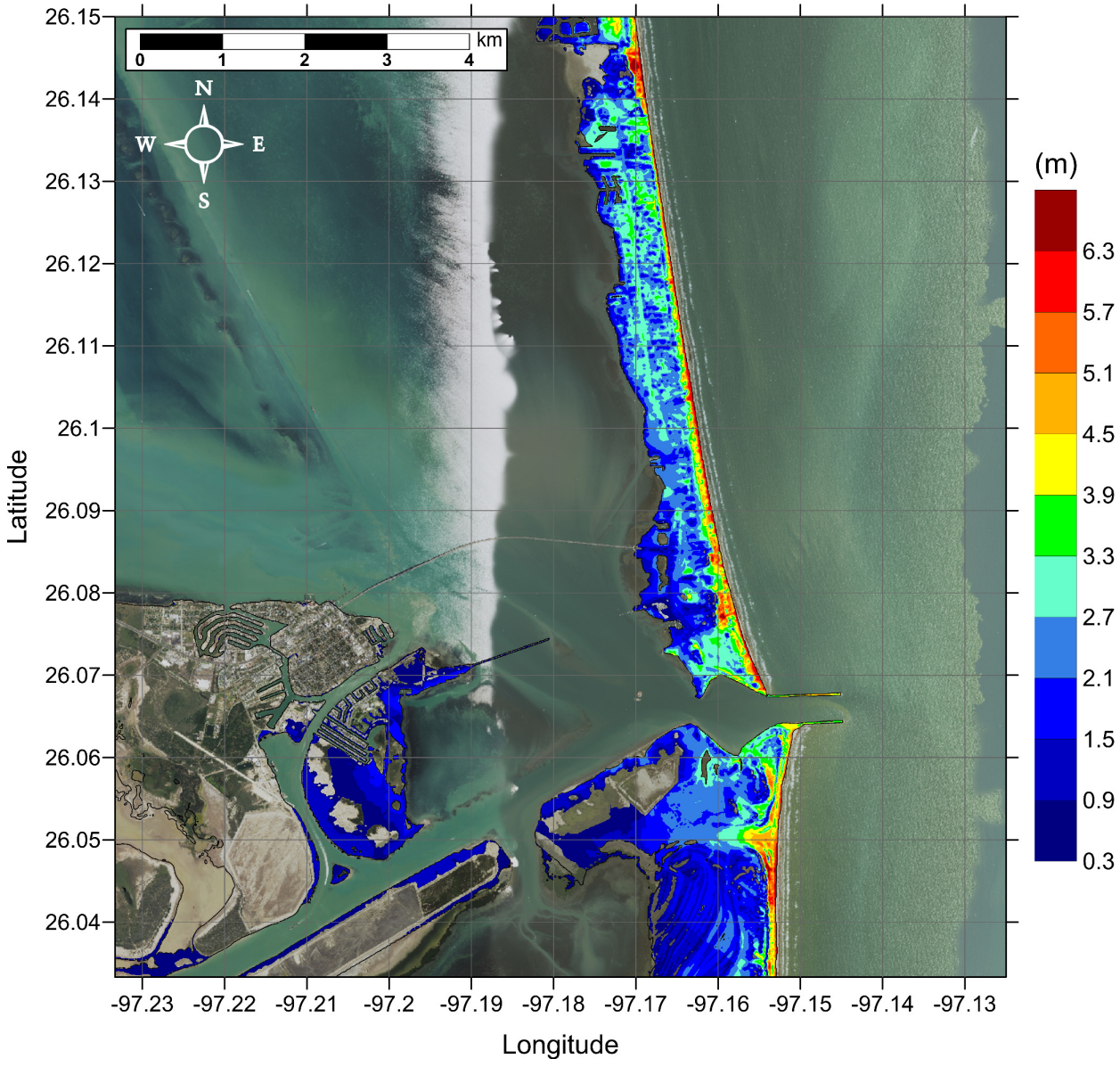

Figure 37: Maximum inundation depth (m) caused by the East Breaks submarine landslide in South Padre Island, TX. Contour drawn is the zero-meter contour for land elevation.

South Padre Island, TX
East Breaks Submarine Landslide
Maximum Momentum Flux

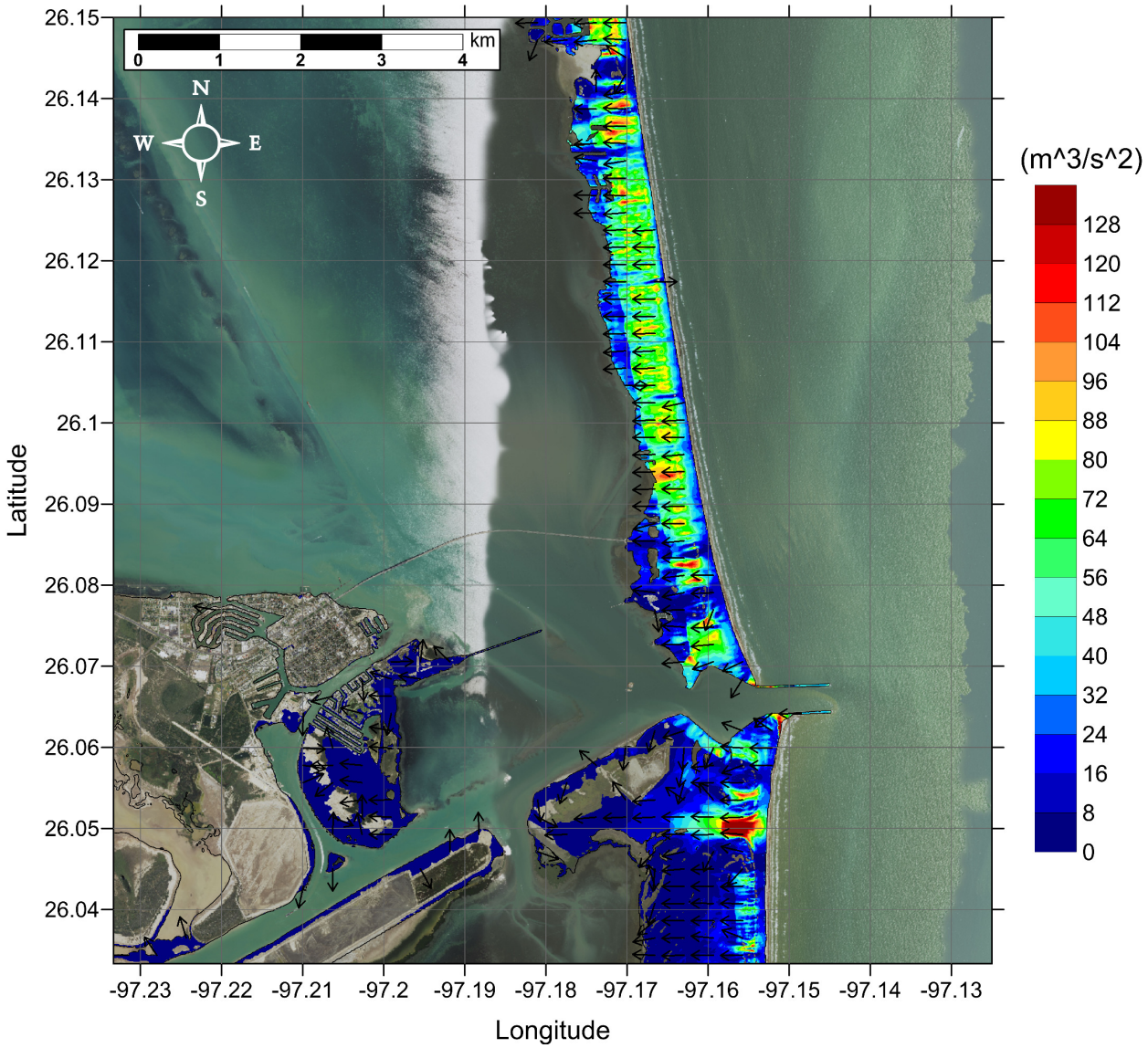

Figure 38: Maximum momentum flux (m^3/s^2) caused by the East Breaks submarine landslide in South Padre Island, TX. Arrows represent direction of maximum momentum flux. Contour drawn is the zero-meter contour for land elevation.

South Padre Island, TX
Probabilistic Submarine Landslide A (PSL-A)
Maximum Inundation Depth

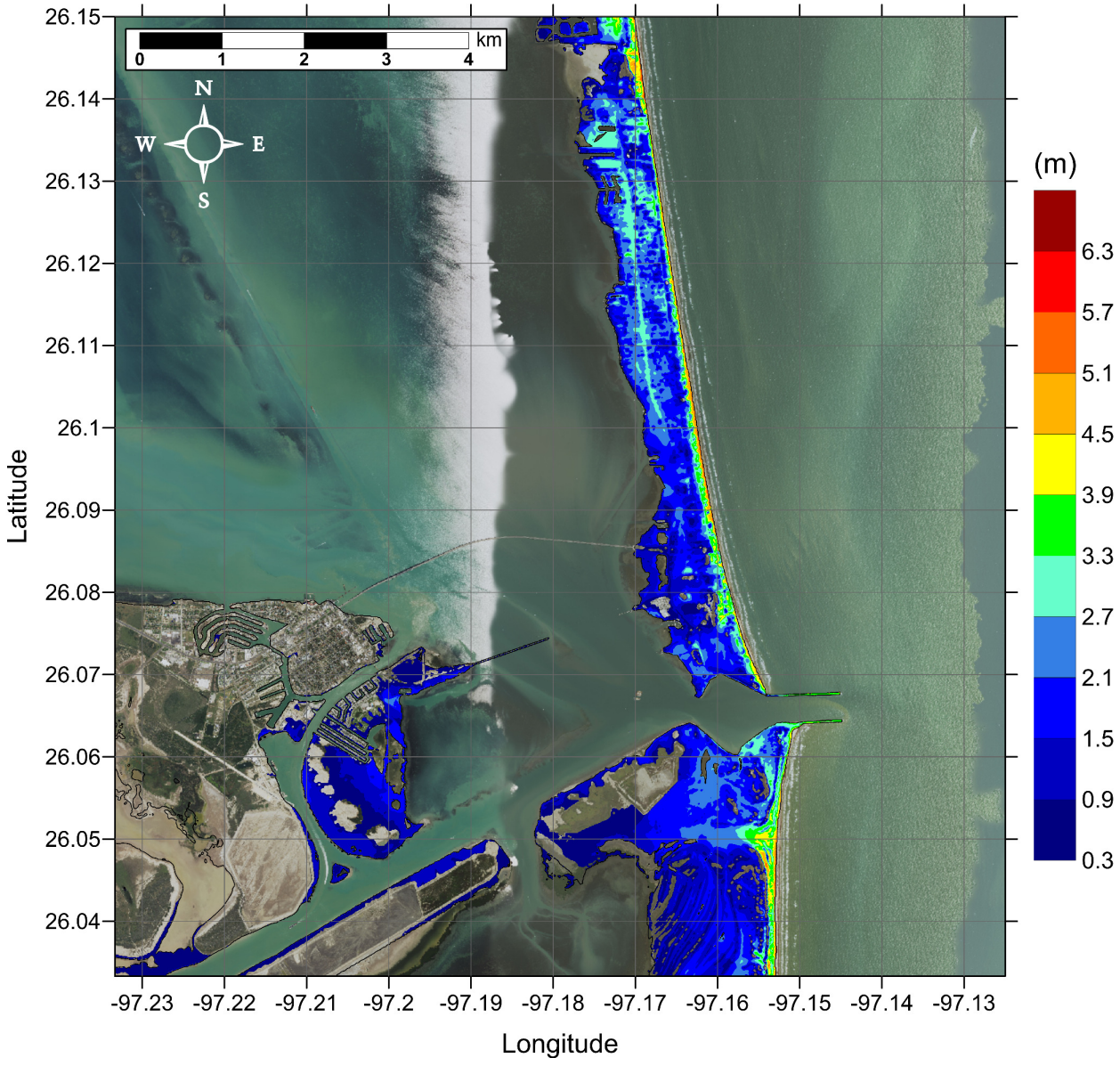

Figure 39: Maximum inundation depth (m) caused by the Probabilistic Submarine Landslide A in South Padre Island, TX. Contour drawn is the zero-meter contour for land elevation.

South Padre Island, TX
Probabilistic Submarine Landslide A (PSL-A)
Maximum Momentum Flux

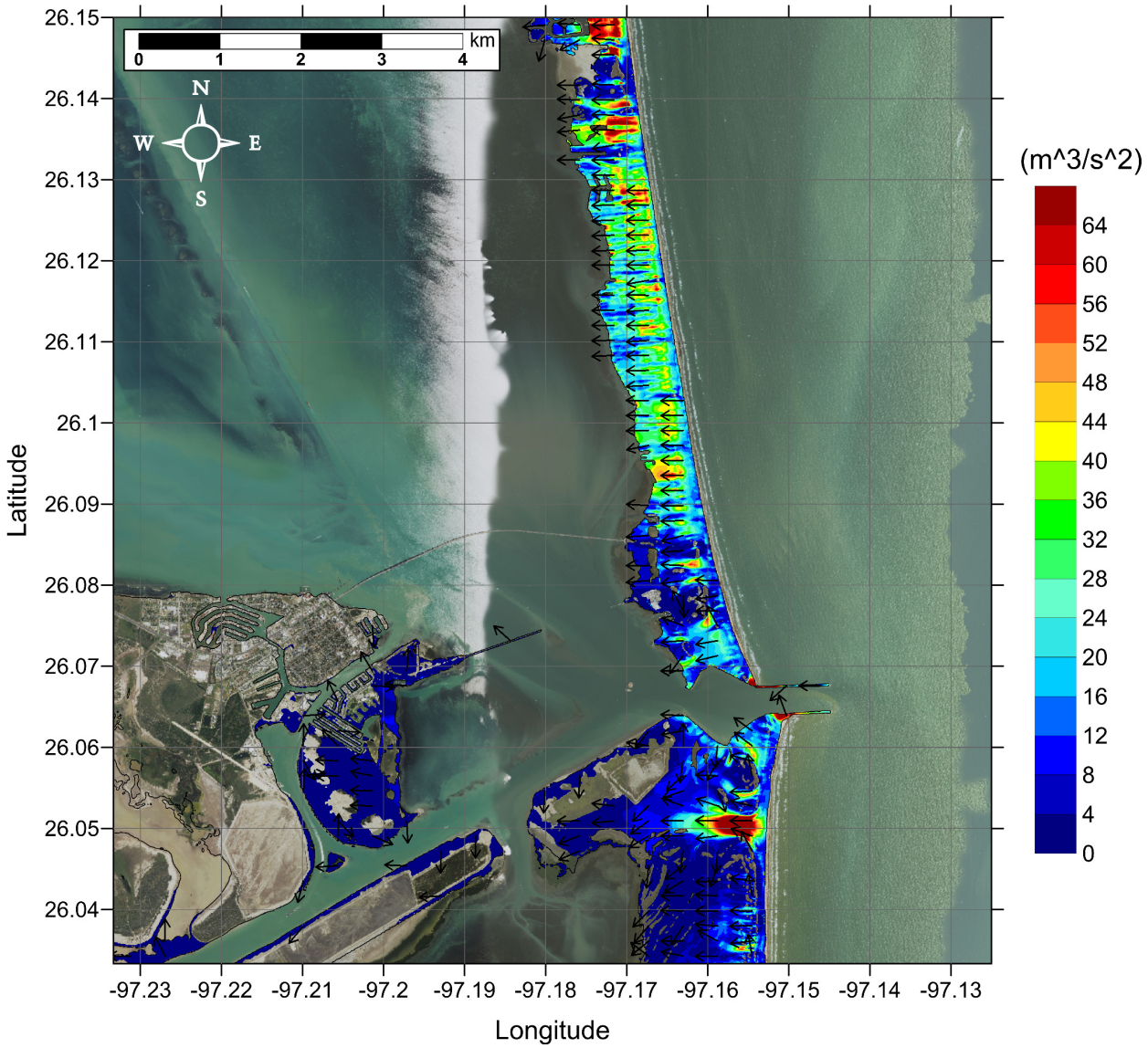

Figure 40: Maximum momentum flux (m^3/s^2) caused by the Probabilistic Submarine Landslide A in South Padre Island, TX. Arrows represent direction of maximum momentum flux. Contour drawn is the zero-meter contour for land elevation.

South Padre Island, TX
Probabilistic Submarine Landslide B1 (PSL-B1)
Maximum Inundation Depth

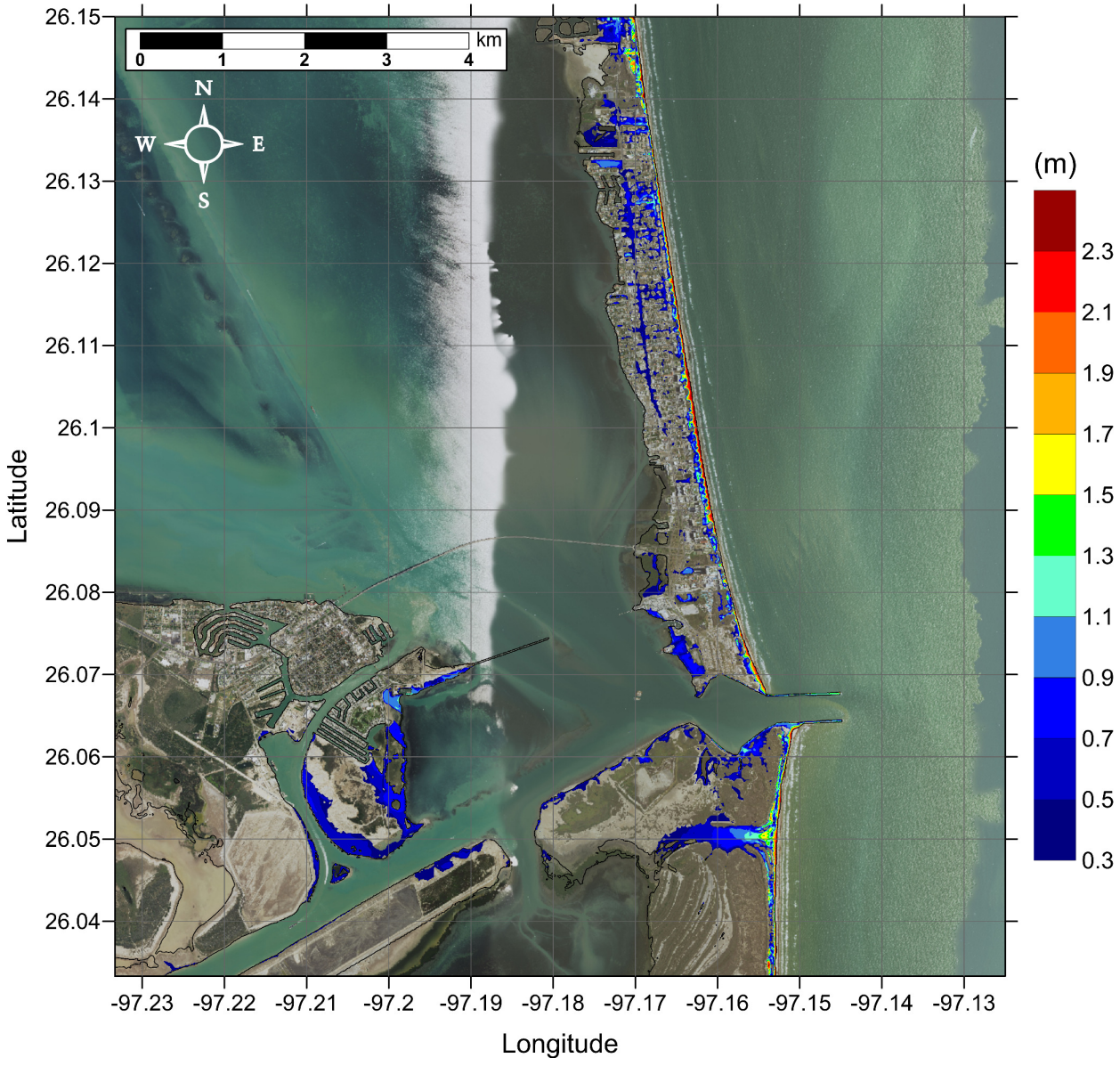

Figure 41: Maximum inundation depth (m) caused by the Probabilistic Submarine Landslide B-1 in South Padre Island, TX. Contour drawn is the zero-meter contour for land elevation.

South Padre Island, TX
Probabilistic Submarine Landslide B1 (PSL-B1)
Maximum Momentum Flux

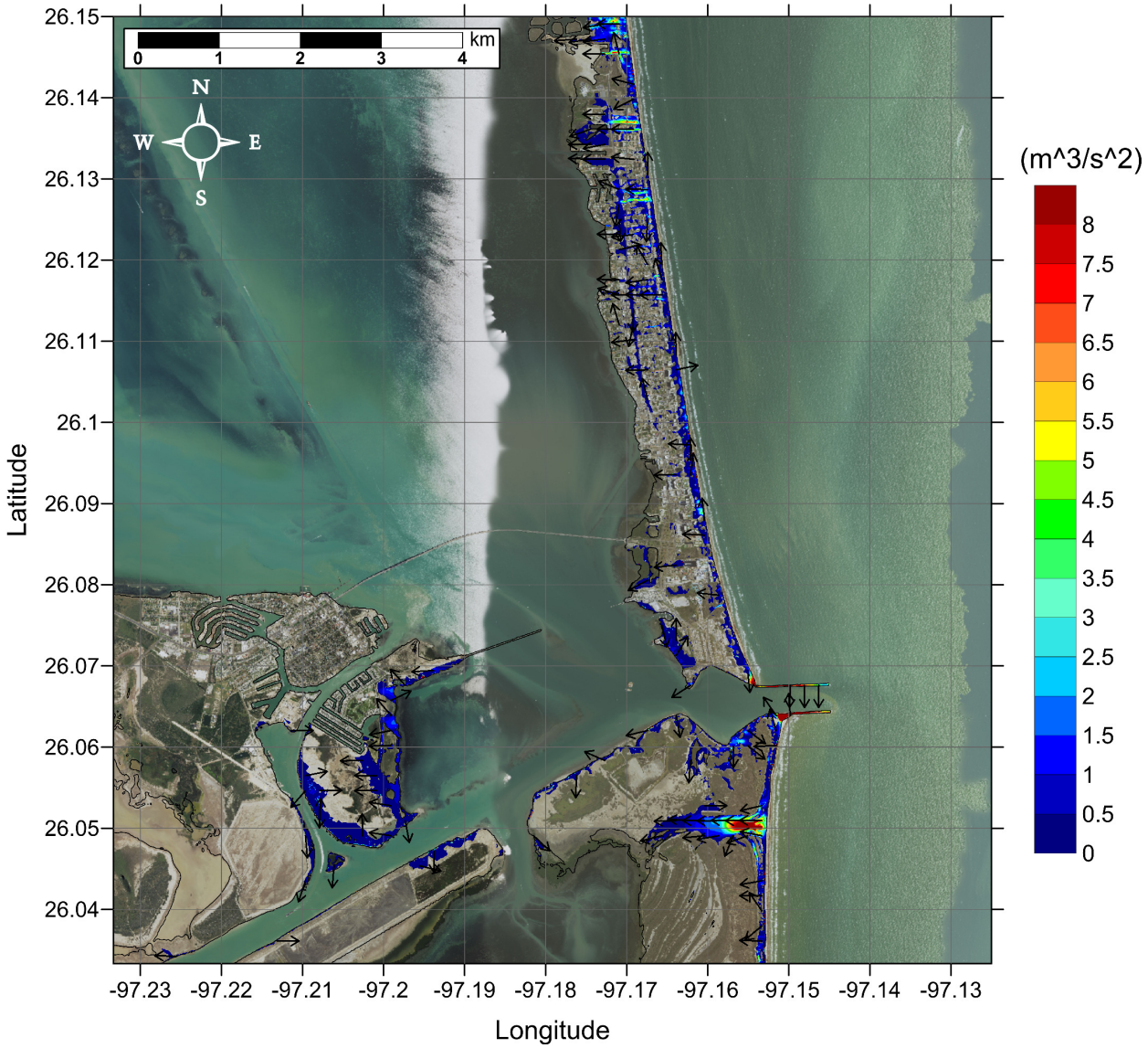

Figure 42: Maximum momentum flux (m^3/s^2) caused by the Probabilistic Submarine Landslide B-1 in South Padre Island, TX. Arrows represent direction of maximum momentum flux. Contour drawn is the zero-meter contour for land elevation.

South Padre Island, TX
Probabilistic Submarine Landslide B2 (PSL-B2)
Maximum Inundation Depth

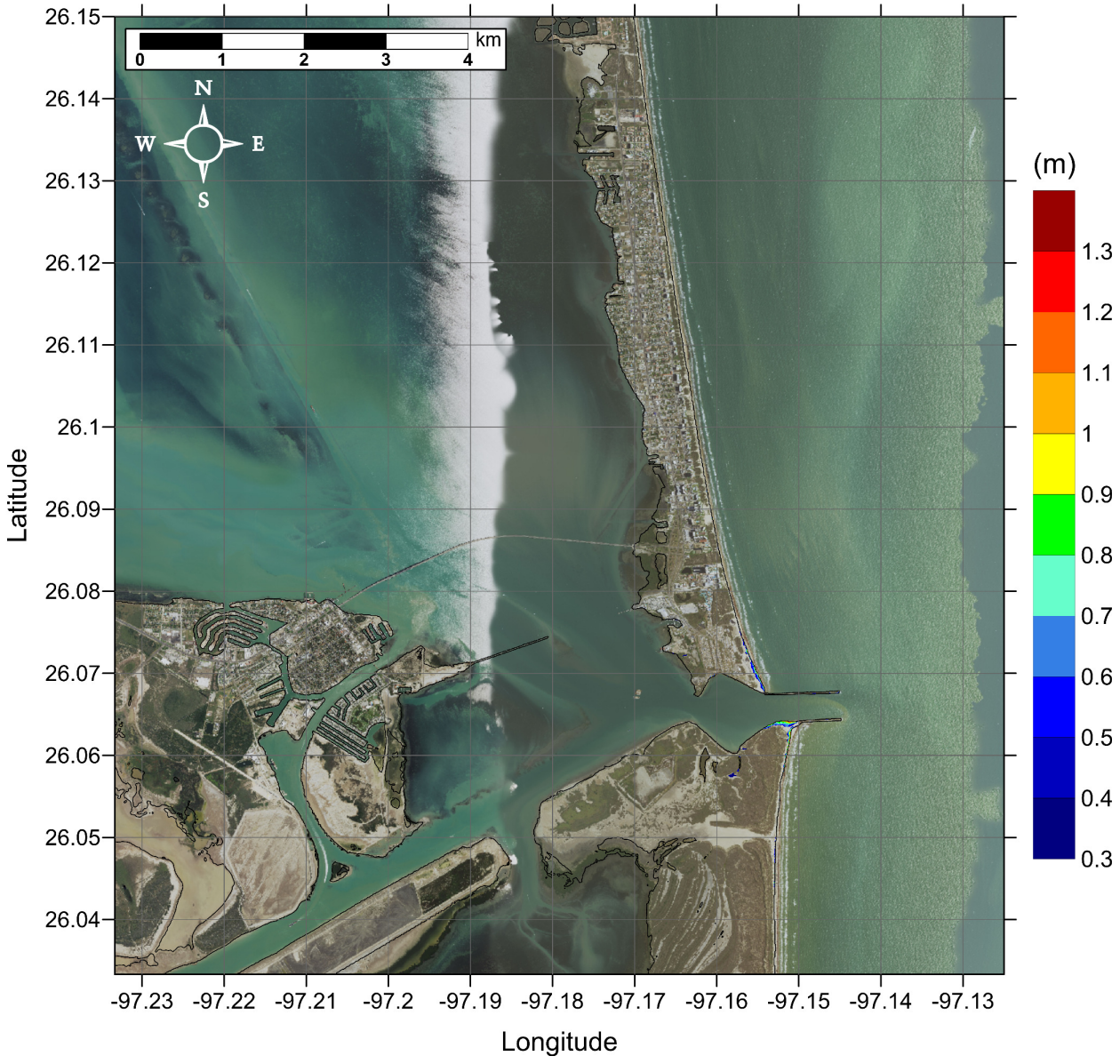

Figure 43: Maximum inundation depth (m) caused by the Probabilistic Submarine Landslide B-2 in South Padre Island, TX. Contour drawn is the zero-meter contour for land elevation. (Note: negligible inundation is seen from this source.)

South Padre Island, TX
Probabilistic Submarine Landslide B2 (PSL-B2)
Maximum Momentum Flux

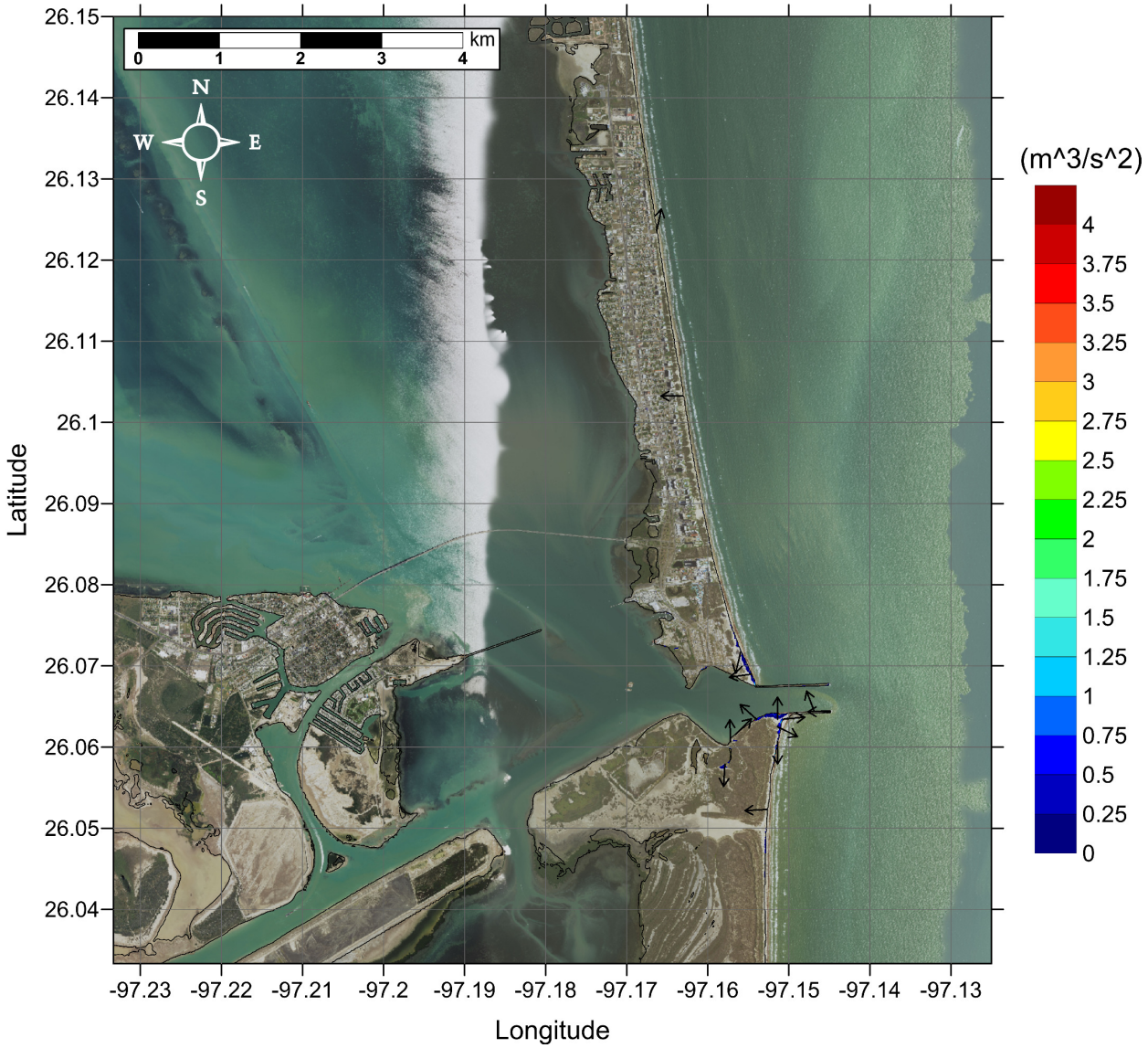

Figure 44: Maximum momentum flux (m^3/s^2) caused by the Probabilistic Submarine Landslide B-2 in South Padre Island, TX. Arrows represent direction of maximum momentum flux. Contour drawn is the zero-meter contour for land elevation. (Note: negligible inundation is seen from this source.)

South Padre Island, TX
Mississippi Canyon Submarine Landslide
Maximum Inundation Depth

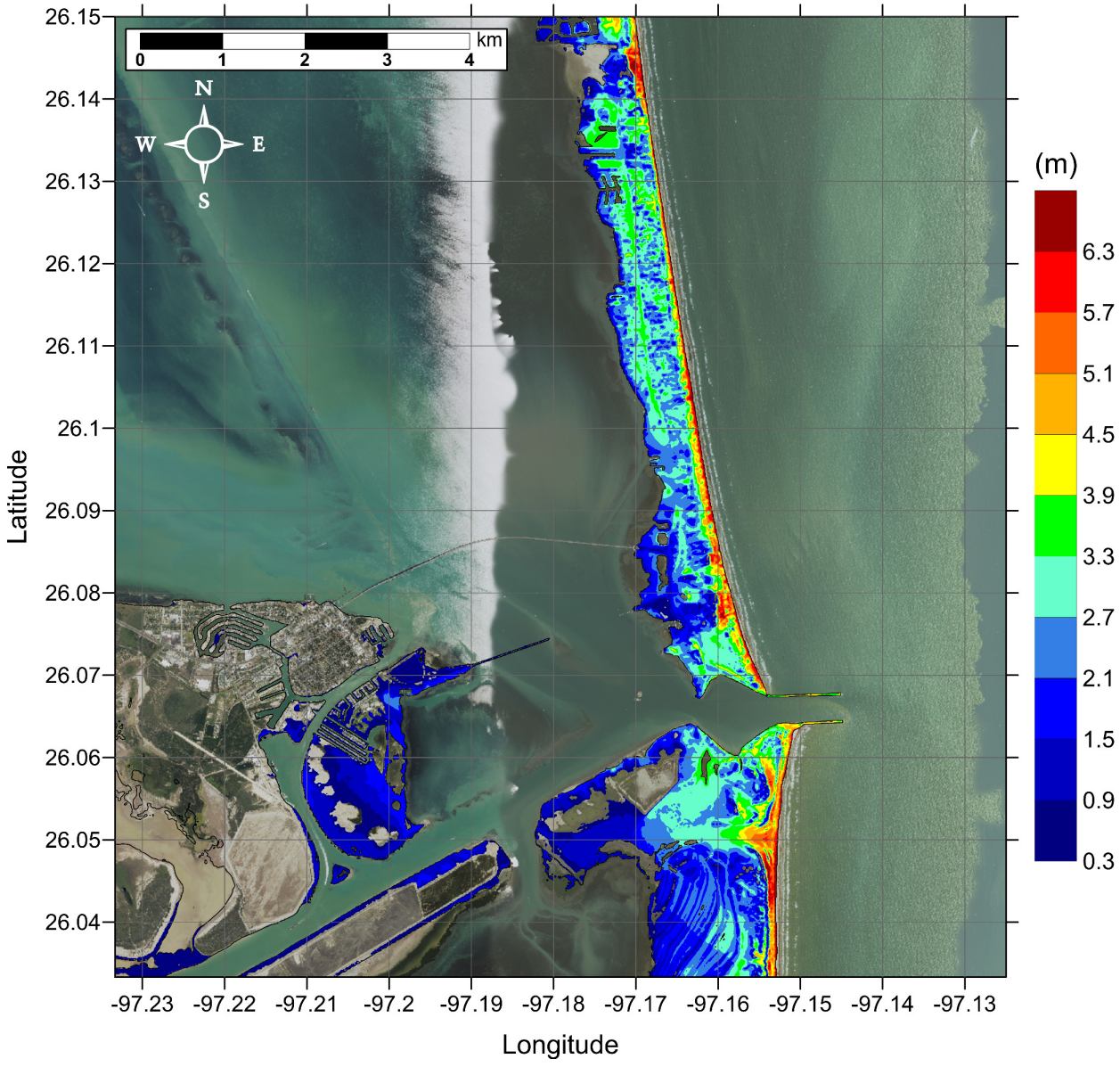

Figure 45: Maximum inundation depth (m) caused by the Mississippi Canyon submarine landslide in South Padre Island, TX. Contour drawn is the zero-meter contour for land elevation.

South Padre Island, TX
Mississippi Canyon Submarine Landslide
Maximum Momentum Flux

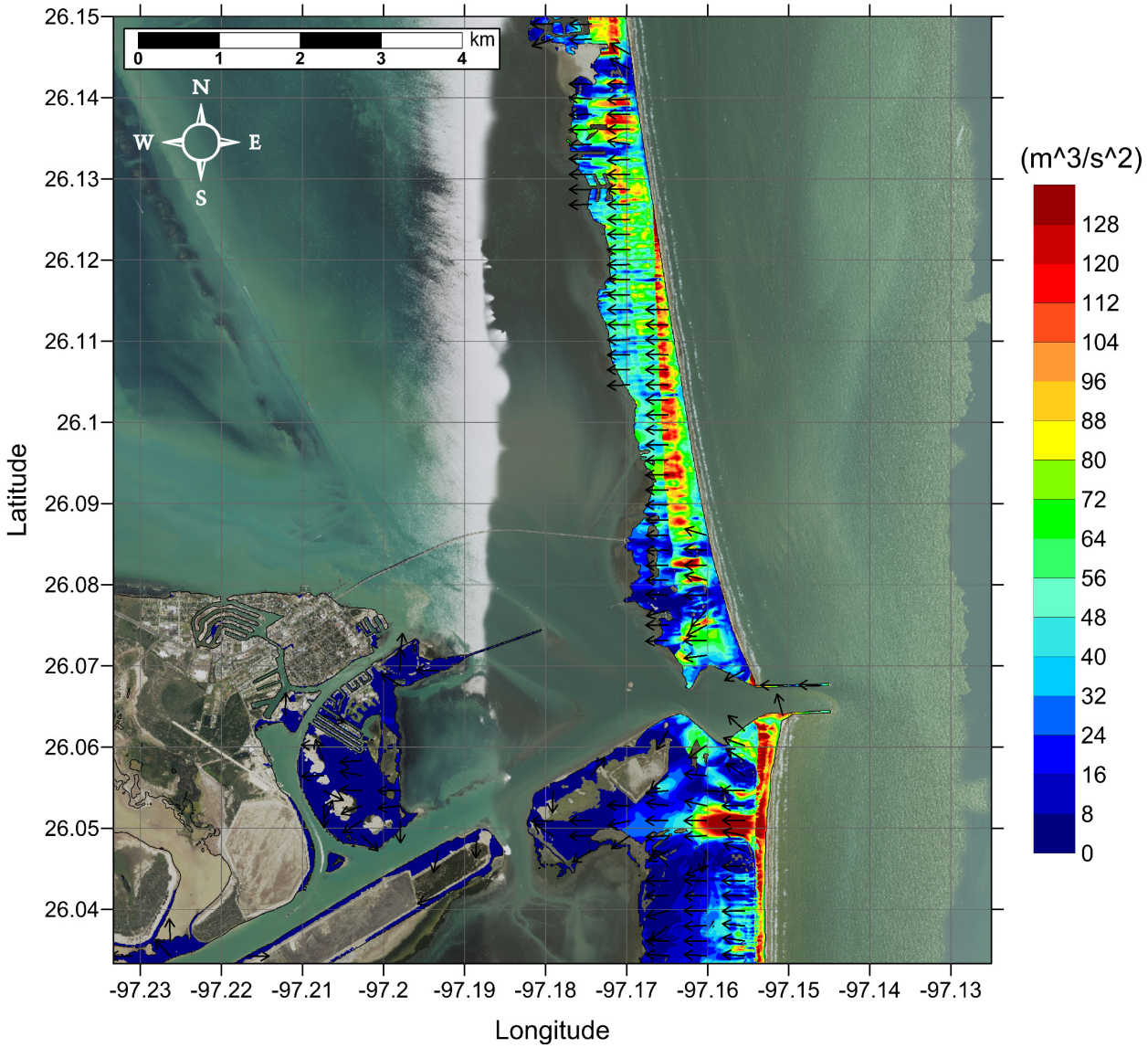

Figure 46: Maximum momentum flux (m^3/s^2) caused by the Mississippi Canyon submarine landslide in South Padre Island, TX. Arrows represent direction of maximum momentum flux. Contour drawn is the zero-meter contour for land elevation.

South Padre Island, TX
Probabilistic Submarine Landslide C (PSL-C)
Maximum Inundation Depth

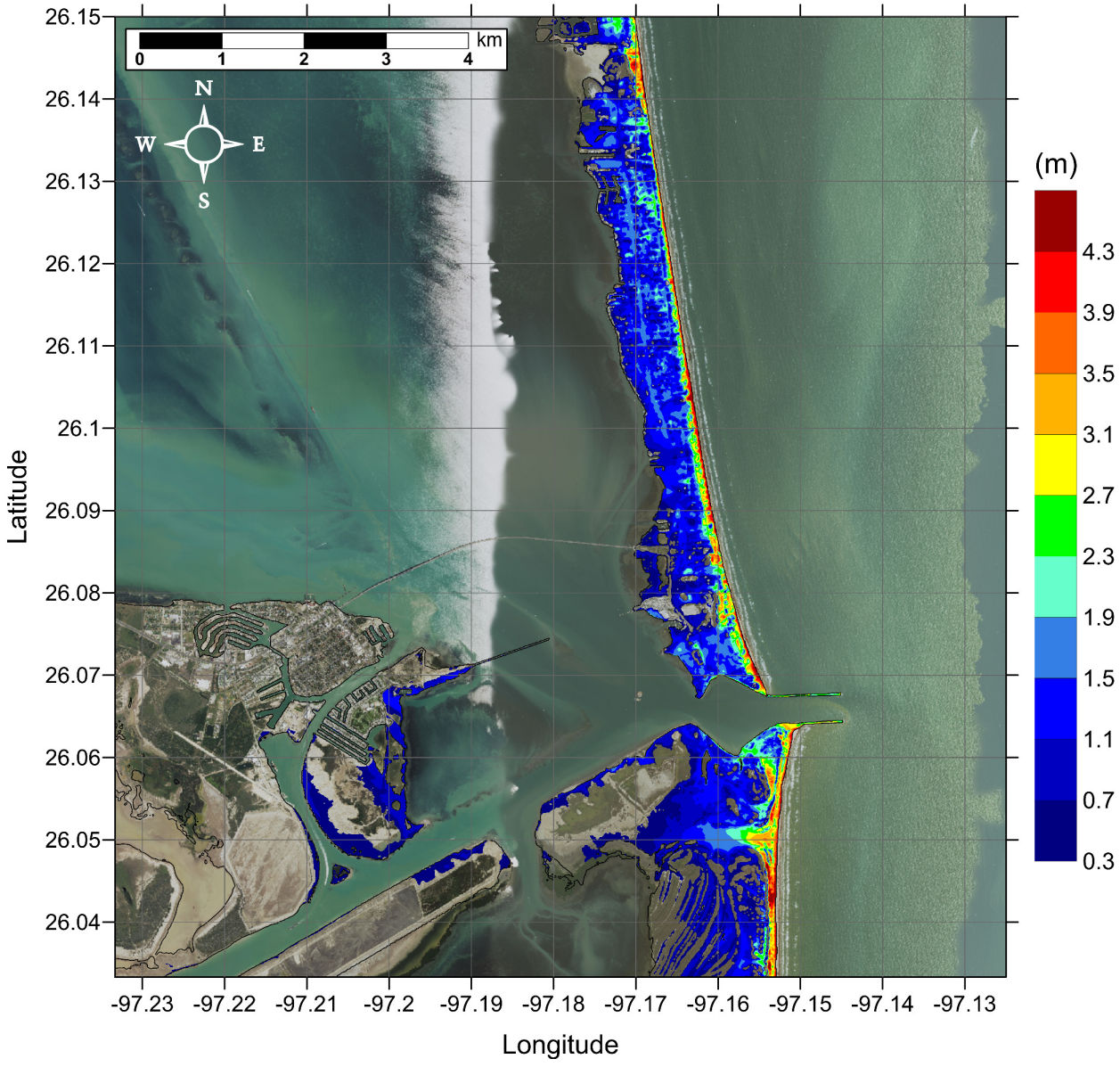

Figure 47: Maximum inundation depth (m) caused by the Probabilistic Submarine Landslide C in South Padre Island, TX. Contour drawn is the zero-meter contour for land elevation.

South Padre Island, TX
Probabilistic Submarine Landslide C (PSL-C)
Maximum Momentum Flux

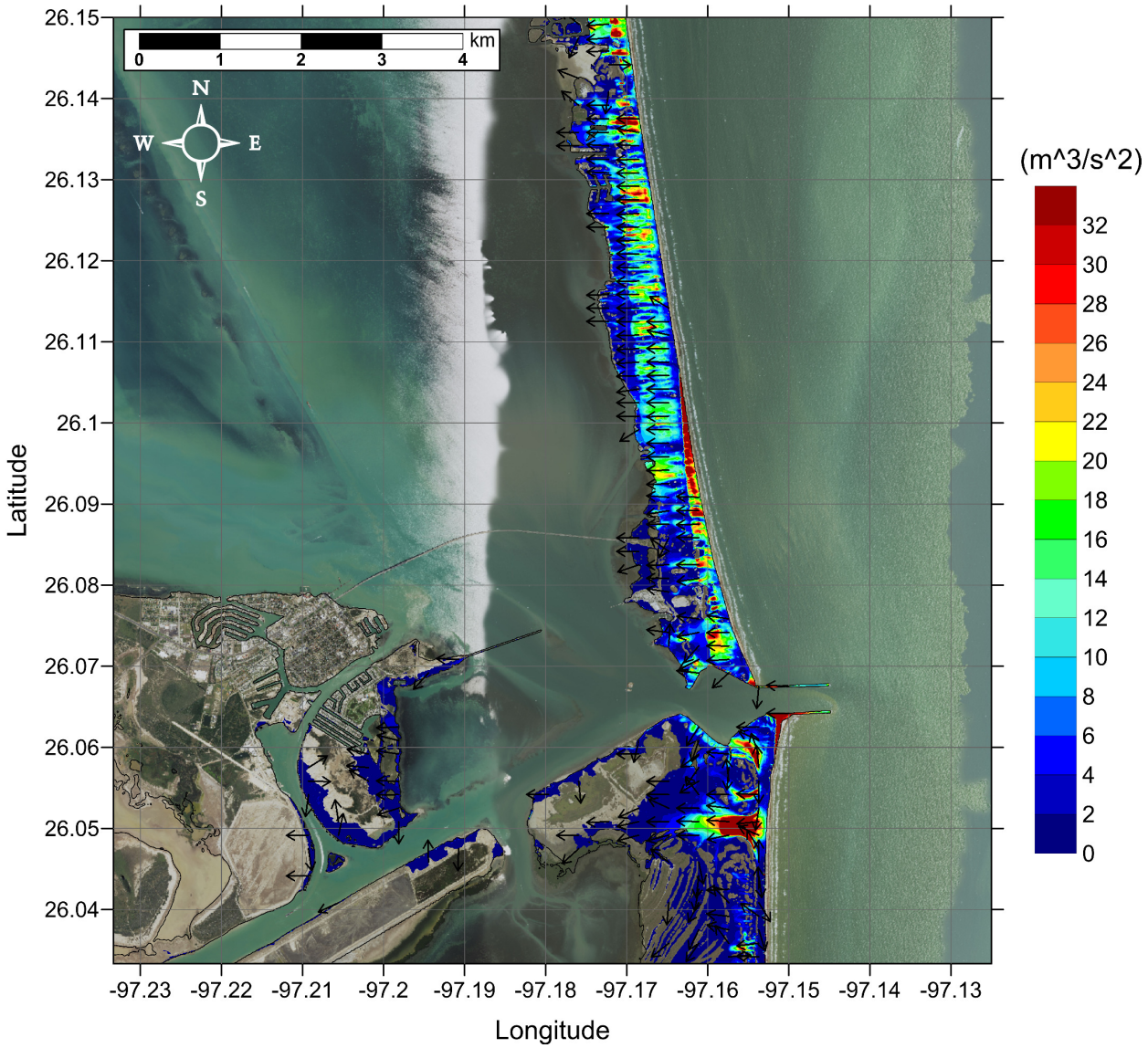

Figure 48: Maximum momentum flux (m^3/s^2) caused by the Probabilistic Submarine Landslide C in South Padre Island, TX. Arrows represent direction of maximum momentum flux. Contour drawn is the zero-meter contour for land elevation.

South Padre Island, TX
West Florida Submarine Landslide
Maximum Inundation Depth

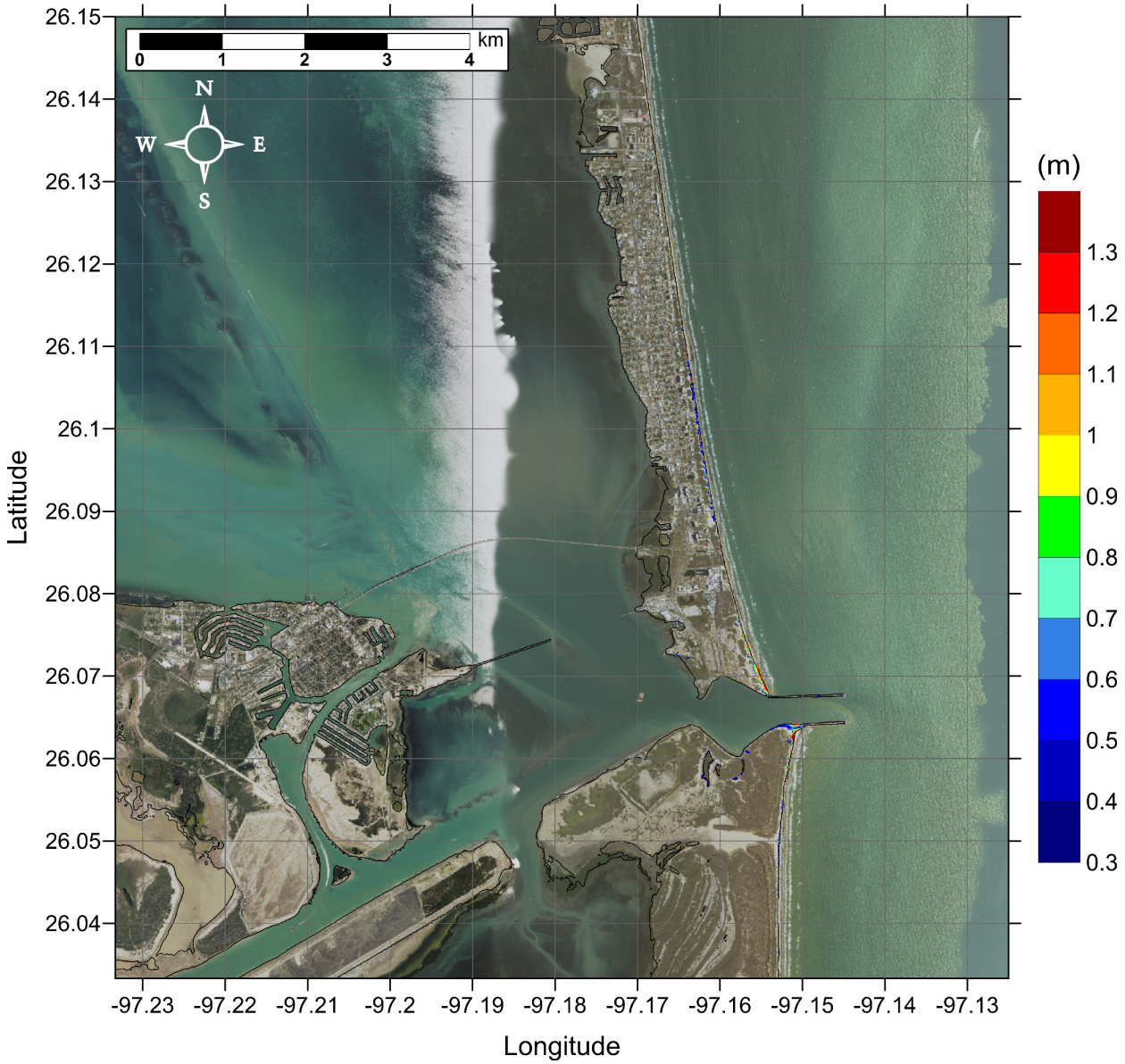

Figure 49: Maximum inundation depth (m) caused by the West Florida submarine landslide in South Padre Island, TX. Contour drawn is the zero-meter contour for land elevation. (Note: negligible inundation is seen from this source.)

South Padre Island, TX
West Florida Submarine Landslide
Maximum Momentum Flux

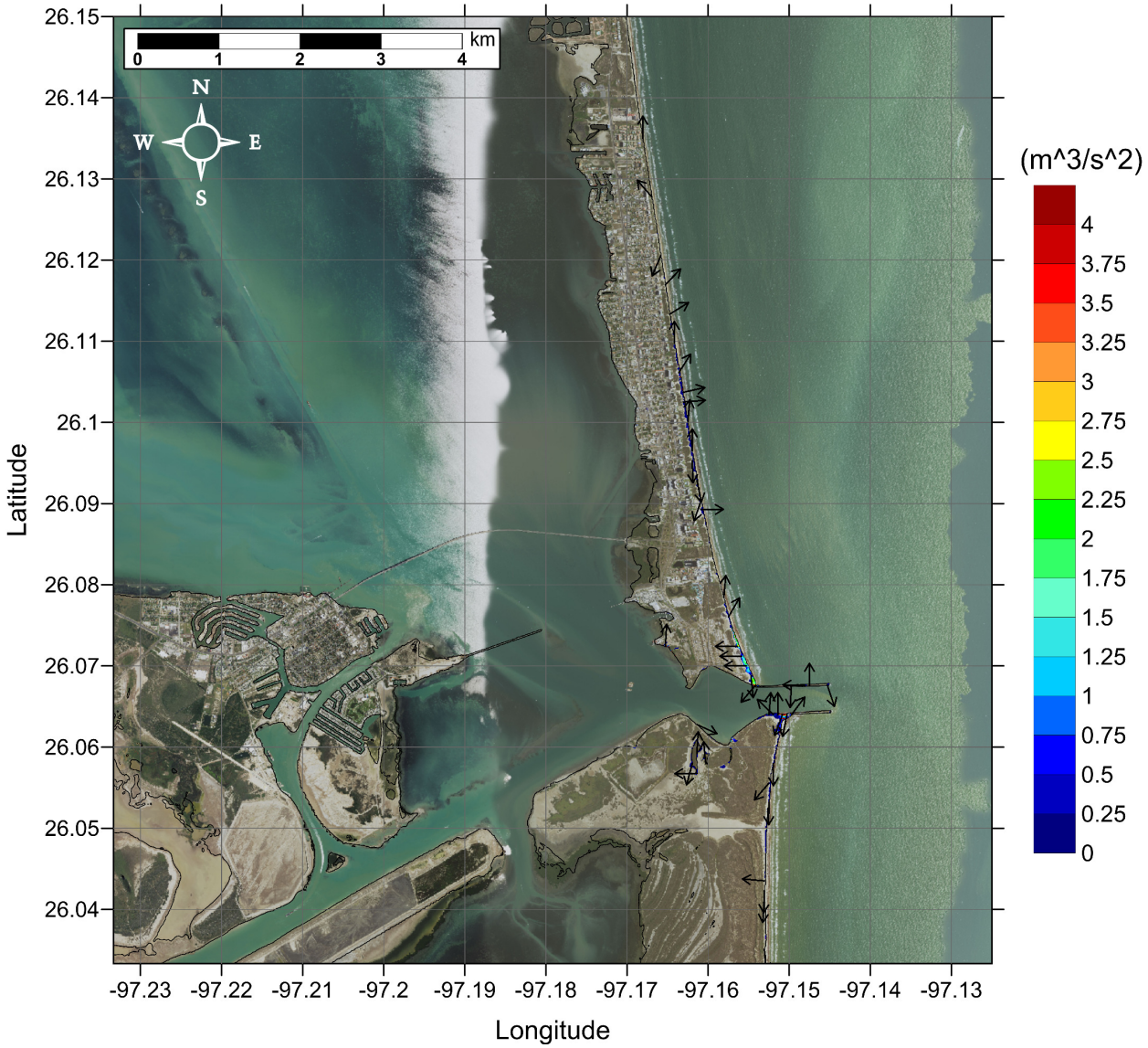

Figure 50: Maximum momentum flux (m^3/s^2) caused by the West Florida submarine landslide in South Padre Island, TX. Arrows represent direction of maximum momentum flux. Contour drawn is the zero-meter contour for land elevation. (Note: negligible inundation is seen from this source.)

South Padre Island, TX
Maximum of Maximums Inundation Depth

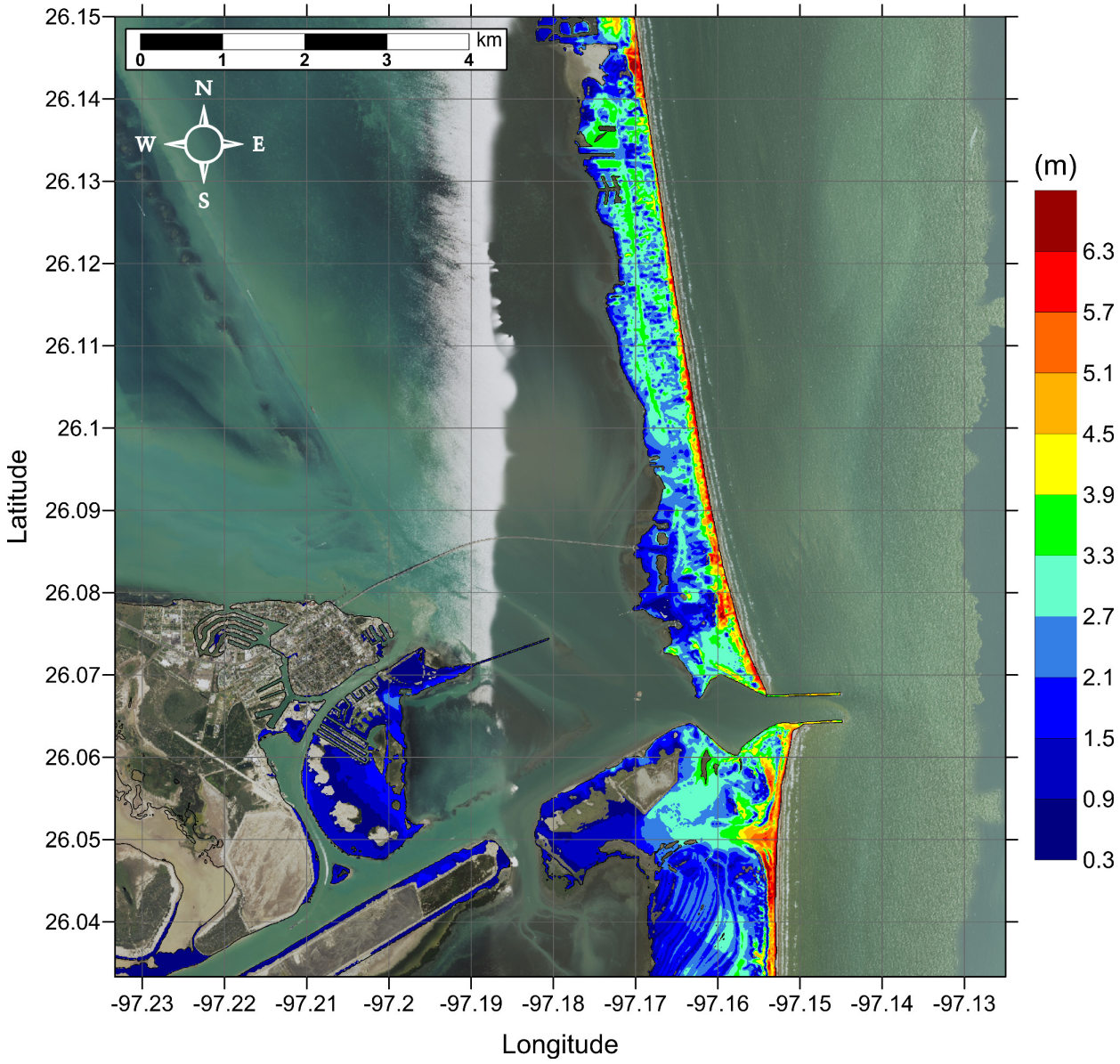

Figure 51: Maximum of maximums inundation depth (m) in South Padre Island, TX, calculated as the maximum inundation depth in each grid cell from an ensemble of all tsunami sources considered. Contour drawn is the zero-meter contour for land elevation.

South Padre Island, TX
Maximum Inundation Depth by Source

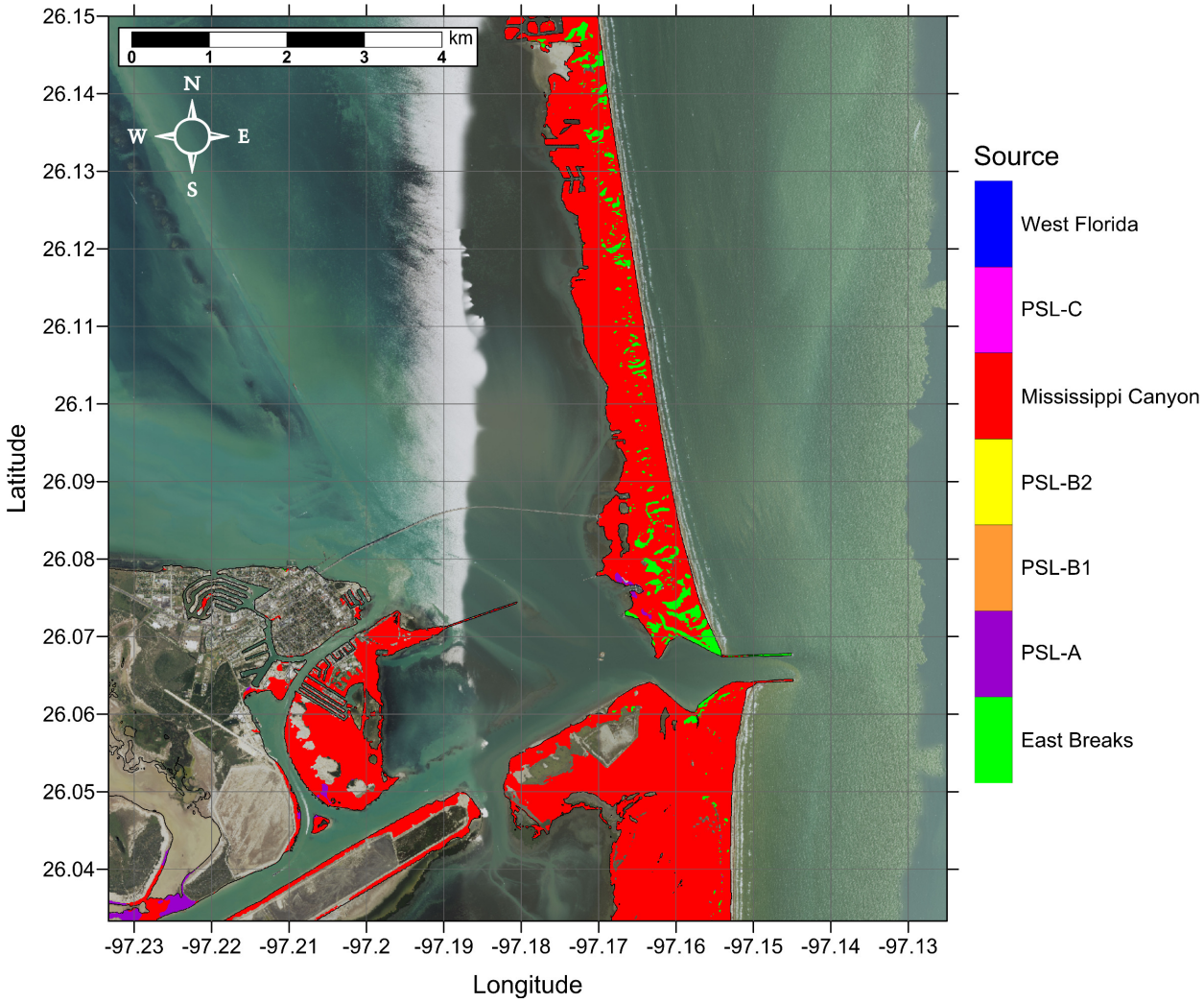

Figure 52: Indication of the tsunami source which causes the maximum of maximums inundation depth (m) in each grid cell from an ensemble of all tsunami sources considered (see Figure 51). Contour drawn is the zero-meter contour for land elevation.

5.2 Galveston Island, TX

Galveston, TX
Amplitude and Arrival Time of Maximum Tsunami Wave Recorded at Numerical Wave Gauge

Table 22: Maximum tsunami wave amplitude and corresponding arrival time after landslide failure at Galveston, TX numerical wave gauge: 28°59'16.32"N, 94°8'8.89"W (Figure 1), approximate water depth 18m. *The two values for wave amplitude and arrival time given for the West Florida landslide correspond to the first positive wave, which was not the maximum amplitude wave, and the second positive wave, which produced the absolute maximum wave amplitude recorded at this gauge.

Tsunami Source	Maximum Wave Amplitude (m)	Arrival Time After Landslide Failure (hr)
East Breaks	1.47	2.2
PSL-A	1.17	2.1
PSL-B1	2.18	2.6
PSL-B2	0.77	2.8
Mississippi Canyon	4.26	3.1
PSL-C	3.66	3.3
West Florida*	0.48, 0.78	3.6, 3.8

Galveston, TX
East Breaks Submarine Landslide
Maximum Inundation Depth

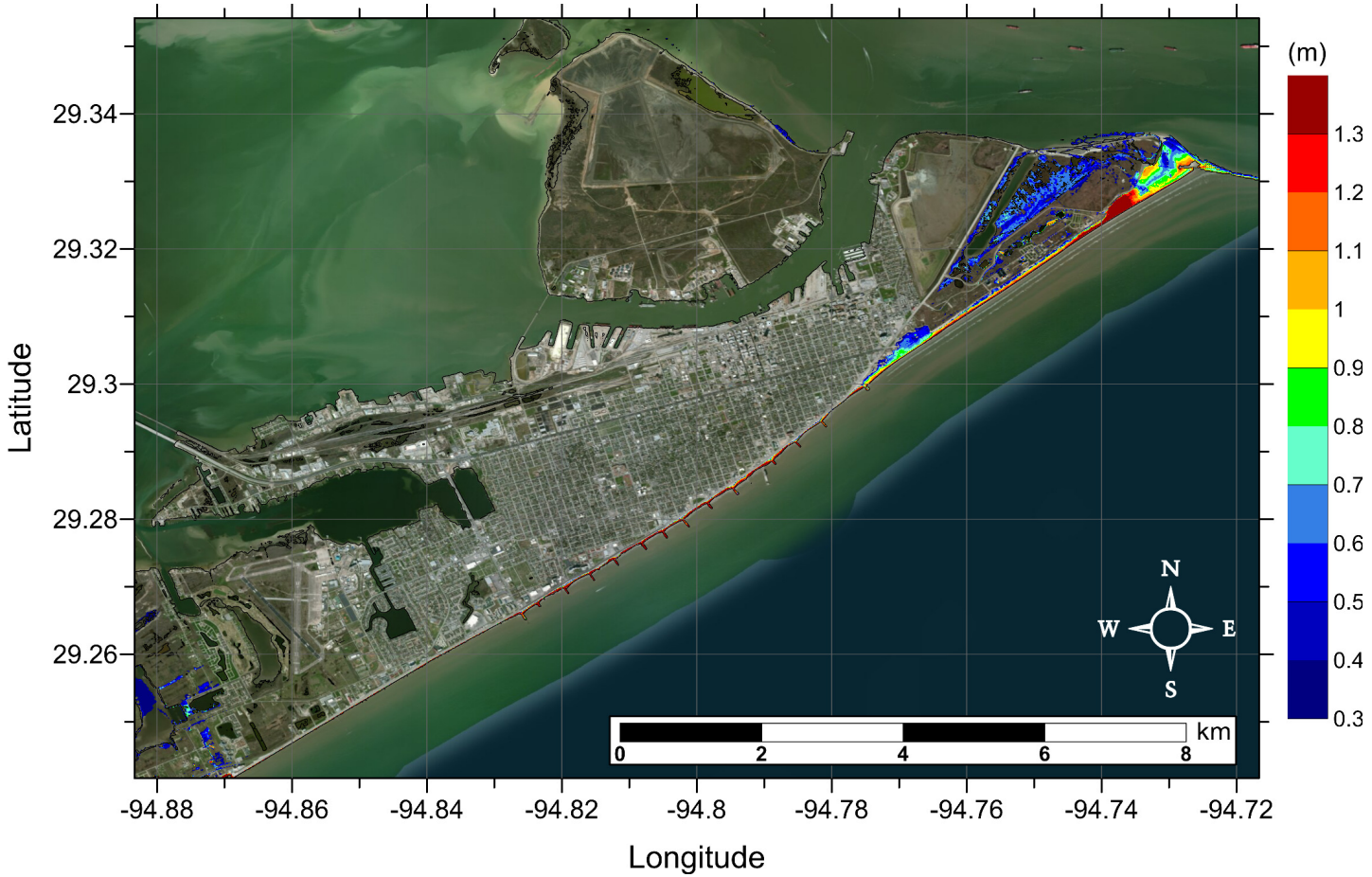

Figure 53: Maximum inundation depth (m) caused by the East Breaks submarine landslide in Galveston, TX. Contour drawn is the zero-meter contour for land elevation.

Galveston, TX
East Breaks Submarine Landslide
Maximum Momentum Flux

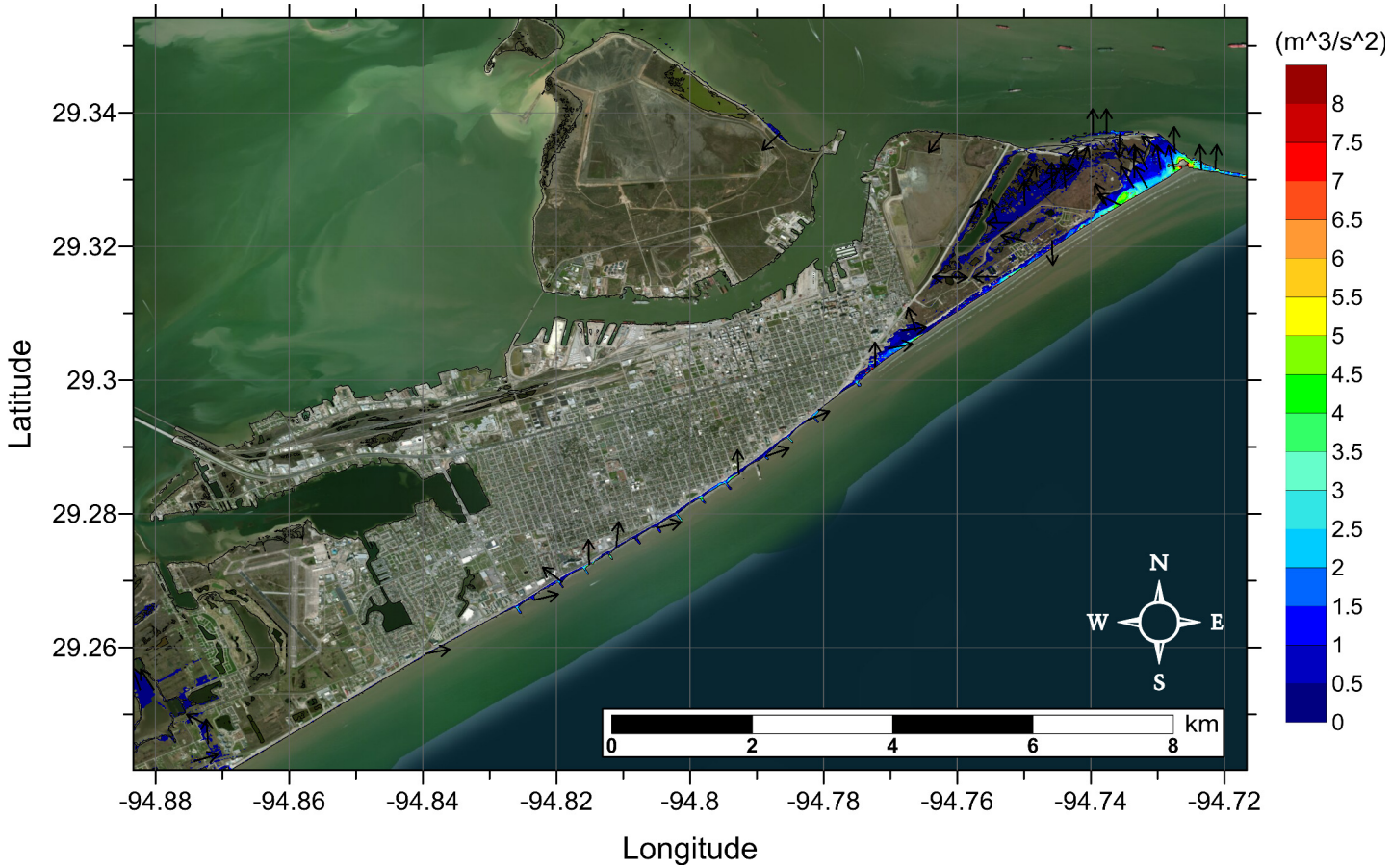

Figure 54: Maximum momentum flux (m^3/s^2) caused by the East Breaks submarine landslide in Galveston, TX. Arrows represent direction of maximum momentum flux. Contour drawn is the zero-meter contour for land elevation.

Galveston, TX
Probabilistic Submarine Landslide A (PSL-A)
Maximum Inundation Depth

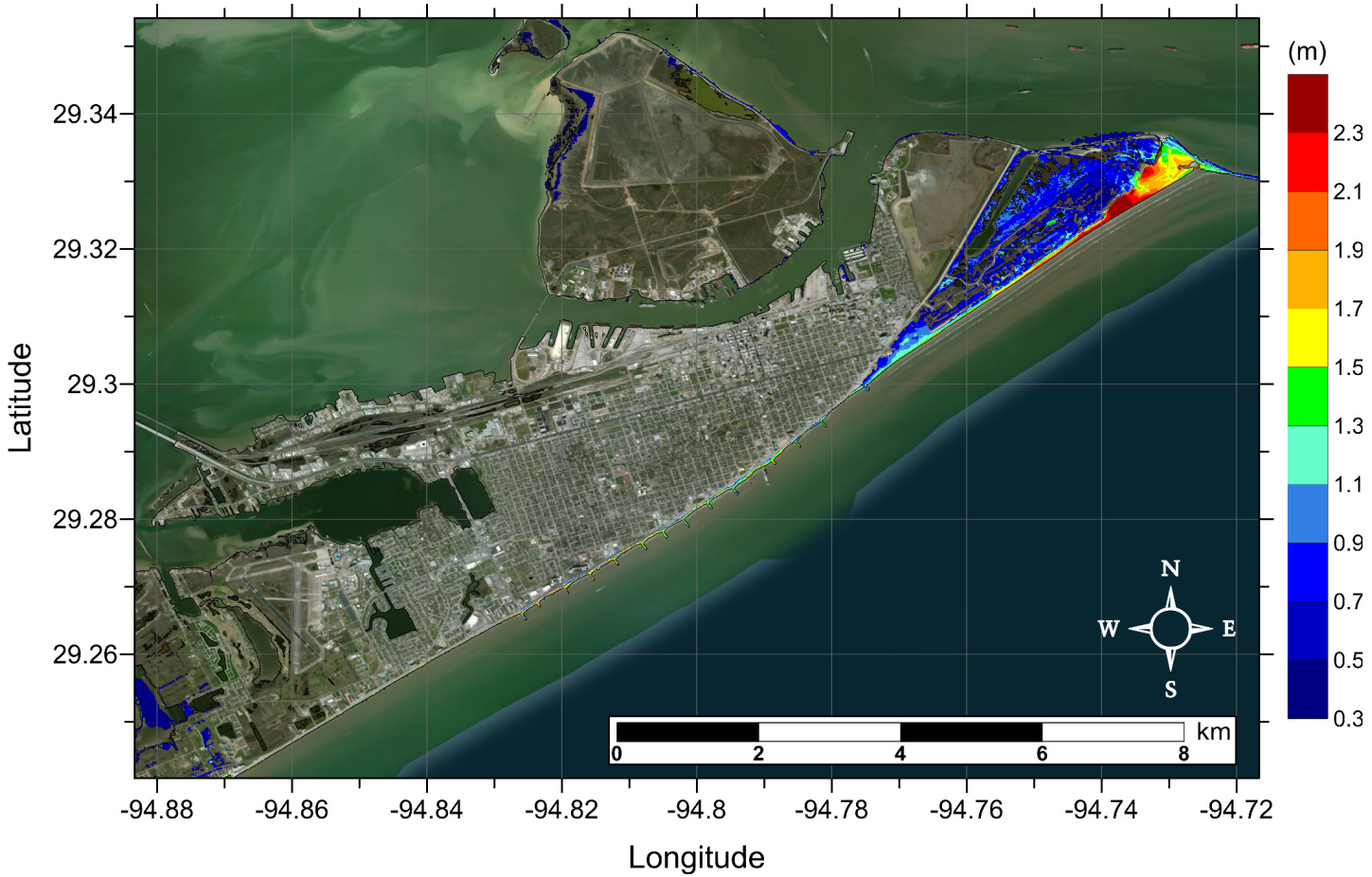

Figure 55: Maximum inundation depth (m) caused by the Probabilistic Submarine Landslide A in Galveston, TX. Contour drawn is the zero-meter contour for land elevation.

Galveston, TX
Probabilistic Submarine Landslide A (PSL-A)
Maximum Momentum Flux

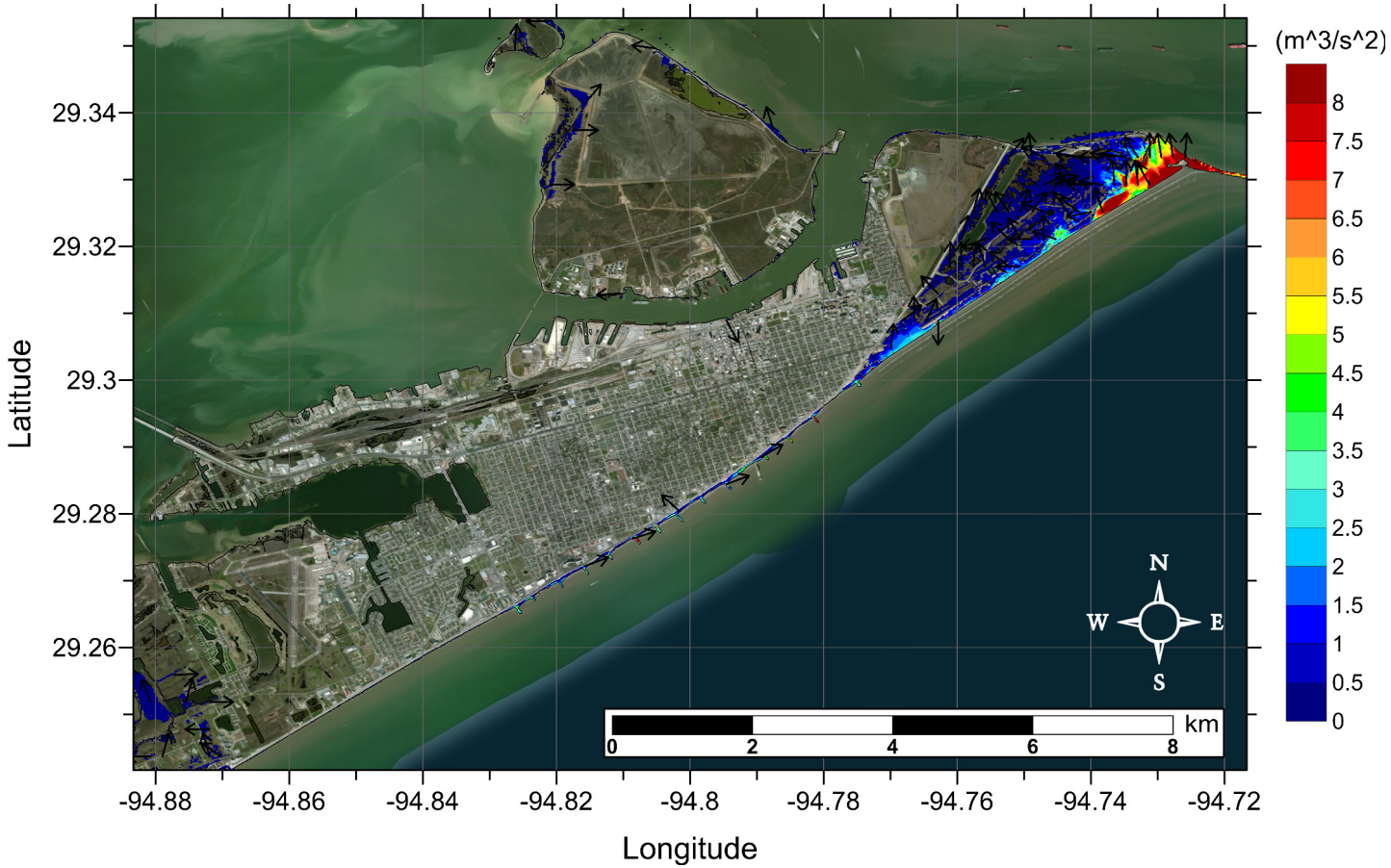

Figure 56: Maximum momentum flux (m^3/s^2) caused by the Probabilistic Submarine Landslide A in Galveston, TX. Arrows represent direction of maximum momentum flux. Contour drawn is the zero-meter contour for land elevation.

Galveston, TX
Probabilistic Submarine Landslide B1 (PSL-B1)
Maximum Inundation Depth

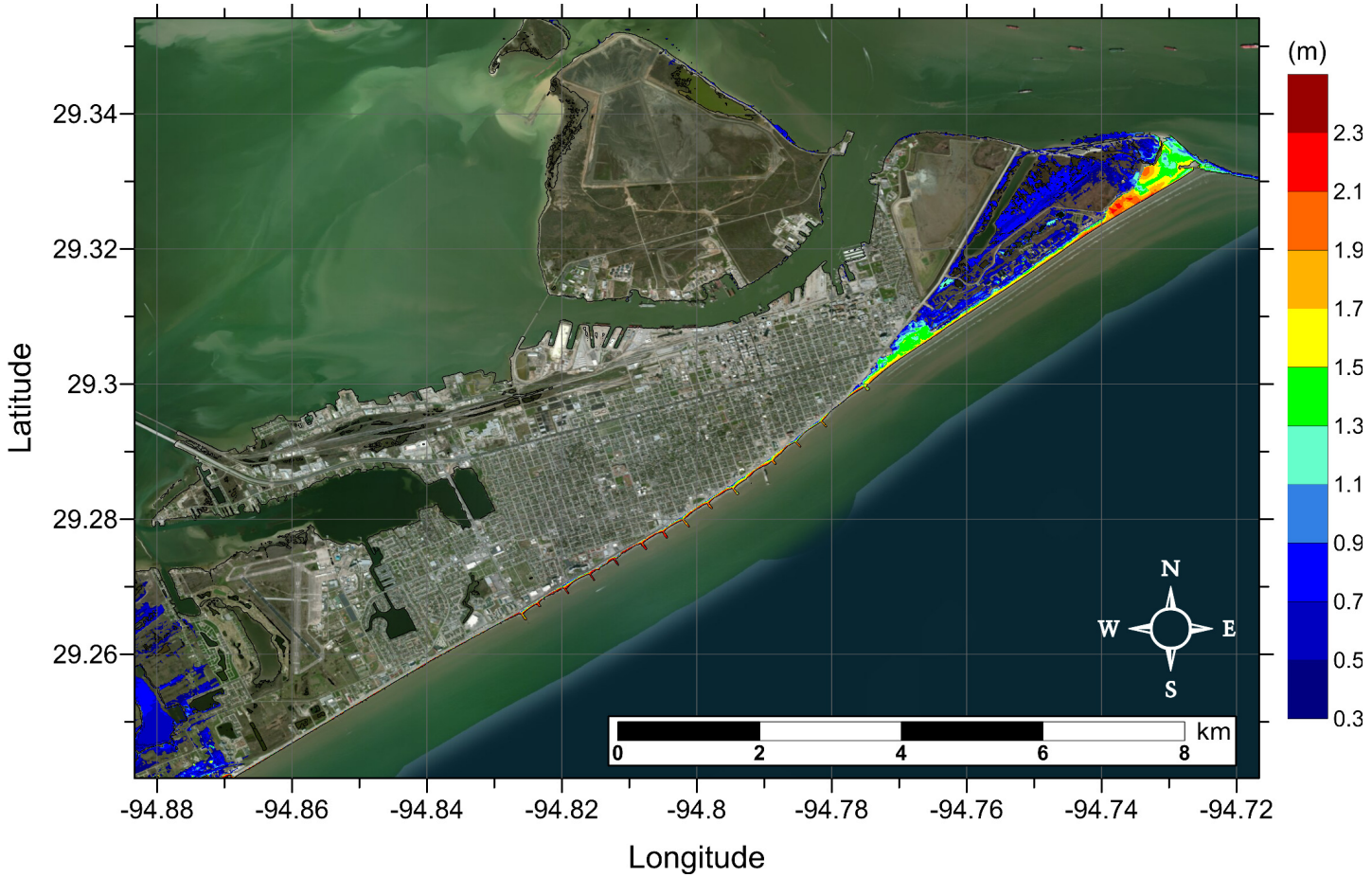

Figure 57: Maximum inundation depth (m) caused by the Probabilistic Submarine Landslide B-1 in Galveston, TX. Contour drawn is the zero-meter contour for land elevation.

Galveston, TX
Probabilistic Submarine Landslide B1 (PSL-B1)
Maximum Momentum Flux

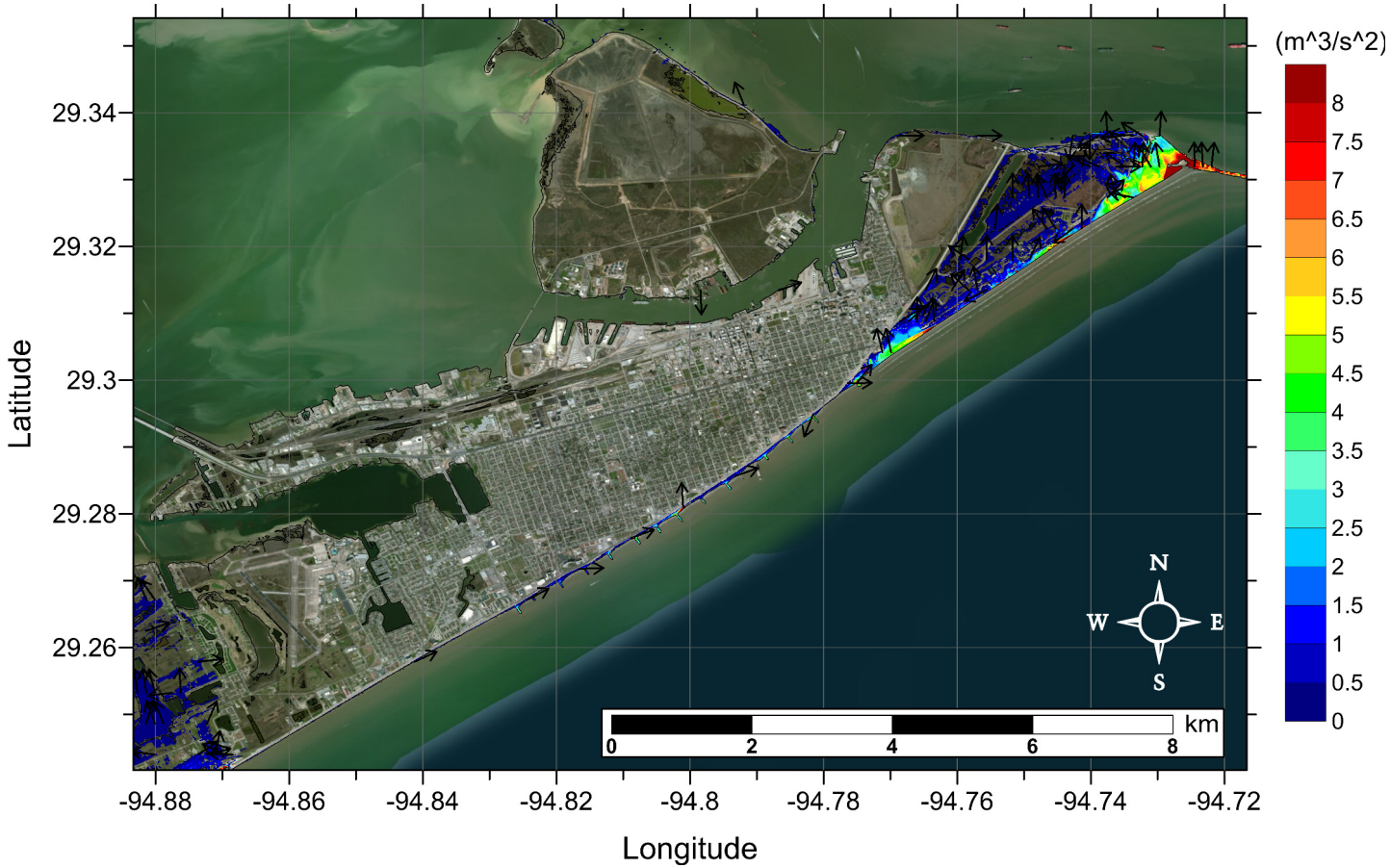

Figure 58: Maximum momentum flux (m^3/s^2) caused by the Probabilistic Submarine Landslide B-1 in Galveston, TX. Arrows represent direction of maximum momentum flux. Contour drawn is the zero-meter contour for land elevation.

Galveston, TX
Probabilistic Submarine Landslide B2 (PSL-B2)
Maximum Inundation Depth

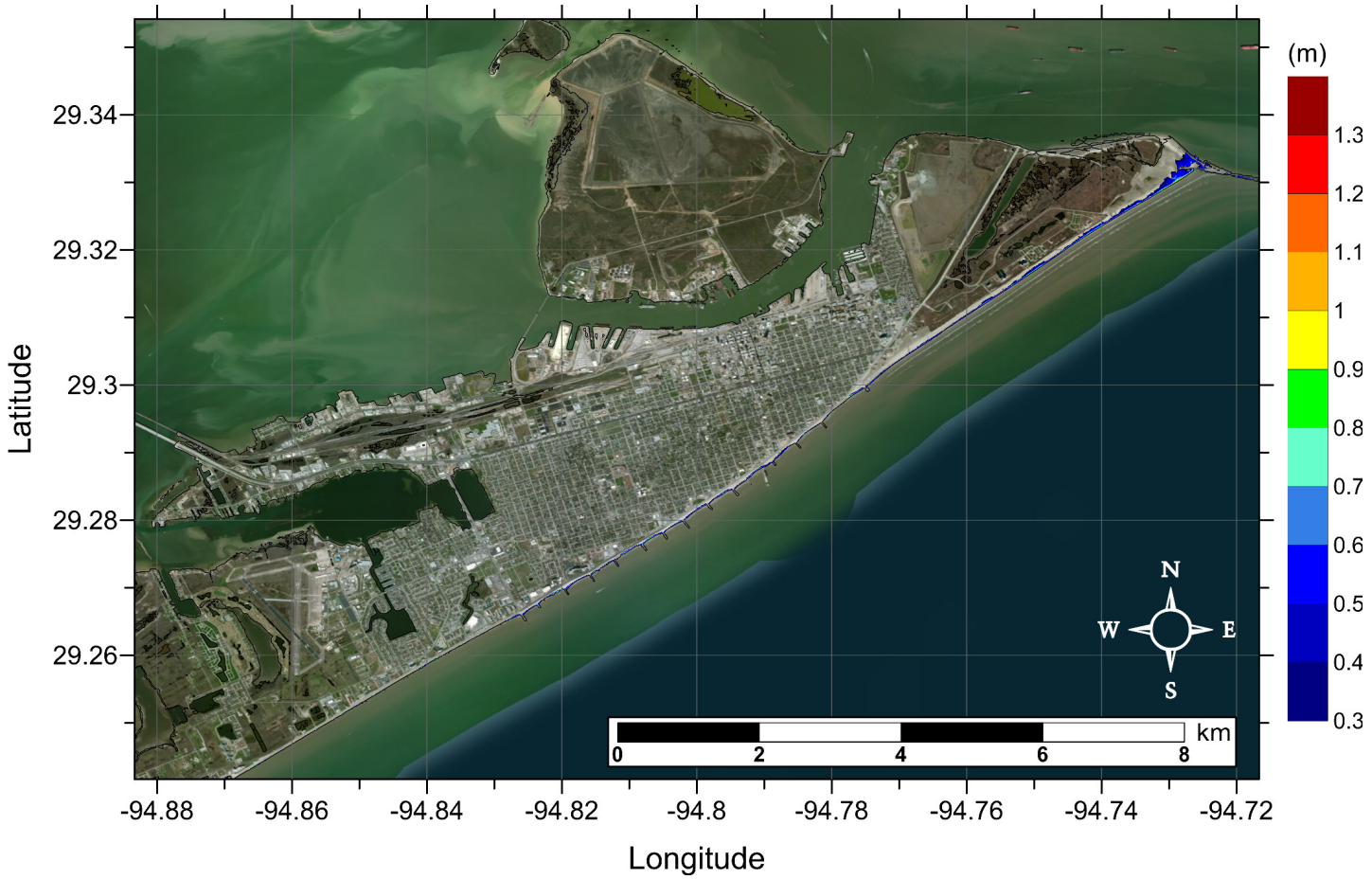

Figure 59: Maximum inundation depth (m) caused by the Probabilistic Submarine Landslide B-2 in Galveston, TX. Contour drawn is the zero-meter contour for land elevation. (Note: negligible inundation is seen from this source.)

Galveston, TX
Probabilistic Submarine Landslide B2 (PSL-B2)
Maximum Momentum Flux

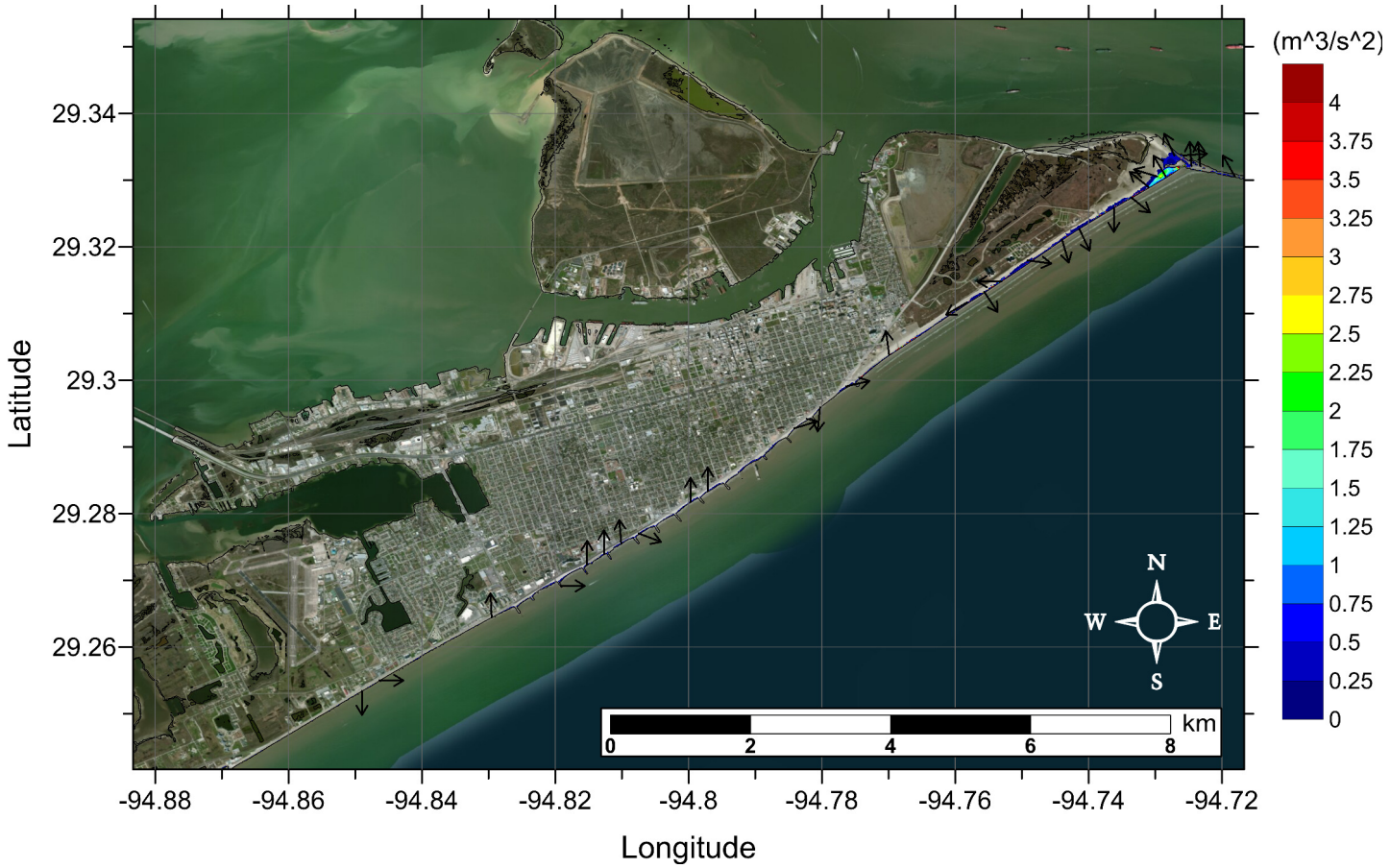

Figure 60: Maximum momentum flux (m^3/s^2) caused by the Probabilistic Submarine Landslide B-2 in Galveston, TX. Arrows represent direction of maximum momentum flux. Contour drawn is the zero-meter contour for land elevation. (Note: negligible inundation is seen from this source.)

Galveston, TX
Mississippi Canyon Submarine Landslide
Maximum Inundation Depth

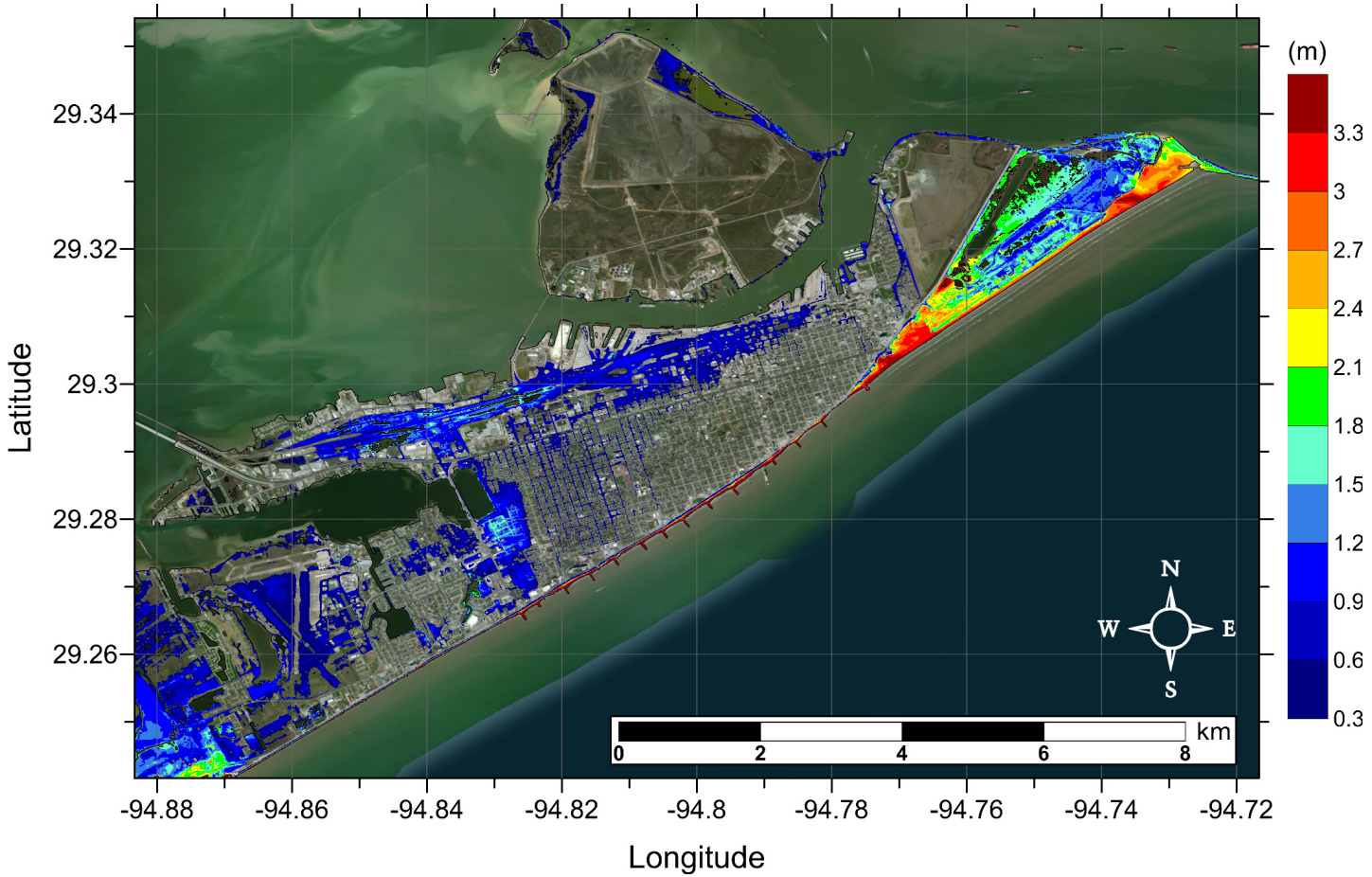

Figure 61: Maximum inundation depth (m) caused by the Mississippi Canyon submarine landslide in Galveston, TX. Contour drawn is the zero-meter contour for land elevation.

Galveston, TX
Mississippi Canyon Submarine Landslide
Maximum Momentum Flux

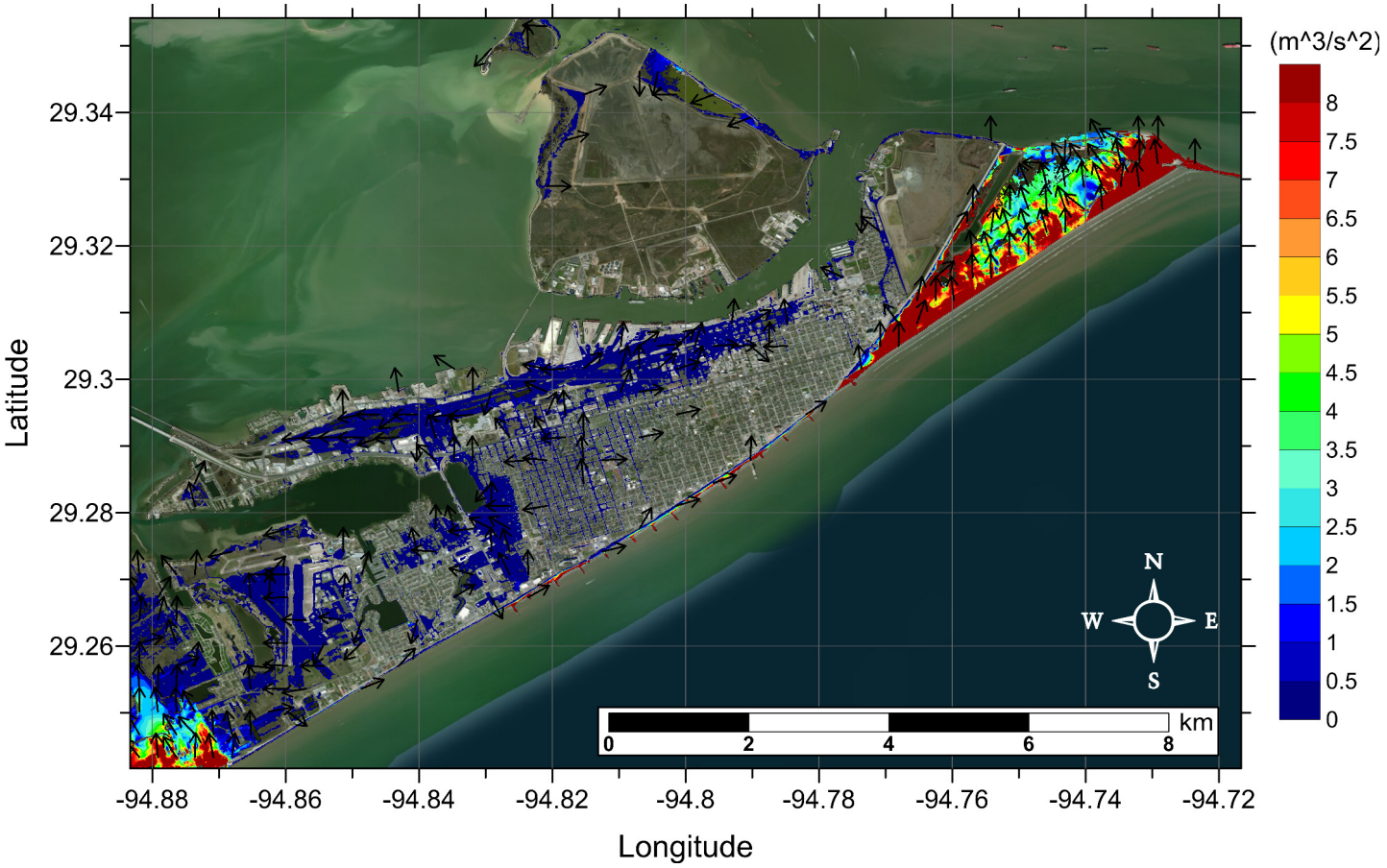

Figure 62: Maximum momentum flux (m^3/s^2) caused by the Mississippi Canyon submarine landslide in Galveston, TX. Arrows represent direction of maximum momentum flux. Contour drawn is the zero-meter contour for land elevation.

Galveston, TX
Probabilistic Submarine Landslide C (PSL-C)
Maximum Inundation Depth

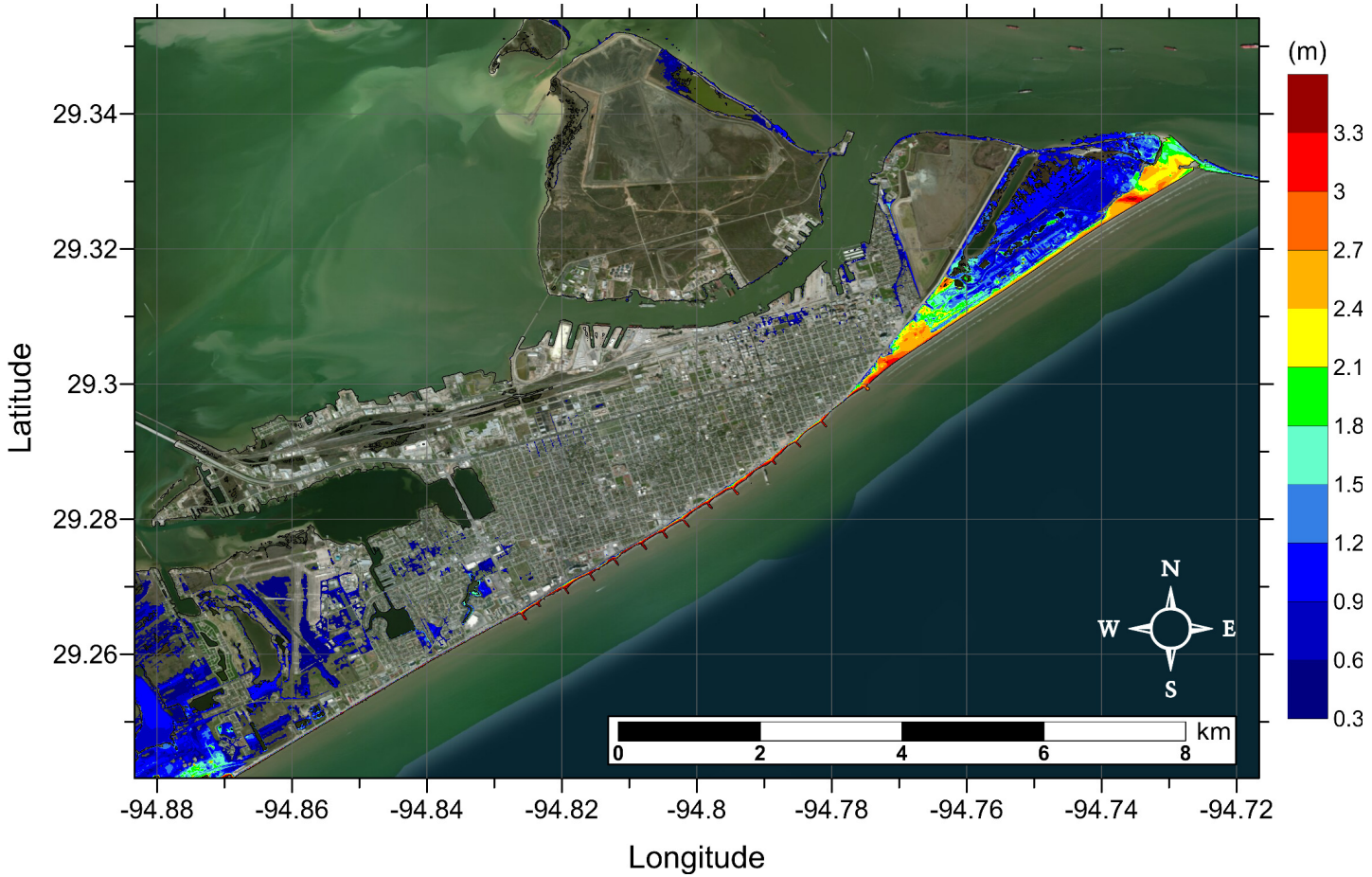

Figure 63: Maximum inundation depth (m) caused by the Probabilistic Submarine Landslide C in Galveston, TX. Contour drawn is the zero-meter contour for land elevation.

Galveston, TX
Probabilistic Submarine Landslide C (PSL-C)
Maximum Momentum Flux

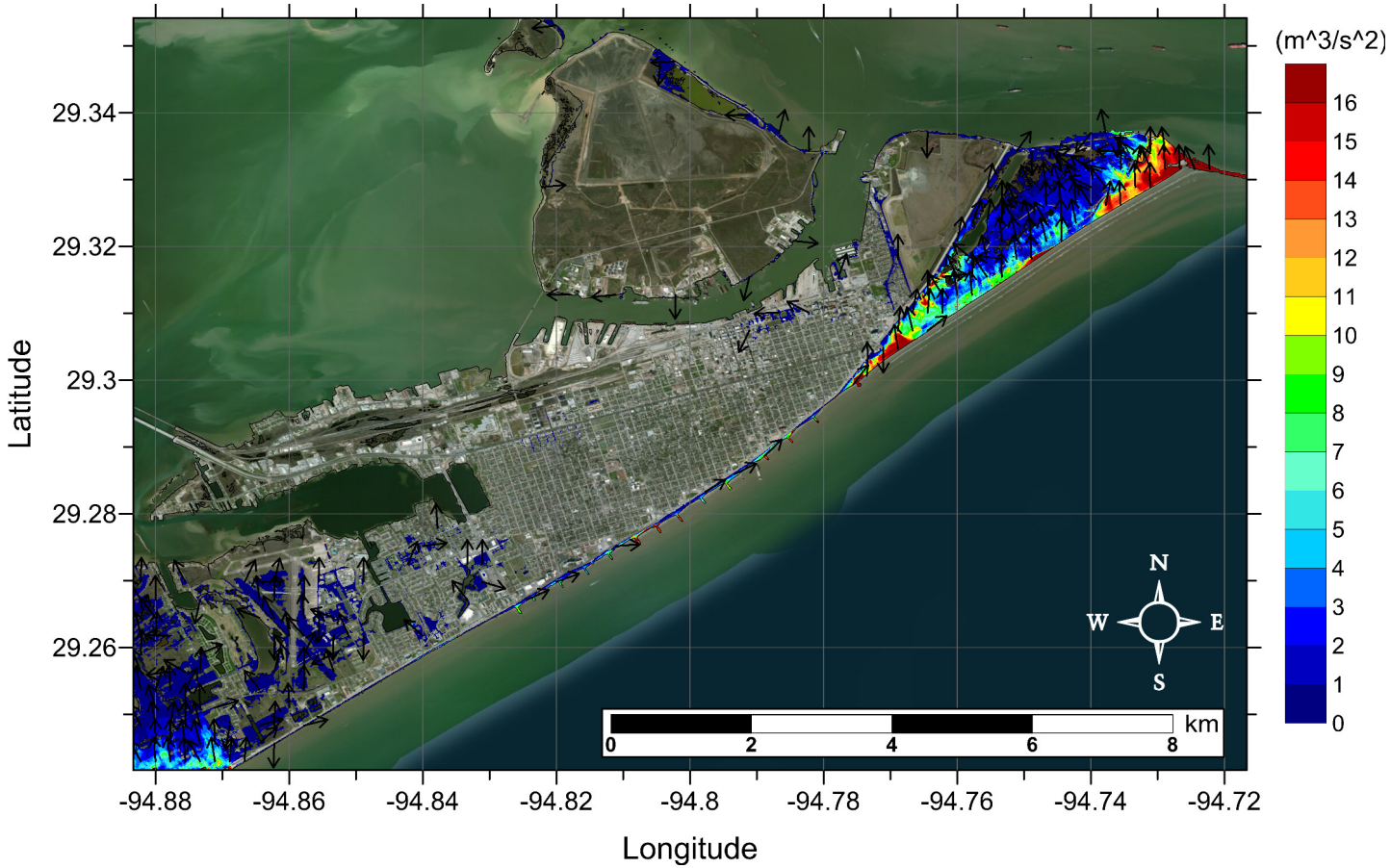

Figure 64: Maximum momentum flux (m^3/s^2) caused by the Probabilistic Submarine Landslide C in Galveston, TX. Arrows represent direction of maximum momentum flux. Contour drawn is the zero-meter contour for land elevation.

Galveston, TX
West Florida Submarine Landslide
Maximum Inundation Depth

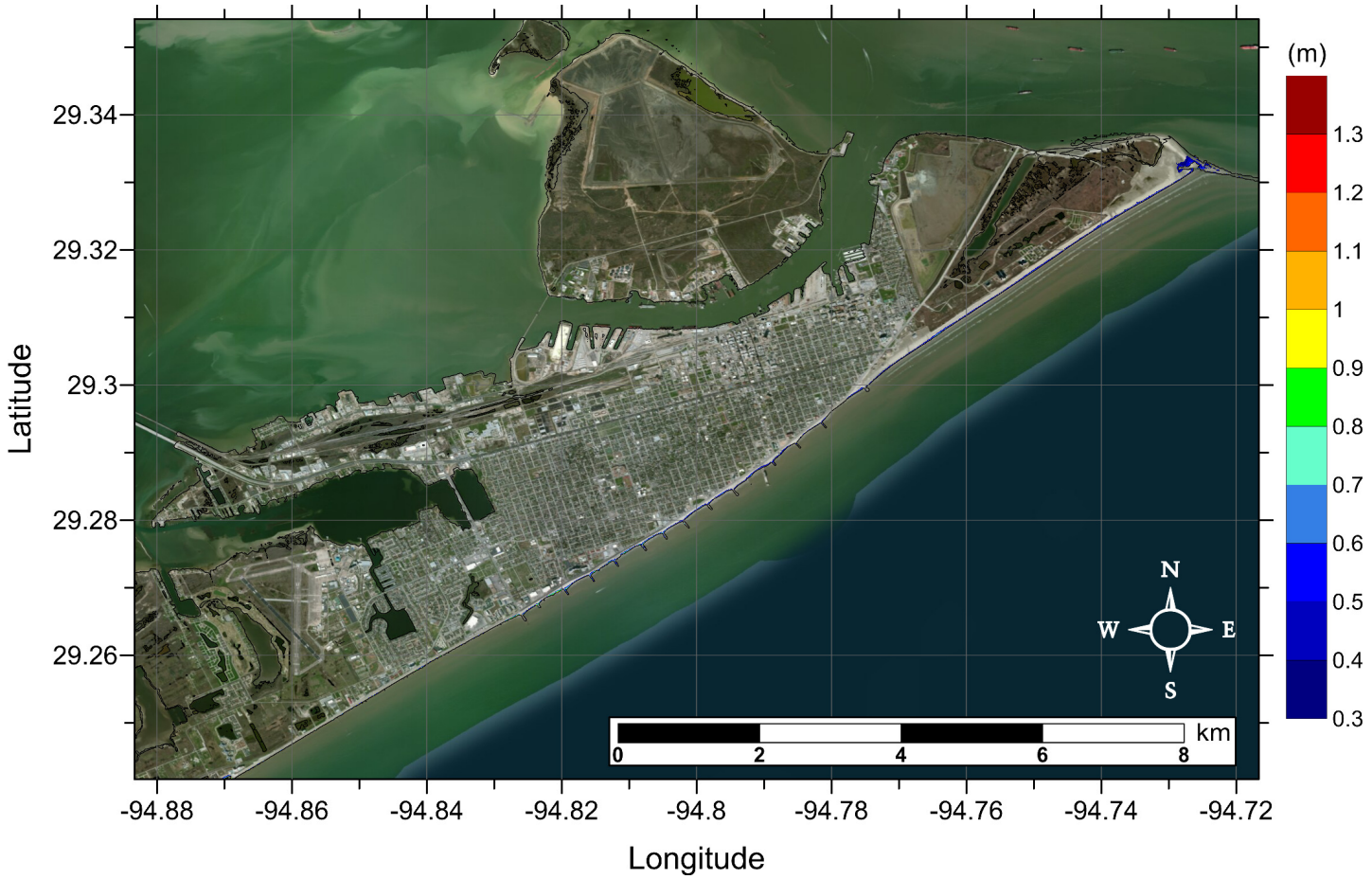

Figure 65: Maximum inundation depth (m) caused by the West Florida submarine landslide in Galveston, TX. Contour drawn is the zero-meter contour for land elevation. (Note: negligible inundation is seen from this source.)

Galveston, TX
West Florida Submarine Landslide
Maximum Momentum Flux

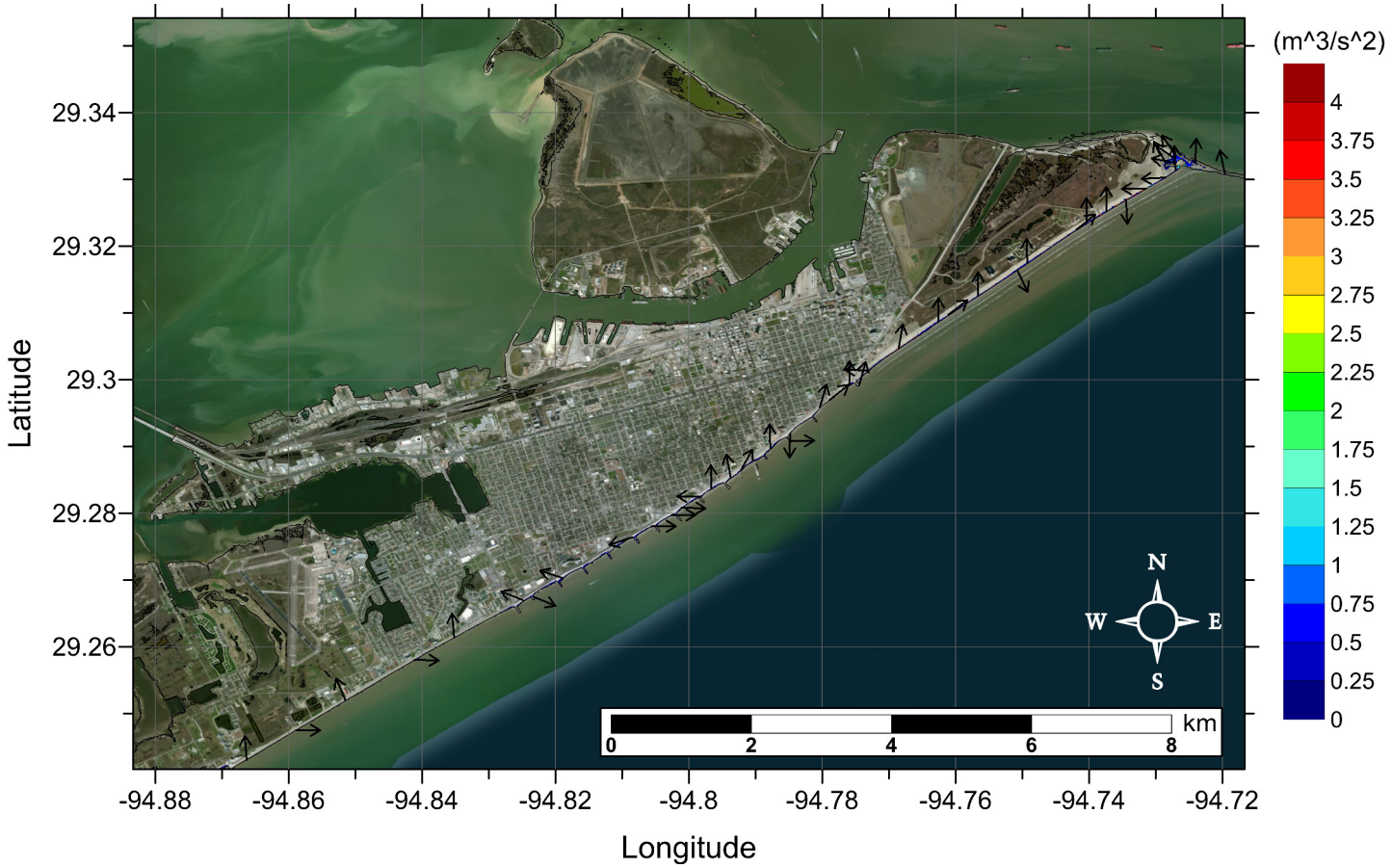

Figure 66: Maximum momentum flux (m^3/s^2) caused by the West Florida submarine landslide in Galveston, TX. Arrows represent direction of maximum momentum flux. Contour drawn is the zero-meter contour for land elevation. (Note: negligible inundation is seen from this source.)

Galveston, TX
Maximum of Maximums Inundation Depth

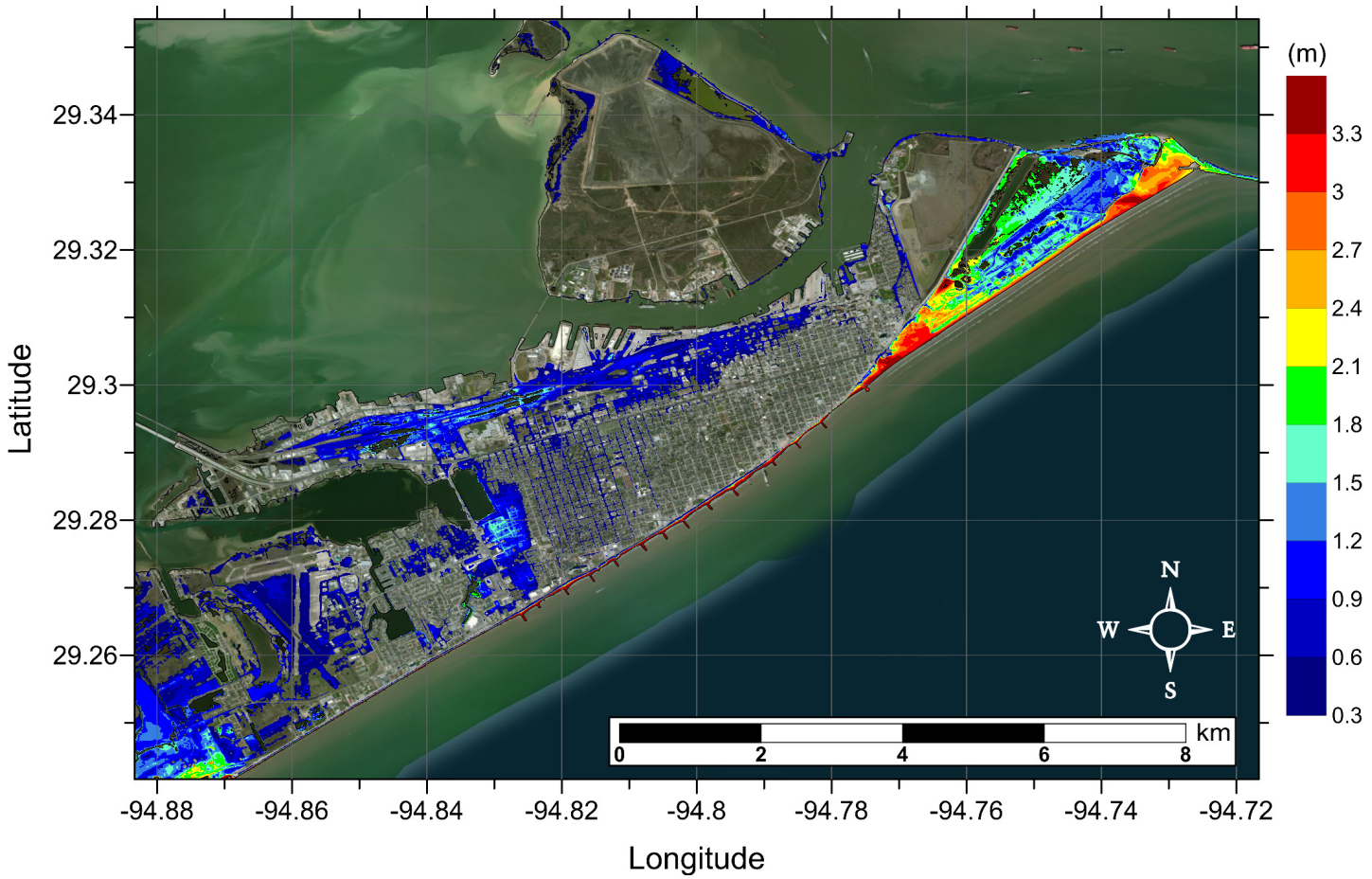

Figure 67: Maximum of maximums inundation depth (m) in Galveston, TX, calculated as the maximum inundation depth in each grid cell from an ensemble of all tsunami sources considered. Contour drawn is the zero-meter contour for land elevation.

Galveston, TX
Maximum Inundation Depth by Source

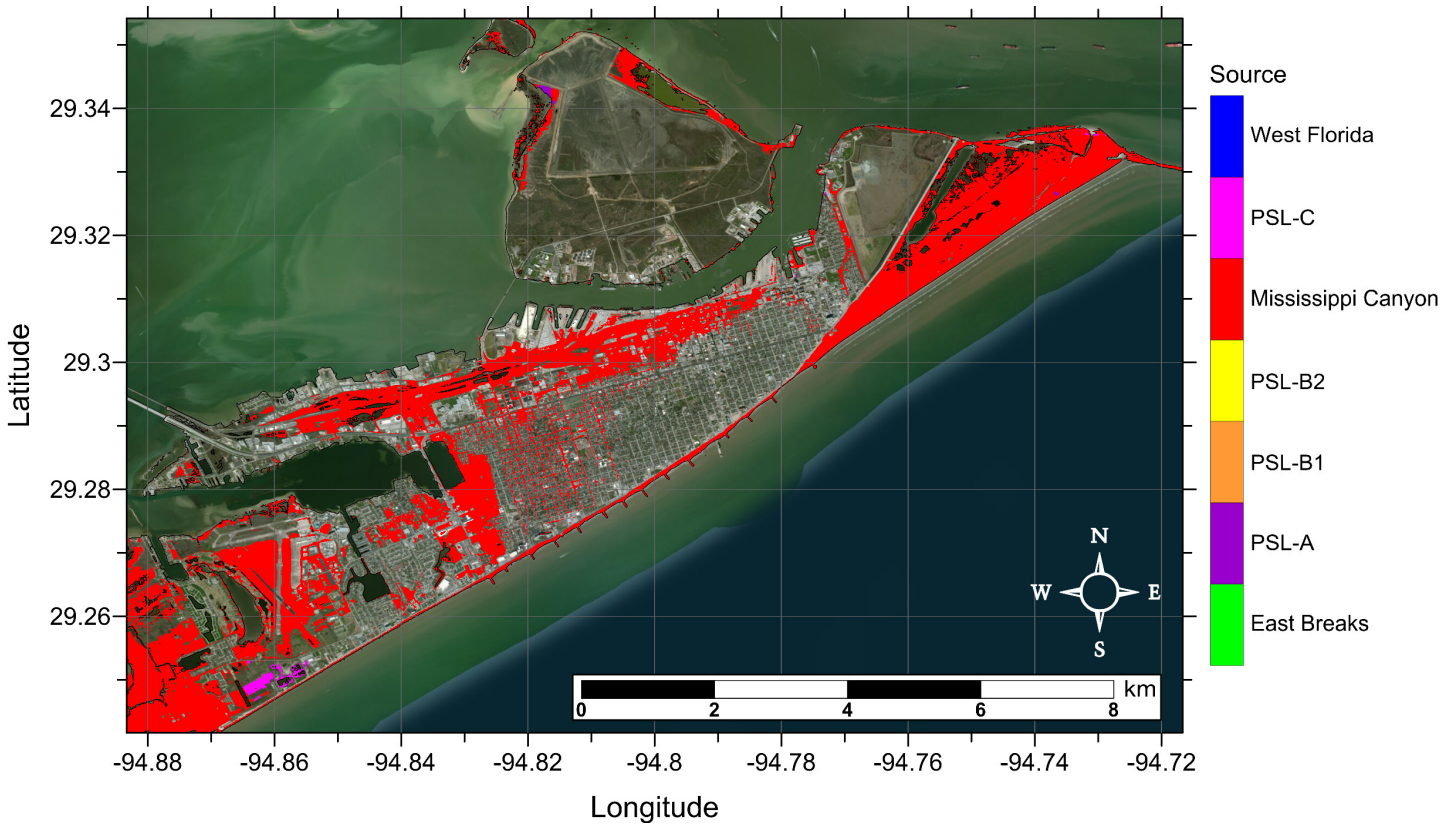

Figure 68: Indication of the tsunami source which causes the maximum of maximums inundation depth (m) in each grid cell from an ensemble of all tsunami sources considered (see Figure 67). Contour drawn is the zero-meter contour for land elevation.

5.3 Mobile, AL

Mobile, AL
Amplitude and Arrival Time of Maximum Tsunami Wave Recorded at Numerical Wave Gauge

Table 23: Maximum tsunami wave amplitude and corresponding arrival time after landslide failure at Mobile, AL numerical wave gauge: 30°6'15"N, 88°3'30"W (Figure 1), approximate water depth 20m.

Tsunami Source	Maximum Wave Amplitude (m)	Arrival Time After Landslide Failure (hr)
East Breaks	0.47	3.4
PSL-A	0.64	3.2
PSL-B1	0.68	2.5
PSL-B2	0.66	2.2
Mississippi Canyon	5.17	1.7
PSL-C	2.56	1.4
West Florida	0.46	2.2

Mobile, AL
East Breaks Submarine Landslide
Maximum Inundation Depth on Grid A

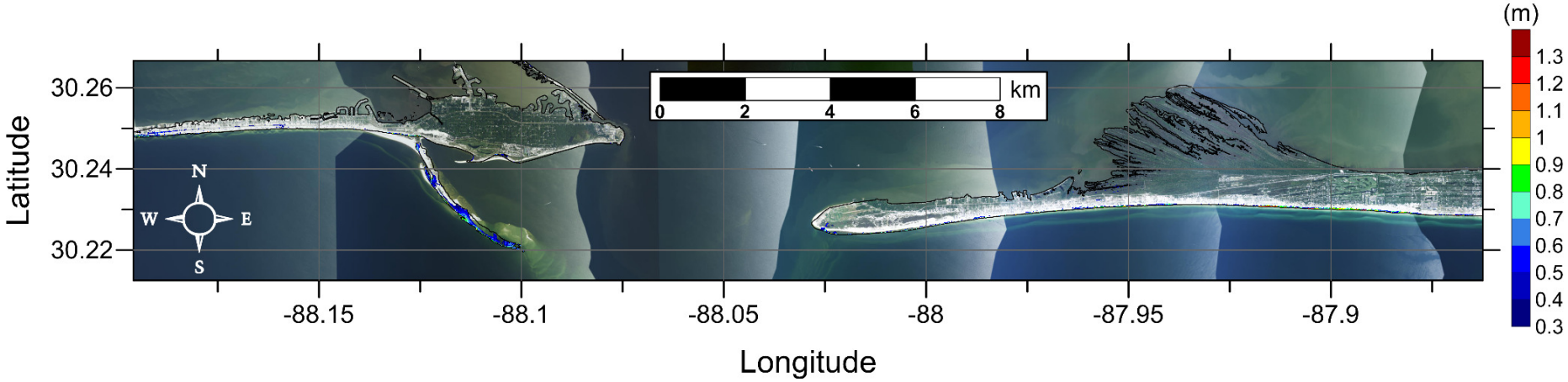

Figure 69: Maximum inundation depth (m) caused by the East Breaks submarine landslide in Dauphin Isl./Gulf Highlands, AL. Contour drawn is the zero-meter contour for land elevation.

Mobile, AL
East Breaks Submarine Landslide
Maximum Momentum Flux on Grid A

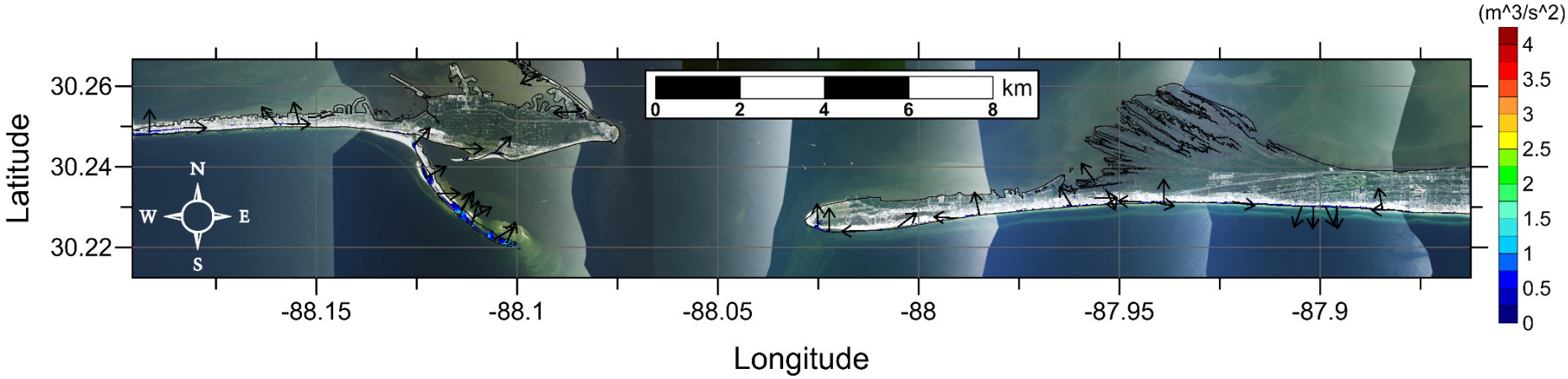

Figure 70: Maximum momentum flux (m^3/s^2) caused by the East Breaks submarine landslide in Dauphin Isl./Gulf Highlands, AL. Arrows represent direction of maximum momentum flux. Contour drawn is the zero-meter contour for land elevation.

Mobile, AL
East Breaks Submarine Landslide
Maximum Inundation Depth on Grid B

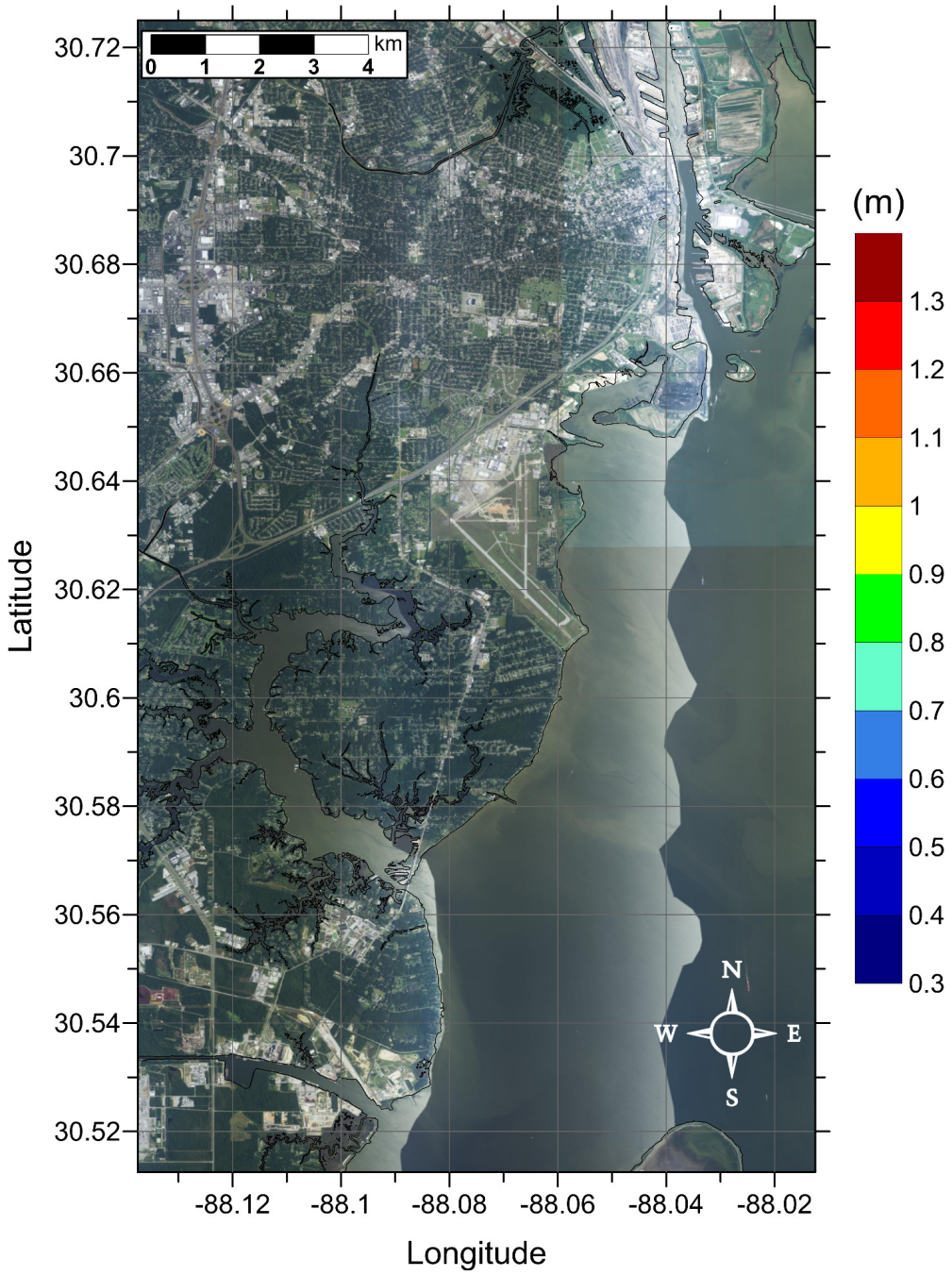

Figure 71: Maximum inundation depth (m) caused by the East Breaks submarine landslide in Mobile, AL. Contour drawn is the zero-meter contour for land elevation. (Note: negligible inundation is seen from this source.)

Mobile, AL
East Breaks Submarine Landslide
Maximum Momentum Flux on Grid B

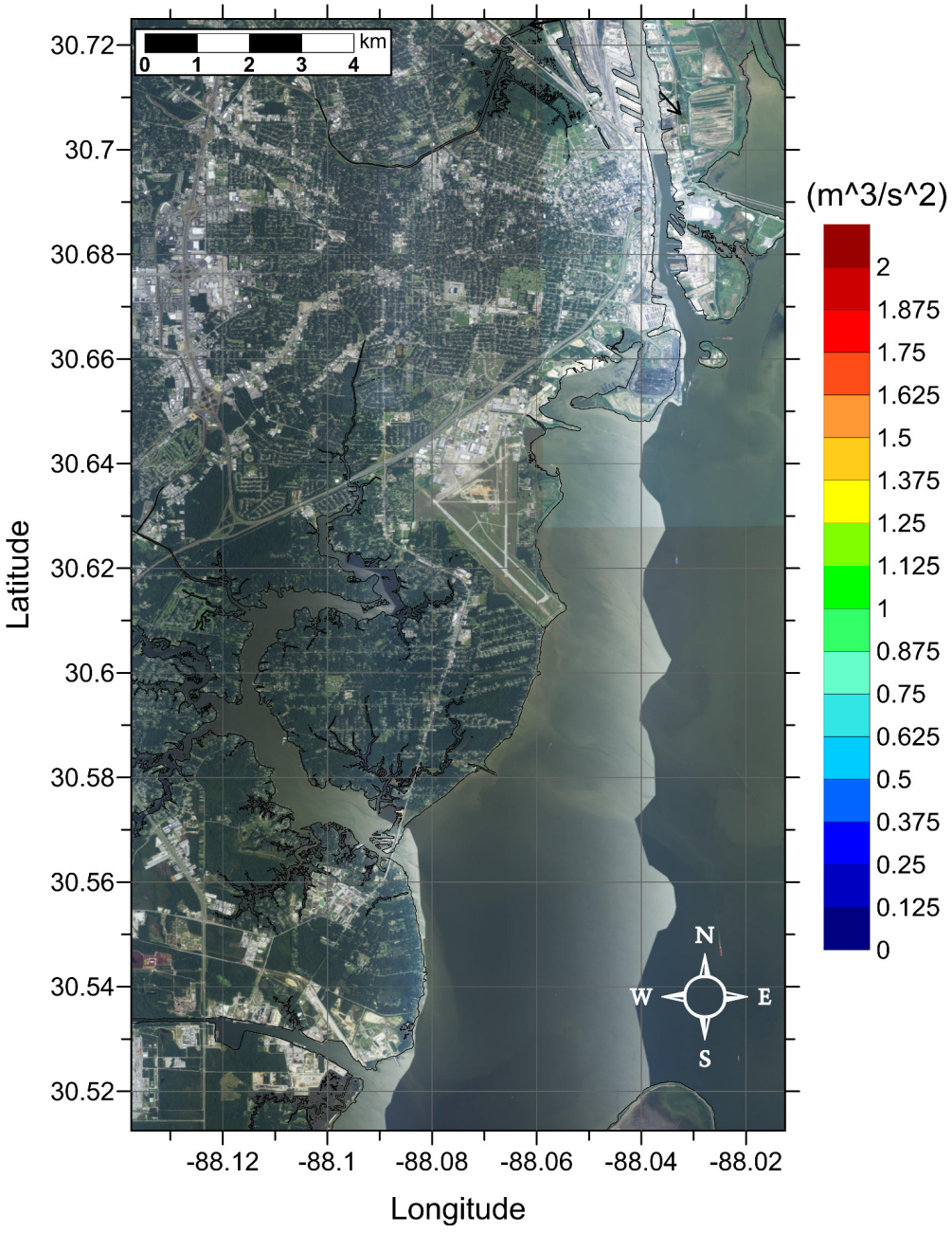

Figure 72: Maximum momentum flux (m^3/s^2) caused by the East Breaks submarine landslide in Mobile, AL. Arrows represent direction of maximum momentum flux. Contour drawn is the zero-meter contour for land elevation. (Note: negligible inundation is seen from this source.)

Mobile, AL
Probabilistic Submarine Landslide A (PSL-A)
Maximum Inundation Depth on Grid A

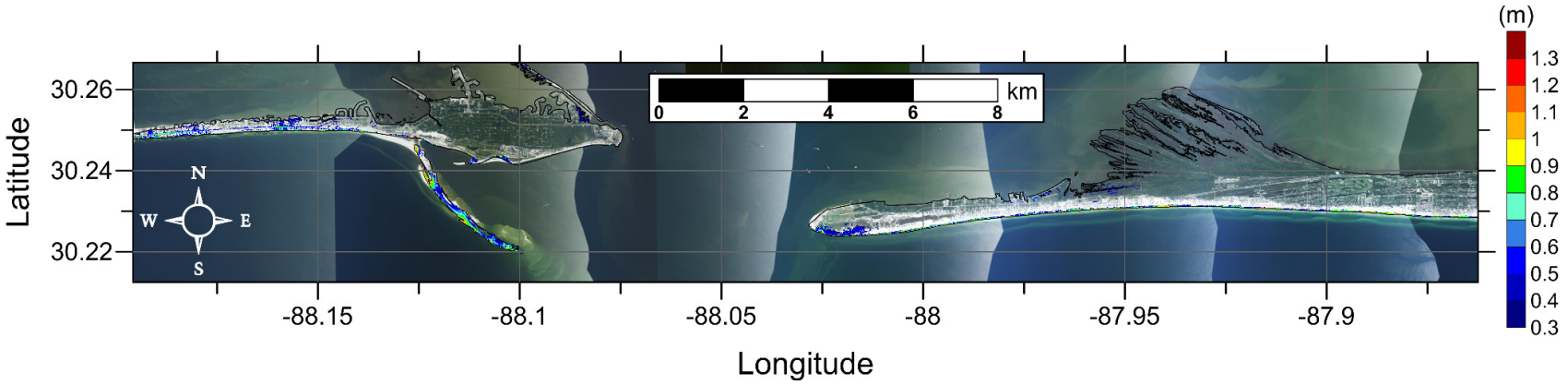

Figure 73: Maximum inundation depth (m) caused by the Probabilistic Submarine Landslide A in Dauphin Isl./Gulf Highlands, AL. Contour drawn is the zero-meter contour for land elevation.

Mobile, AL
Probabilistic Submarine Landslide A (PSL-A)
Maximum Momentum Flux on Grid A

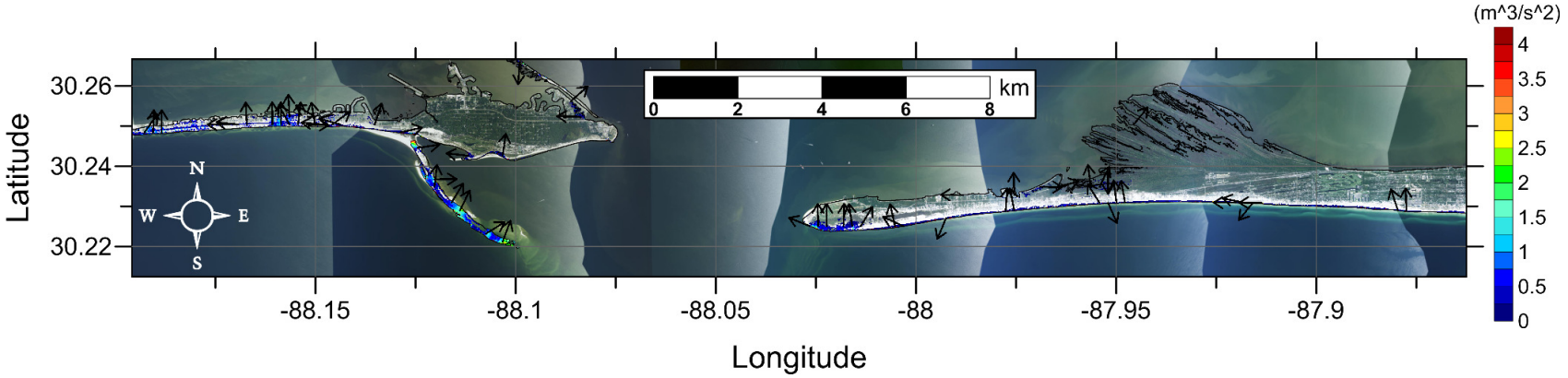

Figure 74: Maximum momentum flux (m^3/s^2) caused by the Probabilistic Submarine Landslide A in Dauphin Isl./Gulf Highlands, AL. Arrows represent direction of maximum momentum flux. Contour drawn is the zero-meter contour for land elevation.

Mobile, AL
Probabilistic Submarine Landslide A (PSL-A)
Maximum Inundation Depth on Grid B

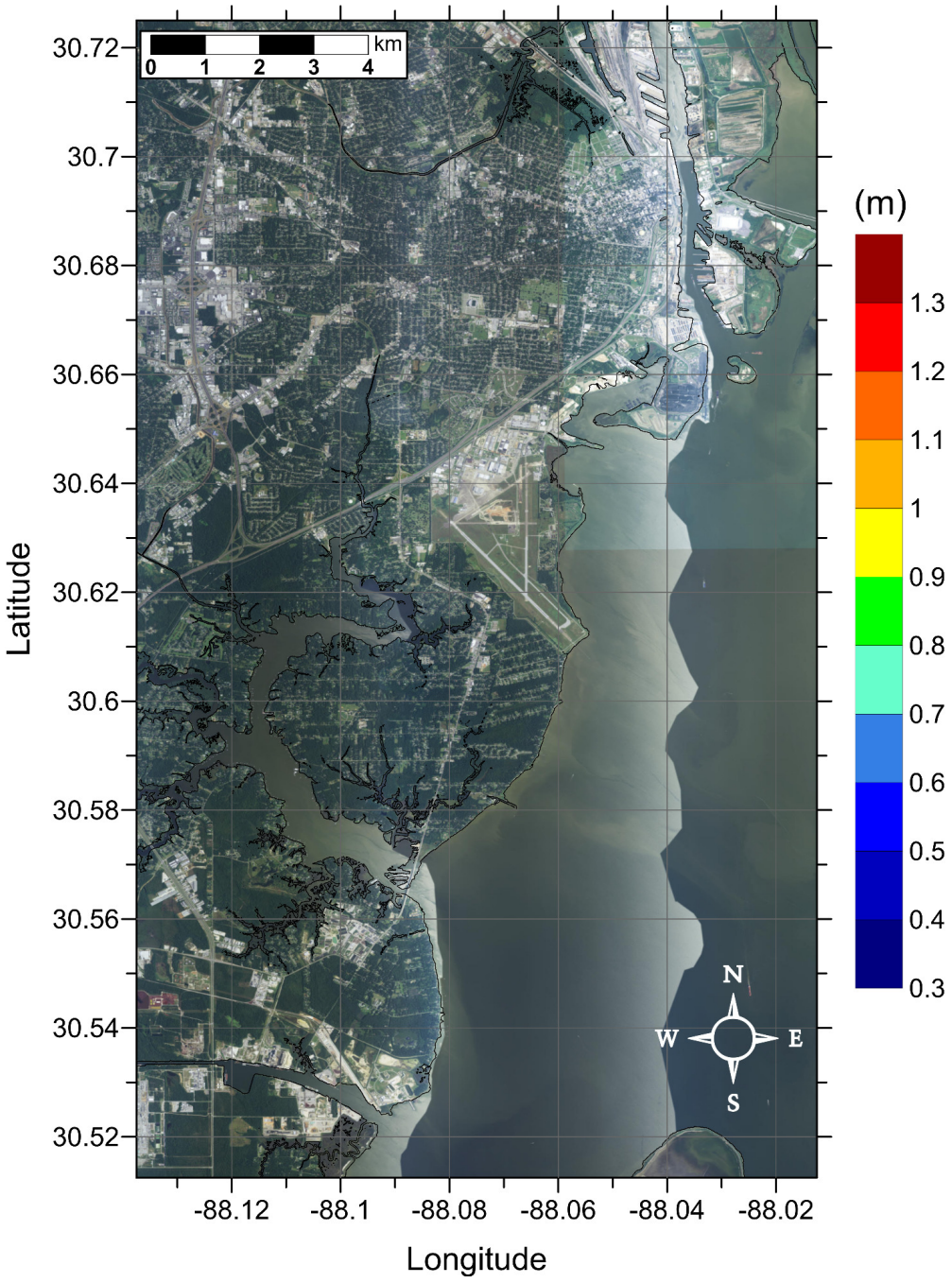

Figure 75: Maximum inundation depth (m) caused by the Probabilistic Submarine Landslide A in Mobile, AL. Contour drawn is the zero-meter contour for land elevation. (Note: negligible inundation is seen from this source.)

Mobile, AL
Probabilistic Submarine Landslide A (PSL-A)
Maximum Momentum Flux on Grid B

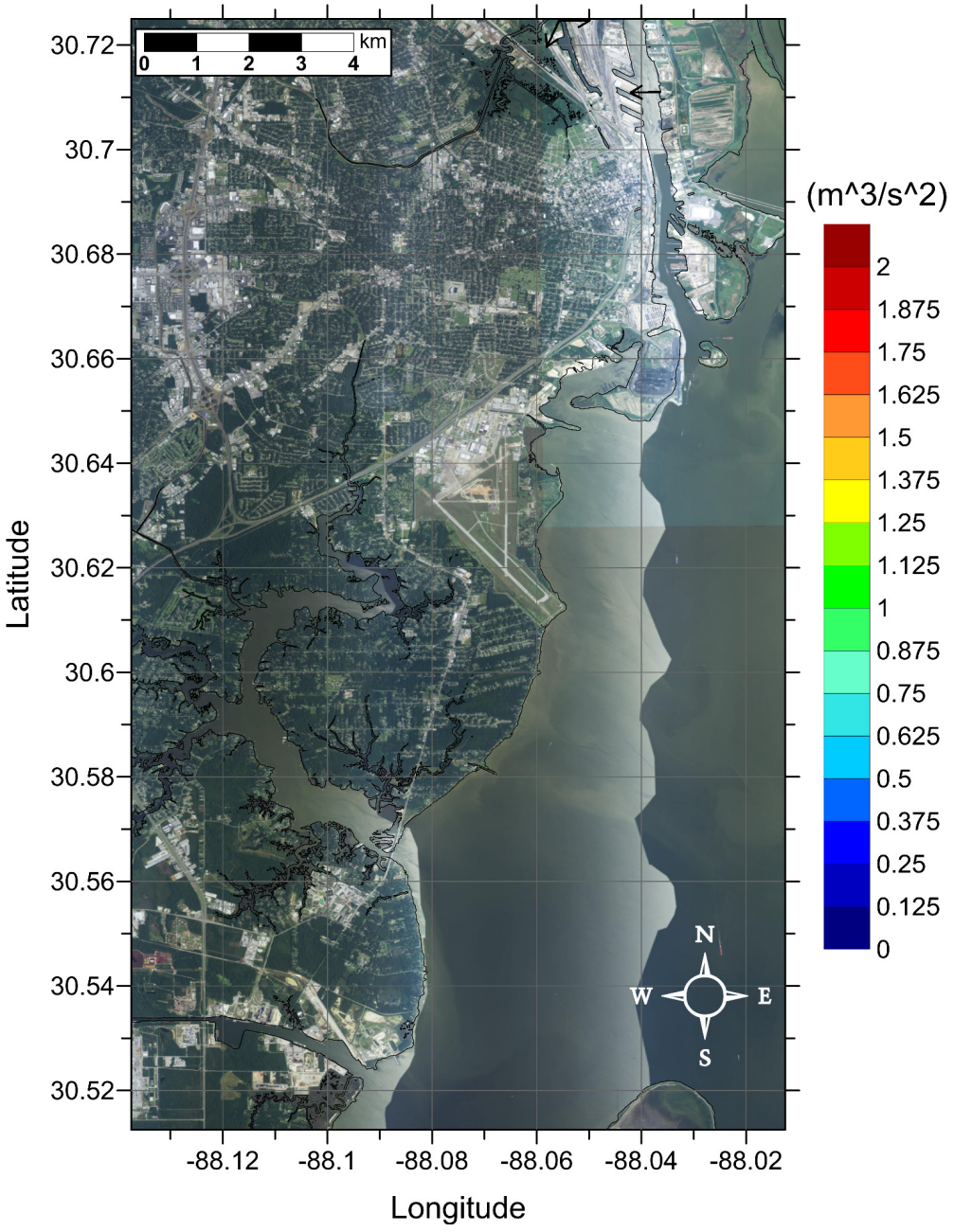

Figure 76: Maximum momentum flux (m^3/s^2) caused by the Probabilistic Submarine Landslide A in Mobile, AL. Arrows represent direction of maximum momentum flux. Contour drawn is the zero-meter contour for land elevation. (Note: negligible inundation is seen from this source.)

Mobile, AL
Probabilistic Submarine Landslide B1 (PSL-B1)
Maximum Inundation Depth on Grid A

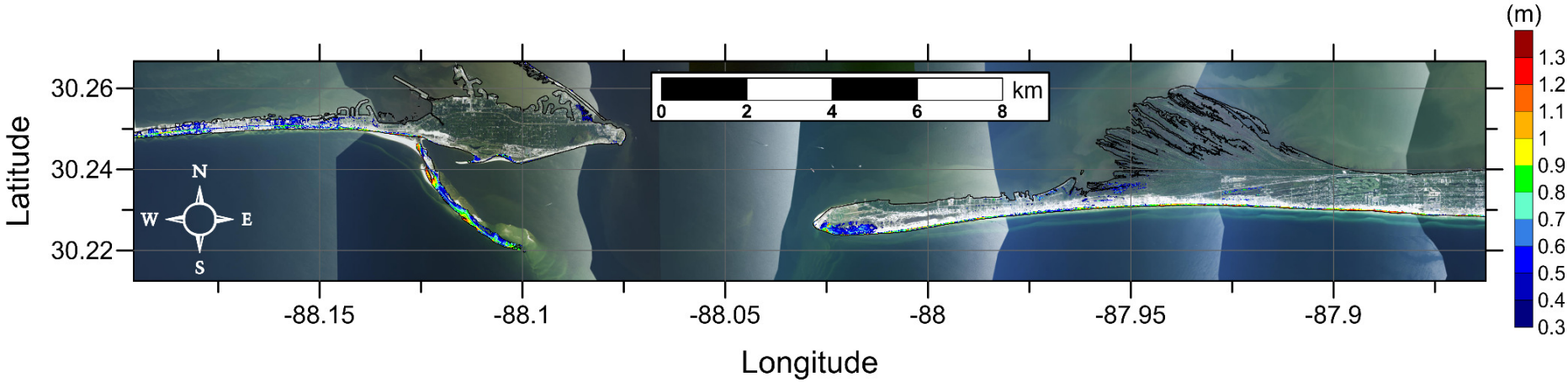

Figure 77: Maximum inundation depth (m) caused by the Probabilistic Submarine Landslide B-1 in Dauphin Isl./Gulf Highlands, AL. Contour drawn is the zero-meter contour for land elevation.

Mobile, AL
Probabilistic Submarine Landslide B1 (PSL-B1)
Maximum Momentum Flux on Grid A

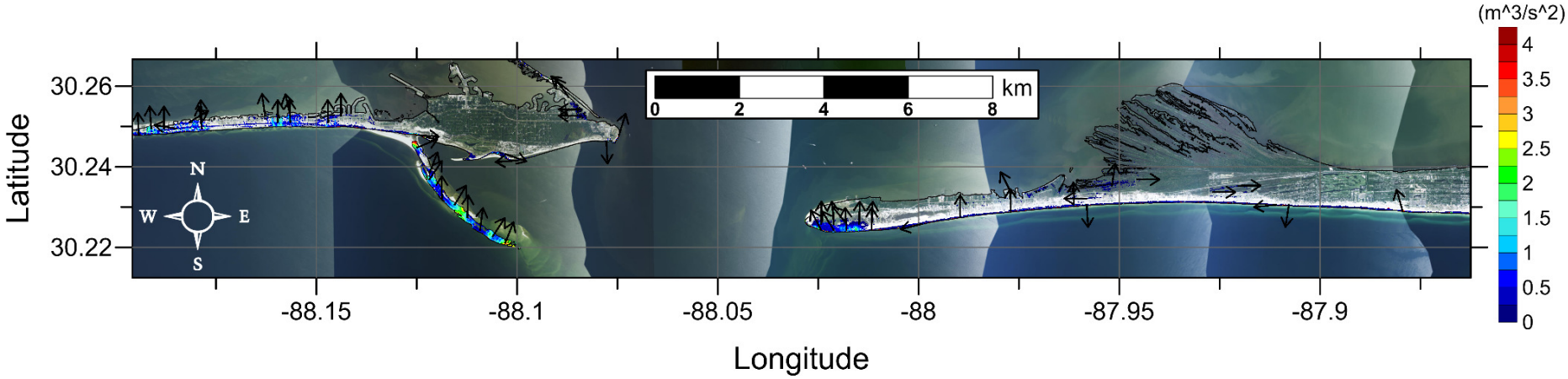

Figure 78: Maximum momentum flux (m^3/s^2) caused by the Probabilistic Submarine Landslide B-1 in Dauphin Isl./Gulf Highlands, AL. Arrows represent direction of maximum momentum flux. Contour drawn is the zero-meter contour for land elevation.

Mobile, AL
Probabilistic Submarine Landslide B1 (PSL-B1)
Maximum Inundation Depth on Grid B

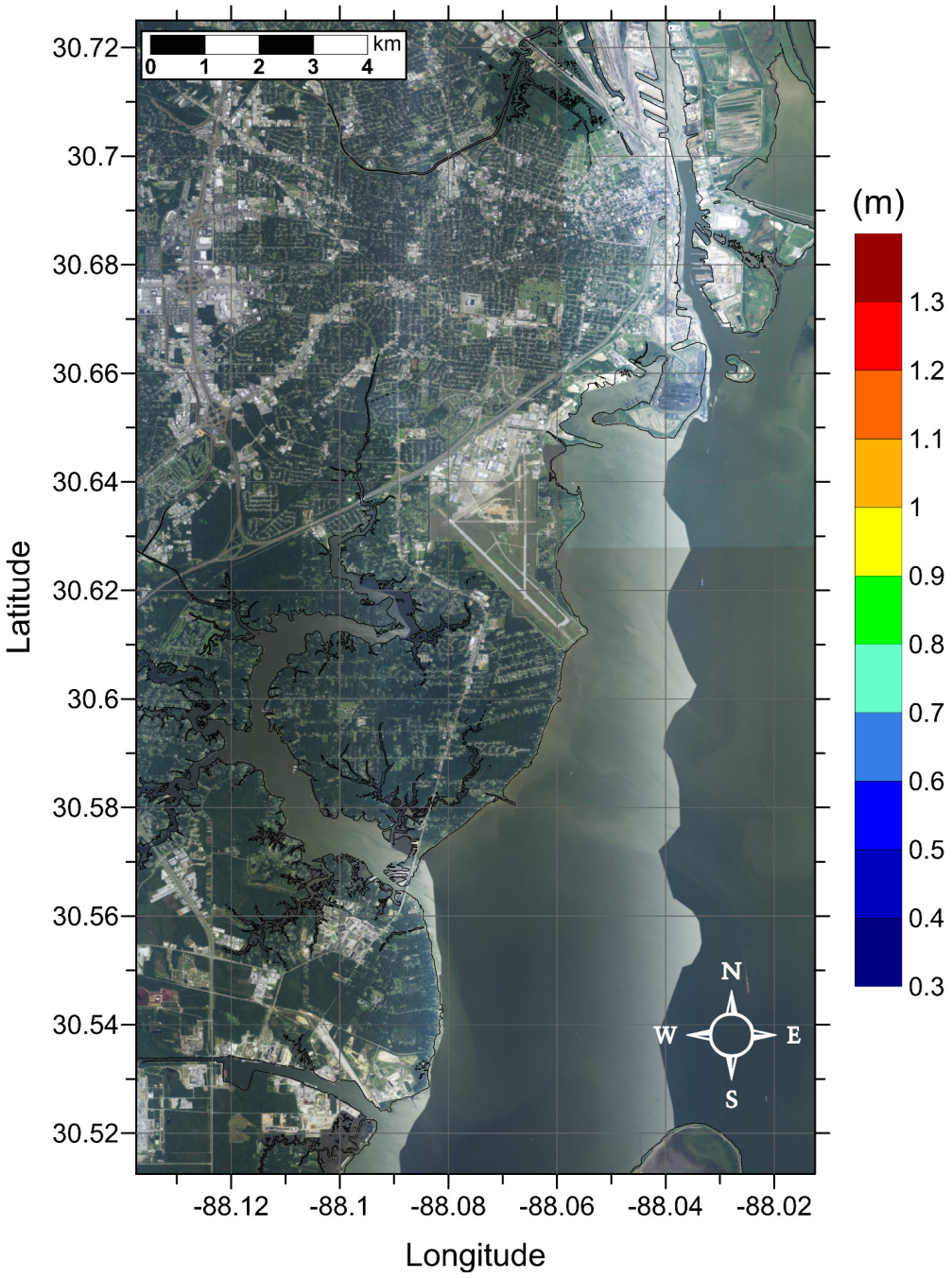

Figure 79: Maximum inundation depth (m) caused by the Probabilistic Submarine Landslide B-1 in Mobile, AL. Contour drawn is the zero-meter contour for land elevation. (Note: negligible inundation is seen from this source.)

Mobile, AL
Probabilistic Submarine Landslide B1 (PSL-B1)
Maximum Momentum Flux on Grid B

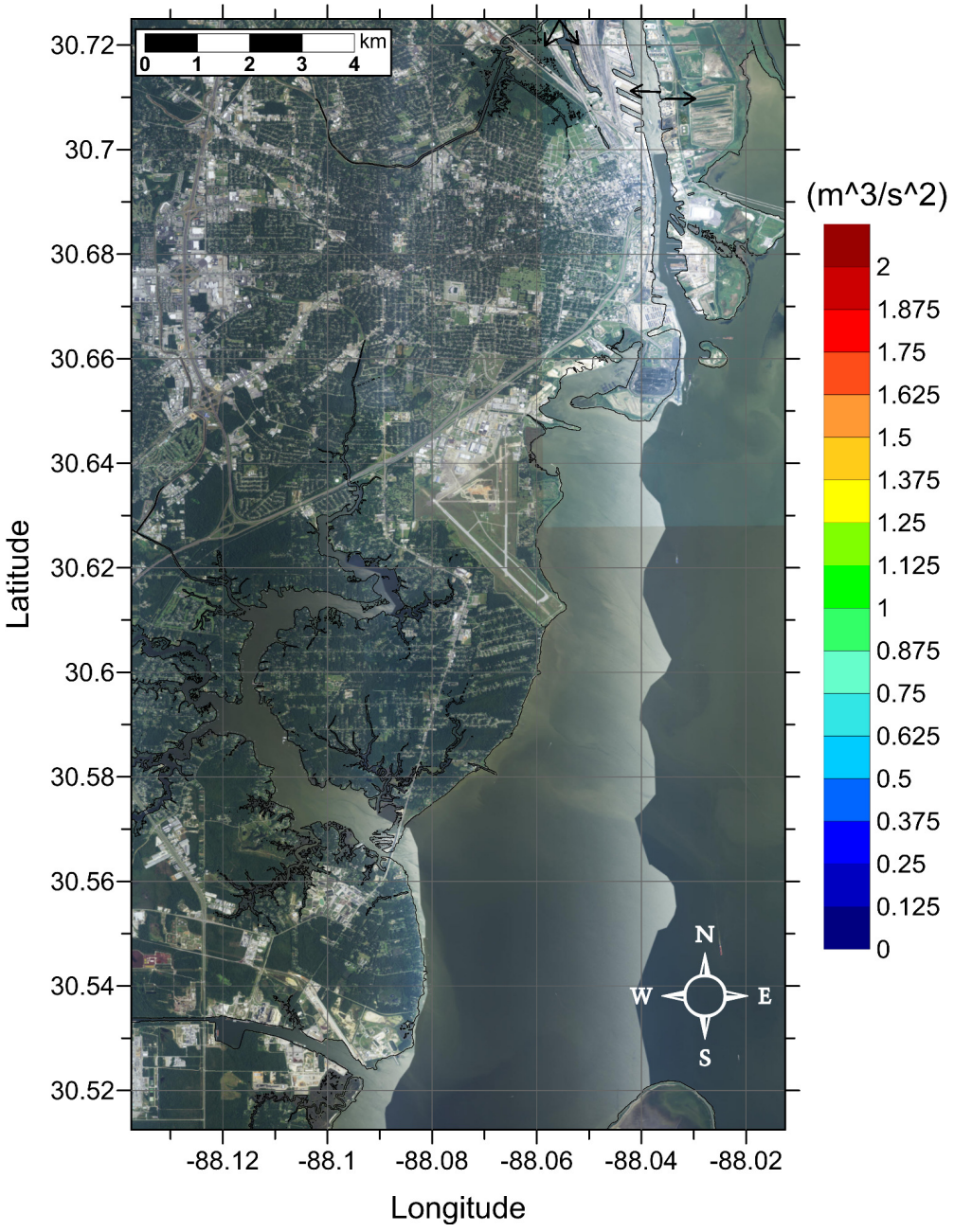

Figure 80: Maximum momentum flux (m^3/s^2) caused by the Probabilistic Submarine Landslide B-1 in Mobile, AL. Arrows represent direction of maximum momentum flux. Contour drawn is the zero-meter contour for land elevation. (Note: negligible inundation is seen from this source.)

Mobile, AL
Probabilistic Submarine Landslide B2 (PSL-B2)
Maximum Inundation Depth on Grid A

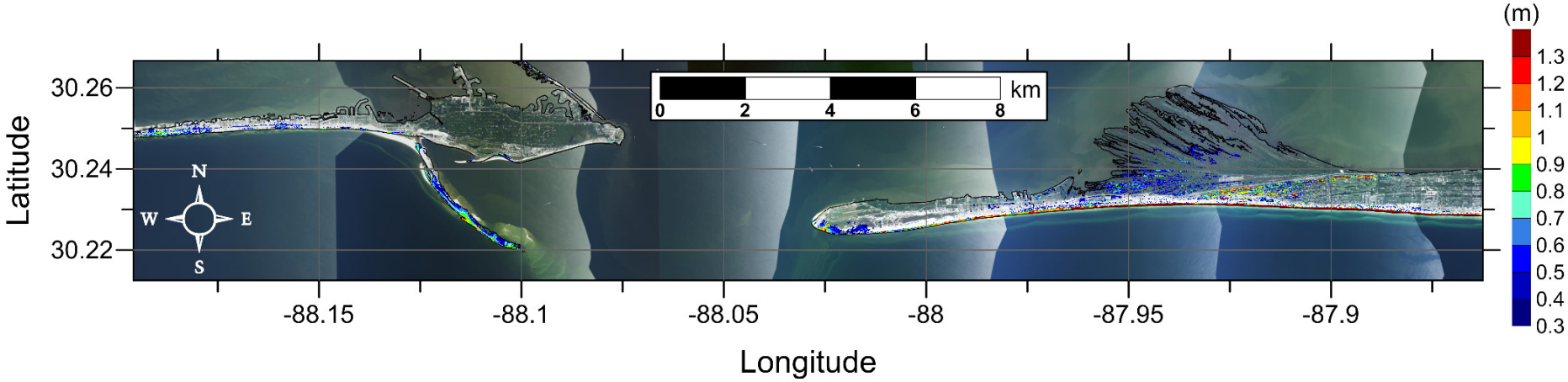

Figure 81: Maximum inundation depth (m) caused by the Probabilistic Submarine Landslide B-2 in Dauphin Isl./Gulf Highlands, AL. Contour drawn is the zero-meter contour for land elevation.

Mobile, AL
Probabilistic Submarine Landslide B2 (PSL-B2)
Maximum Momentum Flux on Grid A

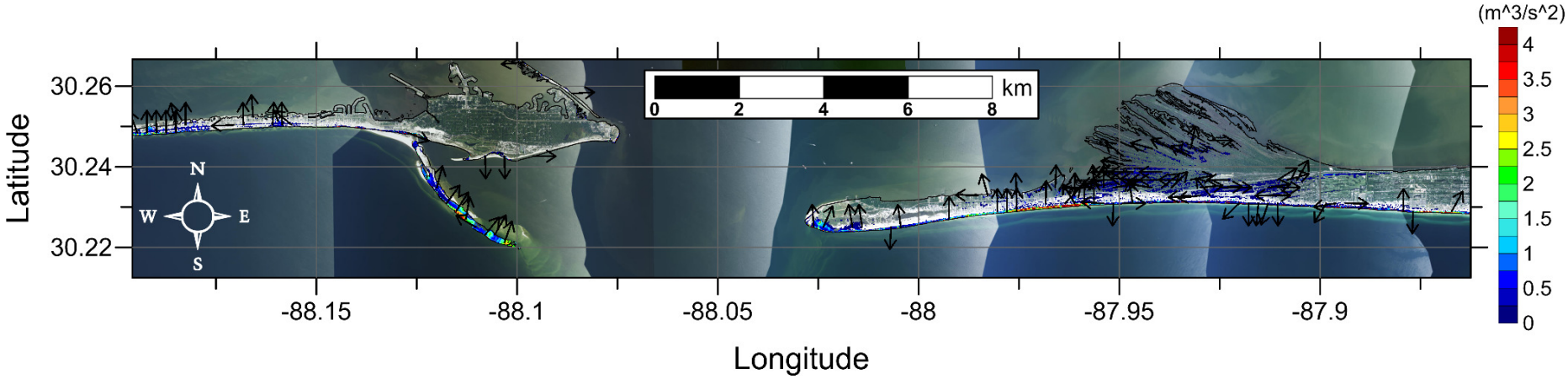

Figure 82: Maximum momentum flux (m^3/s^2) caused by the Probabilistic Submarine Landslide B-2 in Dauphin Isl./Gulf Highlands, AL. Arrows represent direction of maximum momentum flux. Contour drawn is the zero-meter contour for land elevation.

Mobile, AL
Probabilistic Submarine Landslide B2 (PSL-B2)
Maximum Inundation Depth on Grid B

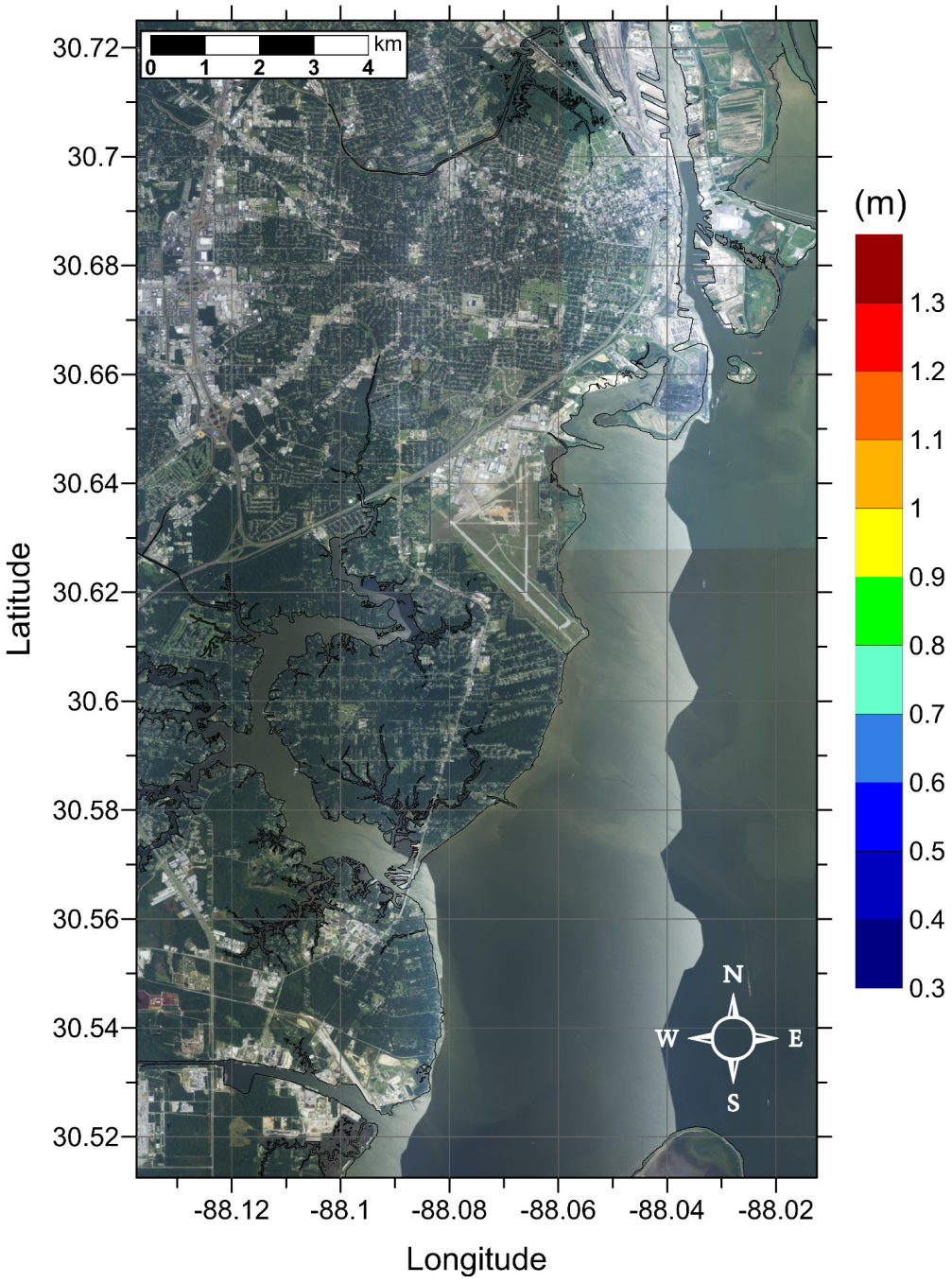

Figure 83: Maximum inundation depth (m) caused by the Probabilistic Submarine Landslide B-2 in Mobile, AL. Contour drawn is the zero-meter contour for land elevation. (Note: negligible inundation is seen from this source.)

Mobile, AL
Probabilistic Submarine Landslide B2 (PSL-B2)
Maximum Momentum Flux on Grid B

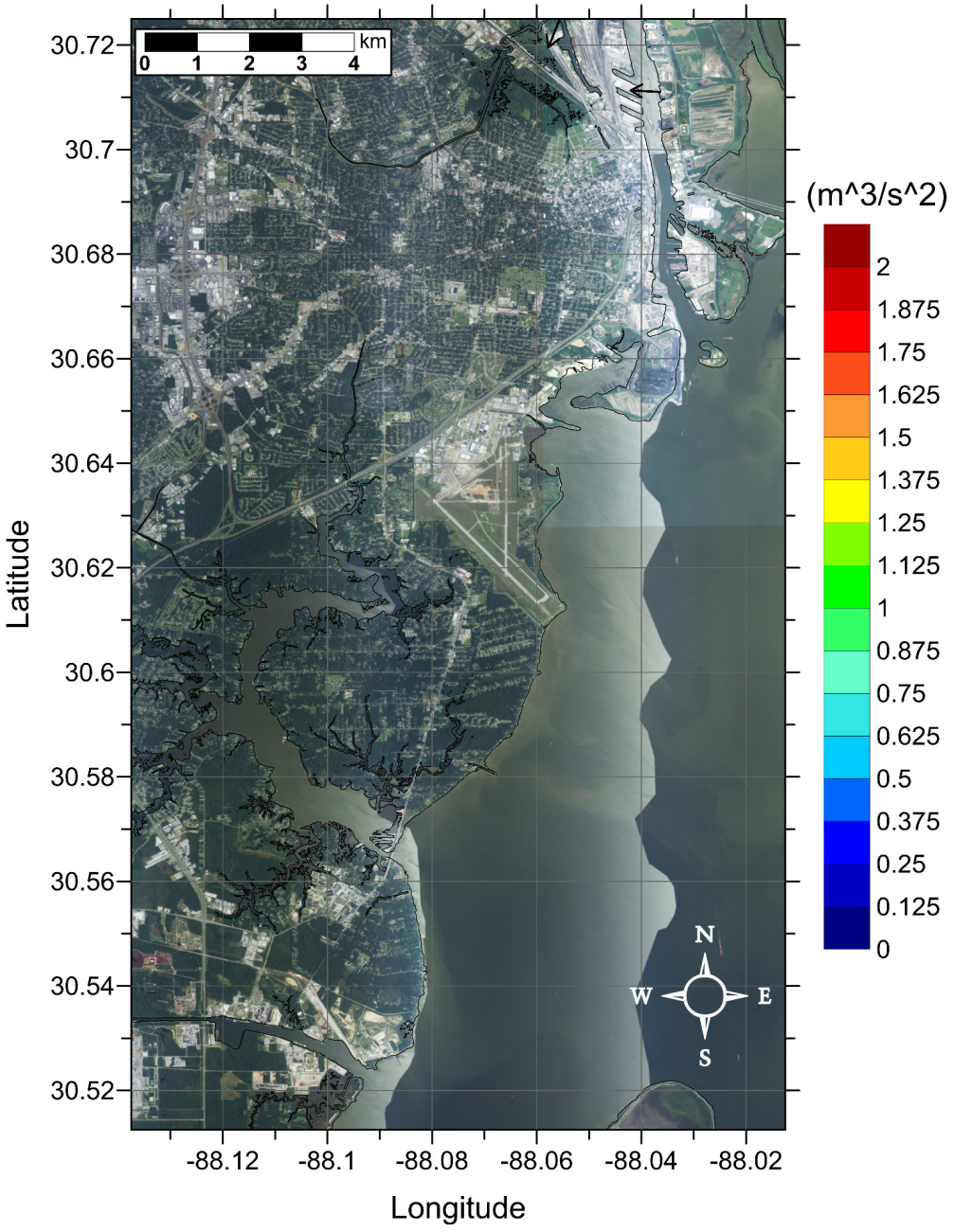

Figure 84: Maximum momentum flux (m^3/s^2) caused by the Probabilistic Submarine Landslide B-2 in Mobile, AL. Arrows represent direction of maximum momentum flux. Contour drawn is the zero-meter contour for land elevation. (Note: negligible inundation is seen from this source.)

Mobile, AL
Mississippi Canyon Submarine Landslide
Maximum Inundation Depth on Grid A

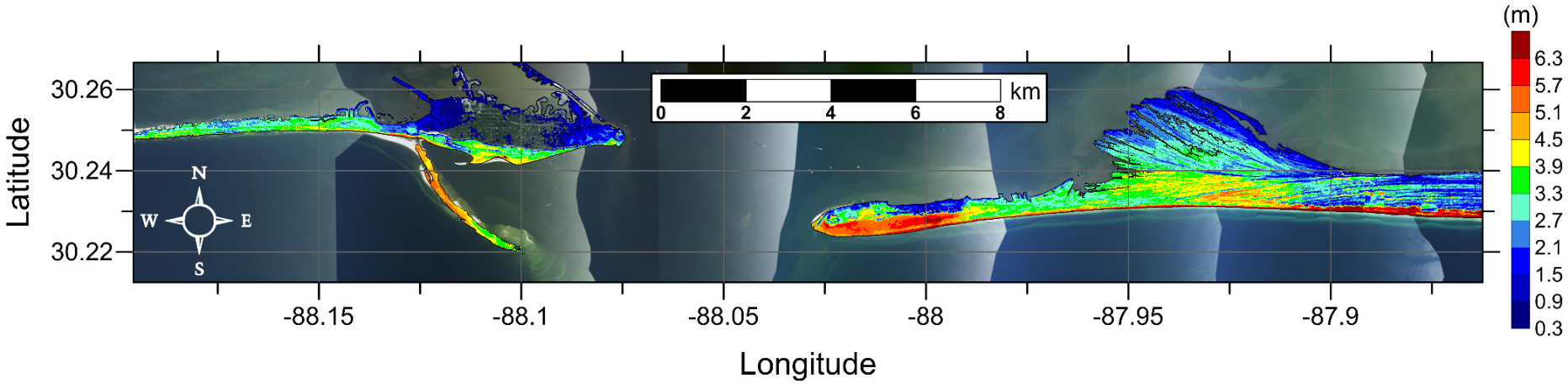

Figure 85: Maximum inundation depth (m) caused by the Mississippi Canyon submarine landslide in Dauphin Isl./Gulf Highlands, AL. Contour drawn is the zero-meter contour for land elevation.

Mobile, AL
Mississippi Canyon Submarine Landslide
Maximum Momentum Flux on Grid A

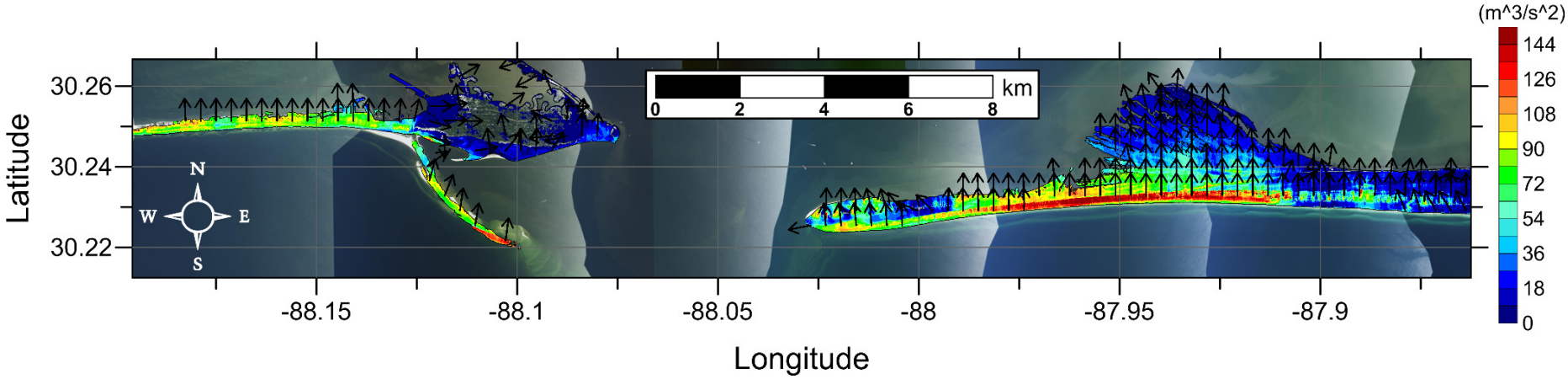

Figure 86: Maximum momentum flux (m^3/s^2) caused by the Mississippi Canyon submarine landslide in Dauphin Isl./Gulf Highlands, AL. Arrows represent direction of maximum momentum flux. Contour drawn is the zero-meter contour for land elevation.

Mobile, AL
Mississippi Canyon Submarine Landslide
Maximum Inundation Depth on Grid B

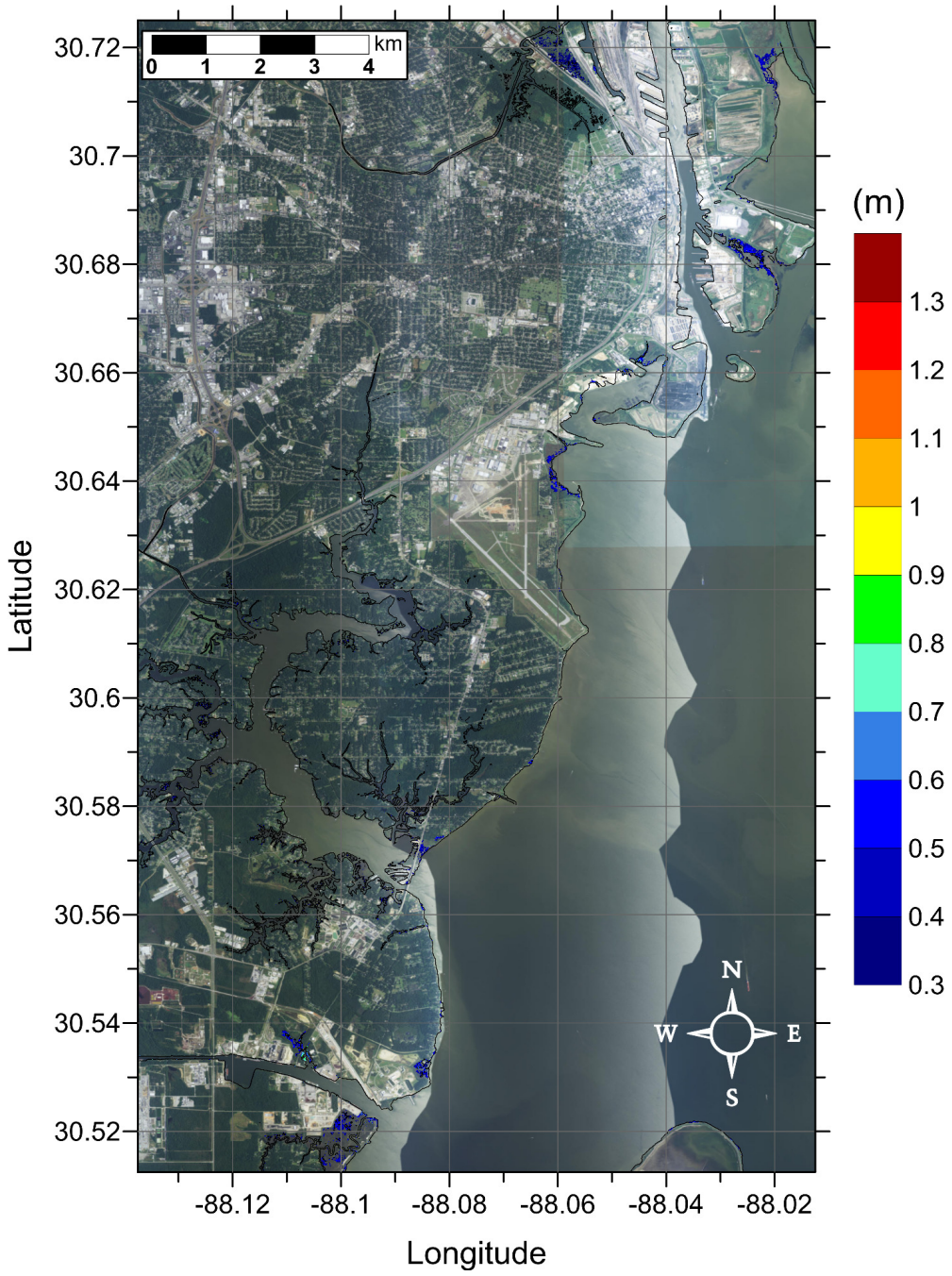

Figure 87: Maximum inundation depth (m) caused by the Mississippi Canyon submarine landslide in Mobile, AL. Contour drawn is the zero-meter contour for land elevation.

Mobile, AL
Mississippi Canyon Submarine Landslide
Maximum Momentum Flux on Grid B

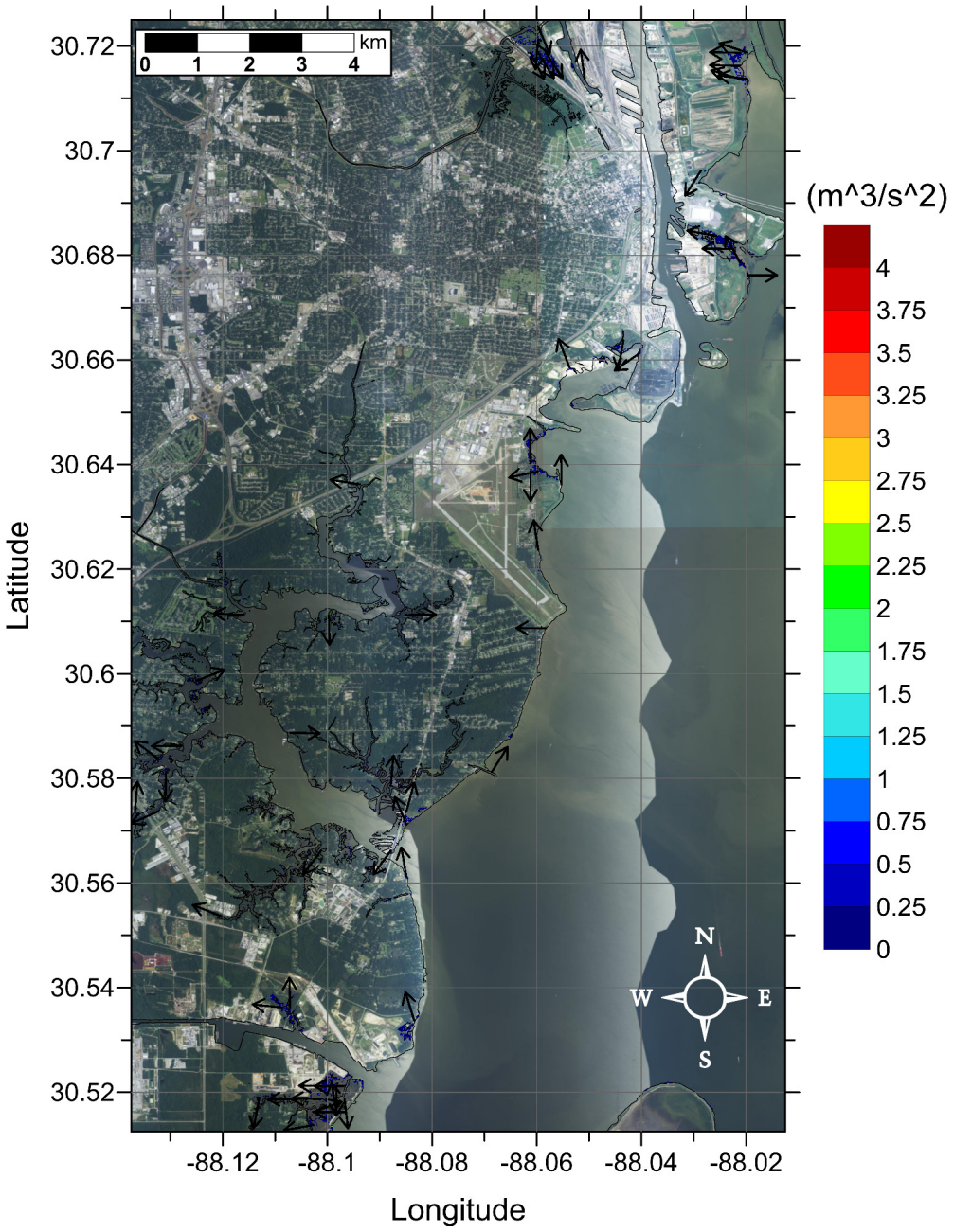

Figure 88: Maximum momentum flux (m^3/s^2) caused by the Mississippi Canyon submarine landslide in Mobile, AL. Arrows represent direction of maximum momentum flux. Contour drawn is the zero-meter contour for land elevation.

Mobile, AL
Probabilistic Submarine Landslide C (PSL-C)
Maximum Inundation Depth on Grid A

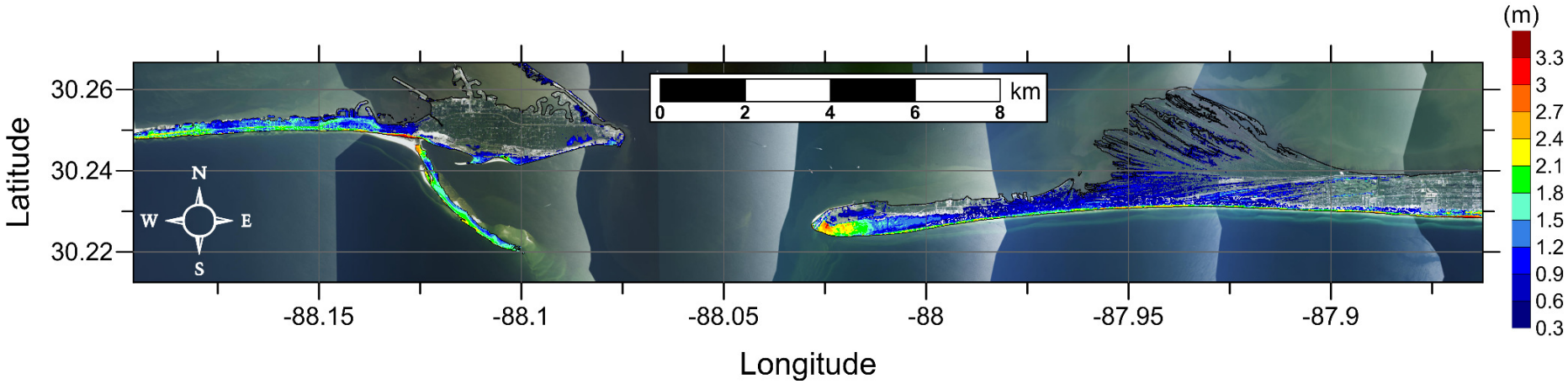

Figure 89: Maximum inundation depth (m) caused by the Probabilistic Submarine Landslide C in Dauphin Isl./Gulf Highlands, AL. Contour drawn is the zero-meter contour for land elevation.

Mobile, AL
Probabilistic Submarine Landslide C (PSL-C)
Maximum Momentum Flux on Grid A

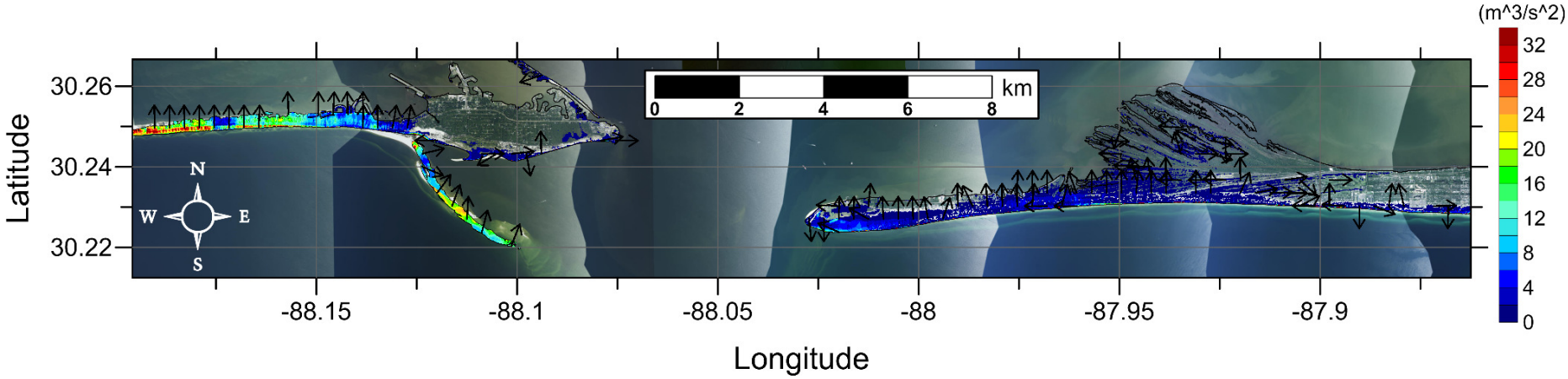

Figure 90: Maximum momentum flux (m^3/s^2) caused by the Probabilistic Submarine Landslide C in Dauphin Isl./Gulf Highlands, AL. Arrows represent direction of maximum momentum flux. Contour drawn is the zero-meter contour for land elevation.

Mobile, AL
Probabilistic Submarine Landslide C (PSL-C)
Maximum Inundation Depth on Grid B

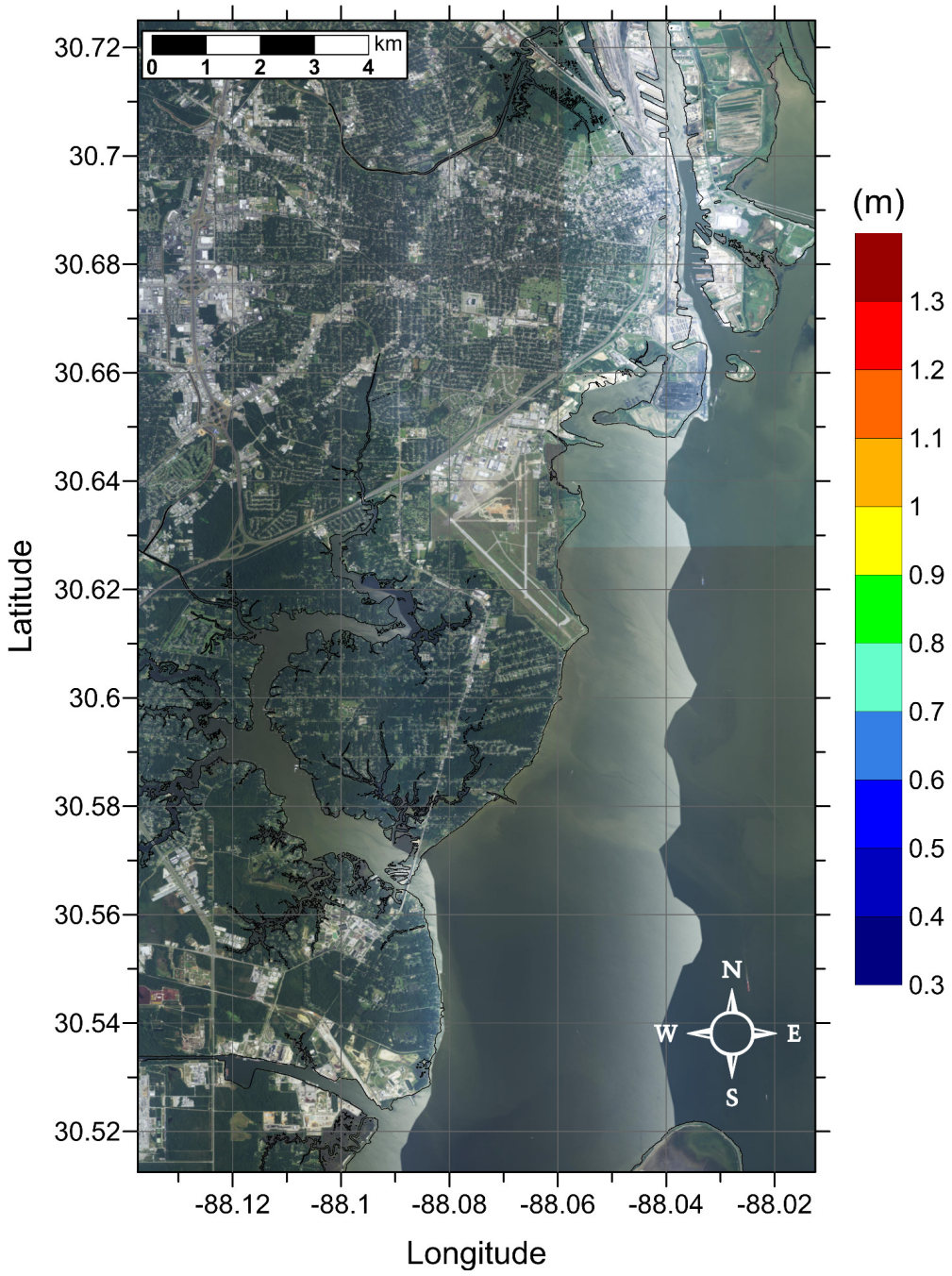

Figure 91: Maximum inundation depth (m) caused by the Probabilistic Submarine Landslide C in Mobile, AL. Contour drawn is the zero-meter contour for land elevation. (Note: negligible inundation is seen from this source.)

Mobile, AL
Probabilistic Submarine Landslide C (PSL-C)
Maximum Momentum Flux on Grid B

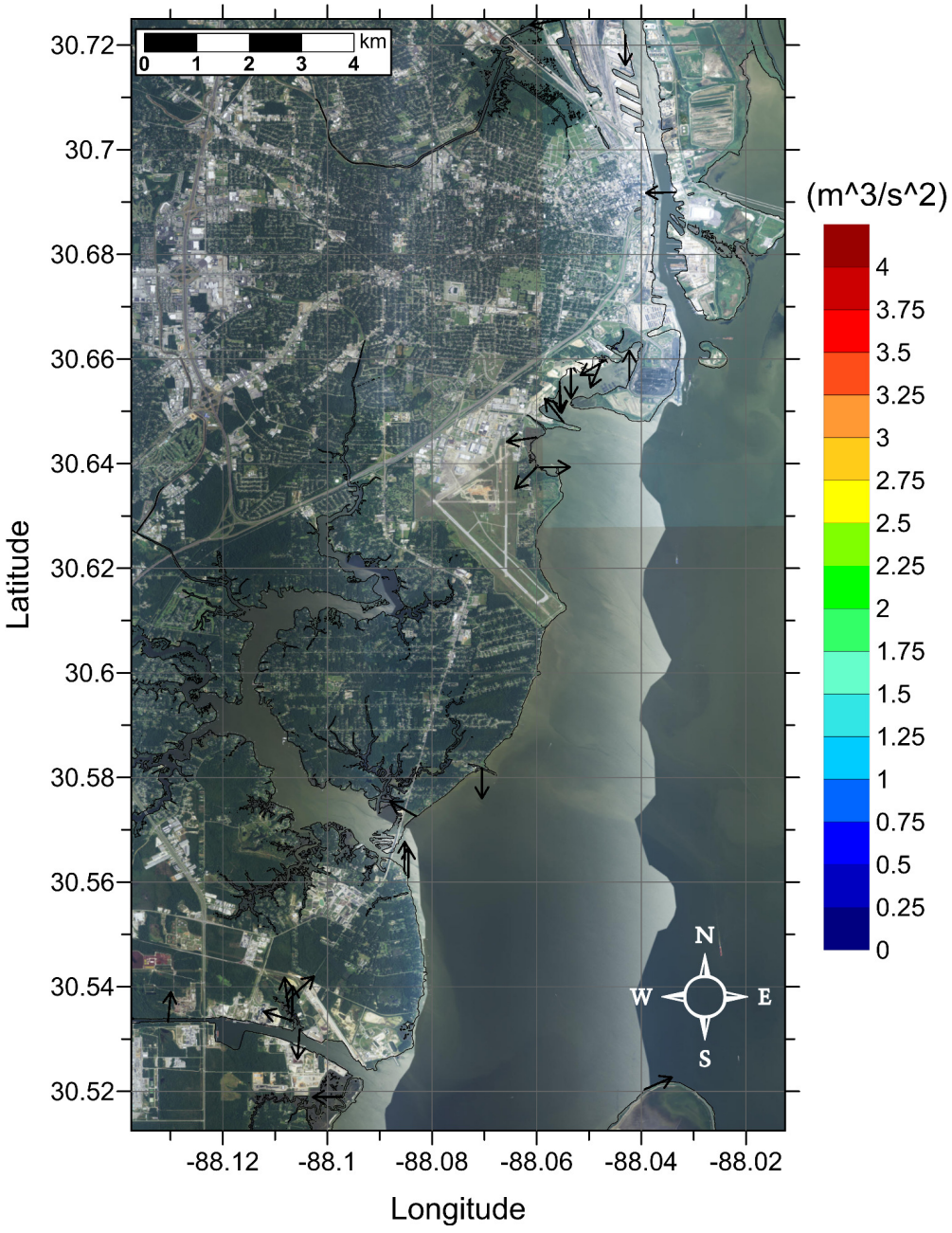

Figure 92: Maximum momentum flux (m^3/s^2) caused by the Probabilistic Submarine Landslide C in Mobile, AL. Arrows represent direction of maximum momentum flux. Contour drawn is the zero-meter contour for land elevation. (Note: negligible inundation is seen from this source.)

Mobile, AL
West Florida Submarine Landslide
Maximum Inundation Depth on Grid A

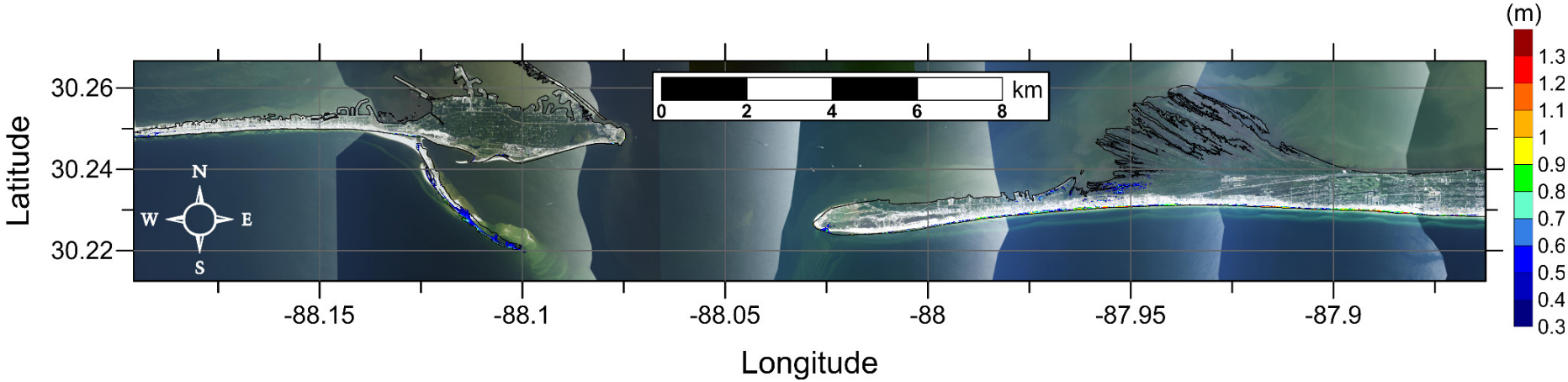

Figure 93: Maximum inundation depth (m) caused by the West Florida submarine landslide in Dauphin Isl./Gulf Highlands, AL. Contour drawn is the zero-meter contour for land elevation.

Mobile, AL
West Florida Submarine Landslide
Maximum Momentum Flux on Grid A

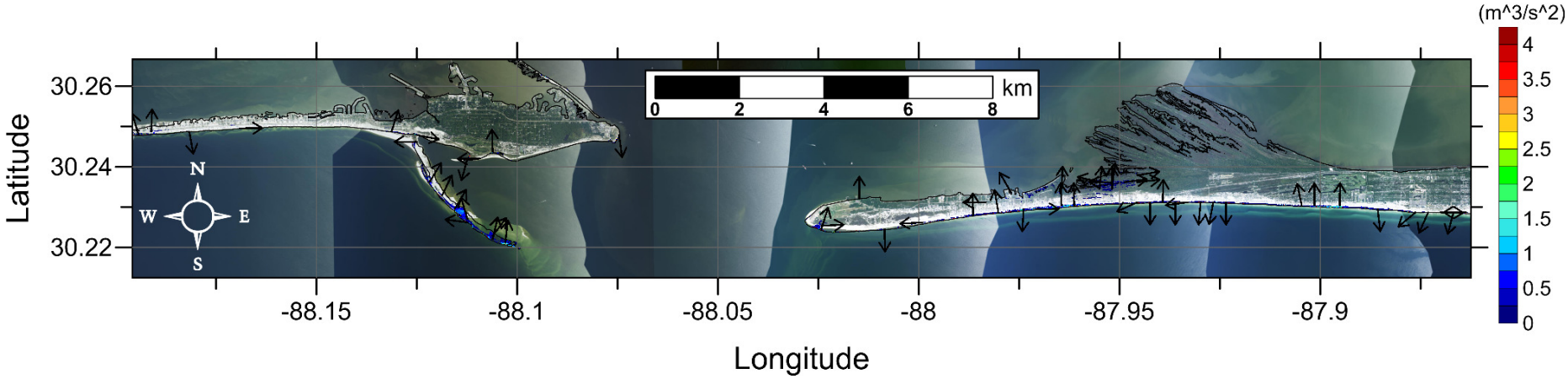

Figure 94: Maximum momentum flux (m^3/s^2) caused by the West Florida submarine landslide in Dauphin Isl./Gulf Highlands, AL. Arrows represent direction of maximum momentum flux. Contour drawn is the zero-meter contour for land elevation.

Mobile, AL
West Florida Submarine Landslide
Maximum Inundation Depth on Grid B

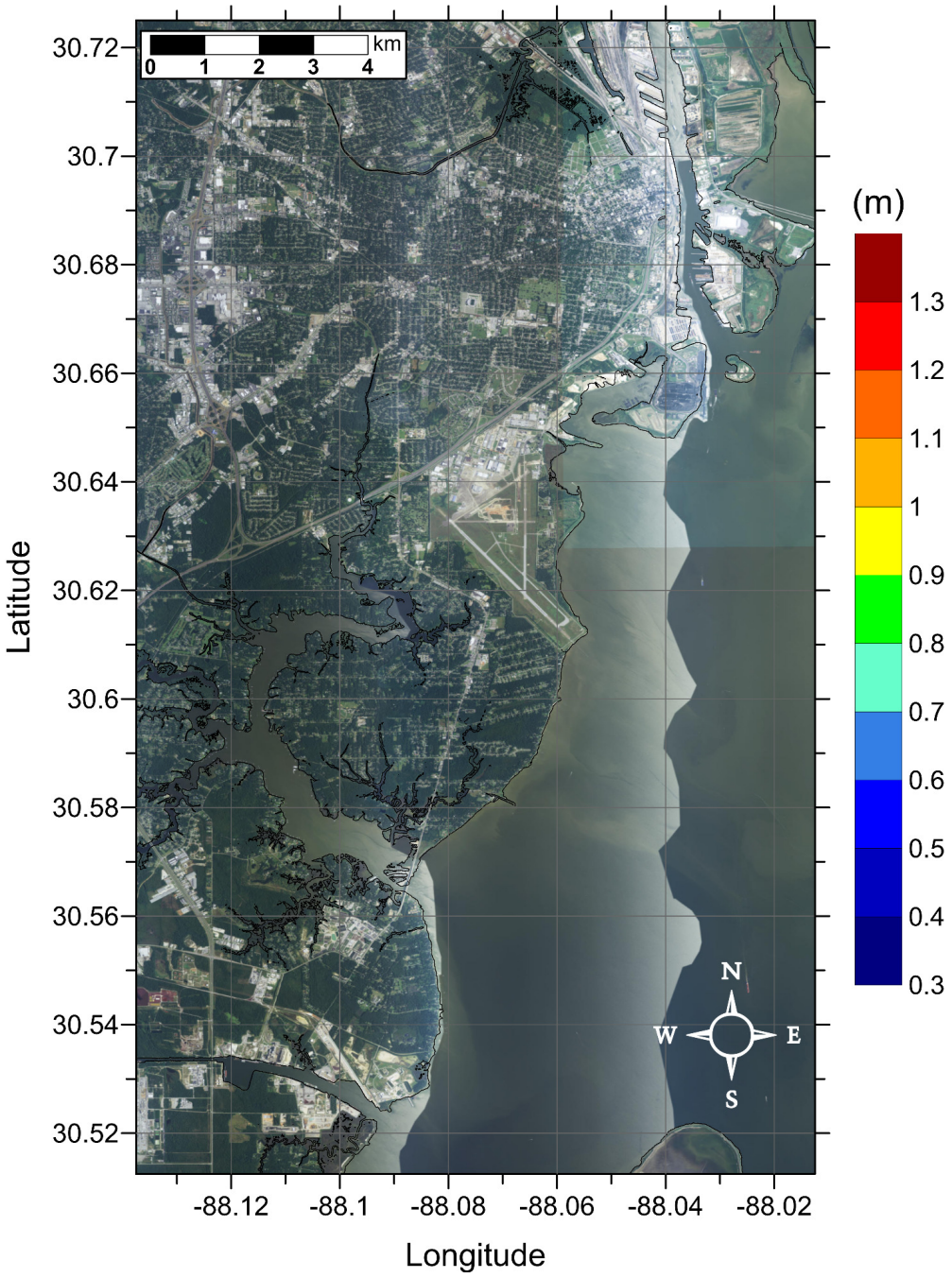

Figure 95: Maximum inundation depth (m) caused by the West Florida submarine landslide in Mobile, AL. Contour drawn is the zero-meter contour for land elevation. (Note: negligible inundation is seen from this source.)

Mobile, AL
West Florida Submarine Landslide
Maximum Momentum Flux on Grid B

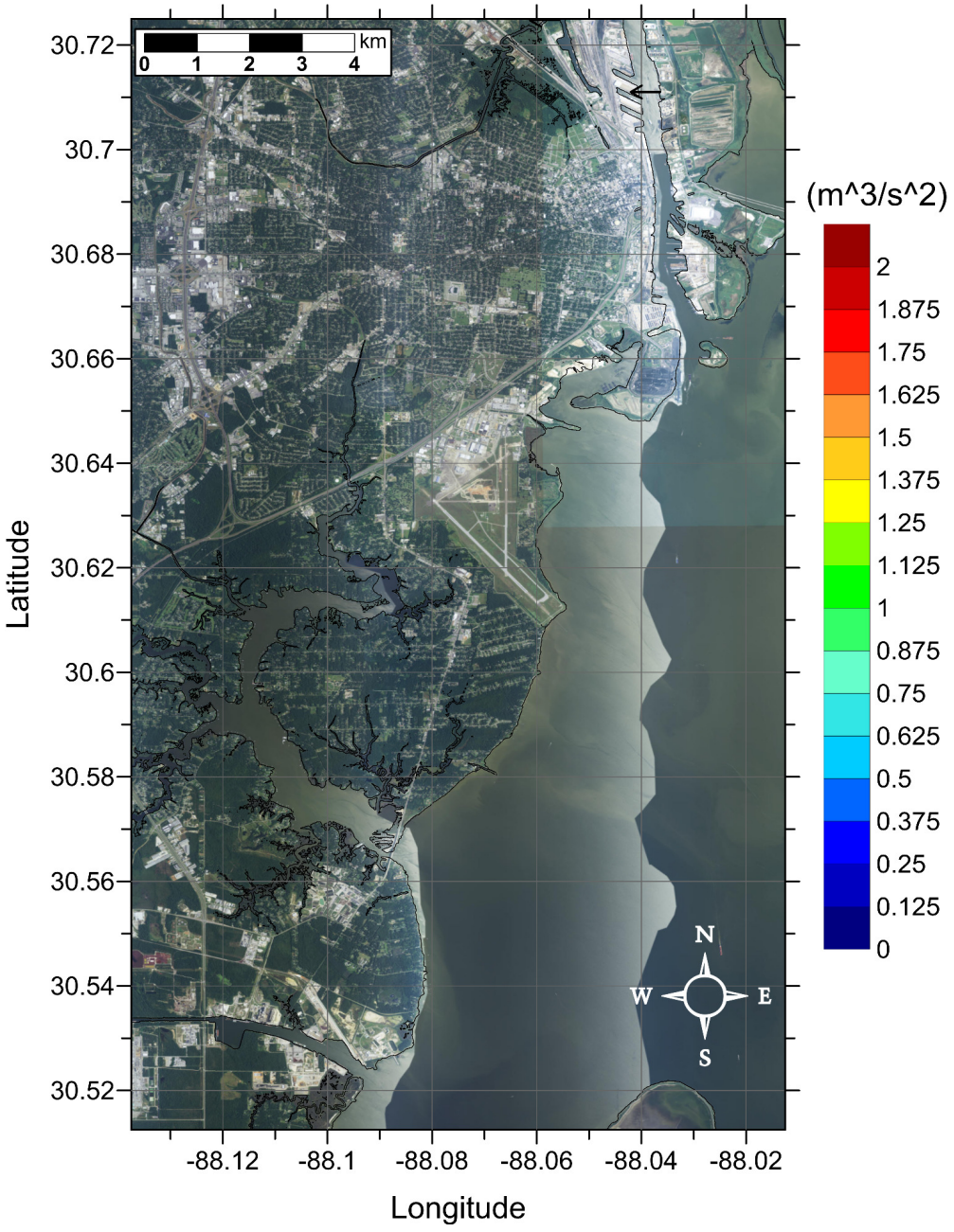

Figure 96: Maximum momentum flux (m^3/s^2) caused by the West Florida submarine landslide in Mobile, AL. Arrows represent direction of maximum momentum flux. Contour drawn is the zero-meter contour for land elevation. (Note: negligible inundation is seen from this source.)

Mobile, AL
Maximum of Maximums Inundation Depth on Grid A

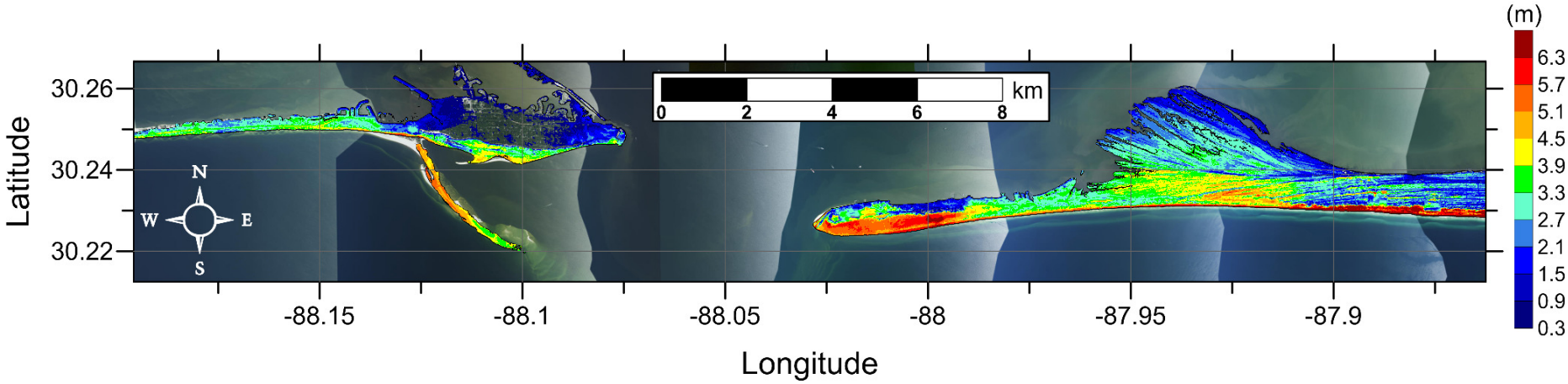

Figure 97: Maximum of maximums inundation depth (m) in Dauphin Isl./Gulf Highlands, AL, calculated as the maximum inundation depth in each grid cell from an ensemble of all tsunami sources considered. Contour drawn is the zero-meter contour for land elevation.

Mobile, AL
Maximum Inundation Depth by Source on Grid A

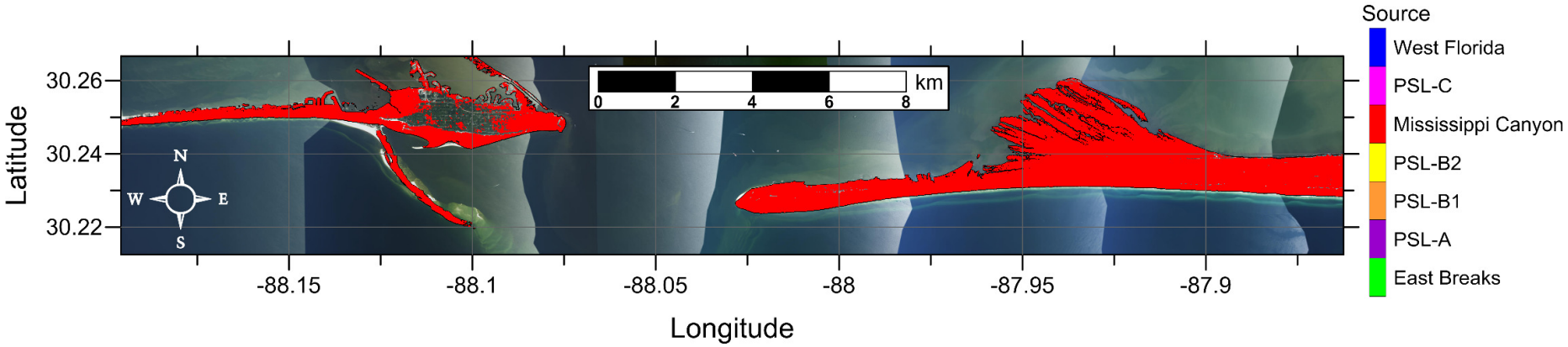

Figure 98: Indication of the tsunami source which causes the maximum of maximums inundation depth (m) in each grid cell from an ensemble of all tsunami sources considered (cf. Figure 97). Contour drawn is the zero-meter contour for land elevation.

Mobile, AL
Maximum of Maximums Inundation Depth on Grid B

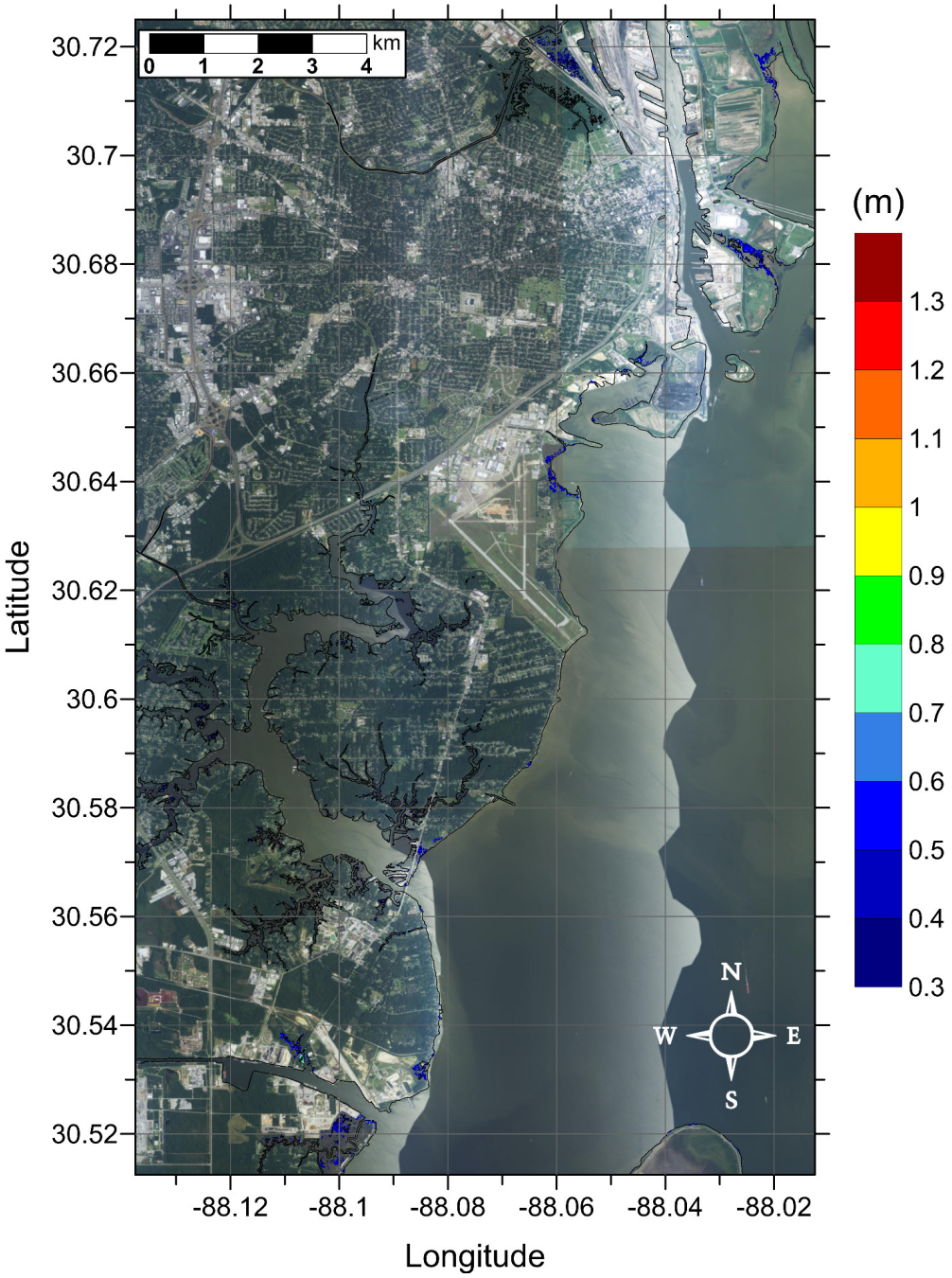

Figure 99: Maximum of maximums inundation depth (m) in Mobile, AL, calculated as the maximum inundation depth in each grid cell from an ensemble of all tsunami sources considered. Contour drawn is the zero-meter contour for land elevation.

Mobile, AL
Maximum Inundation Depth by Source on Grid B

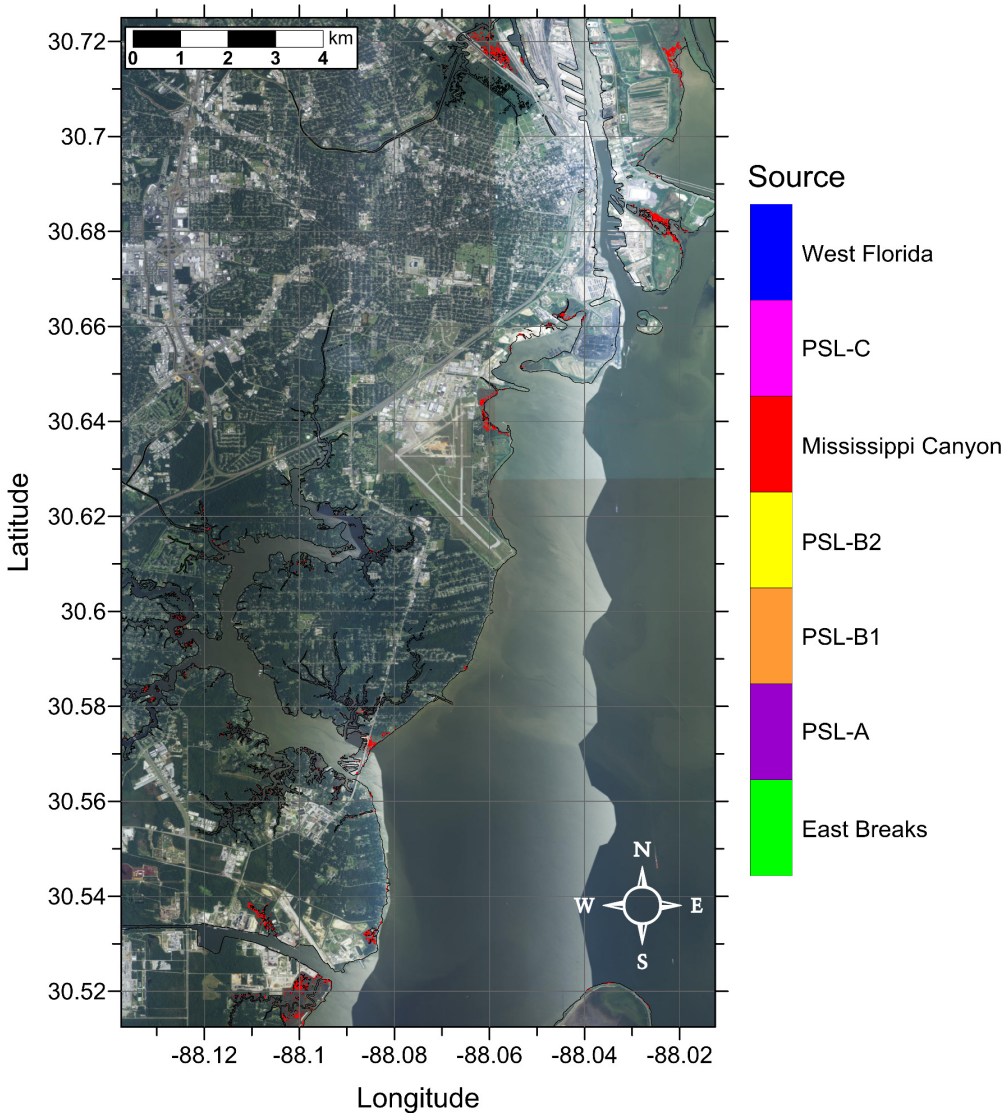

Figure 100: Indication of the tsunami source which causes the maximum of maximums inundation depth (m) in each grid cell from an ensemble of all tsunami sources considered (cf. Figure 99). Contour drawn is the zero-meter contour for land elevation.

5.4 Panama City, FL

Panama City, FL
Amplitude and Arrival Time of Maximum Tsunami Wave Recorded at Numerical Wave Gauge

Table 24: Maximum tsunami wave amplitude and corresponding arrival time after landslide failure at Panama City, FL numerical wave gauge: 30°4'45"N, 85°46'15"W (Figure 1), approximate water depth 21m. *The two values for wave amplitude and arrival time given for the PSL-C landslide correspond to the first positive wave, which was not the maximum amplitude wave, and a later positive wave, which produced the absolute maximum wave amplitude recorded at this gauge.

Tsunami Source	Maximum Wave Amplitude (m)	Arrival Time After Landslide Failure (hr)
East Breaks	0.38	3.6
PSL-A	0.58	3.4
PSL-B1	0.61	2.7
PSL-B2	0.60	2.4
Mississippi Canyon	4.74	2.0
PSL-C*	1.53, 2.52	2.2, 3.7
West Florida	1.12	2.2

Panama City, FL
East Breaks Submarine Landslide
Maximum Inundation Depth

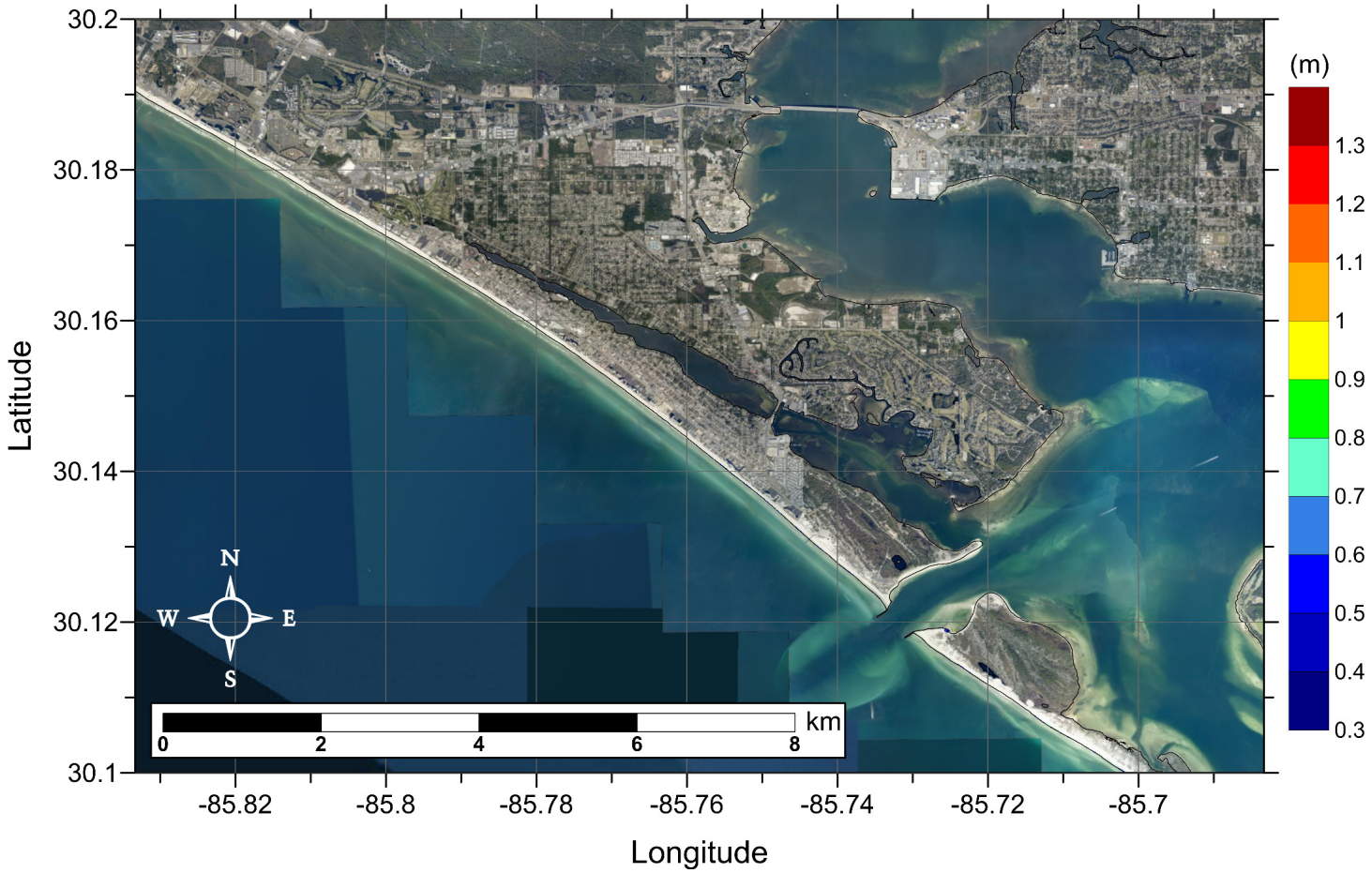

Figure 101: Maximum inundation depth (m) caused by the East Breaks submarine landslide in Panama City, FL. Contour drawn is the zero-meter contour for land elevation. (Note: negligible inundation is seen from this source.)

Panama City, FL
East Breaks Submarine Landslide
Maximum Momentum Flux

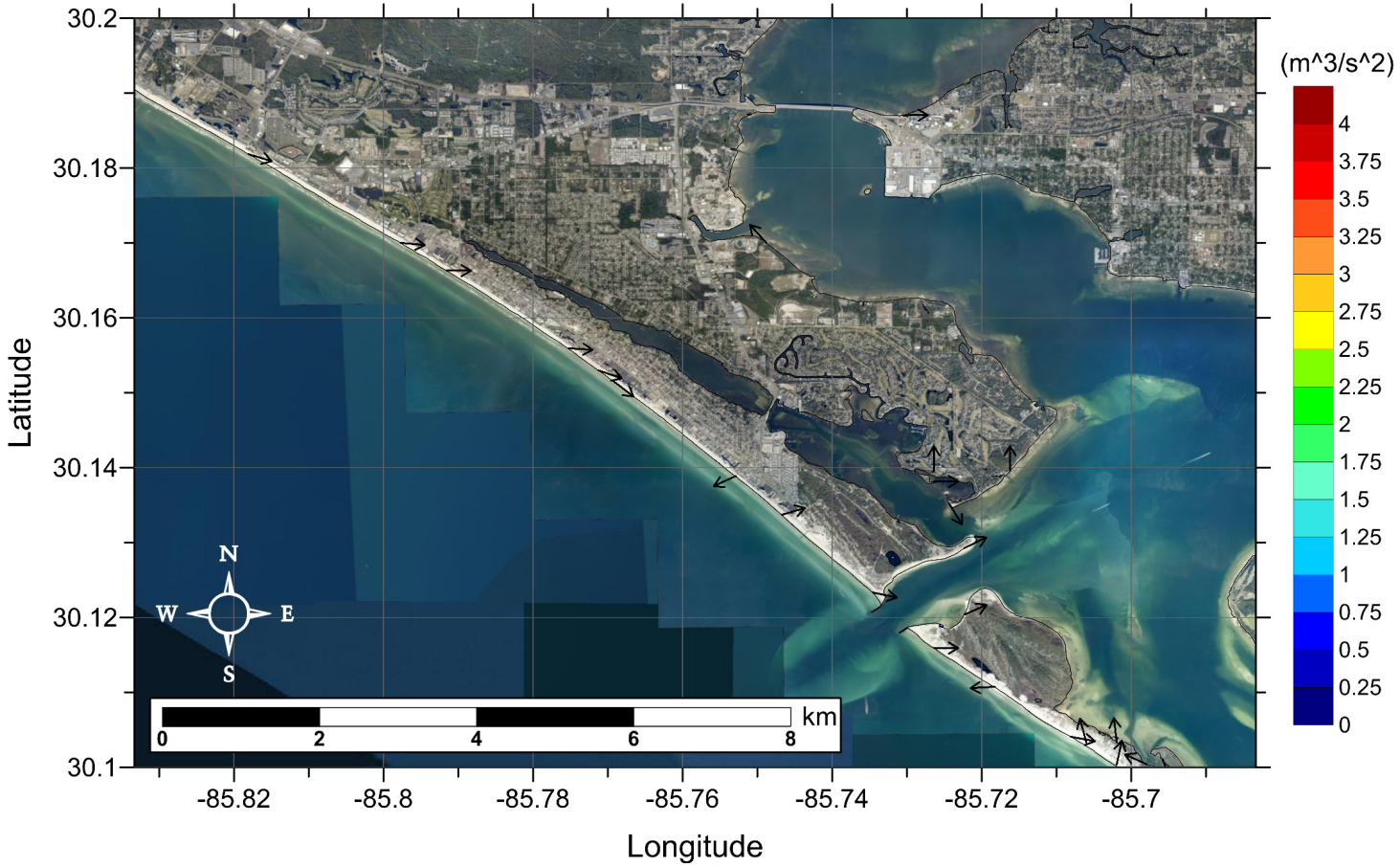

Figure 102: Maximum momentum flux (m^3/s^2) caused by the East Breaks submarine landslide in Panama City, FL. Arrows represent direction of maximum momentum flux. Contour drawn is the zero-meter contour for land elevation. (Note: negligible inundation is seen from this source.)

Panama City, FL
Probabilistic Submarine Landslide A (PSL-A)
Maximum Inundation Depth

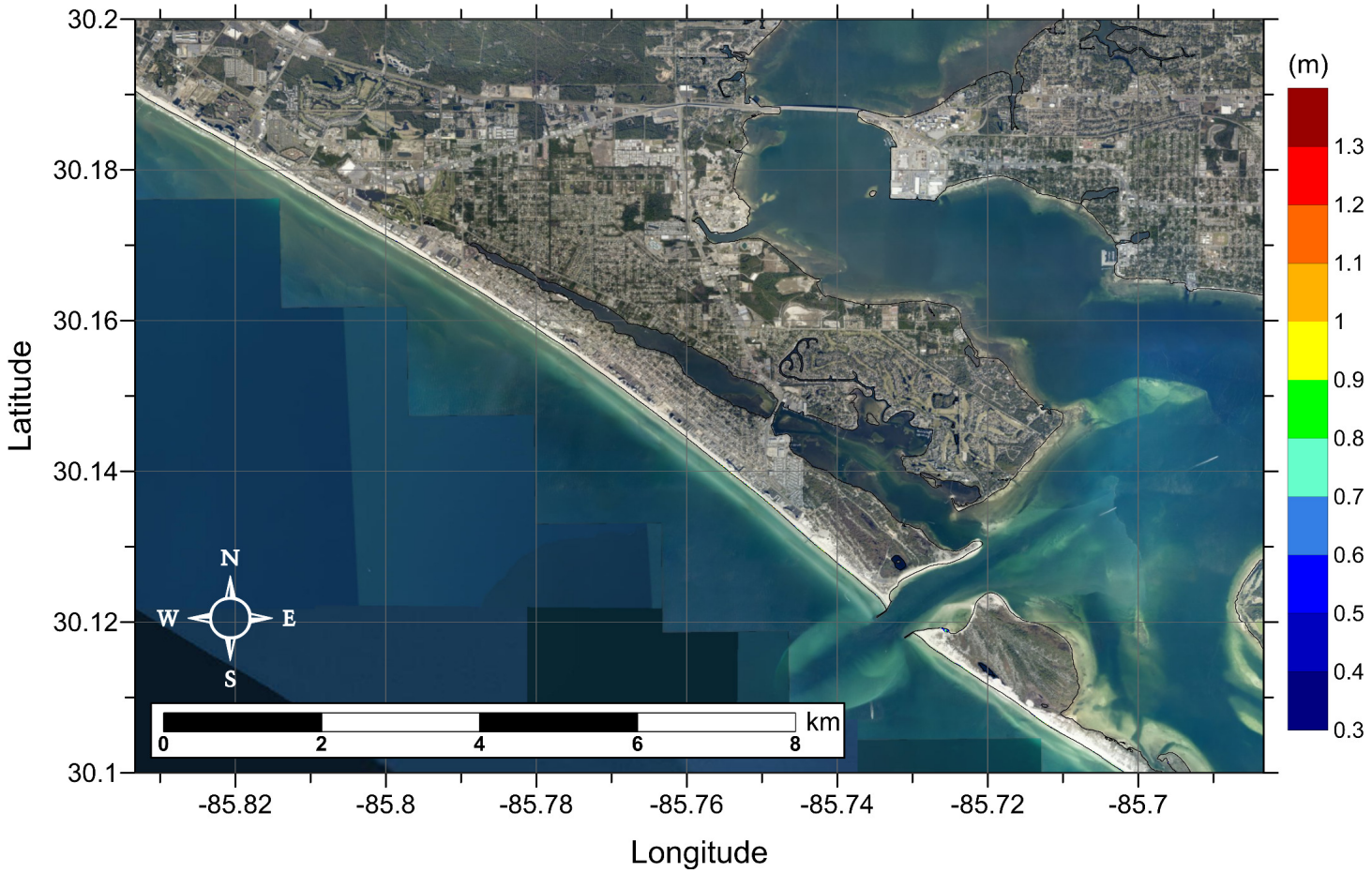

Figure 103: Maximum inundation depth (m) caused by theProbabilistic Submarine Landslide A in Panama City, FL. Contour drawn is the zero-meter contour for land elevation. (Note: negligible inundation is seen from this source.)

Panama City, FL
Probabilistic Submarine Landslide A (PSL-A)
Maximum Momentum Flux

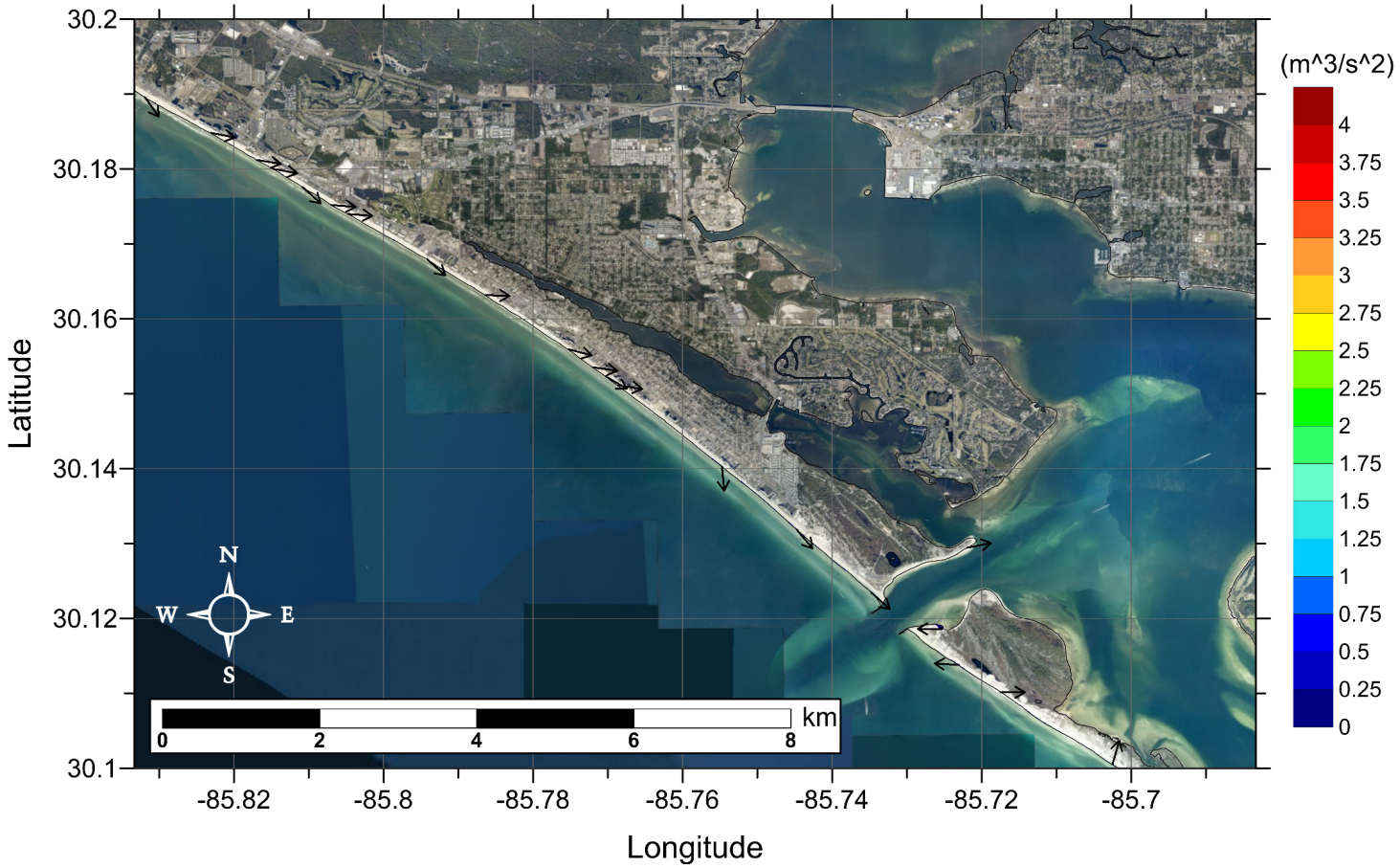

Figure 104: Maximum momentum flux (m^3/s^2) caused by the Probabilistic Submarine Landslide A in Panama City, FL. Arrows represent direction of maximum momentum flux. Contour drawn is the zero-meter contour for land elevation. (Note: negligible inundation is seen from this source.)

Panama City, FL
Probabilistic Submarine Landslide B1 (PSL-B1)
Maximum Inundation Depth

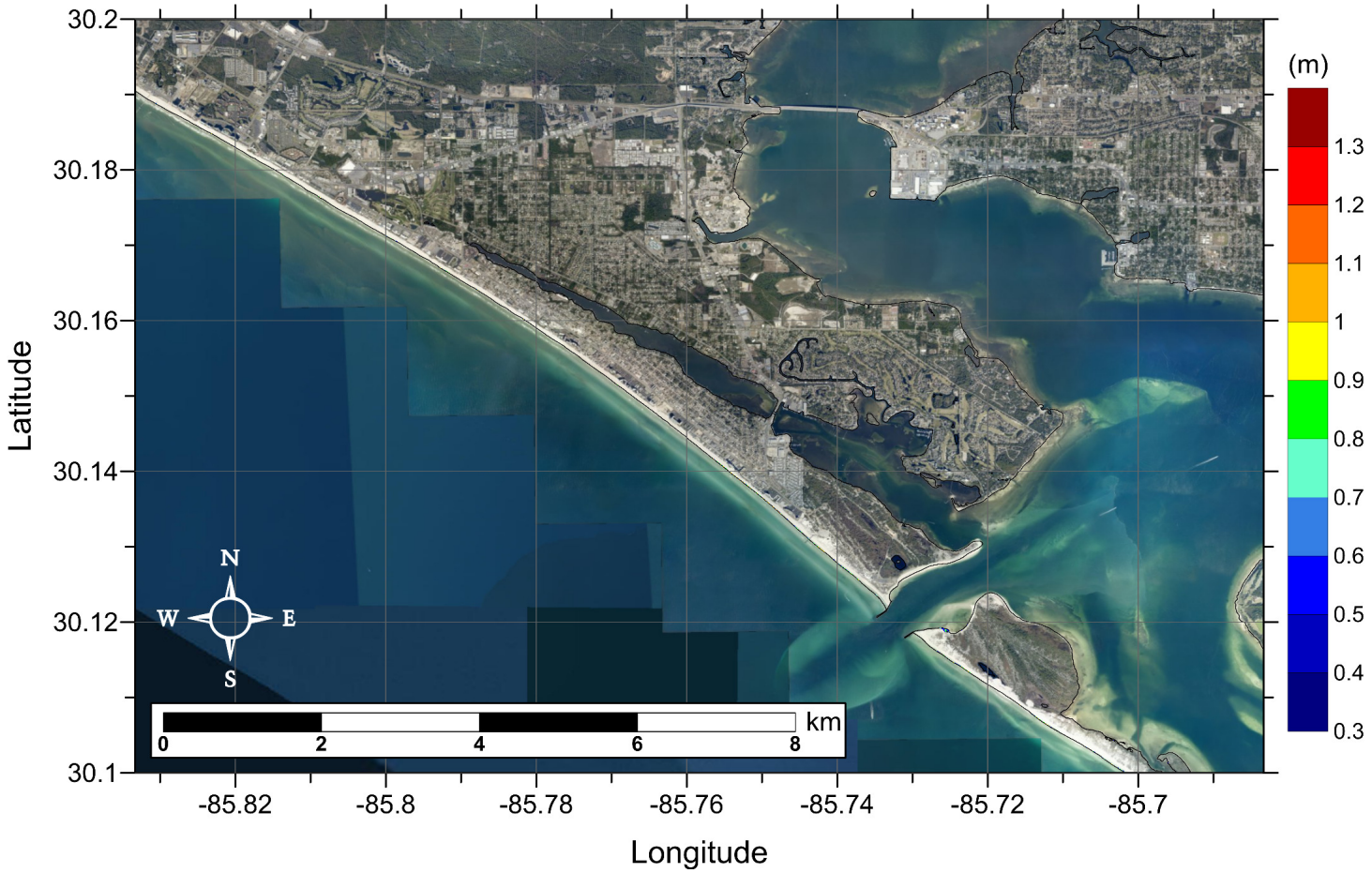

Figure 105: Maximum inundation depth (m) caused by theProbabilistic Submarine Landslide B-1 in Panama City, FL. Contour drawn is the zero-meter contour for land elevation. (Note: negligible inundation is seen from this source.)

Panama City, FL
Probabilistic Submarine Landslide B1 (PSL-B1)
Maximum Momentum Flux

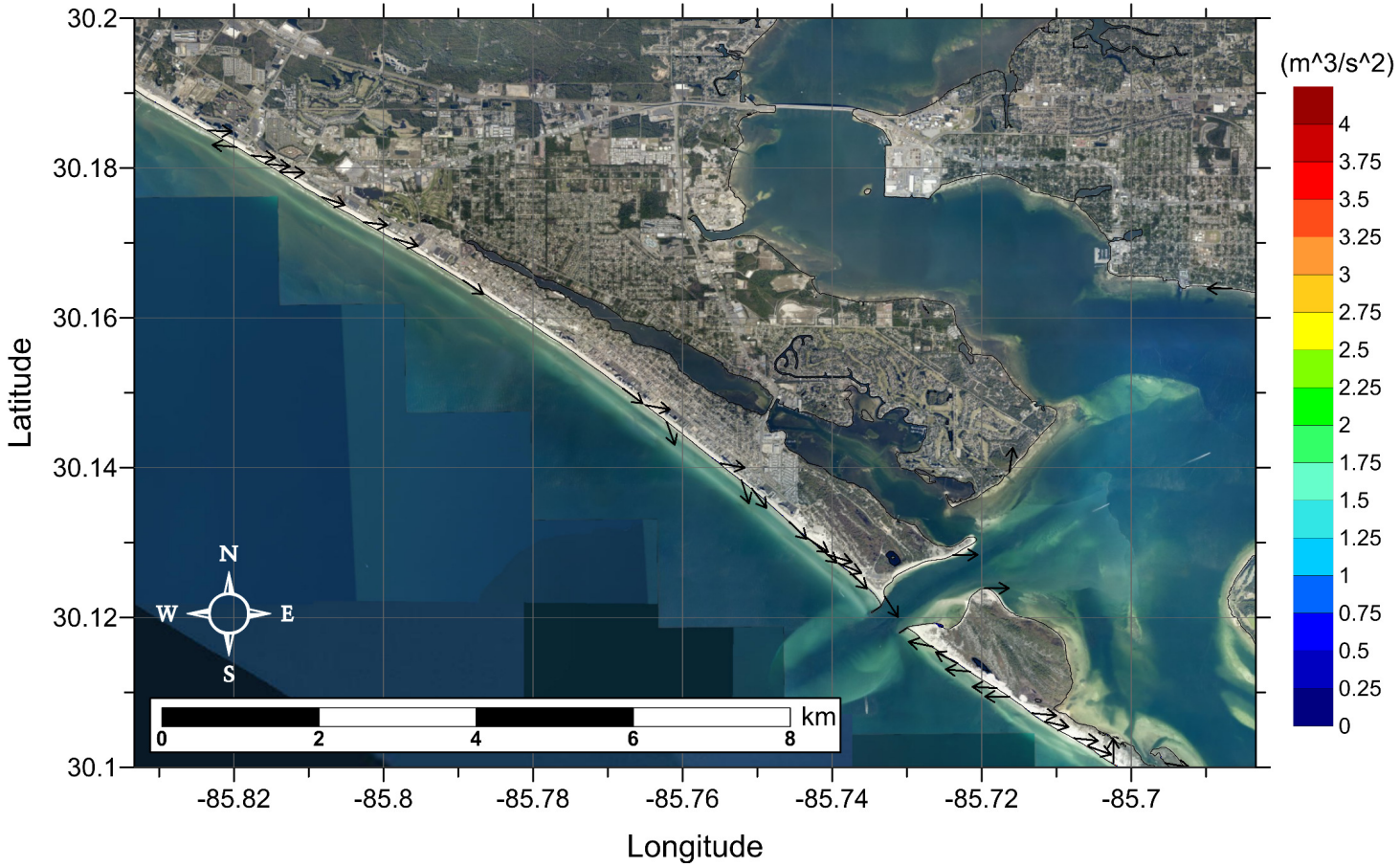

Figure 106: Maximum momentum flux (m^3/s^2) caused by the Probabilistic Submarine Landslide B-1 in Panama City, FL. Arrows represent direction of maximum momentum flux. Contour drawn is the zero-meter contour for land elevation. (Note: negligible inundation is seen from this source.)

Panama City, FL
Probabilistic Submarine Landslide B2 (PSL-B2)
Maximum Inundation Depth

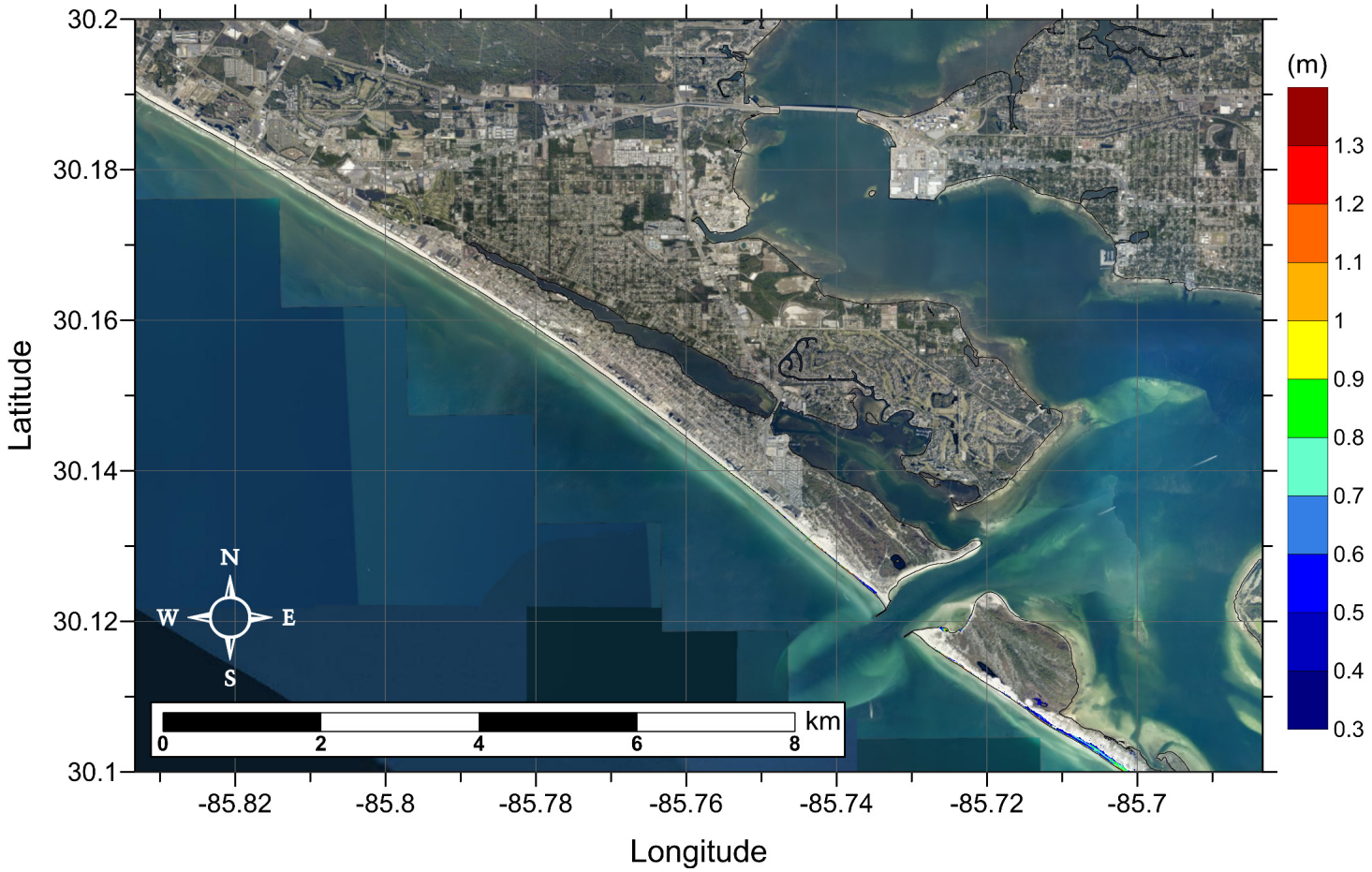

Figure 107: Maximum inundation depth (m) caused by theProbabilistic Submarine Landslide B-2 in Panama City, FL. Contour drawn is the zero-meter contour for land elevation. (Note: negligible inundation is seen from this source.)

Panama City, FL
Probabilistic Submarine Landslide B2 (PSL-B2)
Maximum Momentum Flux

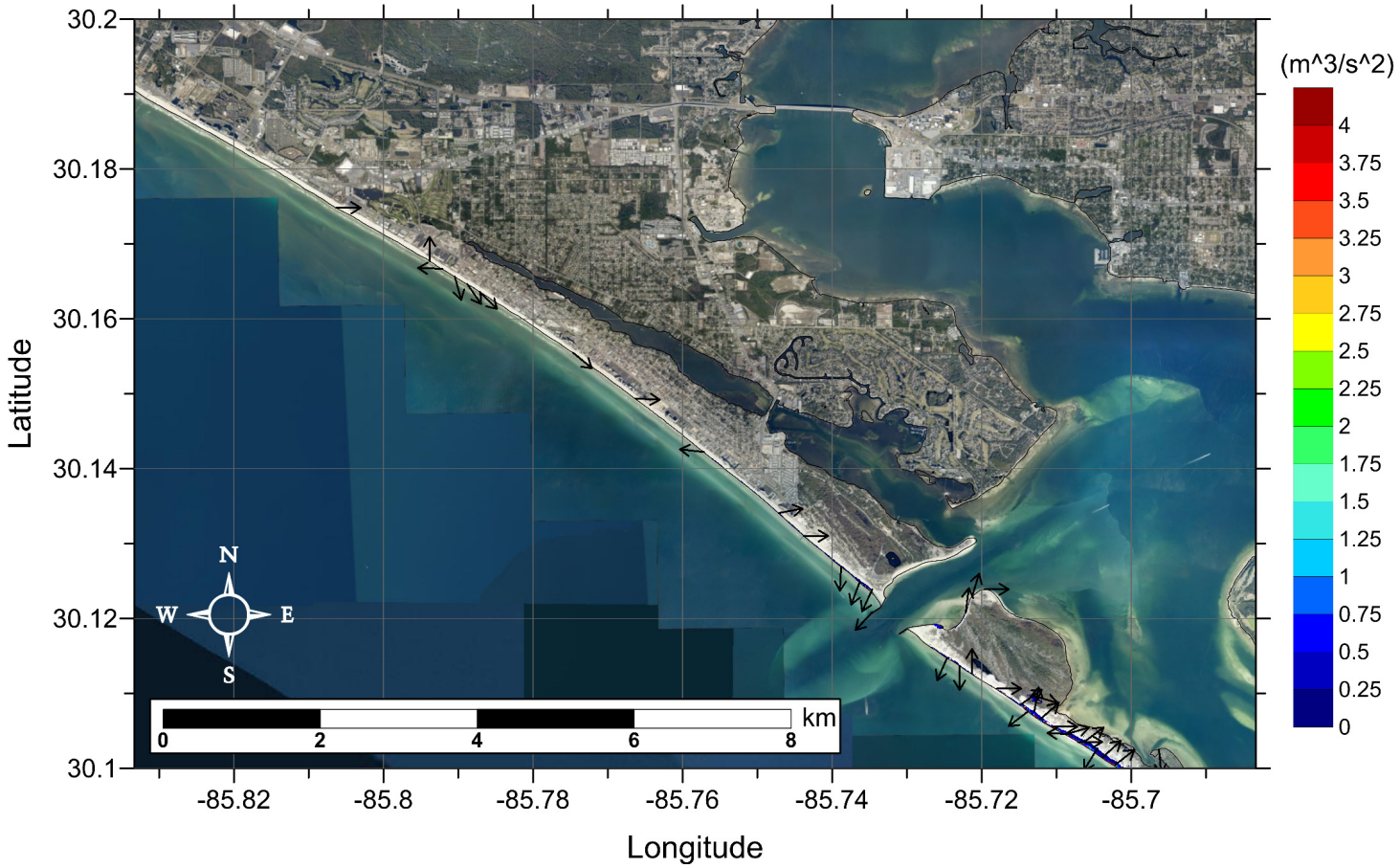

Figure 108: Maximum momentum flux (m^3/s^2) caused by the Probabilistic Submarine Landslide B-2 in Panama City, FL. Arrows represent direction of maximum momentum flux. Contour drawn is the zero-meter contour for land elevation. (Note: negligible inundation is seen from this source.)

Panama City, FL
Mississippi Canyon Submarine Landslide
Maximum Inundation Depth

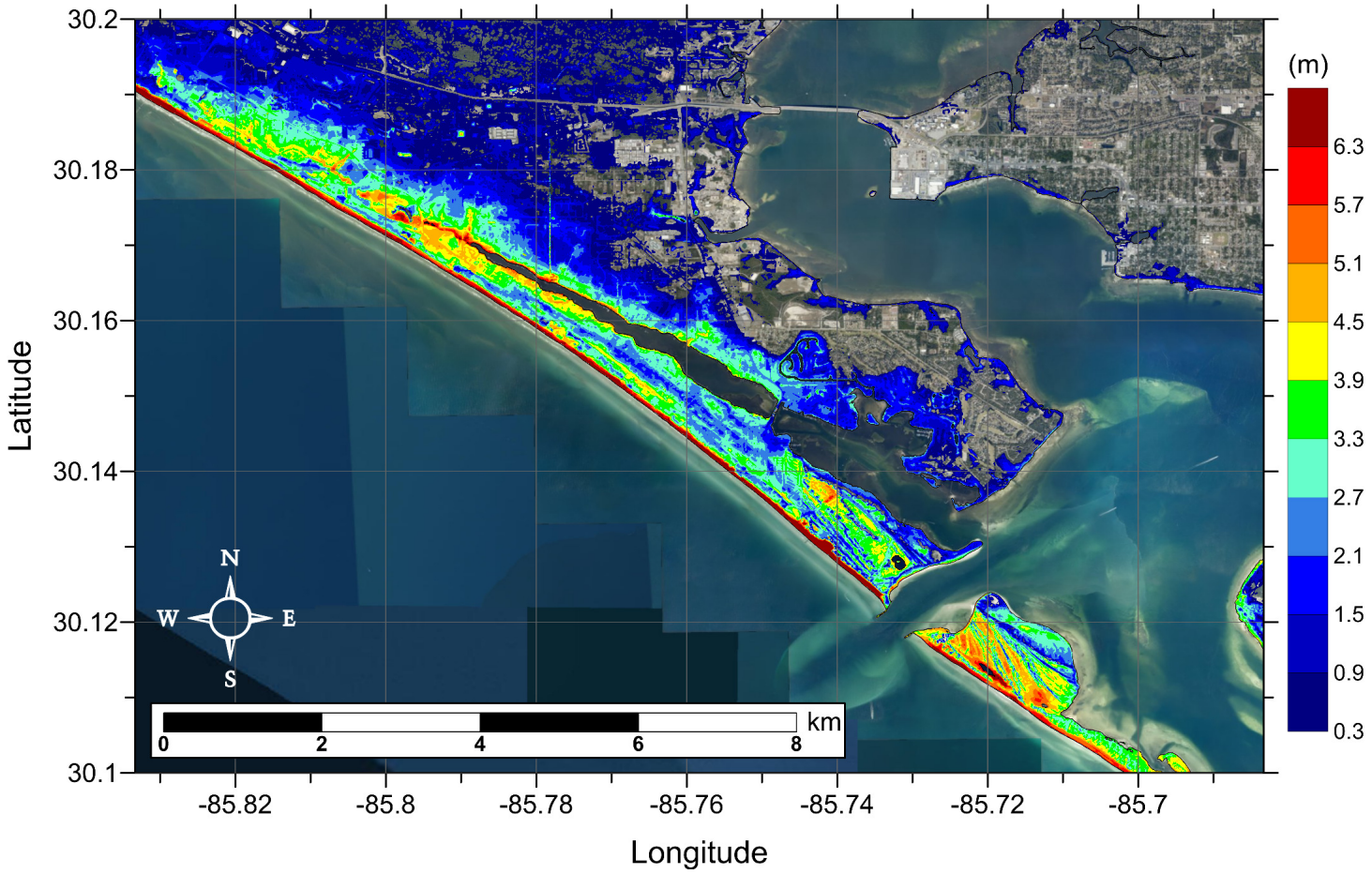

Figure 109: Maximum inundation depth (m) caused by the Mississippi Canyon submarine landslide in Panama City, FL. Contour drawn is the zero-meter contour for land elevation.

Panama City, FL
Mississippi Canyon Submarine Landslide
Maximum Momentum Flux

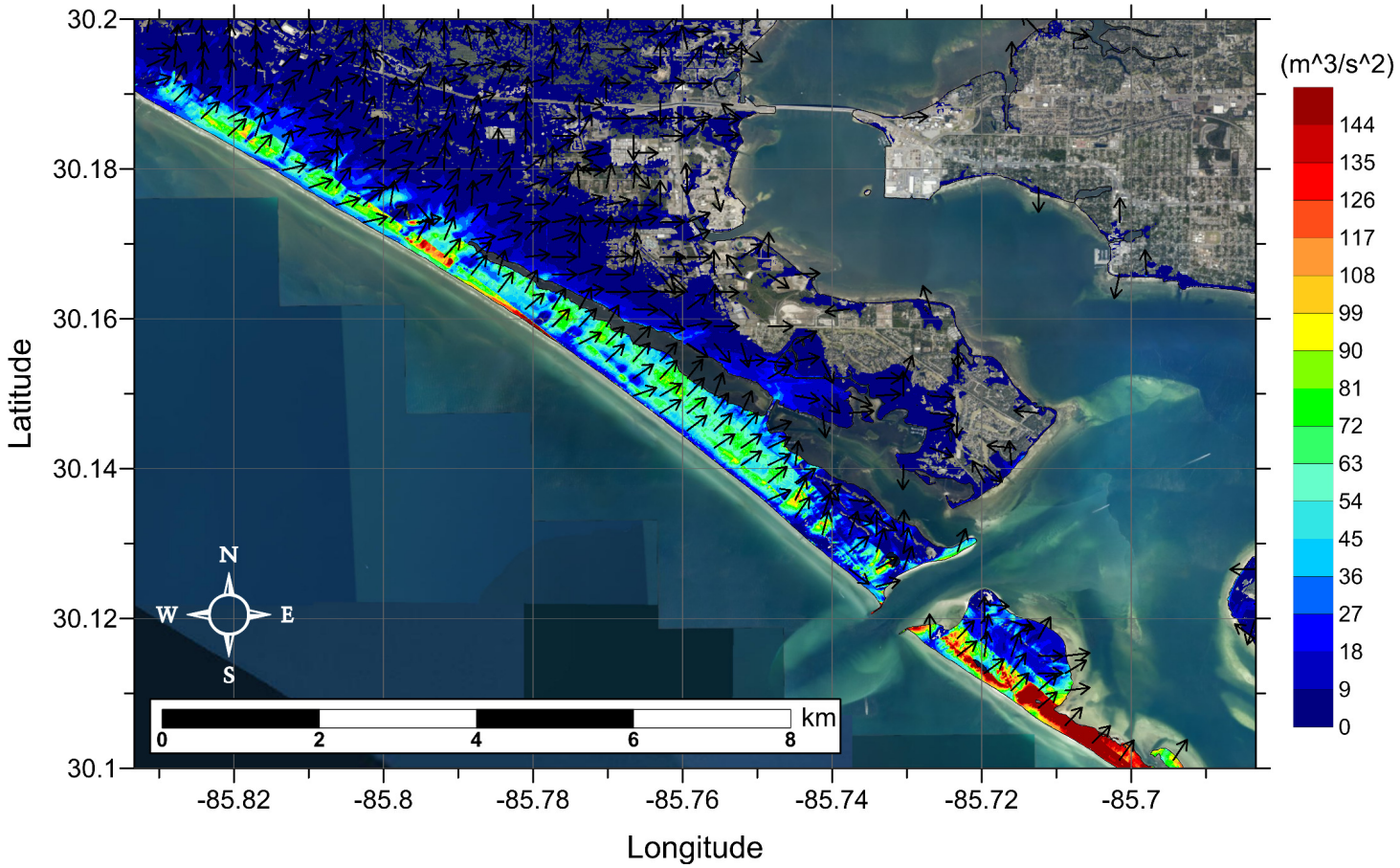

Figure 110: Maximum momentum flux (m^3/s^2) caused by the Mississippi Canyon submarine landslide in Panama City, FL. Arrows represent direction of maximum momentum flux. Contour drawn is the zero-meter contour for land elevation.

Panama City, FL
Probabilistic Submarine Landslide C (PSL-C)
Maximum Inundation Depth

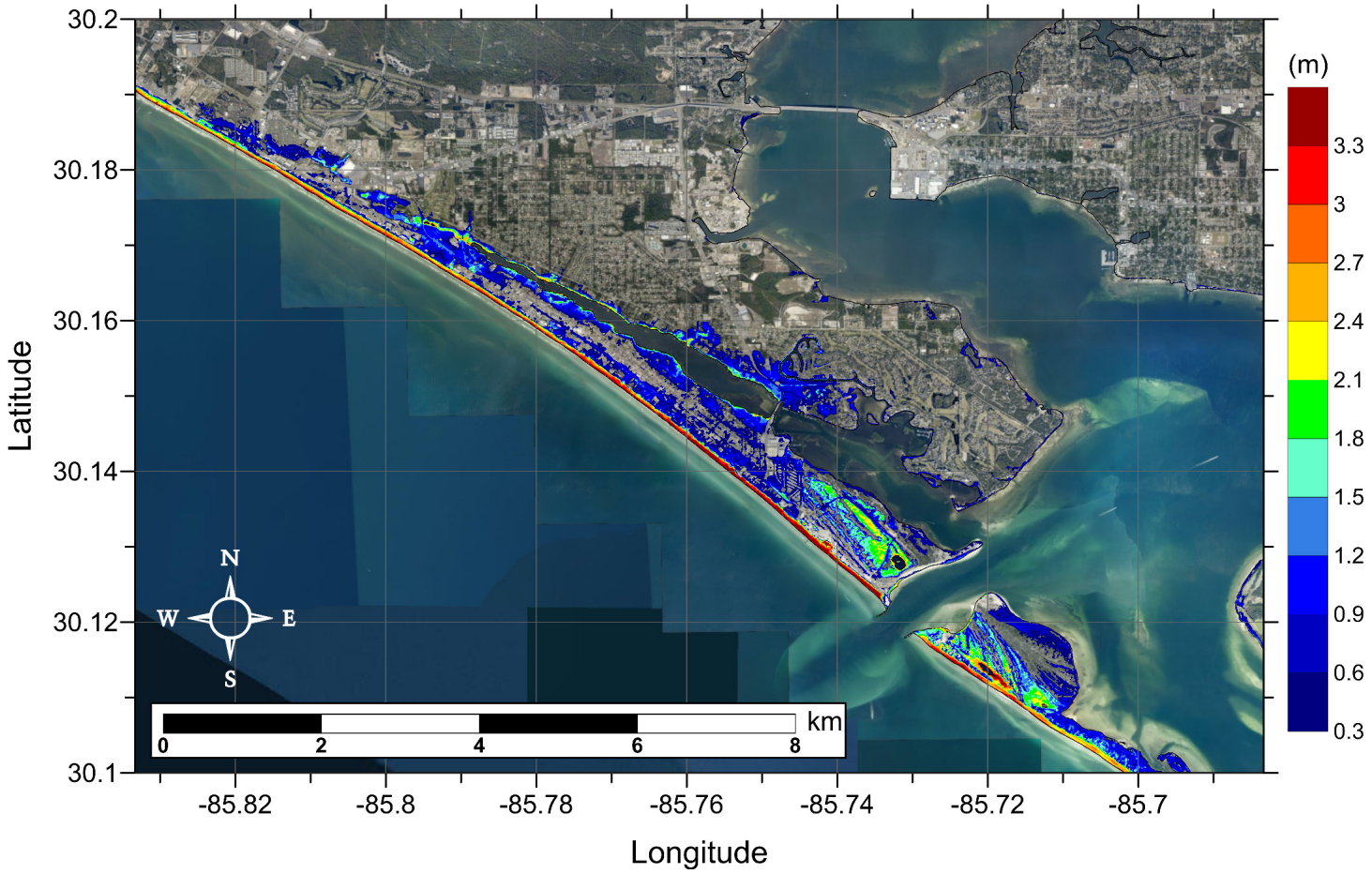

Figure 111: Maximum inundation depth (m) caused by theProbabilistic Submarine Landslide C in Panama City, FL. Contour drawn is the zero-meter contour for land elevation.

Panama City, FL
Probabilistic Submarine Landslide C (PSL-C)
Maximum Momentum Flux

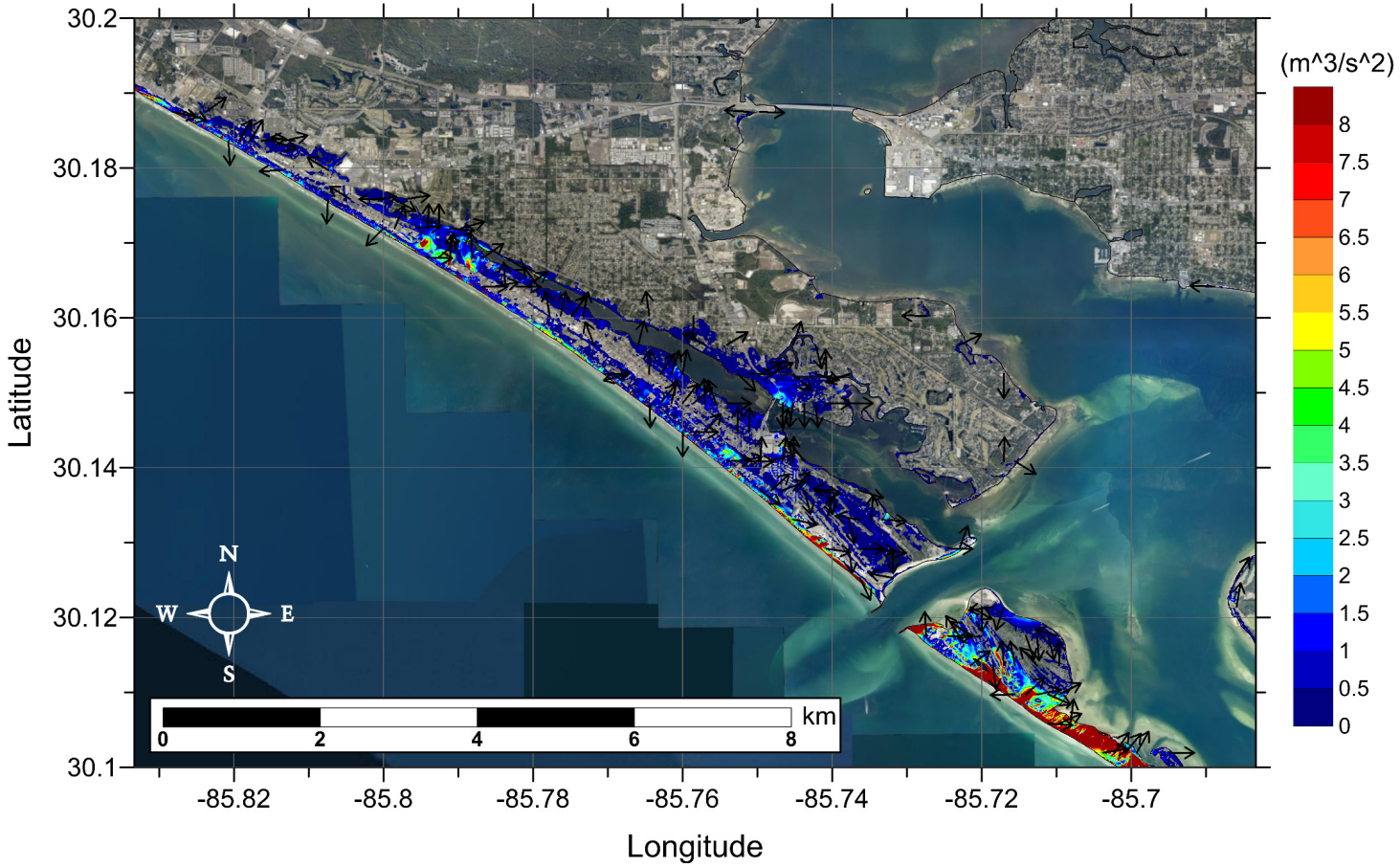

Figure 112: Maximum momentum flux (m^3/s^2) caused by the Probabilistic Submarine Landslide C in Panama City, FL. Arrows represent direction of maximum momentum flux. Contour drawn is the zero-meter contour for land elevation.

Panama City, FL
West Florida Submarine Landslide
Maximum Inundation Depth

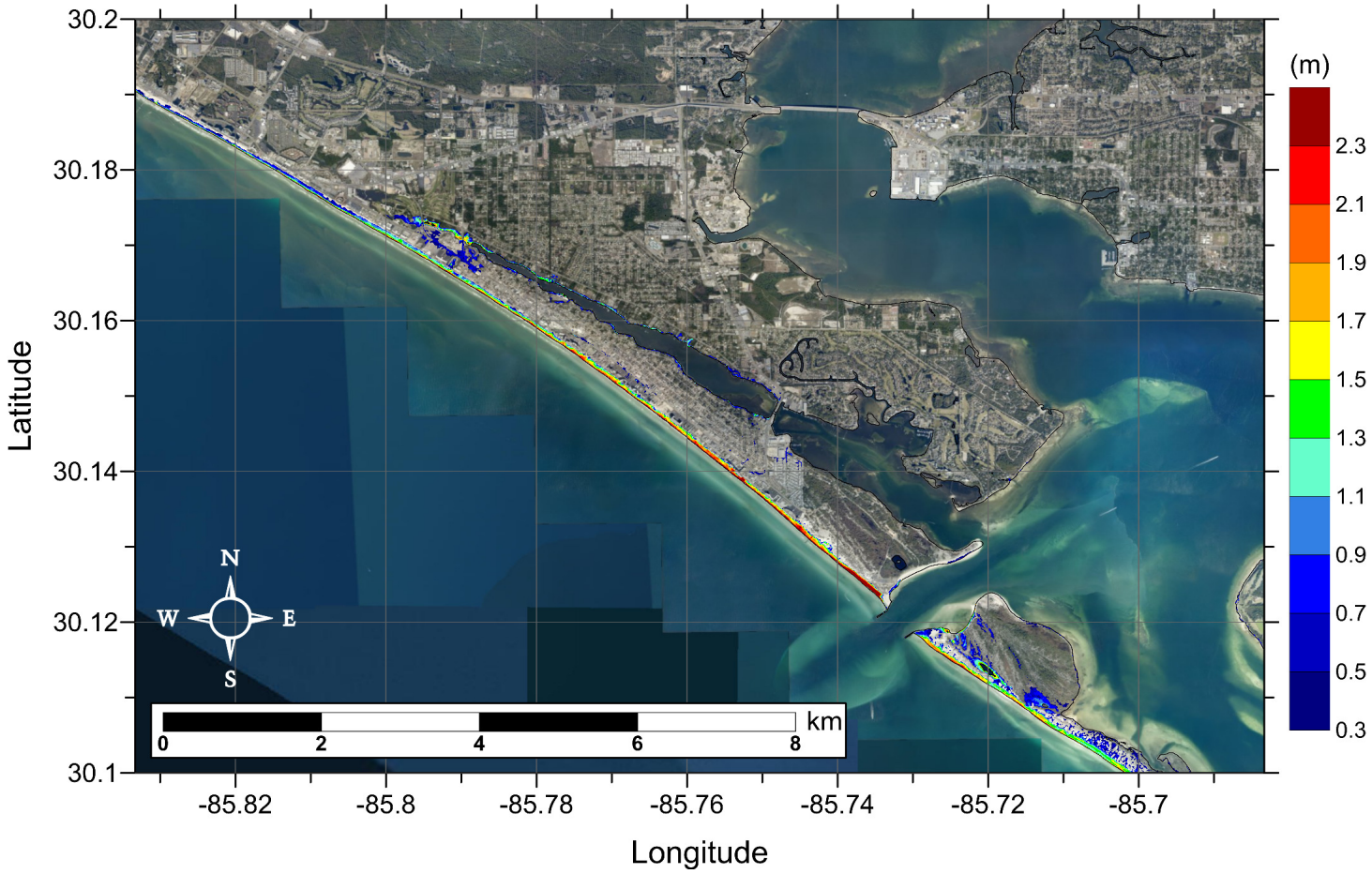

Figure 113: Maximum inundation depth (m) caused by the West Florida submarine landslide in Panama City, FL. Contour drawn is the zero-meter contour for land elevation.

Panama City, FL
West Florida Submarine Landslide
Maximum Momentum Flux

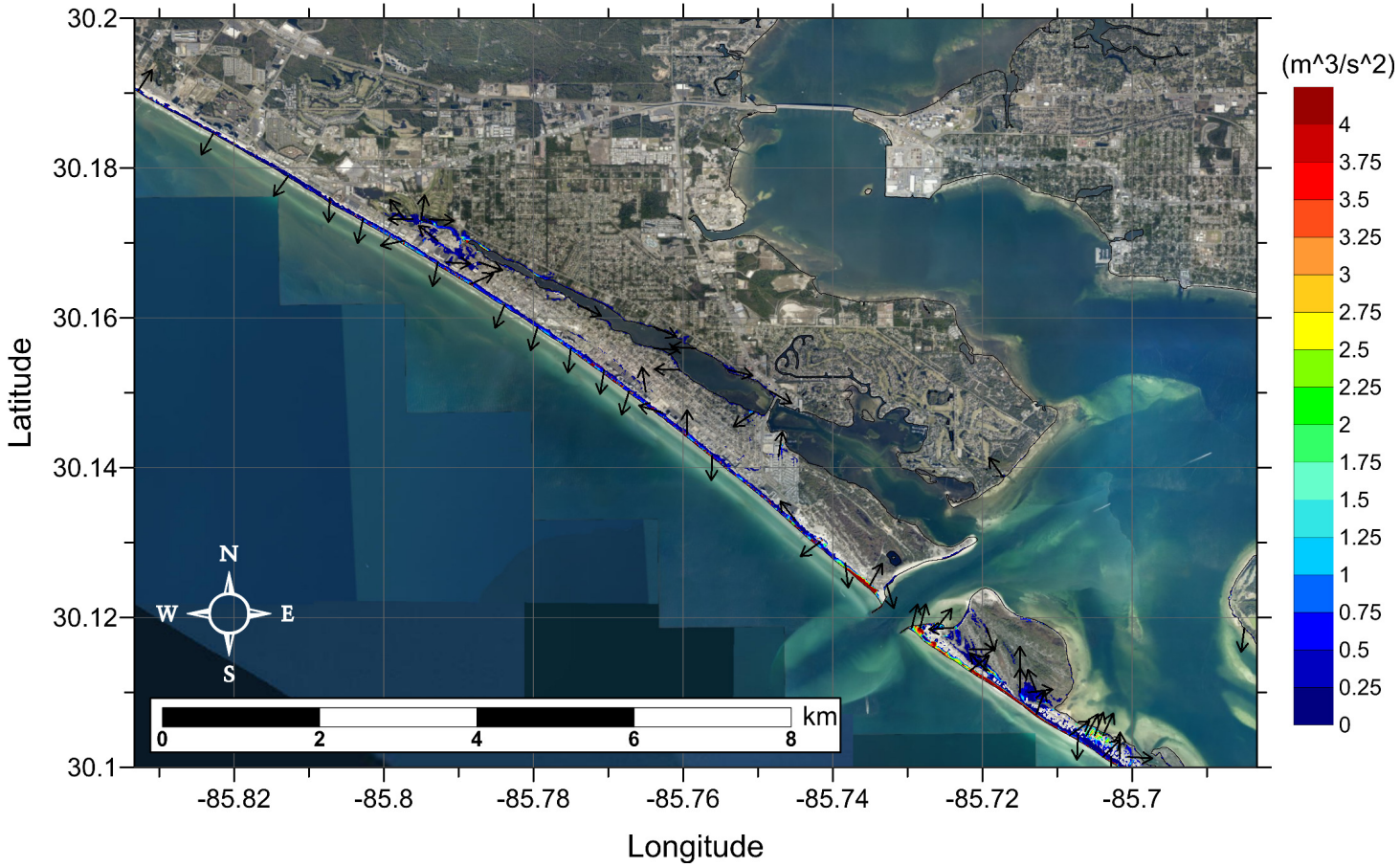

Figure 114: Maximum momentum flux (m^3/s^2) caused by the West Florida submarine landslide in Panama City, FL. Arrows represent direction of maximum momentum flux. Contour drawn is the zero-meter contour for land elevation.

Panama City, FL
Maximum of Maximums Inundation Depth

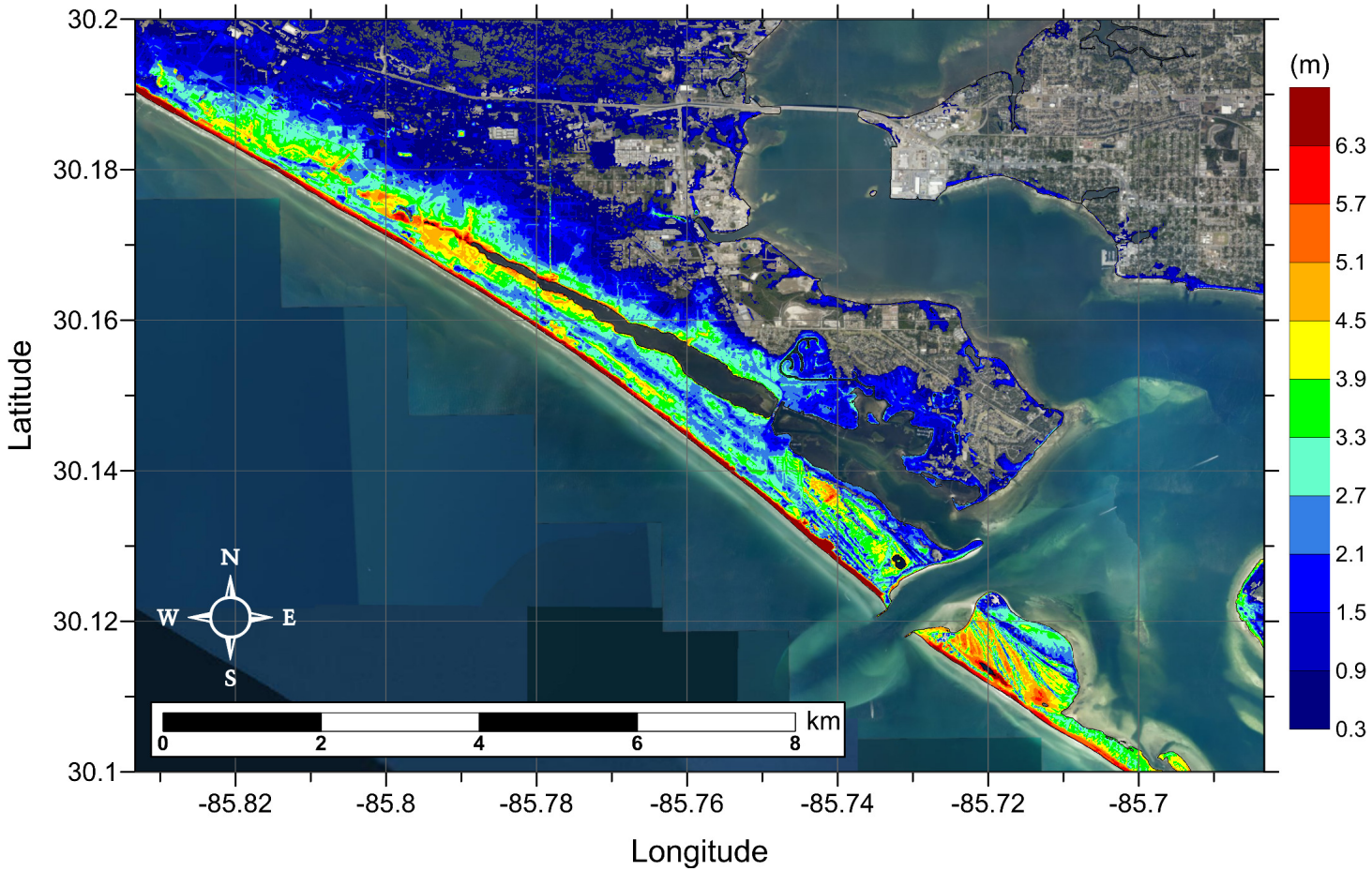

Figure 115: Maximum of maximums inundation depth (m) in Panama City, FL, calculated as the maximum inundation depth in each grid cell from an ensemble of all tsunami sources considered. Contour drawn is the zero-meter contour for land elevation.

Panama City, FL
Maximum Inundation Depth by Source

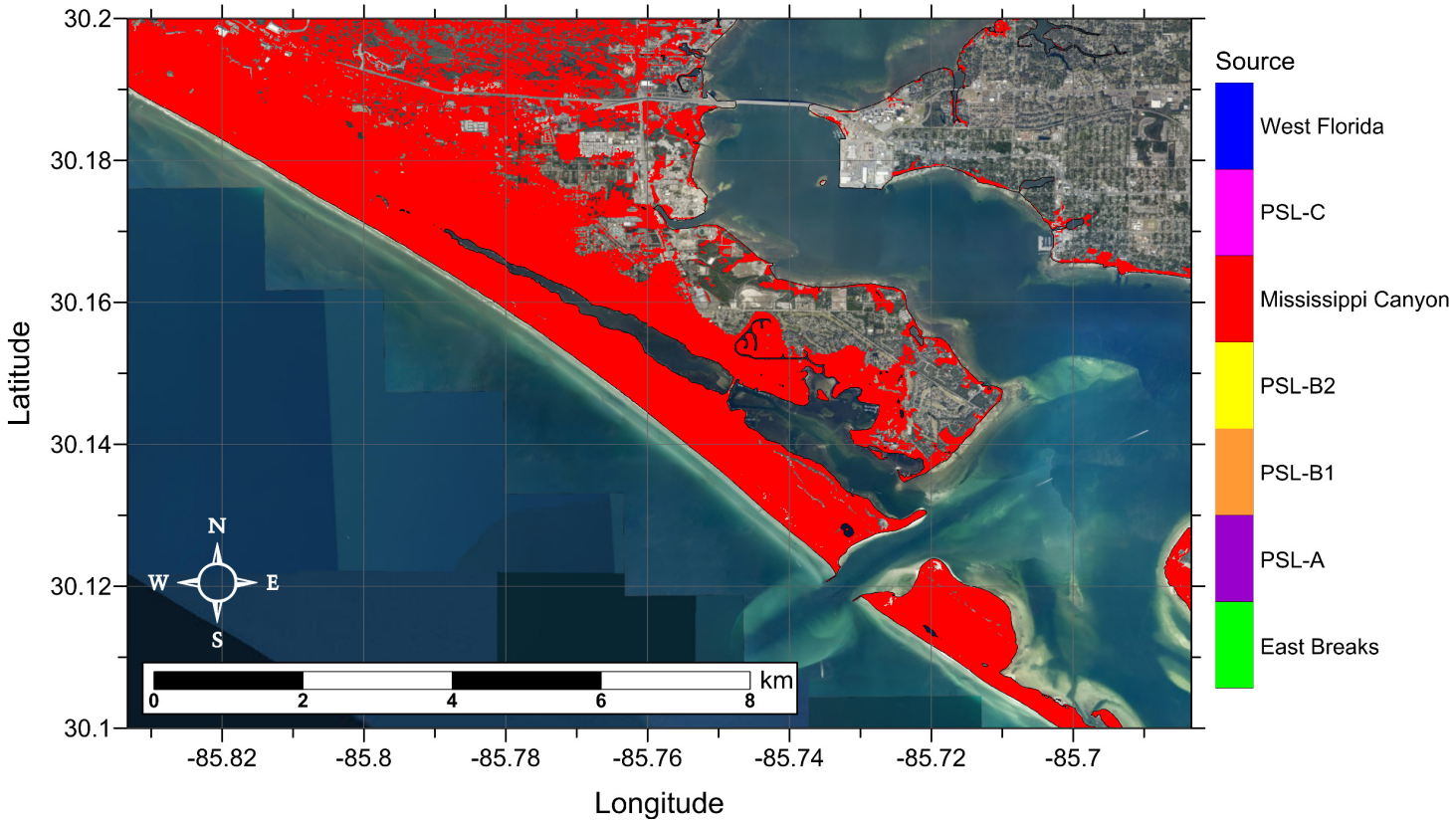

Figure 116: Indication of the tsunami source which causes the maximum of maximums inundation depth (m) in each grid cell from an ensemble of all tsunami sources considered (see Figure 115). Contour drawn is the zero-meter contour for land elevation.

5.5 Tampa Bay, FL

Tampa, FL
Amplitude and Arrival Time of Maximum Tsunami Wave Recorded at Numerical Wave Gauge

Table 25: Maximum tsunami wave amplitude and corresponding arrival time after landslide failure at Tampa, FL numerical wave gauge: 27°35'45"N, 83°3'45"W (Figure 1), approximate water depth 20m. *The two values for wave amplitude and arrival time given for the East Breaks landslide correspond to the first positive wave, which was not the maximum amplitude wave, and the second positive wave, which produced the absolute maximum wave amplitude recorded at this gauge.

Tsunami Source	Maximum Wave Amplitude (m)	Arrival Time After Landslide Failure (hr)
East Breaks*	0.27, 0.35	4.2, 4.4
PSL-A	0.52	4.0
PSL-B1	0.75	3.4
PSL-B2	2.11	3.0
Mississippi Canyon	4.92	2.9
PSL-C	1.95	2.5
West Florida	1.36	2.2

Tampa, FL
East Breaks Submarine Landslide
Maximum Inundation Depth on Grid A

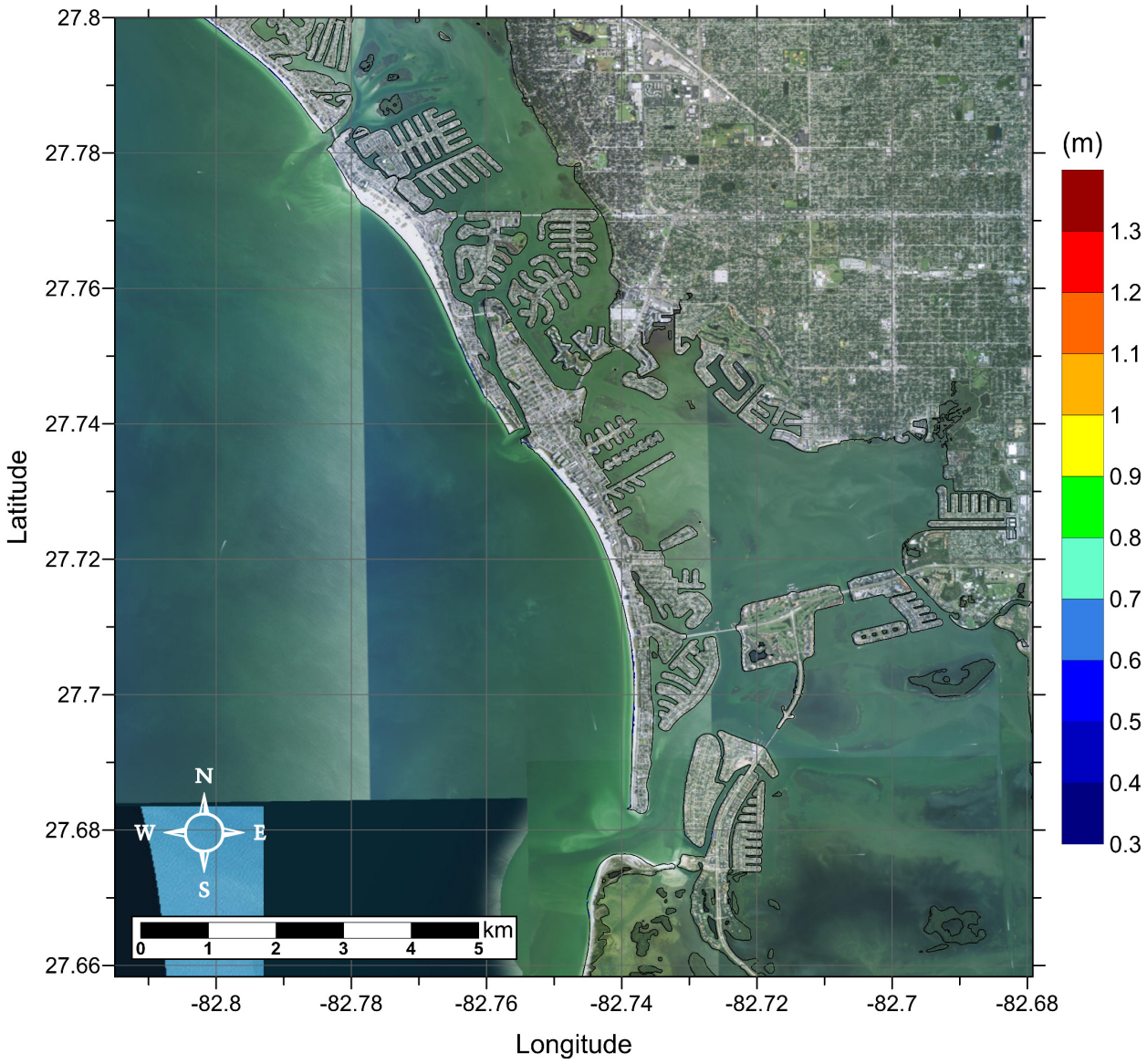

Figure 117: Maximum inundation depth (m) caused by the East Breaks submarine landslide in southern Tampa, FL. Contour drawn is the zero-meter contour for land elevation. (Note: negligible inundation seen from this source.)

Tampa, FL
East Breaks Submarine Landslide
Maximum Momentum Flux on Grid A

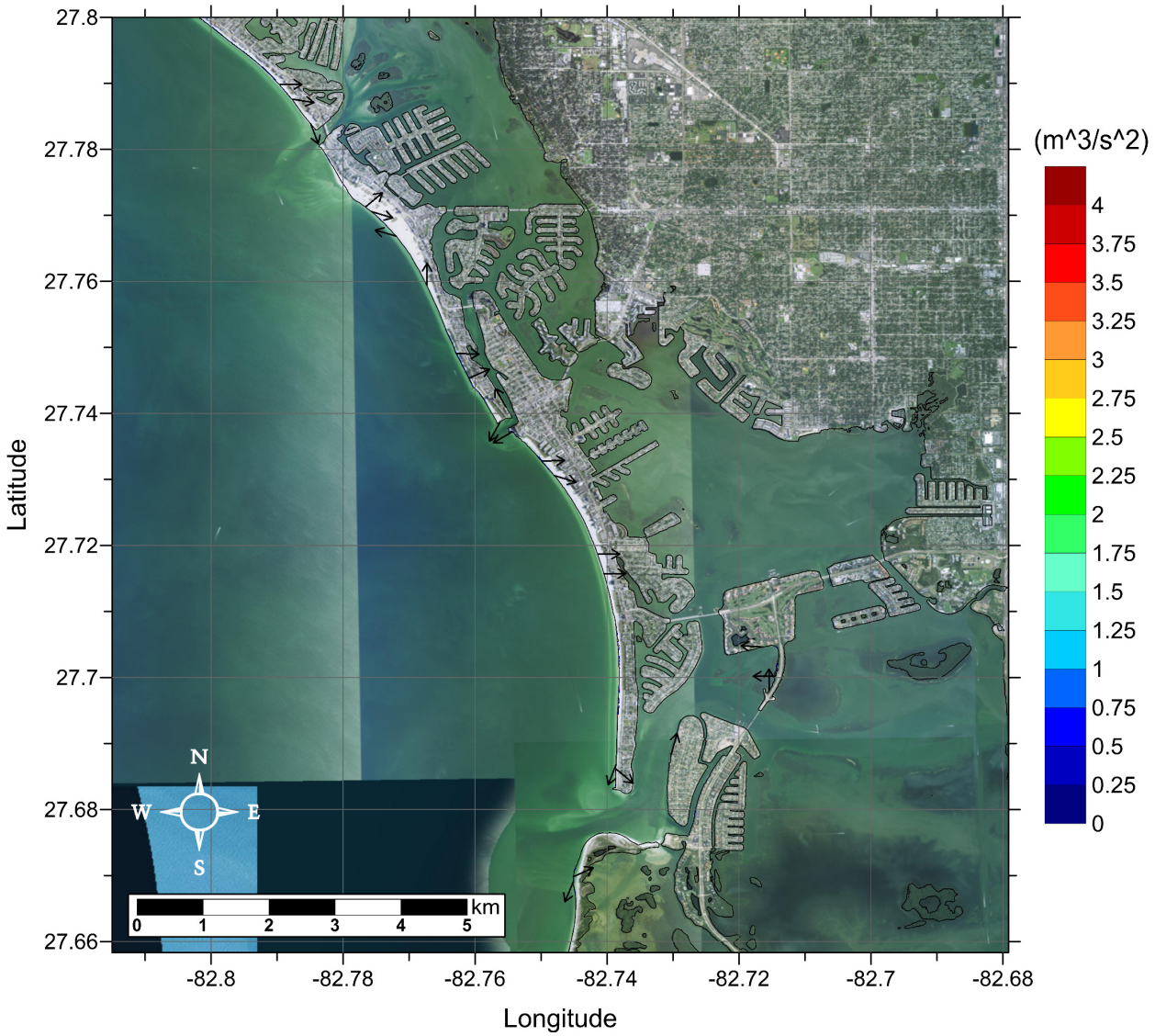

Figure 118: Maximum momentum flux (m^3/s^2) caused by the East Breaks submarine landslide in southern Tampa, FL. Arrows represent direction of maximum momentum flux. Contour drawn is the zero-meter contour for land elevation. (Note: negligible inundation seen from this source.)

Tampa, FL
East Breaks Submarine Landslide
Maximum Inundation Depth on Grid B

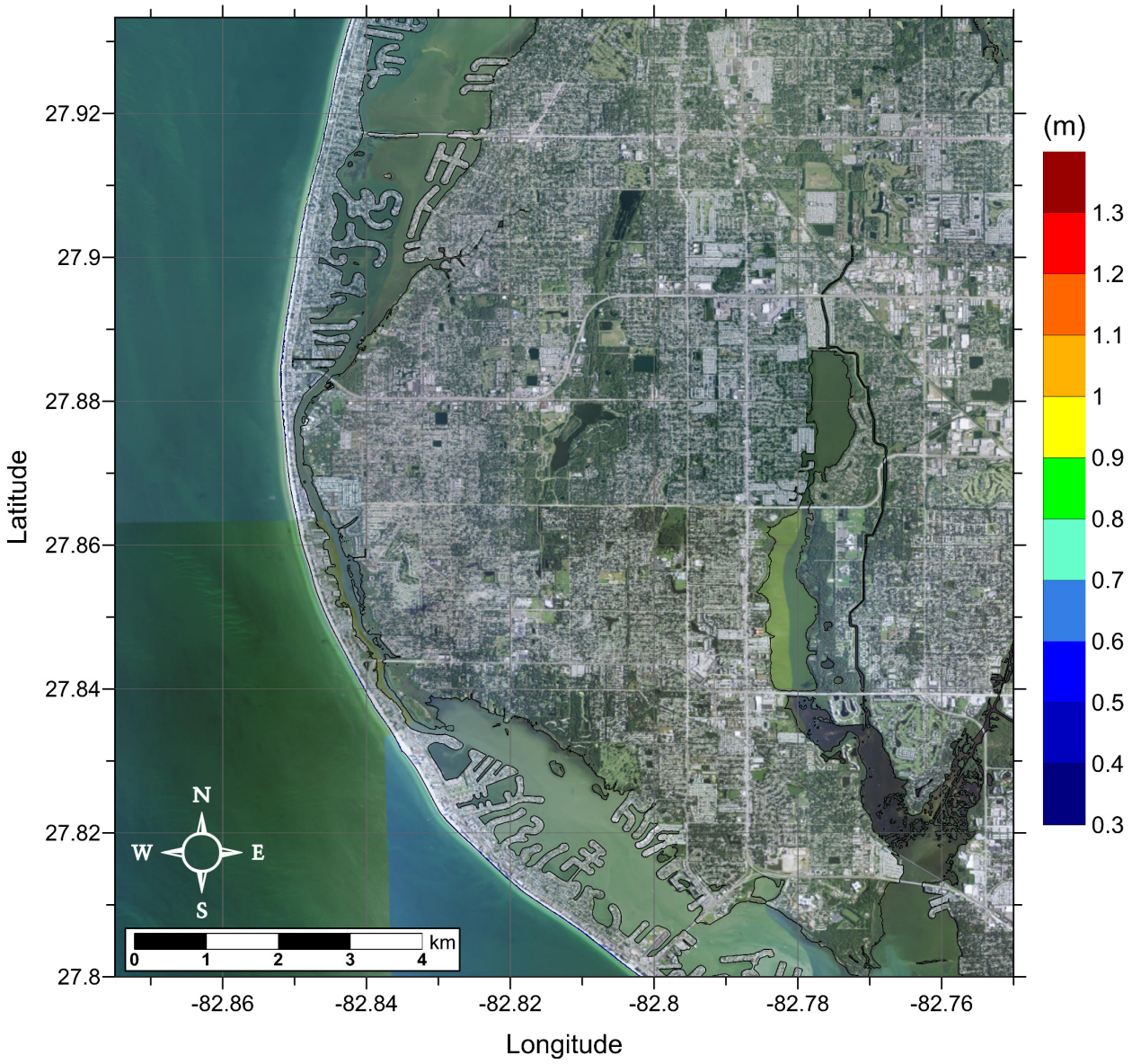

Figure 119: Maximum inundation depth (m) caused by the East Breaks submarine landslide in northern Tampa, FL. Contour drawn is the zero-meter contour for land elevation. (Note: negligible inundation seen from this source.)

Tampa, FL
East Breaks Submarine Landslide
Maximum Momentum Flux on Grid B

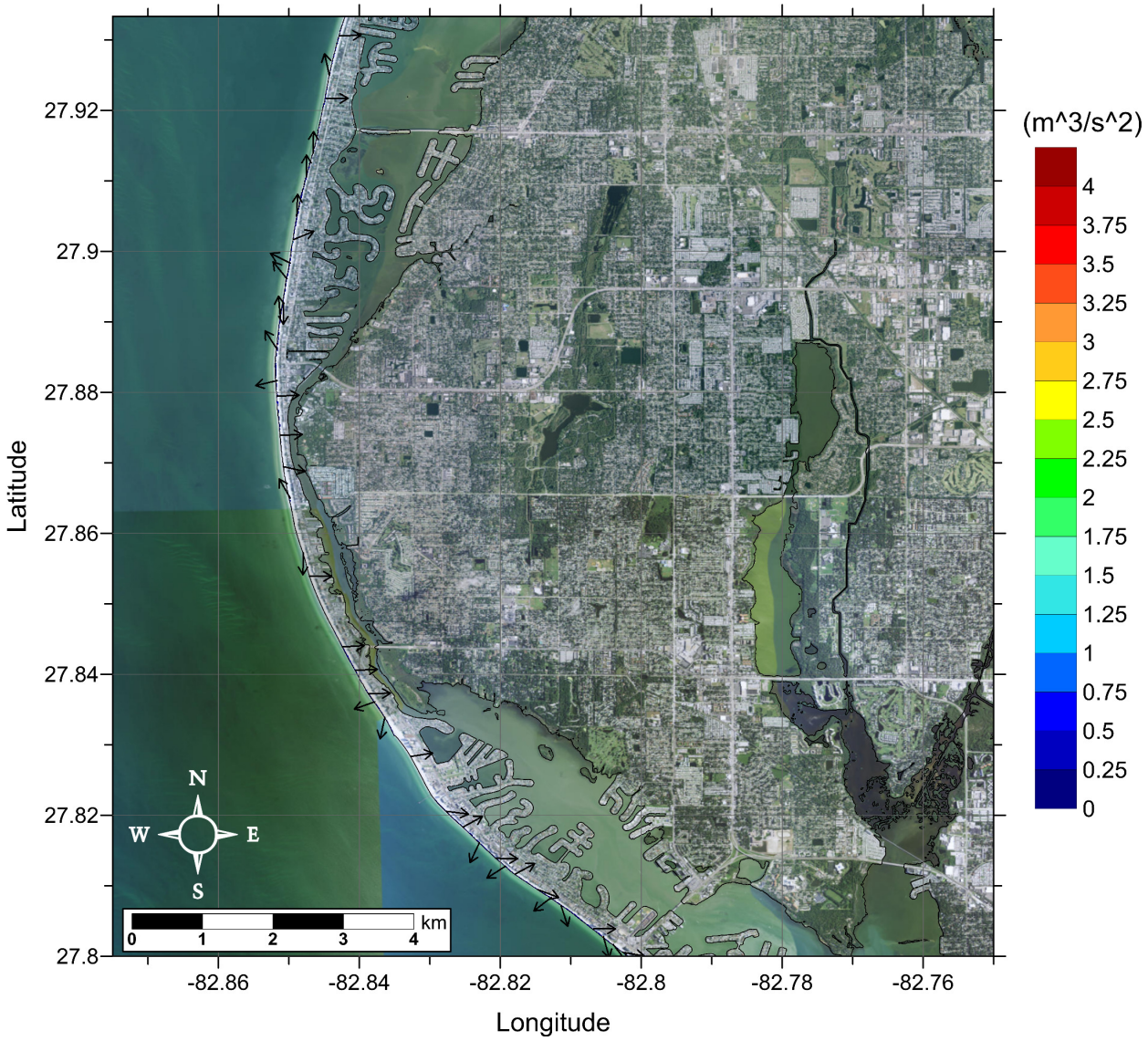

Figure 120: Maximum momentum flux (m^3/s^2) caused by the East Breaks submarine landslide in northern Tampa, FL. Arrows represent direction of maximum momentum flux. Contour drawn is the zero-meter contour for land elevation. (Note: negligible inundation seen from this source.)

Tampa, FL
Probabilistic Submarine Landslide A (PSL-A)
Maximum Inundation Depth on Grid A

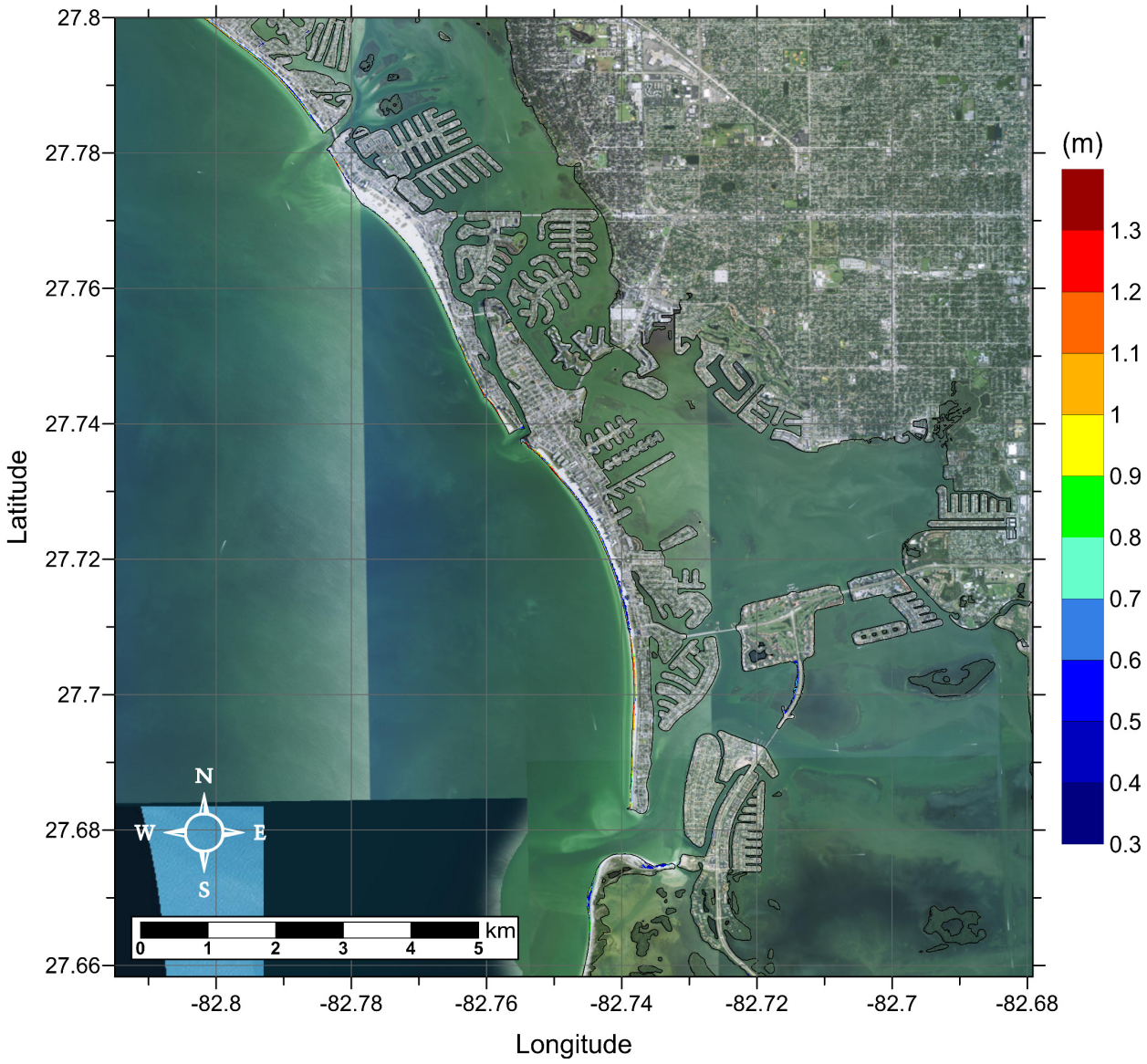

Figure 121: Maximum inundation depth (m) caused by the Probabilistic Submarine Landslide A in southern Tampa, FL. Contour drawn is the zero-meter contour for land elevation. (Note: negligible inundation seen from this source.)

Tampa, FL
Probabilistic Submarine Landslide A (PSL-A)
Maximum Momentum Flux on Grid A

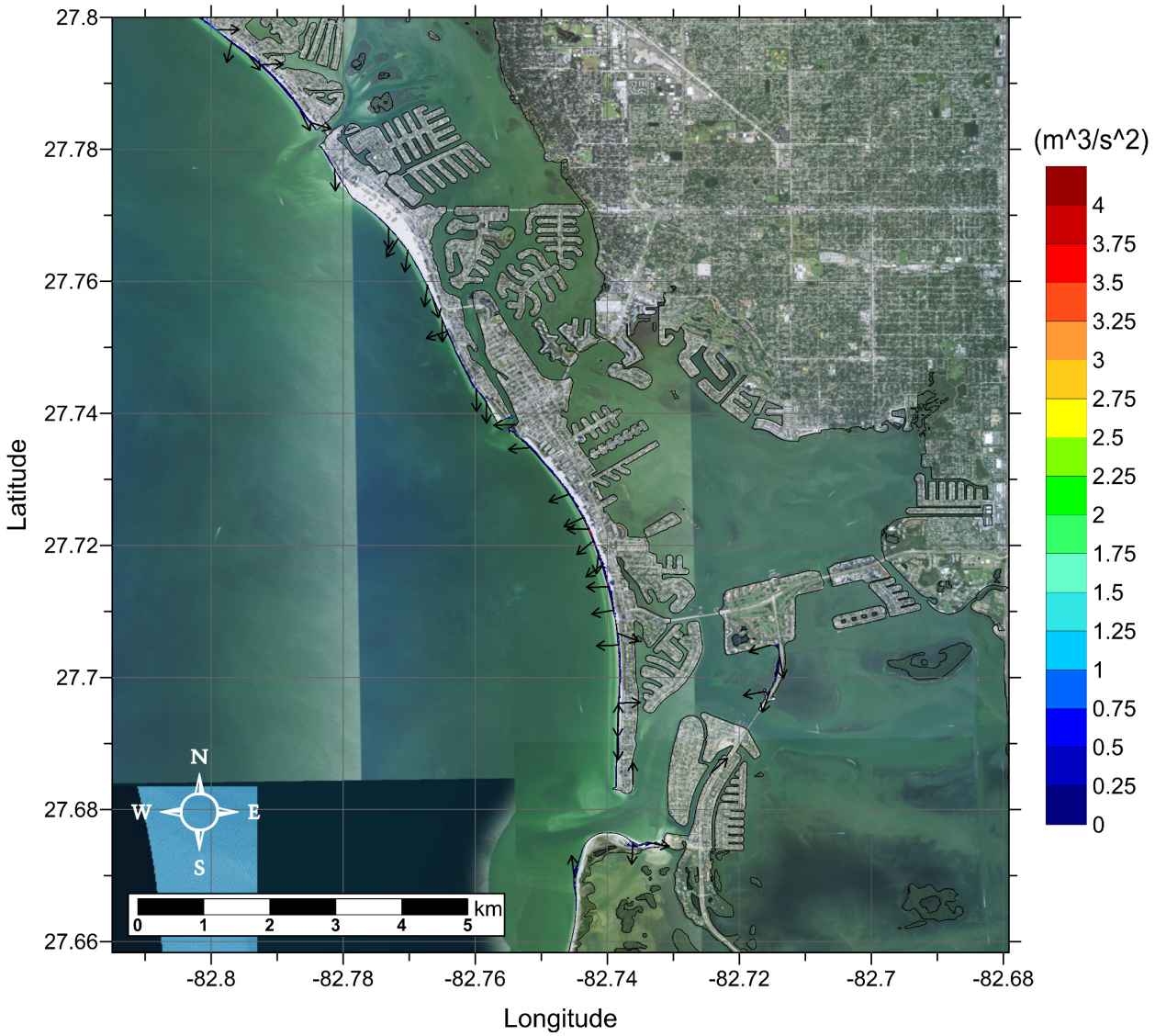

Figure 122: Maximum momentum flux (m^3/s^2) caused by the Probabilistic Submarine Landslide A in southern Tampa, FL. Contour drawn is the zero-meter contour for land elevation. (Note: negligible inundation seen from this source.)

Tampa, FL
Probabilistic Submarine Landslide A (PSL-A)
Maximum Inundation Depth on Grid B

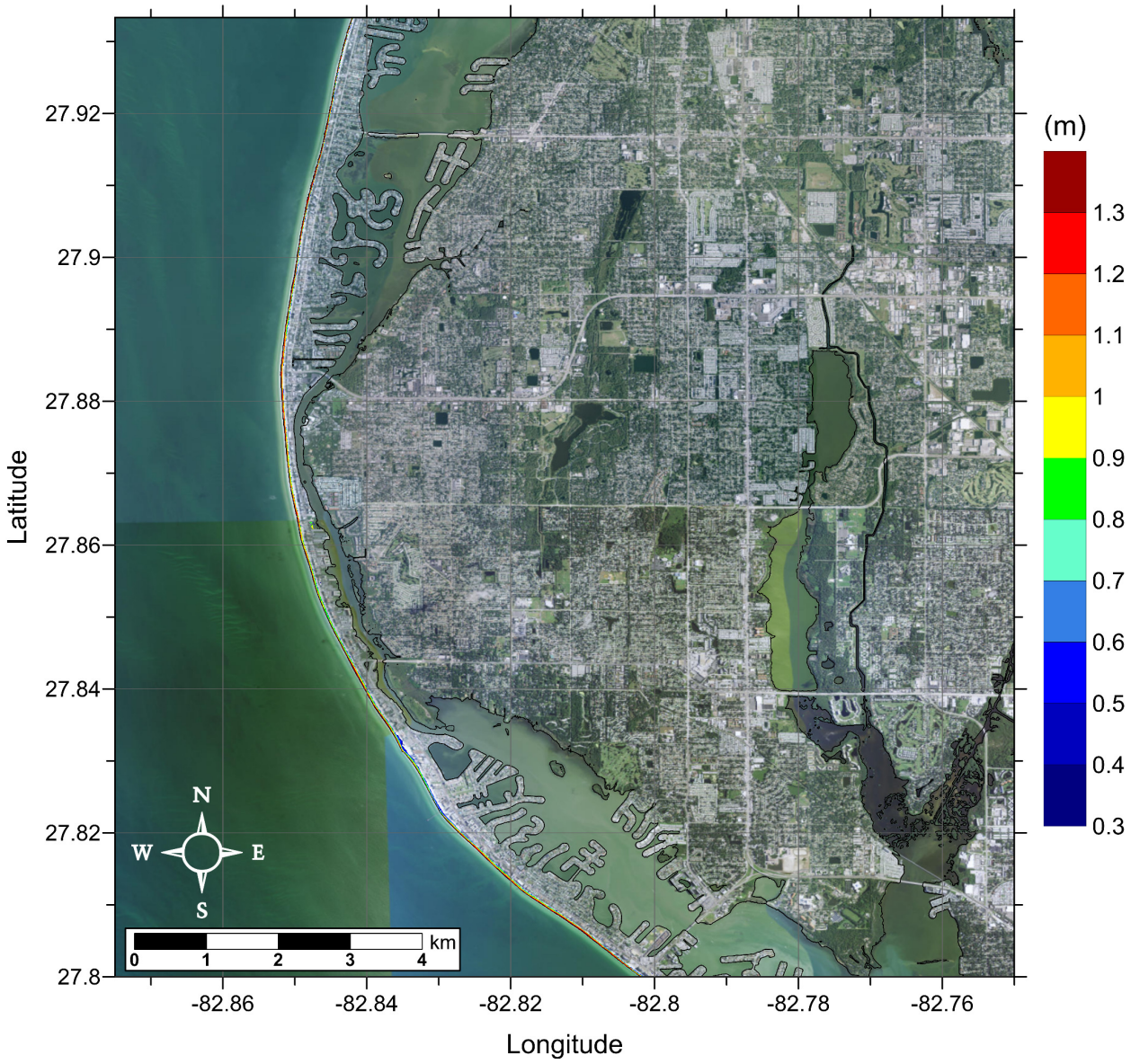

Figure 123: Maximum inundation depth (m) caused by the Probabilistic Submarine Landslide A in northern Tampa, FL. Contour drawn is the zero-meter contour for land elevation.

Tampa, FL
Probabilistic Submarine Landslide A (PSL-A)
Maximum Momentum Flux on Grid B

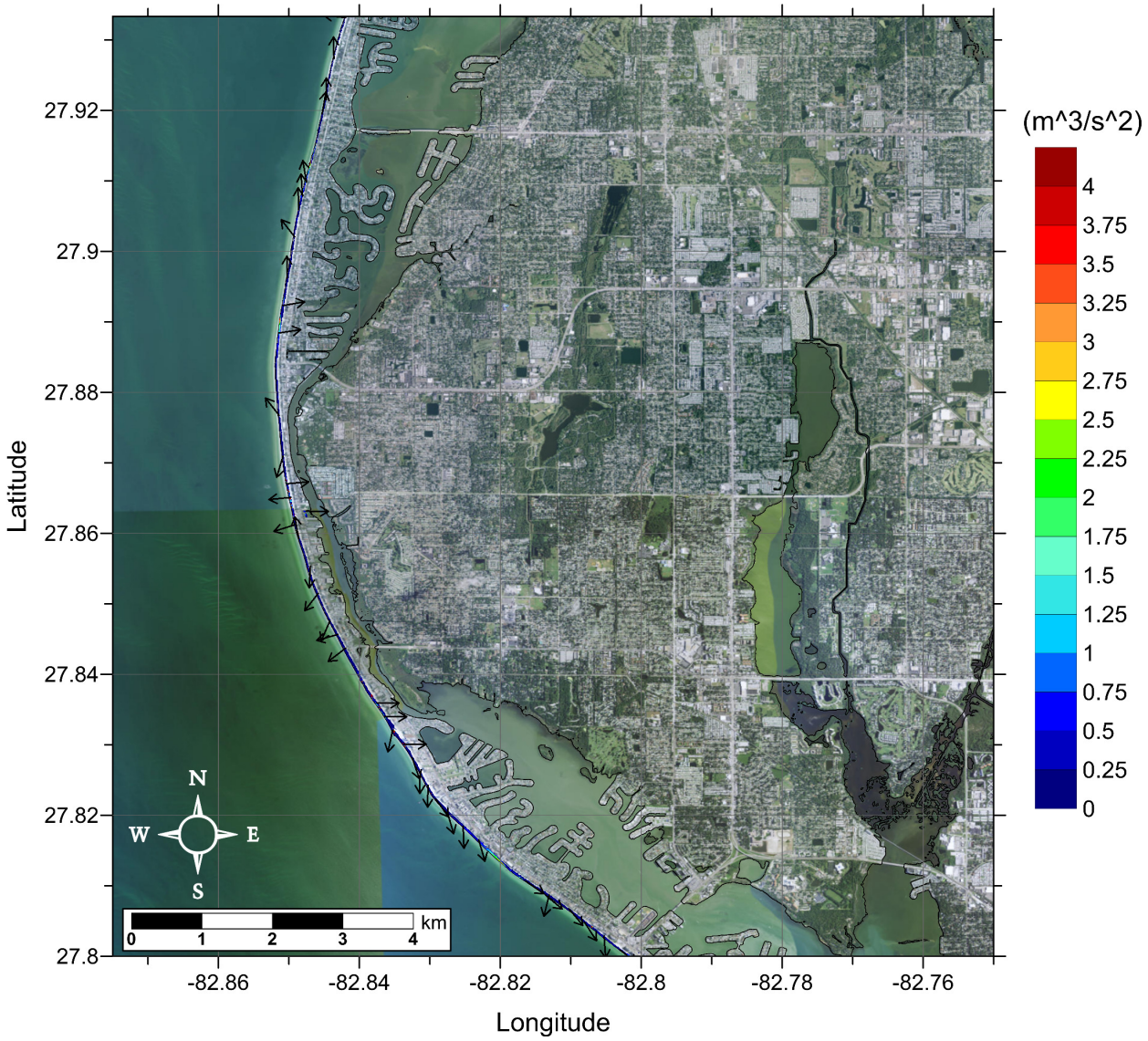

Figure 124: Maximum momentum flux (m^3/s^2) caused by the Probabilistic Submarine Landslide A in northern Tampa, FL. Contour drawn is the zero-meter contour for land elevation.

Tampa, FL
Probabilistic Submarine Landslide B1 (PSL-B1)
Maximum Inundation Depth on Grid A

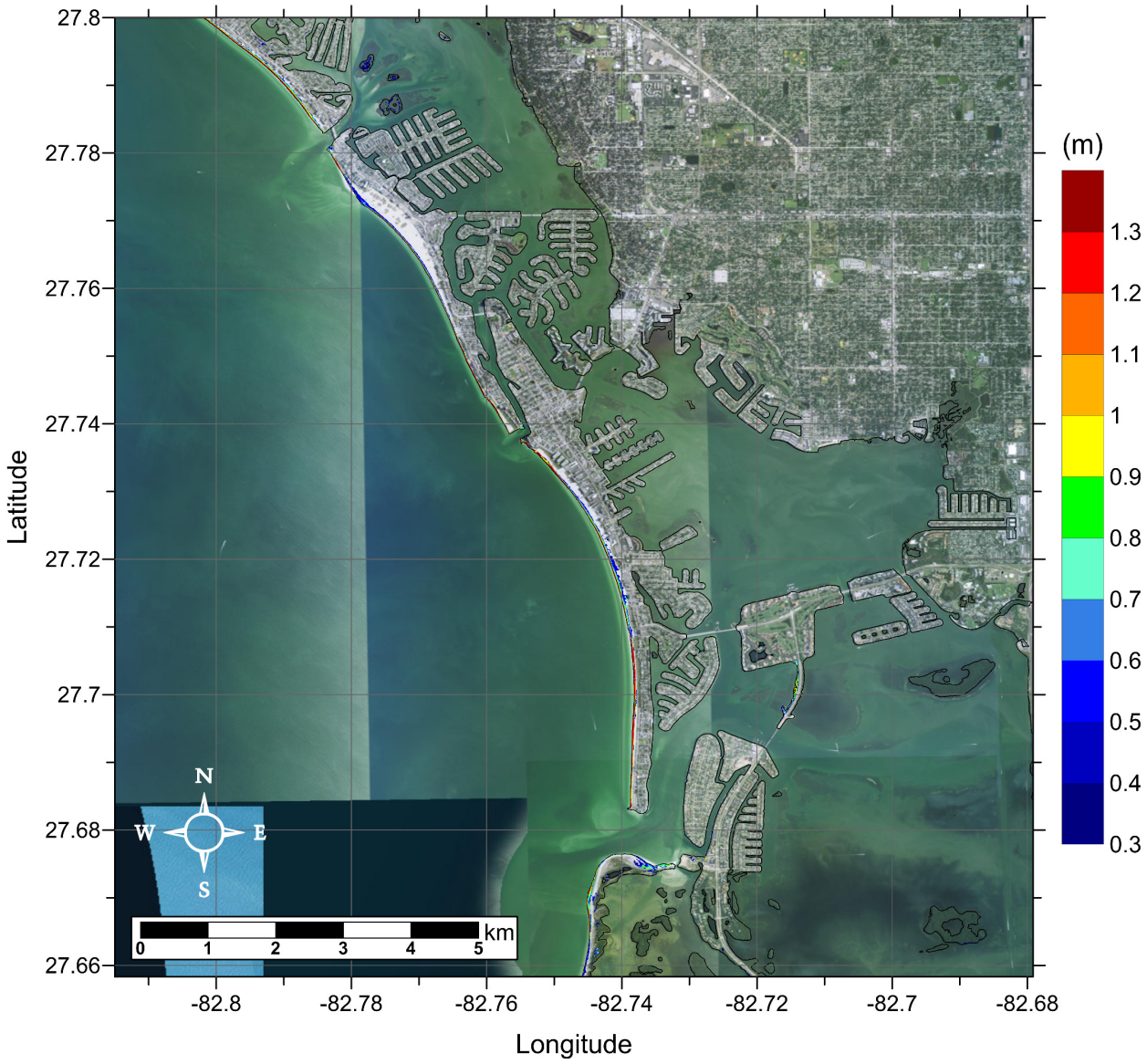

Figure 125: Maximum inundation depth (m) caused by the Probabilistic Submarine Landslide B1 in southern Tampa, FL. Contour drawn is the zero-meter contour for land elevation.

Tampa, FL
Probabilistic Submarine Landslide B1 (PSL-B1)
Maximum Momentum Flux on Grid A

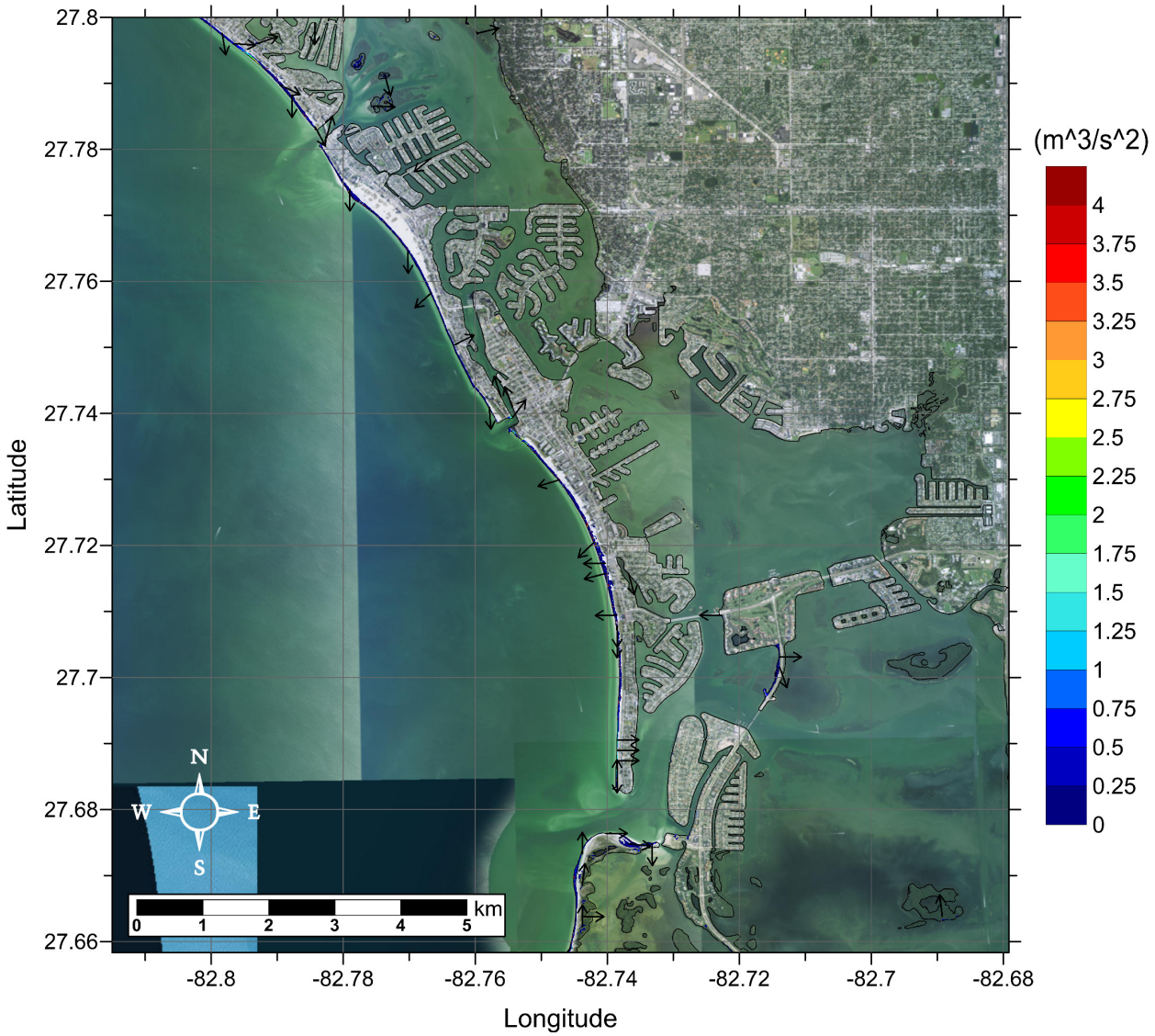

Figure 126: Maximum momentum flux (m^3/s^2) caused by the Probabilistic Submarine Landslide B1 in southern Tampa, FL. Contour drawn is the zero-meter contour for land elevation.

Tampa, FL
Probabilistic Submarine Landslide B1 (PSL-B1)
Maximum Inundation Depth on Grid B

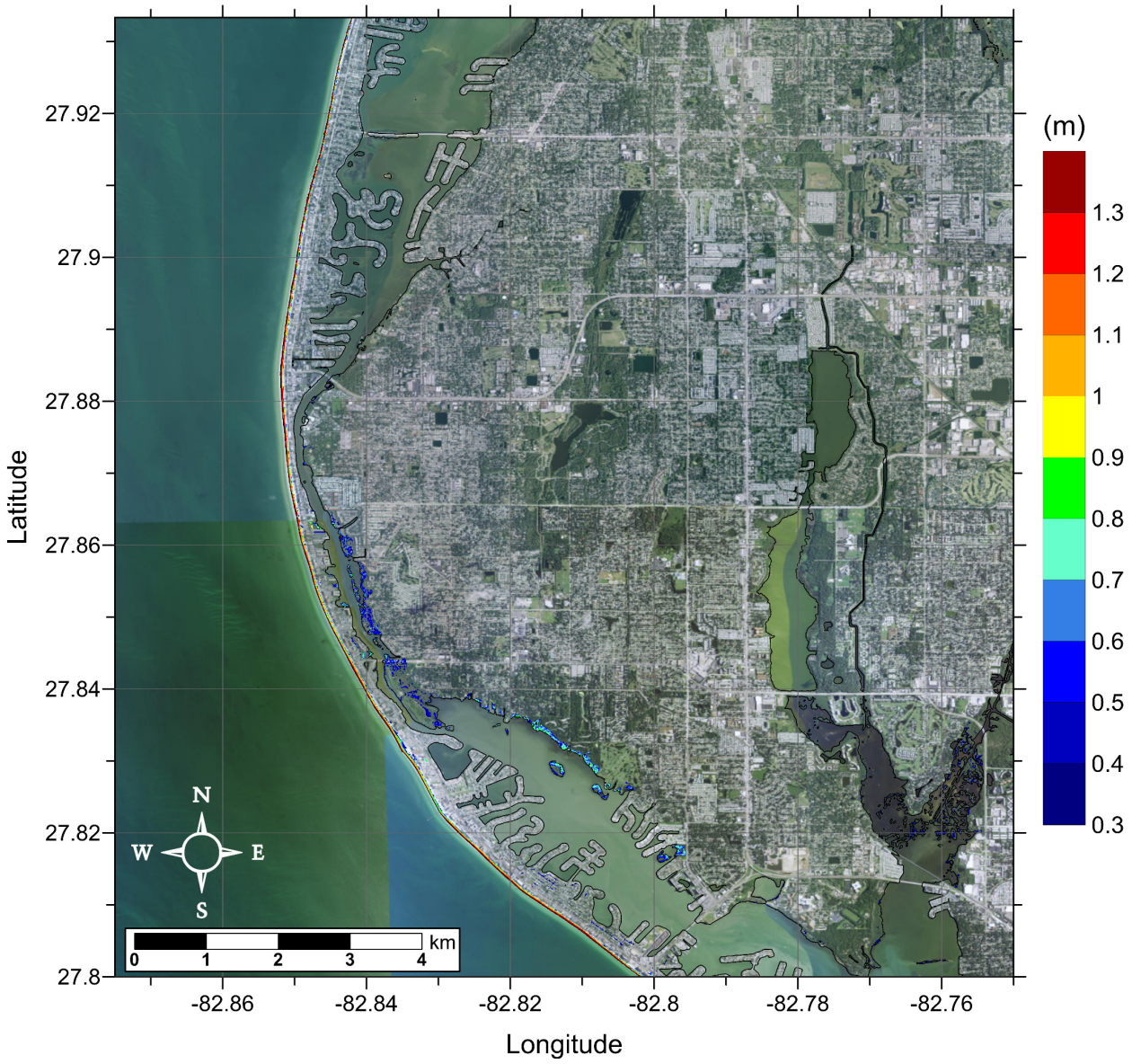

Figure 127: Maximum inundation depth (m) caused by the Probabilistic Submarine Landslide B1 in northern Tampa, FL. Contour drawn is the zero-meter contour for land elevation.

Tampa, FL
Probabilistic Submarine Landslide B1 (PSL-B1)
Maximum Momentum Flux on Grid B

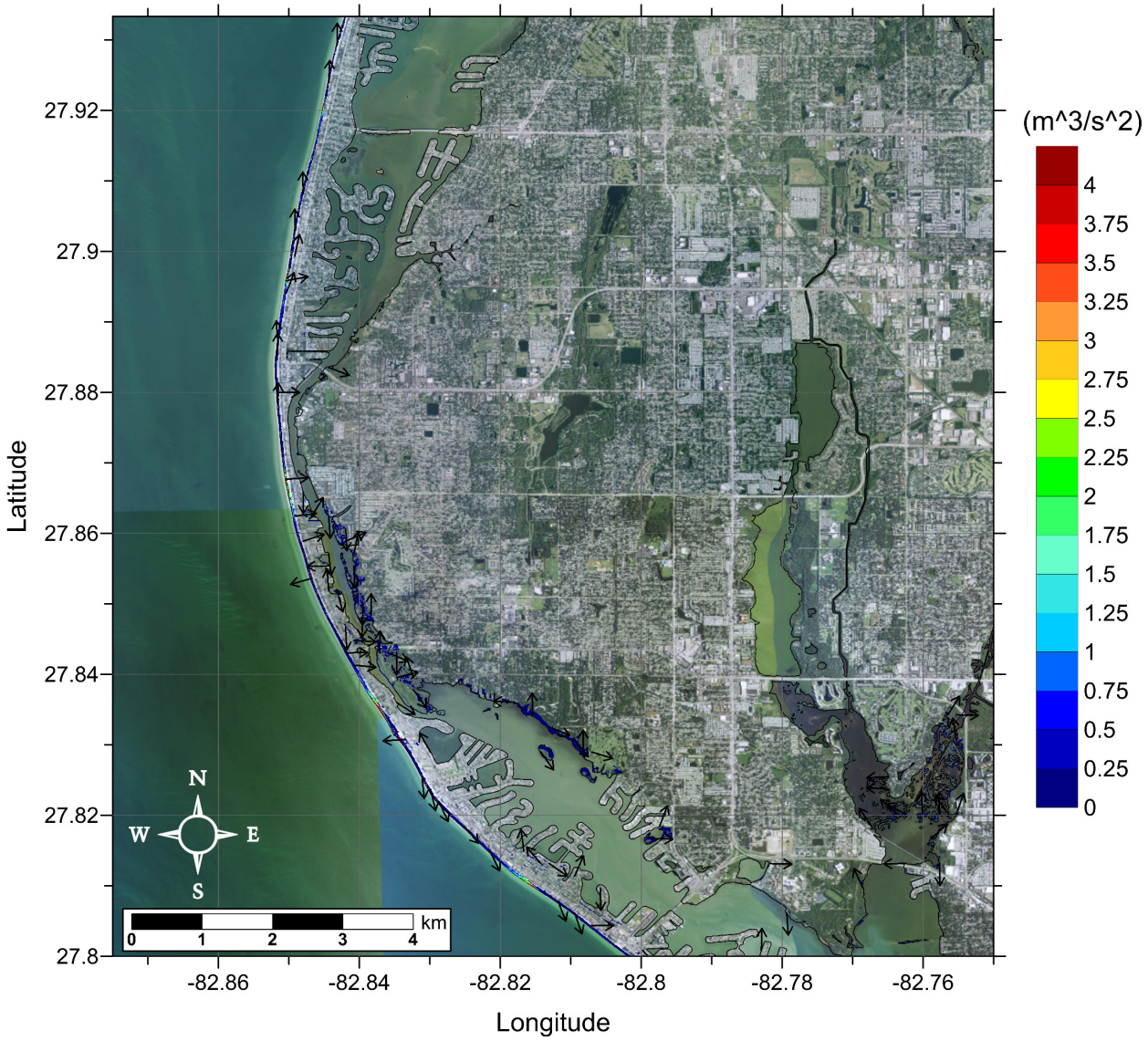

Figure 128: Maximum momentum flux (m^3/s^2) caused by the Probabilistic Submarine Landslide B1 in northern Tampa, FL. Contour drawn is the zero-meter contour for land elevation.

Tampa, FL
Probabilistic Submarine Landslide B2 (PSL-B2)
Maximum Inundation Depth on Grid A

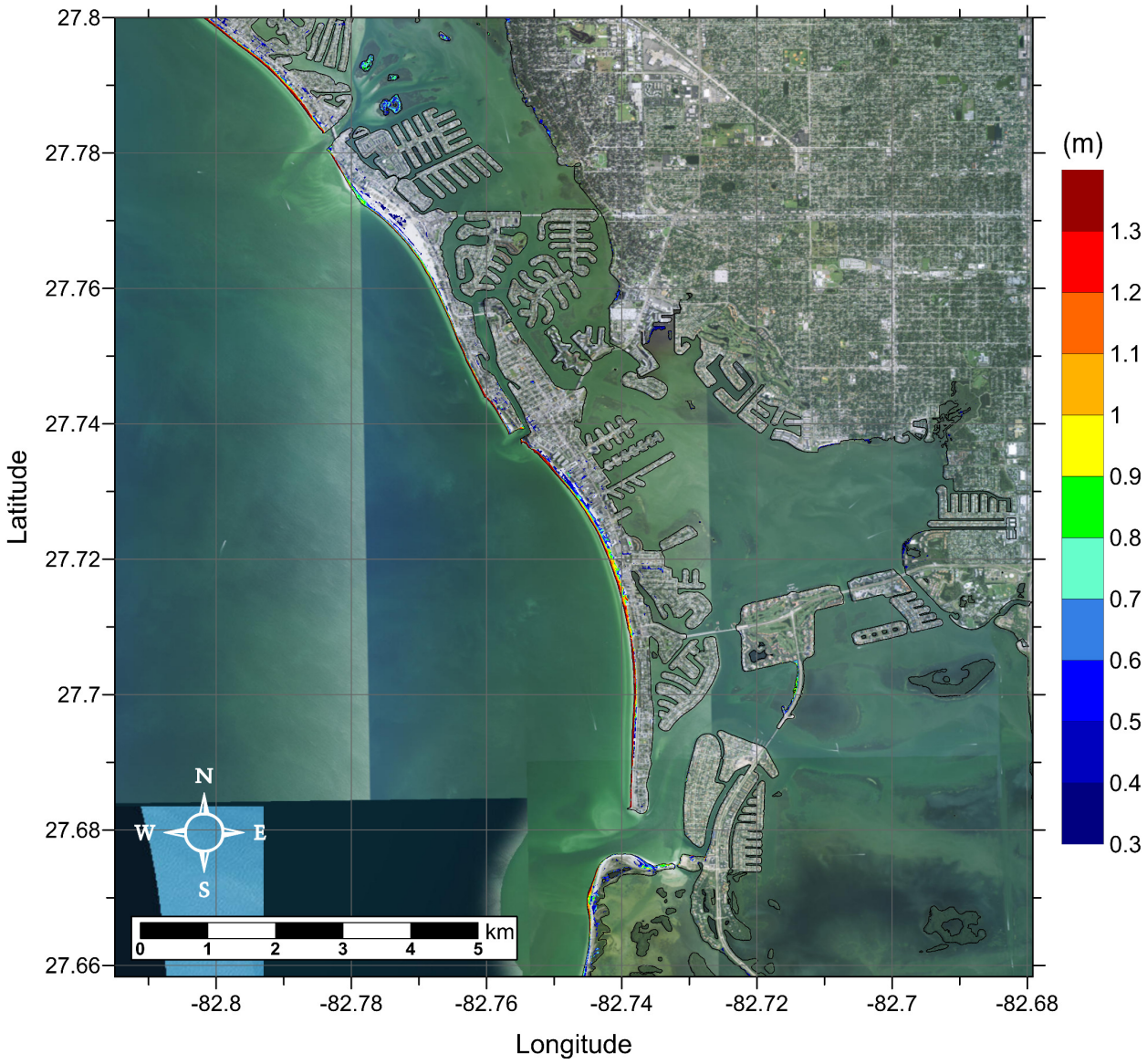

Figure 129: Maximum inundation depth (m) caused by the Probabilistic Submarine Landslide B2 in southern Tampa, FL. Contour drawn is the zero-meter contour for land elevation.

Tampa, FL
Probabilistic Submarine Landslide B2 (PSL-B2)
Maximum Momentum Flux on Grid A

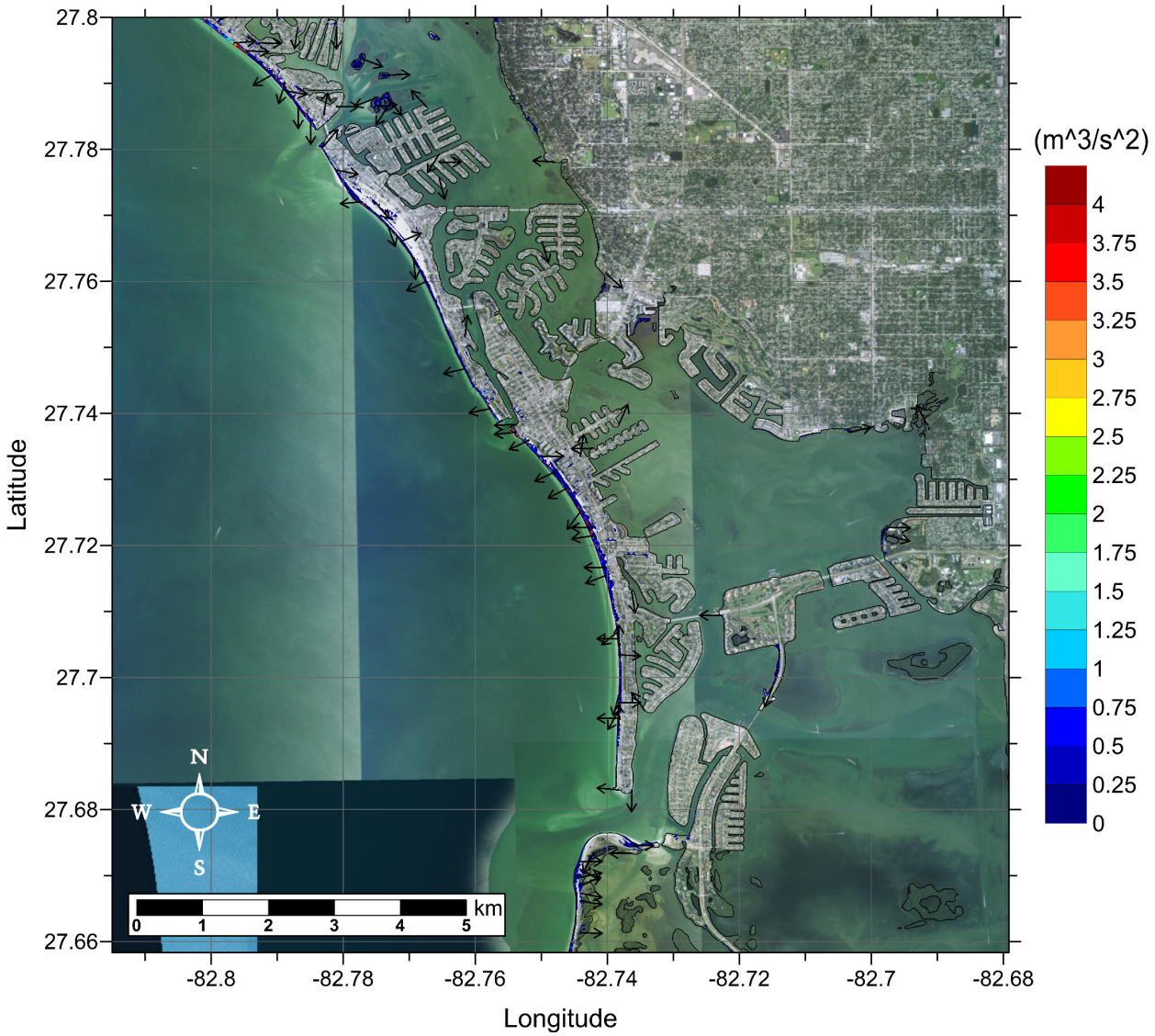

Figure 130: Maximum momentum flux (m^3/s^2) caused by the Probabilistic Submarine Landslide B2 in southern Tampa, FL. Contour drawn is the zero-meter contour for land elevation.

Tampa, FL
Probabilistic Submarine Landslide B2 (PSL-B2)
Maximum Inundation Depth on Grid B

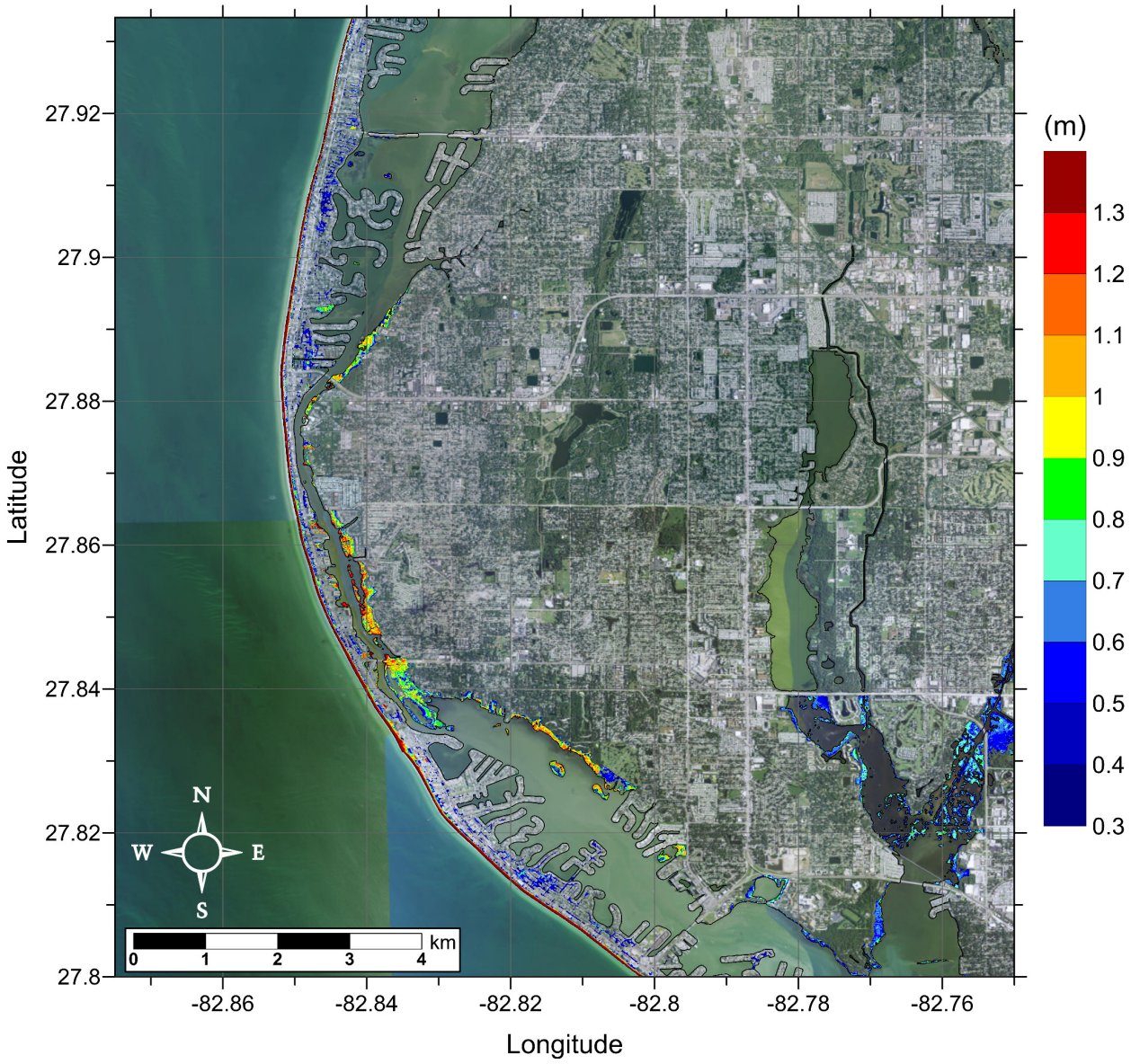

Figure 131: Maximum inundation depth (m) caused by the Probabilistic Submarine Landslide B2 in northern Tampa, FL. Contour drawn is the zero-meter contour for land elevation.

Tampa, FL
Probabilistic Submarine Landslide B2 (PSL-B2)
Maximum Momentum Flux on Grid B

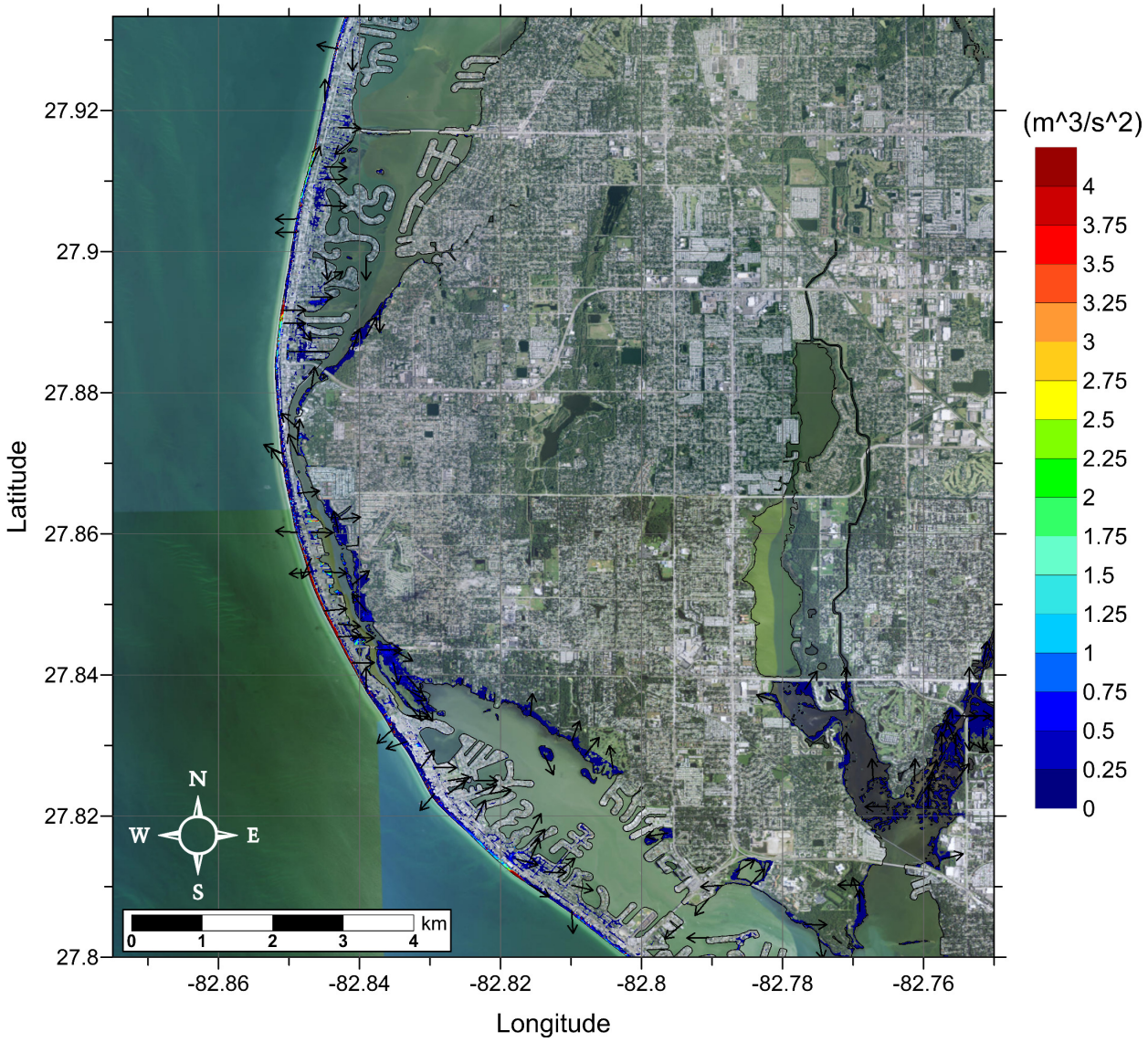

Figure 132: Maximum momentum flux (m^3/s^2) caused by the Probabilistic Submarine Landslide B2 in northern Tampa, FL. Contour drawn is the zero-meter contour for land elevation.

Tampa, FL
Mississippi Canyon Submarine Landslide
Maximum Inundation Depth on Grid A

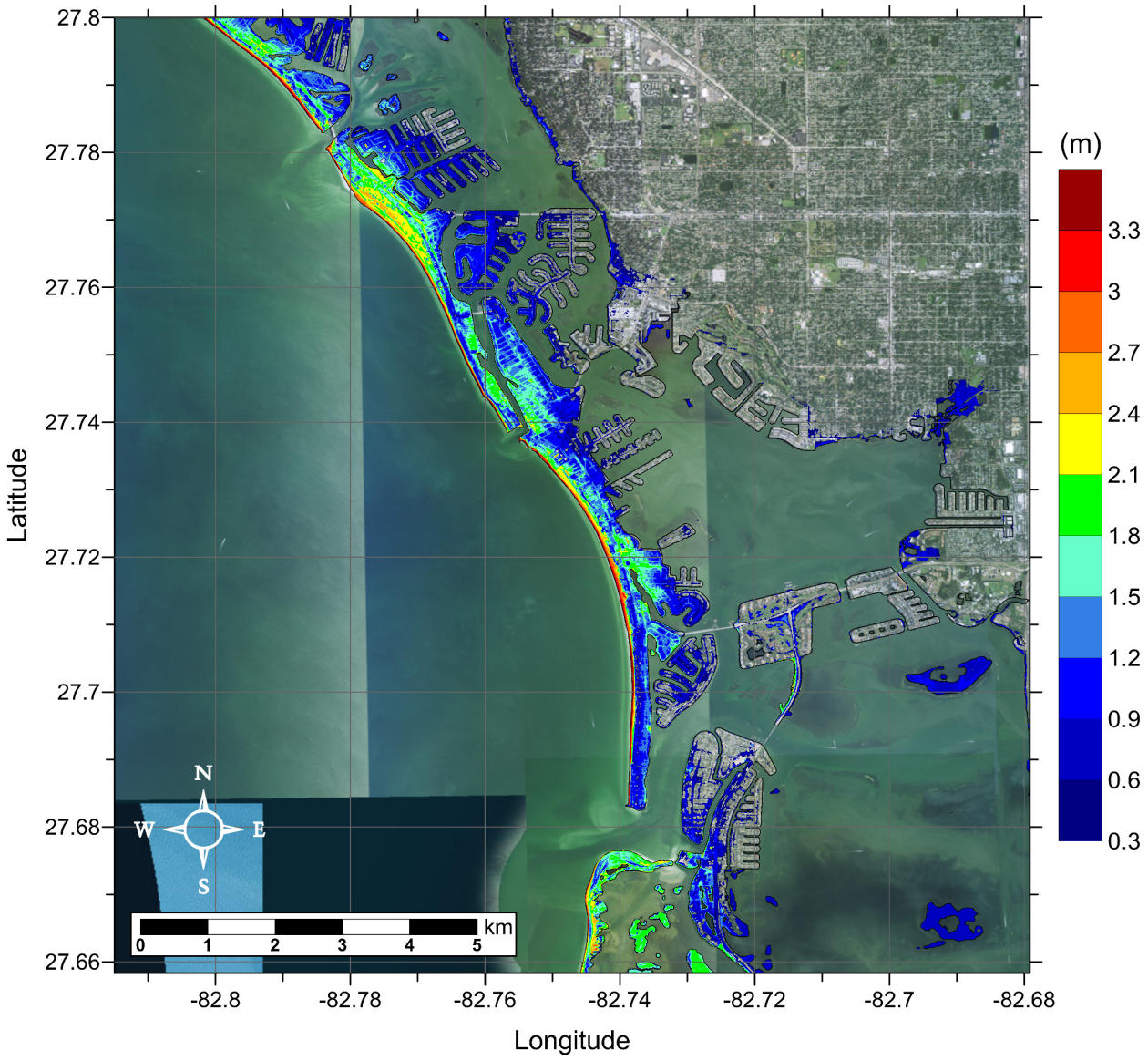

Figure 133: Maximum inundation depth (m) caused by the Mississippi Canyon submarine landslide in southern Tampa, FL. Contour drawn is the zero-meter contour for land elevation.

Tampa, FL
Mississippi Canyon Submarine Landslide
Maximum Momentum Flux on Grid A

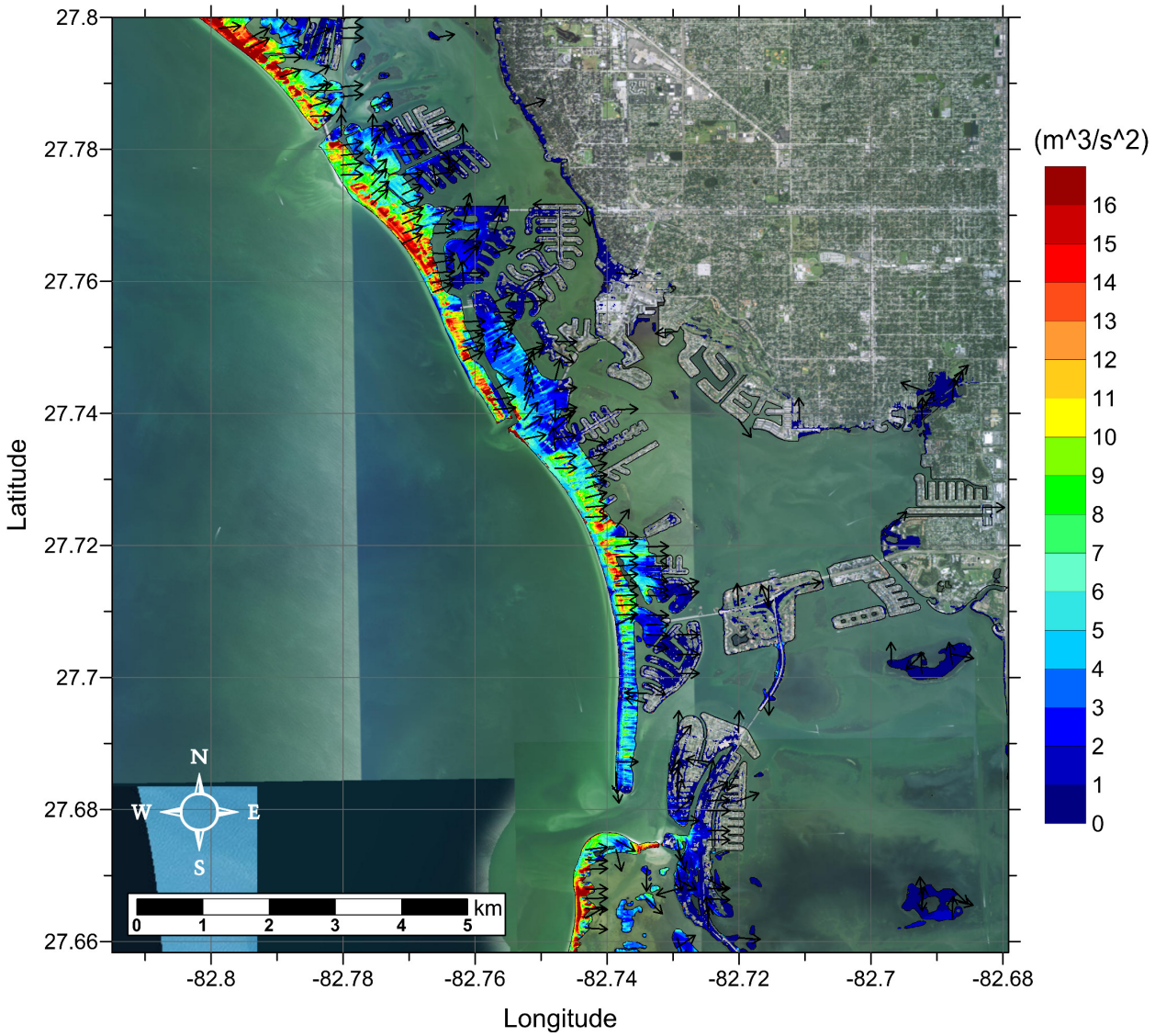

Figure 134: Maximum momentum flux (m^3/s^2) caused by the Mississippi Canyon submarine landslide in southern Tampa, FL. Arrows represent direction of maximum momentum flux. Contour drawn is the zero-meter contour for land elevation.

Tampa, FL
Mississippi Canyon Submarine Landslide
Maximum Inundation Depth on Grid B

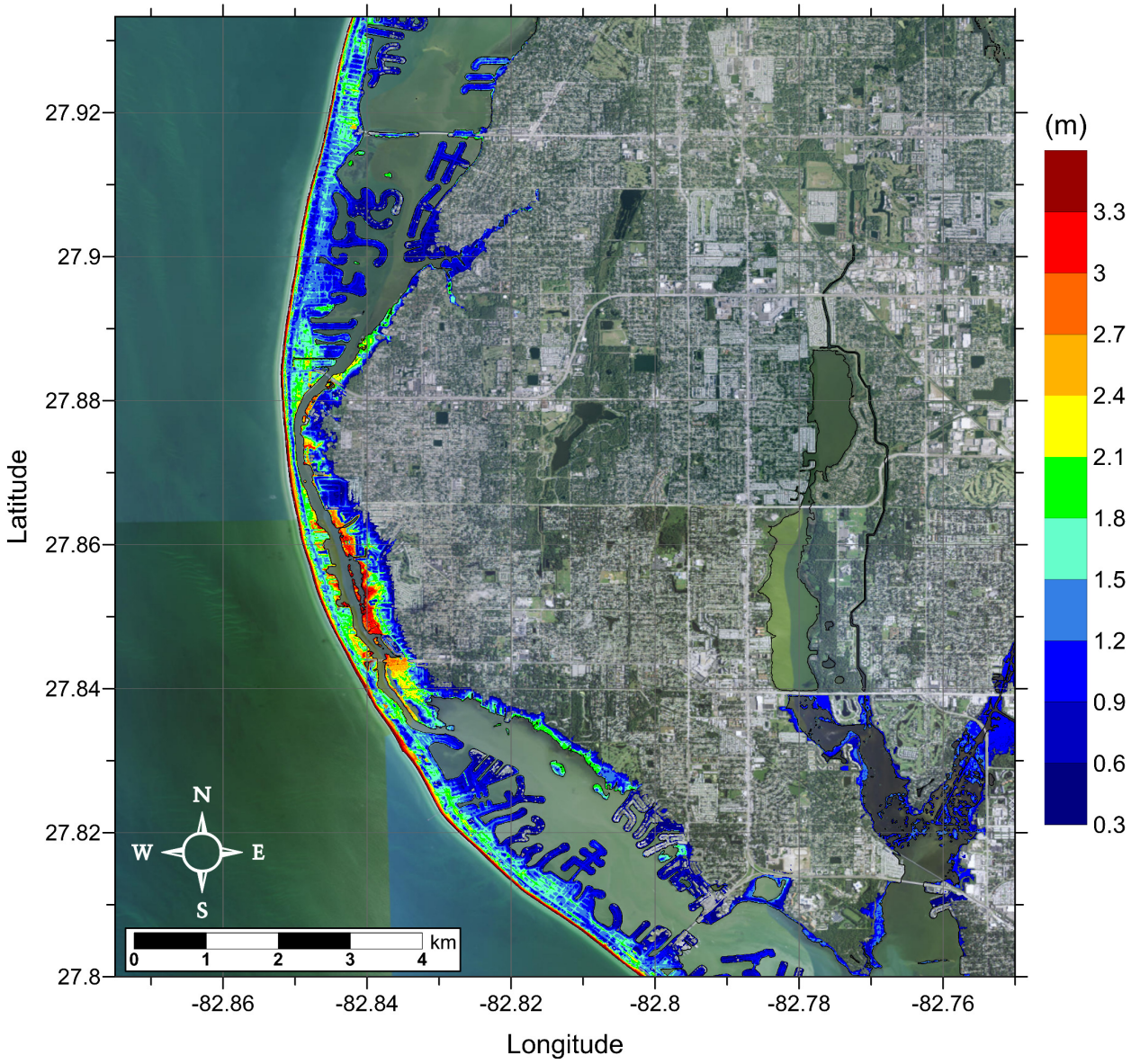

Figure 135: Maximum inundation depth (m) caused by the Mississippi Canyon submarine landslide in northern Tampa, FL. Contour drawn is the zero-meter contour for land elevation.

Tampa, FL
Mississippi Canyon Submarine Landslide
Maximum Momentum Flux on Grid B

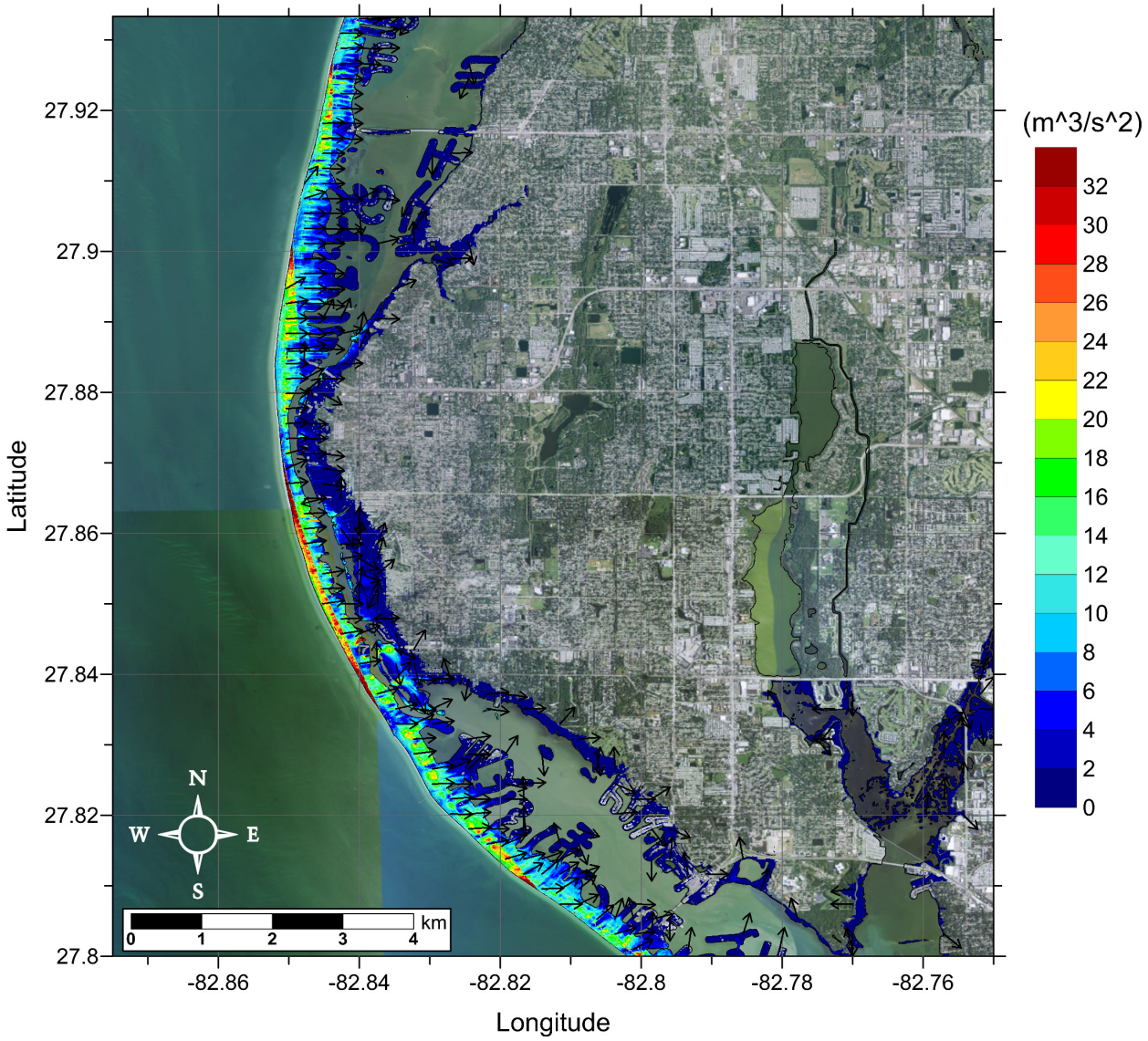

Figure 136: Maximum momentum flux (m^3/s^2) caused by the Mississippi Canyon submarine landslide in northern Tampa, FL. Arrows represent direction of maximum momentum flux. Contour drawn is the zero-meter contour for land elevation.

Tampa, FL
Probabilistic Submarine Landslide C (PSL-C)
Maximum Inundation Depth on Grid A

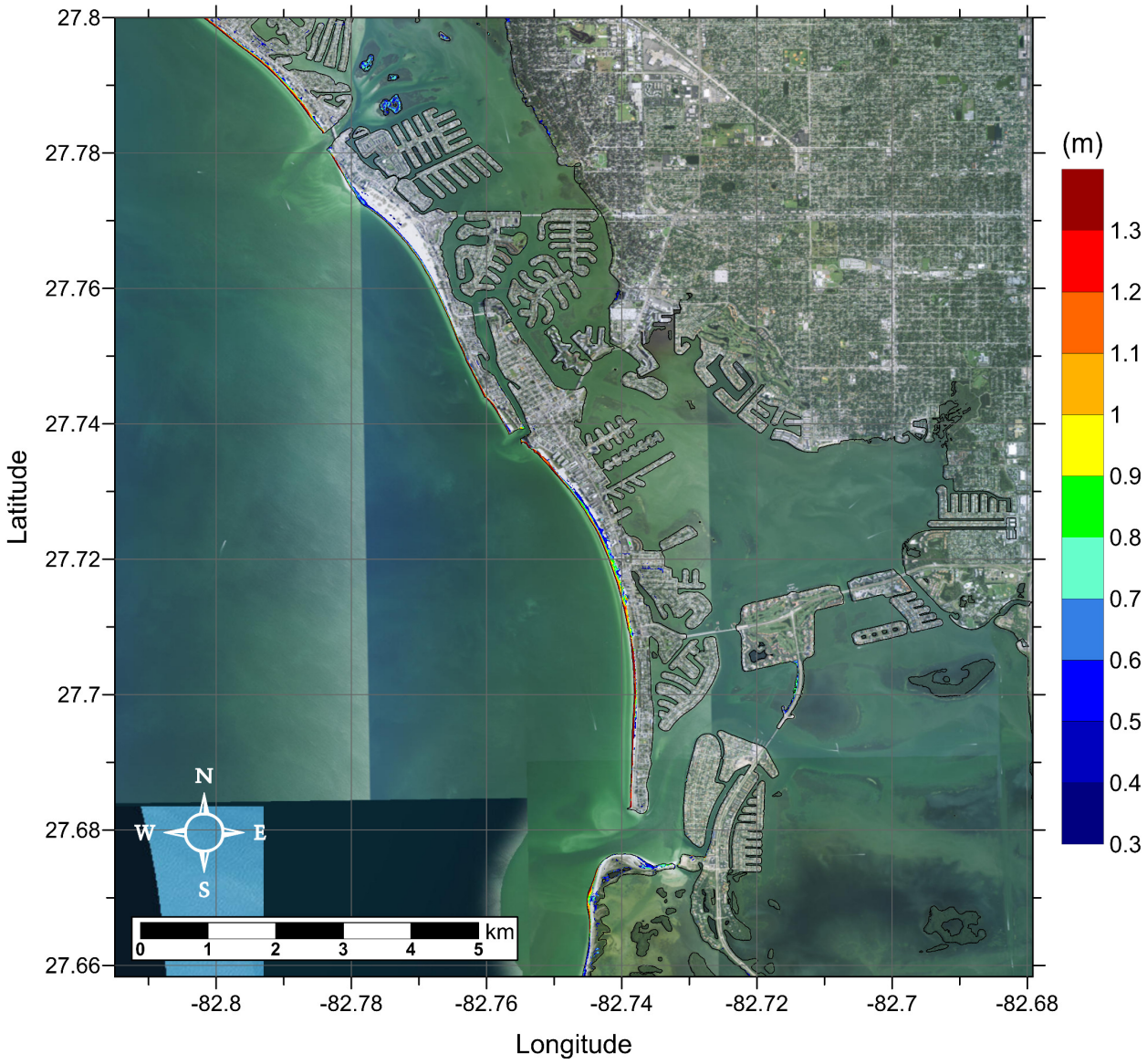

Figure 137: Maximum inundation depth (m) caused by the Probabilistic Submarine Landslide C in southern Tampa, FL. Contour drawn is the zero-meter contour for land elevation.

Tampa, FL
Probabilistic Submarine Landslide C (PSL-C)
Maximum Momentum Flux on Grid A

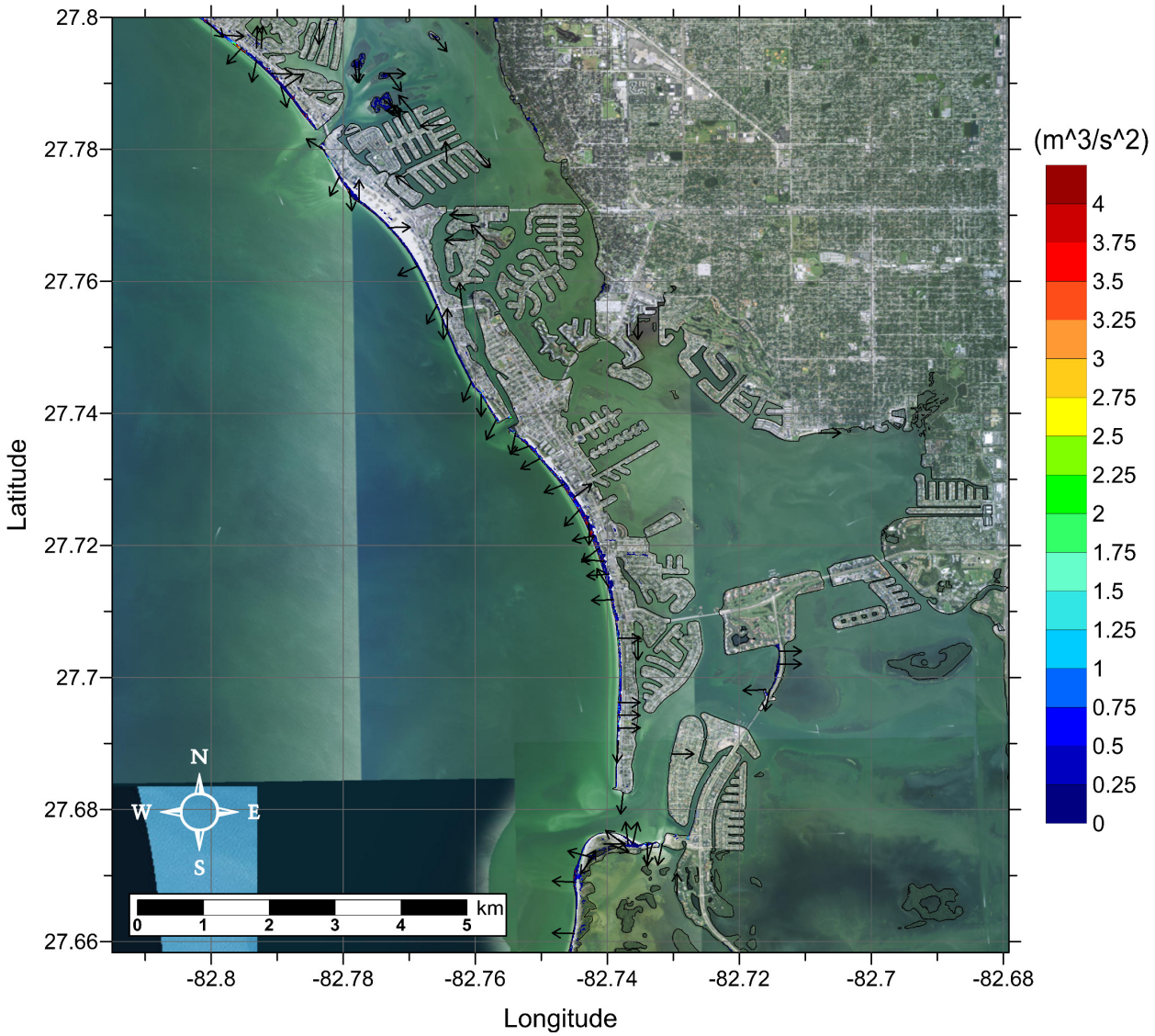

Figure 138: Maximum momentum flux (m^3/s^2) caused by the Probabilistic Submarine Landslide C in southern Tampa, FL. Contour drawn is the zero-meter contour for land elevation.

Tampa, FL
Probabilistic Submarine Landslide C (PSL-C)
Maximum Inundation Depth on Grid B

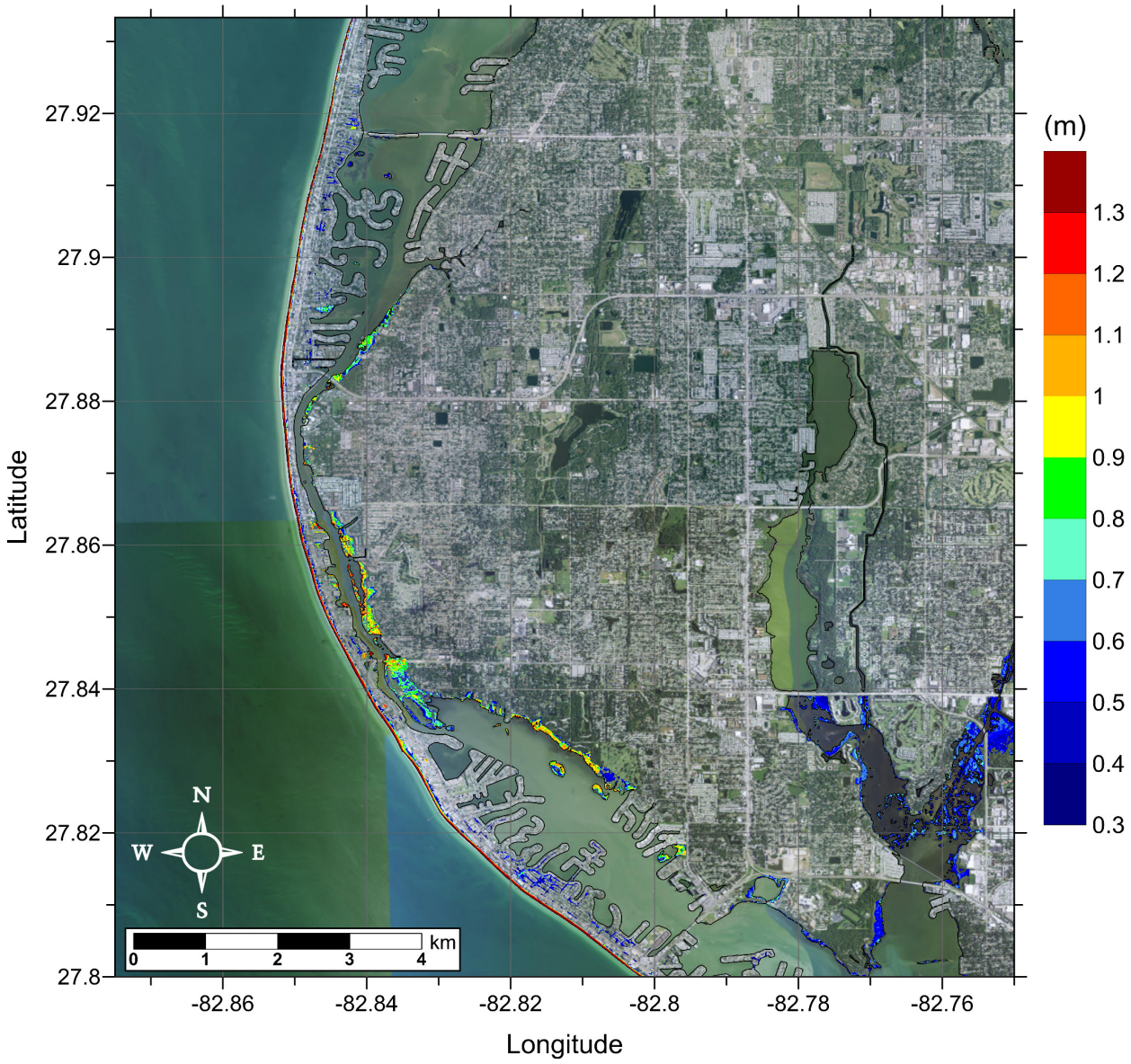

Figure 139: Maximum inundation depth (m) caused by the Probabilistic Submarine Landslide C in northern Tampa, FL. Contour drawn is the zero-meter contour for land elevation.

Tampa, FL
Probabilistic Submarine Landslide C (PSL-C)
Maximum Momentum Flux on Grid B

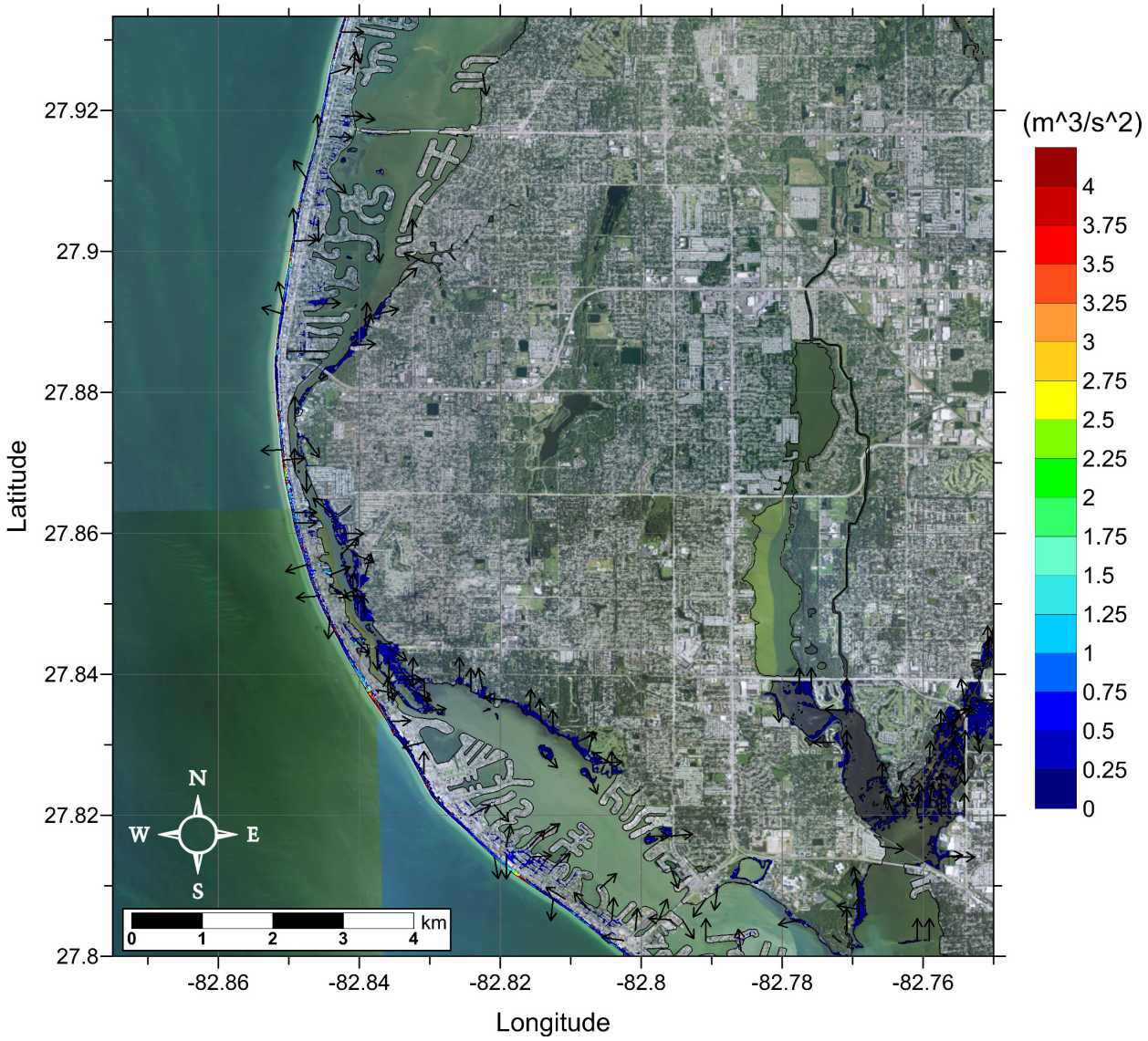

Figure 140: Maximum momentum flux (m^3/s^2) caused by the Probabilistic Submarine Landslide C in northern Tampa, FL. Contour drawn is the zero-meter contour for land elevation.

Tampa, FL
West Florida Submarine Landslide
Maximum Inundation Depth on Grid A

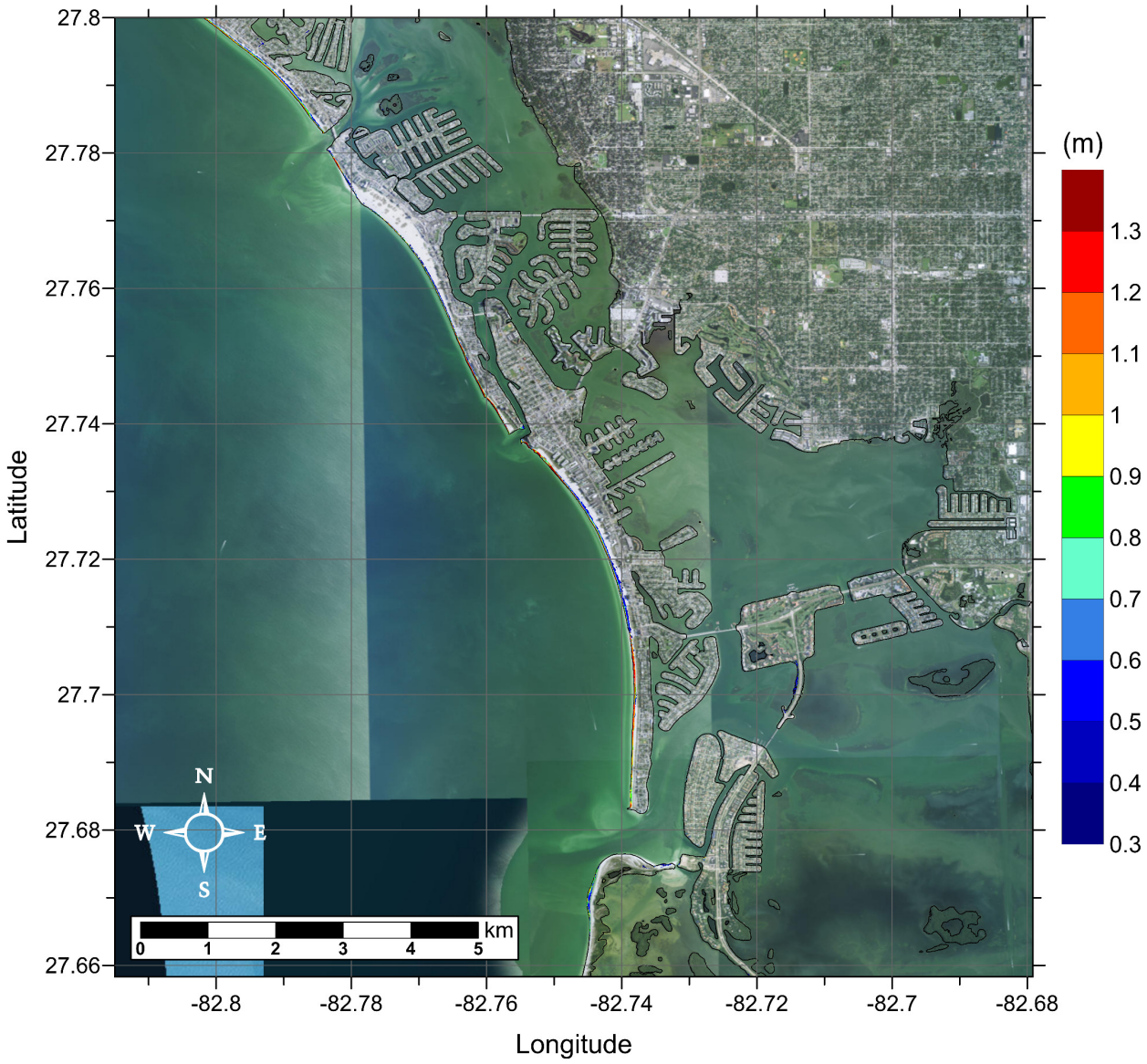

Figure 141: Maximum inundation depth (m) caused by the West Florida submarine landslide in southern Tampa, FL. Contour drawn is the zero-meter contour for land elevation.

Tampa, FL
West Florida Submarine Landslide
Maximum Momentum Flux on Grid A

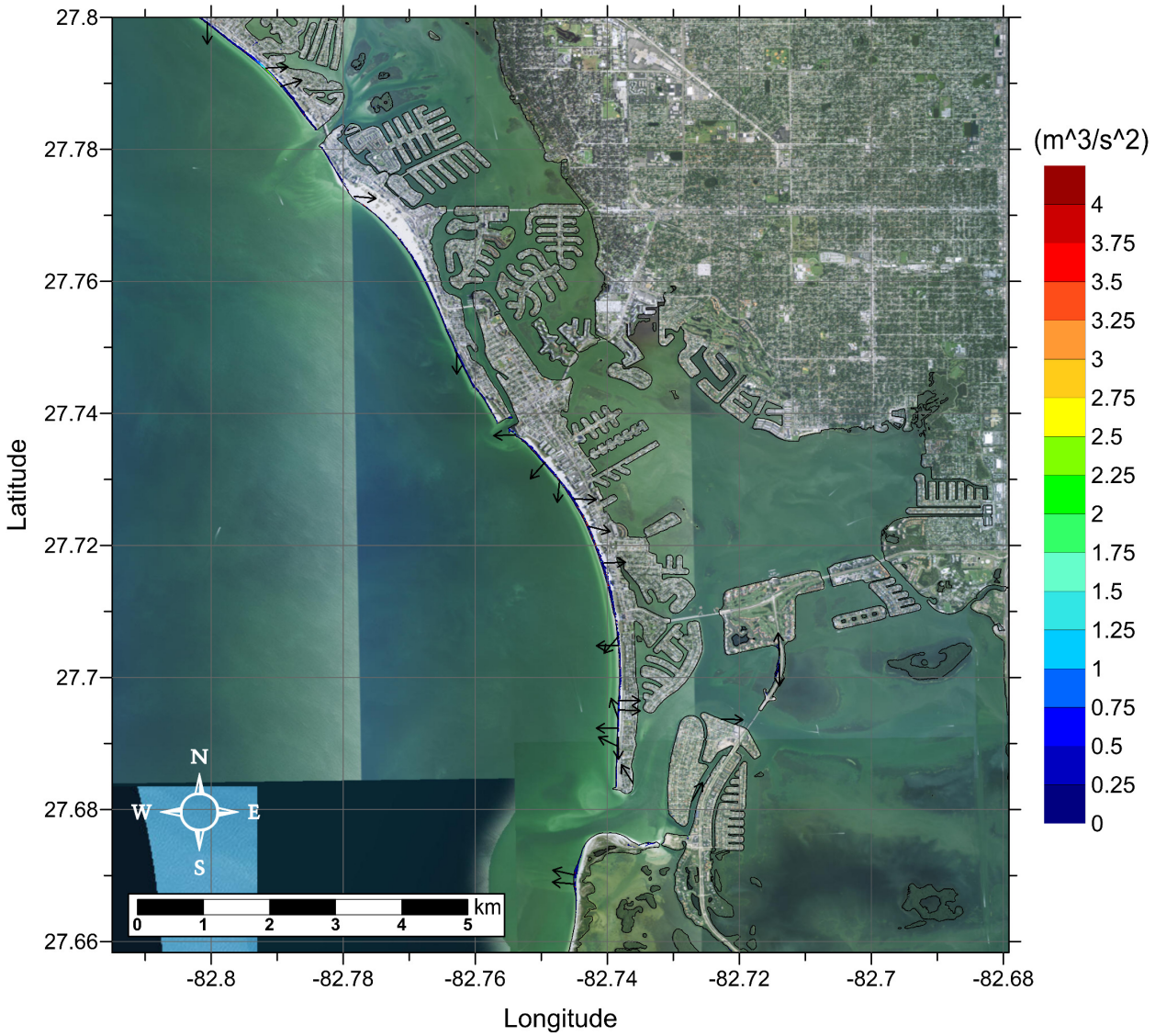

Figure 142: Maximum momentum flux (m^3/s^2) caused by the West Florida submarine landslide in southern Tampa, FL. Arrows represent direction of maximum momentum flux. Contour drawn is the zero-meter contour for land elevation.

Tampa, FL
West Florida Submarine Landslide)
Maximum Inundation Depth on Grid B

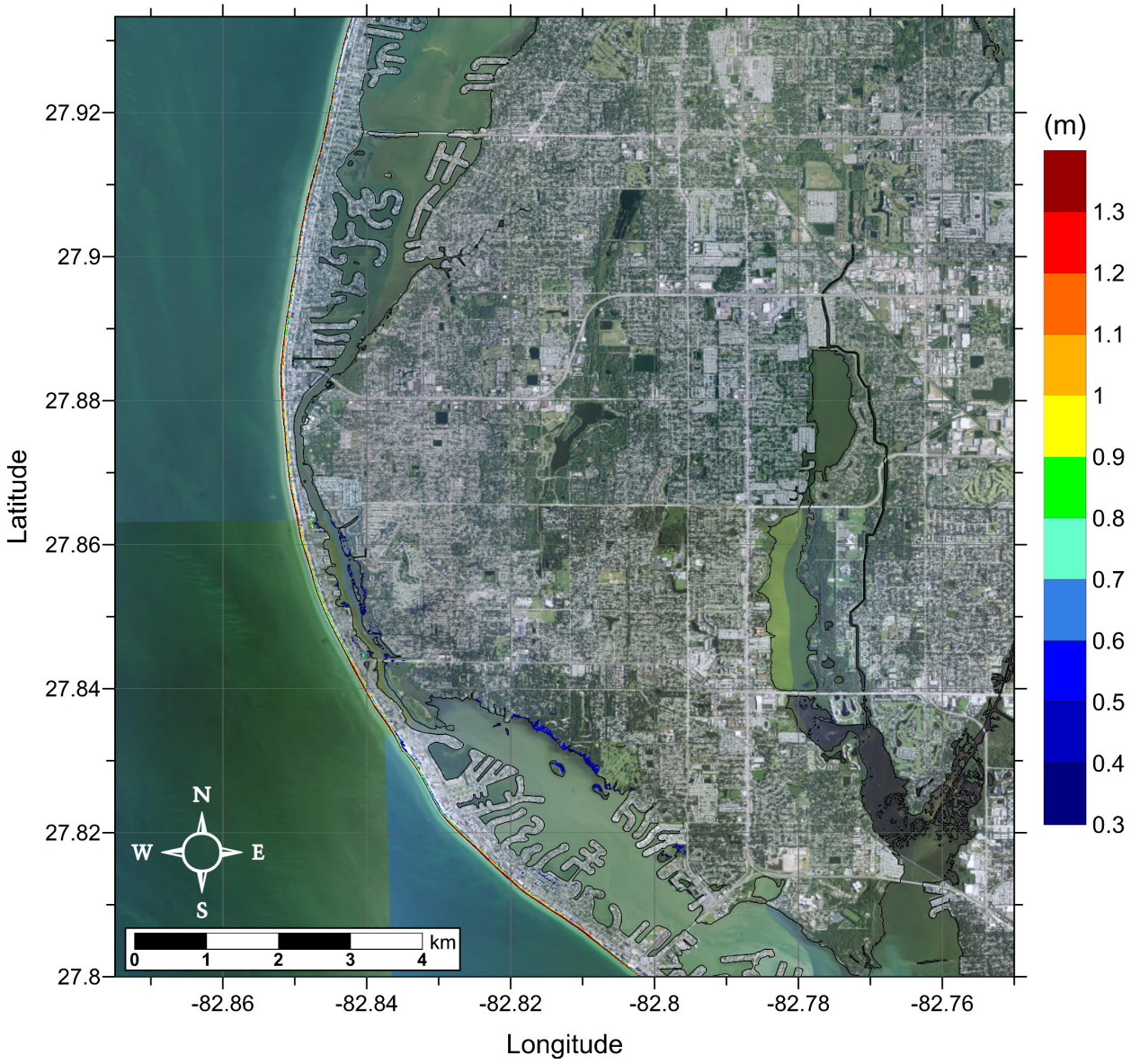

Figure 143: Maximum inundation depth (m) caused by the West Florida submarine landslide in northern Tampa, FL. Contour drawn is the zero-meter contour for land elevation.

Tampa, FL
West Florida Submarine Landslide
Maximum Momentum Flux on Grid B

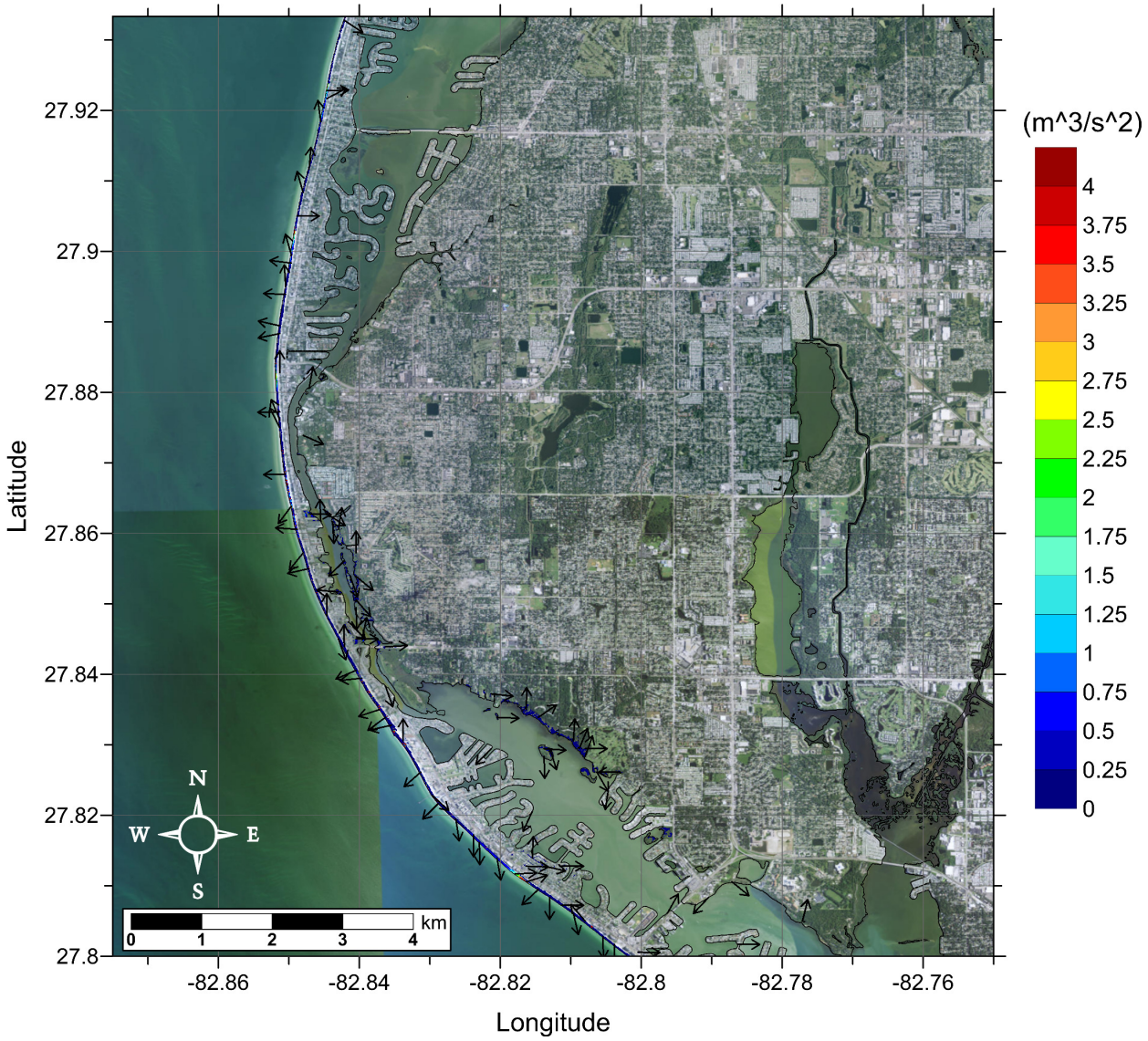

Figure 144: Maximum momentum flux (m^3/s^2) caused by the West Florida submarine landslide in northern Tampa, FL. Arrows represent direction of maximum momentum flux. Contour drawn is the zero-meter contour for land elevation.

Tampa, FL
Maximum of Maximums Inundation Depth on Grid A

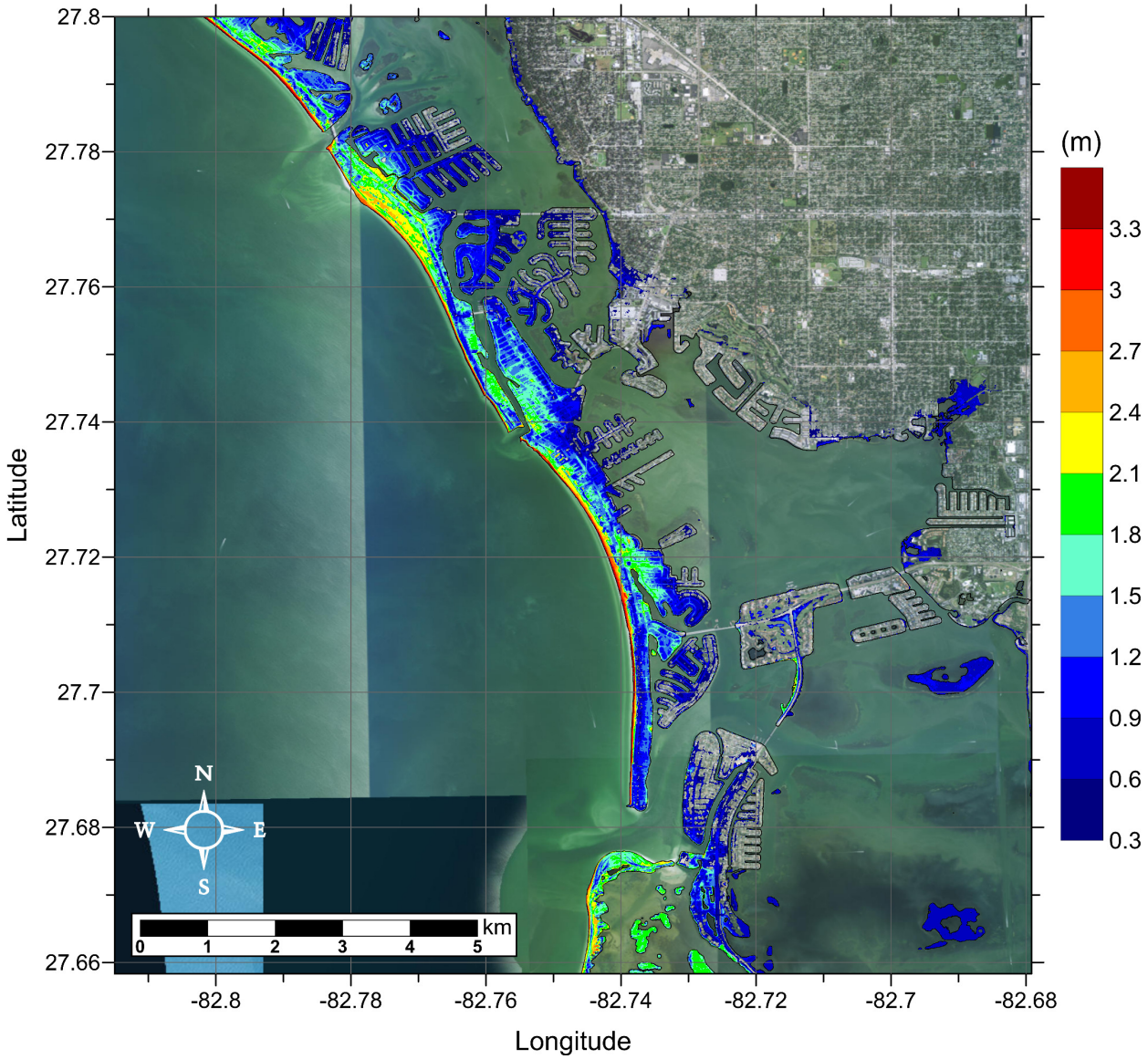

Figure 145: Maximum of maximums inundation depth (m) in southern Tampa, FL, calculated as the maximum inundation depth in each grid cell from an ensemble of all tsunami sources considered. Contour drawn is the zero-meter contour for land elevation.

Tampa, FL
Maximum Inundation Depth by Source on Grid A

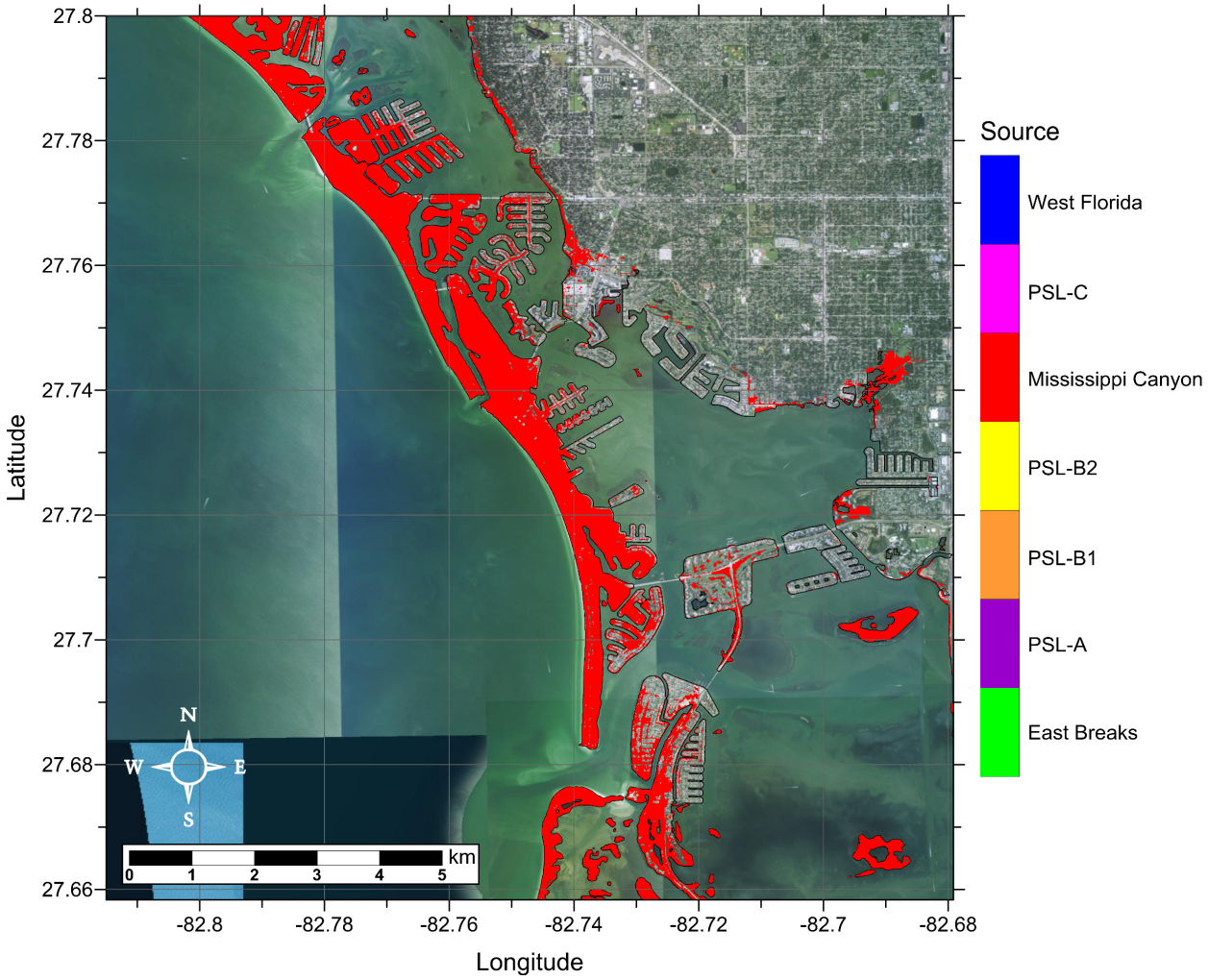

Figure 146: Indication of the tsunami source which causes the maximum of maximums inundation depth (m) in each grid cell from an ensemble of all tsunami sources considered (cf. Figure 145). Contour drawn is the zero-meter contour for land elevation.

Tampa, FL
Maximum of Maximums Inundation Depth on Grid B

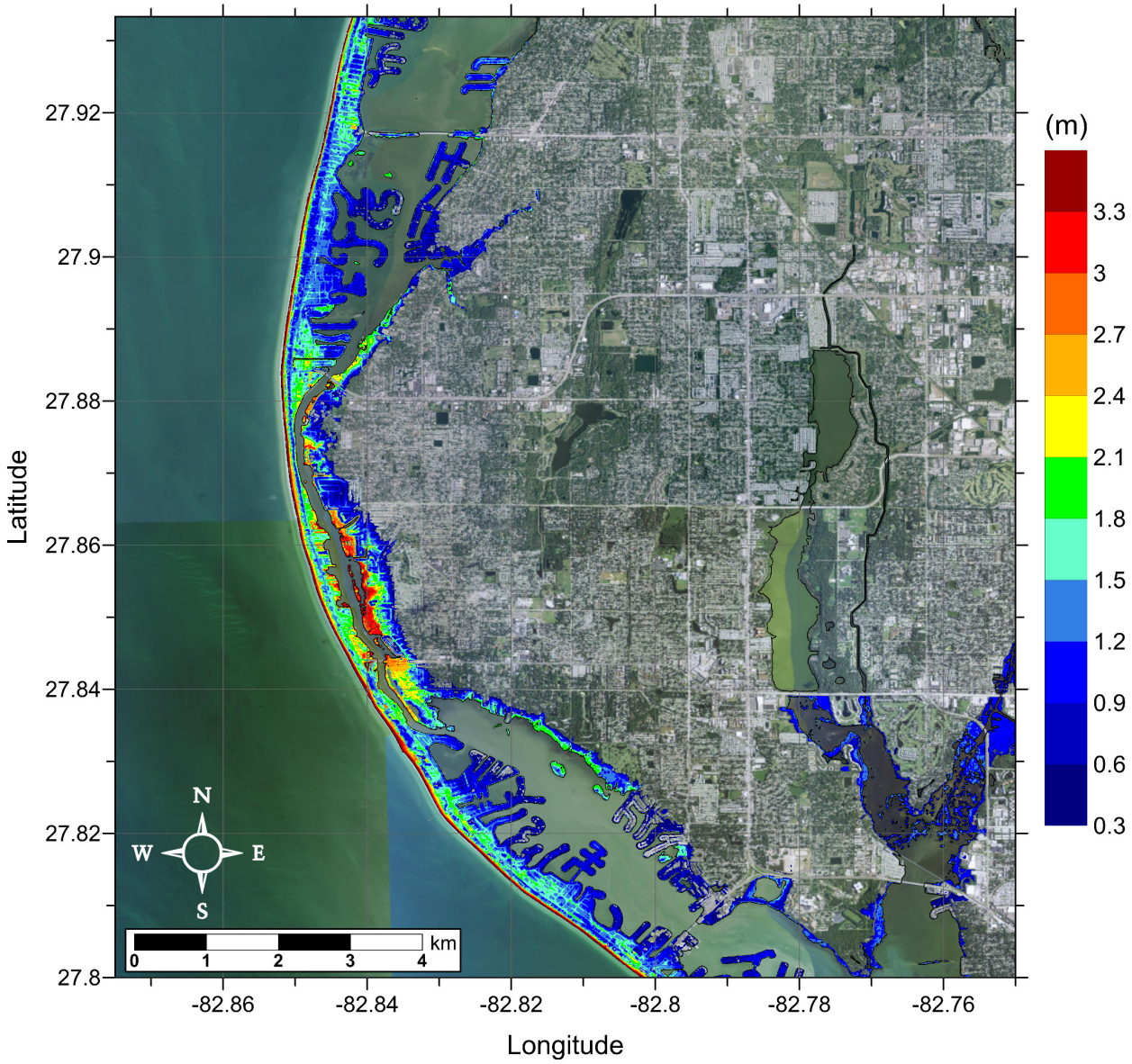

Figure 147: Maximum of maximums inundation depth (m) in northern Tampa, FL, calculated as the maximum inundation depth in each grid cell from an ensemble of all tsunami sources considered. Contour drawn is the zero-meter contour for land elevation.

Tampa, FL
Maximum Inundation Depth by Source on Grid B

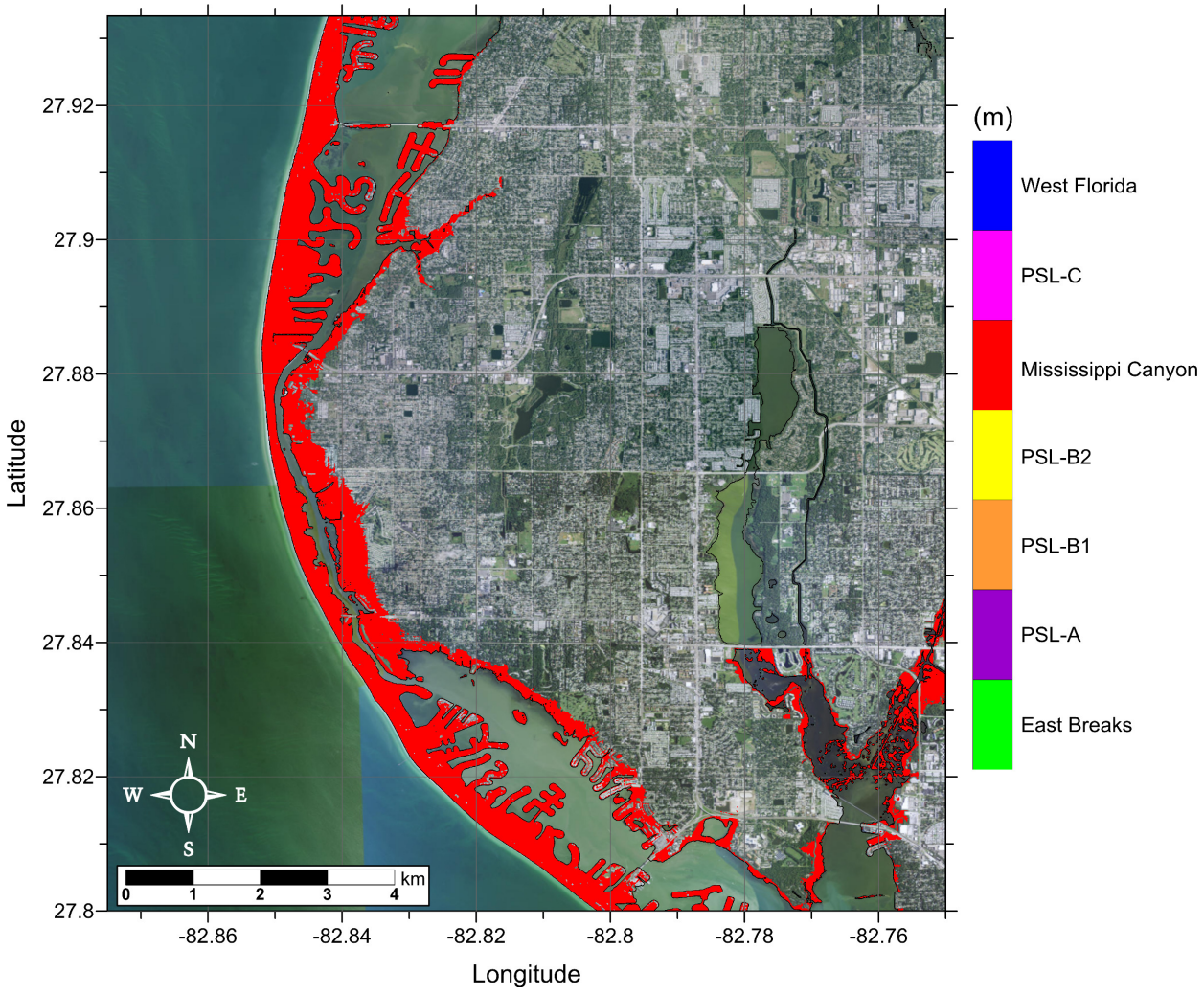

Figure 148: Indication of the tsunami source which causes the maximum of maximums inundation depth (m) in each grid cell from an ensemble of all tsunami sources considered (cf. Figure 147). Contour drawn is the zero-meter contour for land elevation.

6 Pilot Study for Probability of Tsunami Inundation in South Padre Island, TX

As is done for earthquake and flooding hazards, we wish to develop a probabilistic assessment of tsunami inundation for our communities of interest. Standard flood hazard maps required by, e.g., the Federal Emergency Management Agency (FEMA), include 100- and 500-year flood maps, that is, maps showing the areas that will flood on average once in 100 or 500 years, respectively. We have performed a pilot study to develop similar maps for tsunami inundation for South Padre Island, TX. Our study determines tsunami inundation hazard based on 500, 2500, 5000, and 10,000 year exceedance values, as well as probabilities of exceeding 0m, 2m (∼6.6ft), 4m (∼13.1ft), and 6m (∼19.7ft) threshold inundation levels. Details for this process follow from González et al. (2014).

Under the assumption that the seven landslide tsunami sources developed here are independent events governed by a Poisson process, their independent annual probabilities of occurrence are given by

$$p_i = 1 - e^{-1/\lambda_i}$$

with λ_i the return period of the landslide tsunami event E_i. The probability that one event E_i does not produce inundation above a threshold value $\bar{\zeta}$ (in a particular grid cell) is given by

$$1 - p_i P(\zeta > \bar{\zeta} | E_i). \tag{18}$$

For each event E_i, $P(\zeta > \bar{\zeta}|E_i)$ is either zero ($\zeta \leq \bar{\zeta}$) or one ($\zeta > \bar{\zeta}$). Since the seven landslide tsunami events are independent, the probability that no event produces inundation over the threshold value $\bar{\zeta}$ is given by the joint probability of (18) over all seven sources:

$$P(\zeta \leq \bar{\zeta}) = \prod_{i=1}^{7} \left(1 - p_i P(\zeta > \bar{\zeta}|E_i)\right)$$

Thus, the probability that at least one of these events produces inundation above $\bar{\zeta}$ is

$$P(\zeta > \bar{\zeta}) = 1 - \prod_{i=1}^{7} \left(1 - p_i P(\zeta > \bar{\zeta}|E_i)\right). \tag{19}$$

These probabilities lead to hazard curves for each grid point in the computational domain when multiple threshold values are considered. For the study conducted here, since the seven sources are associated to a range of return periods and thus probabilities, we use the highest probability for each event as p_i in (19), e.g. the probability used for the Mississippi Canyon landslide is $1/7500 \approx 0.00013$. In this way, the "worst-case probability" is assumed. Sample hazard curves are shown in Figure 149 for select points within the highest resolution (1/3 arcsecond) domain for South Padre Island, TX.

From these hazard curves, we can directly calculate the inundation exceedance level for a ×-year event, as well as the probability of exceeding a specific inundation level. Figures 150-153 show the inundation level exceeded for annual probabilities corresponding to 500, 2500, 5000, and 10,000 year return periods. The inundation for probabilities of 0.002 (500

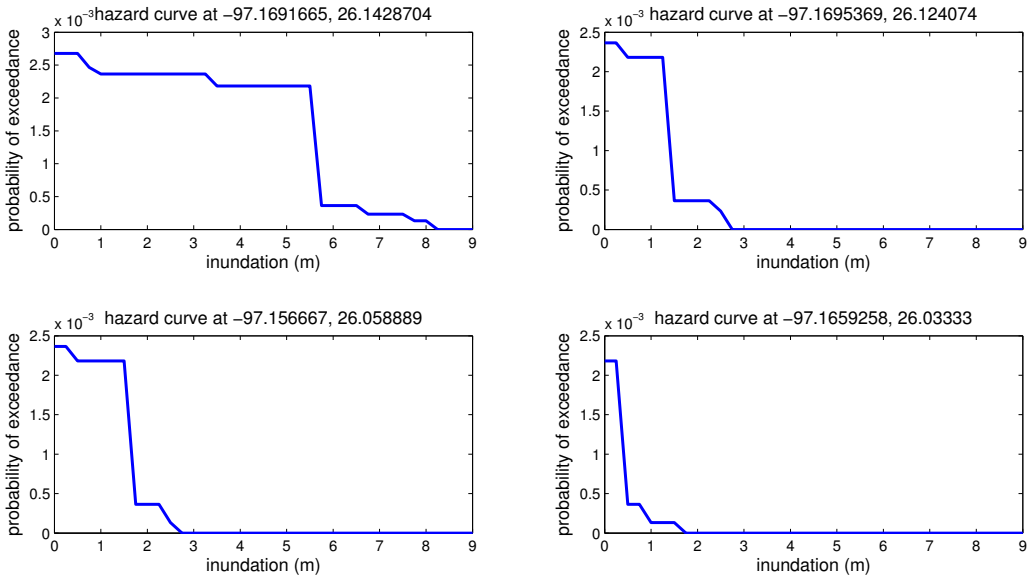

Figure 149: Sample hazard curves for select points within the highest resolution (1/3 arc-second) grid for South Padre Island, TX. Contour drawn is the zero-meter contour for land elevation.

year return period) and 0.0004 (2500 year return period) are quite similar to each other and to the maximum inundation produced by PSL-C for South Padre Island, TX (Figure 47). This could be expected since the probabilities of the other sources are lower than 0.0004 (and return periods are greater than 2500 years), so that the inundation produced by PSL-C dominates the behavior of the hazard curves for this community. Likewise, the inundation corresponding to annual probabilities of 0.0002 (5000 year return period) and 0.0001 (10,000 year return period) is similar to that produced by the PSL-A and Mississippi Canyon sources, which both have maximum probabilities of $\sim$ 0.00013 (7700 and 7500 year return periods, respectively).

González et al. (2014) raised concerns over the information missed by only considering the $\times$-year maps above, showing that significant differences could be seen in results after modifying return periods slightly. The return periods of the events considered here are quite large, and little difference is seen in probability when a return period is varied by a few hundred years. However, if one looks for the inundation that is exceeded by a specific probability or return period, changing the return period of an event by a few hundred years would change the inundation that is seen at that specific probability, even though the probability is essentially the same (González et al., 2014). As a result, we also investigate the probability of exceeding specific inundation levels. Figures 154-157 show probabilities of exceeding threshold inundation levels of 0m, 2m ($\sim$6.6ft), 4m ($\sim$13.1ft), and 6m ($\sim$19.7ft), respectively. Note that only probabilities greater than zero are shown. Probabilities of having any inundation ($\zeta > 0$m) is between 0.002 and 0.0025 (400-500 year return period) throughout most of the barrier island (Figure 154). As would be expected, probabilities quickly decrease with increasing threshold of inundation (note the change in color scale from

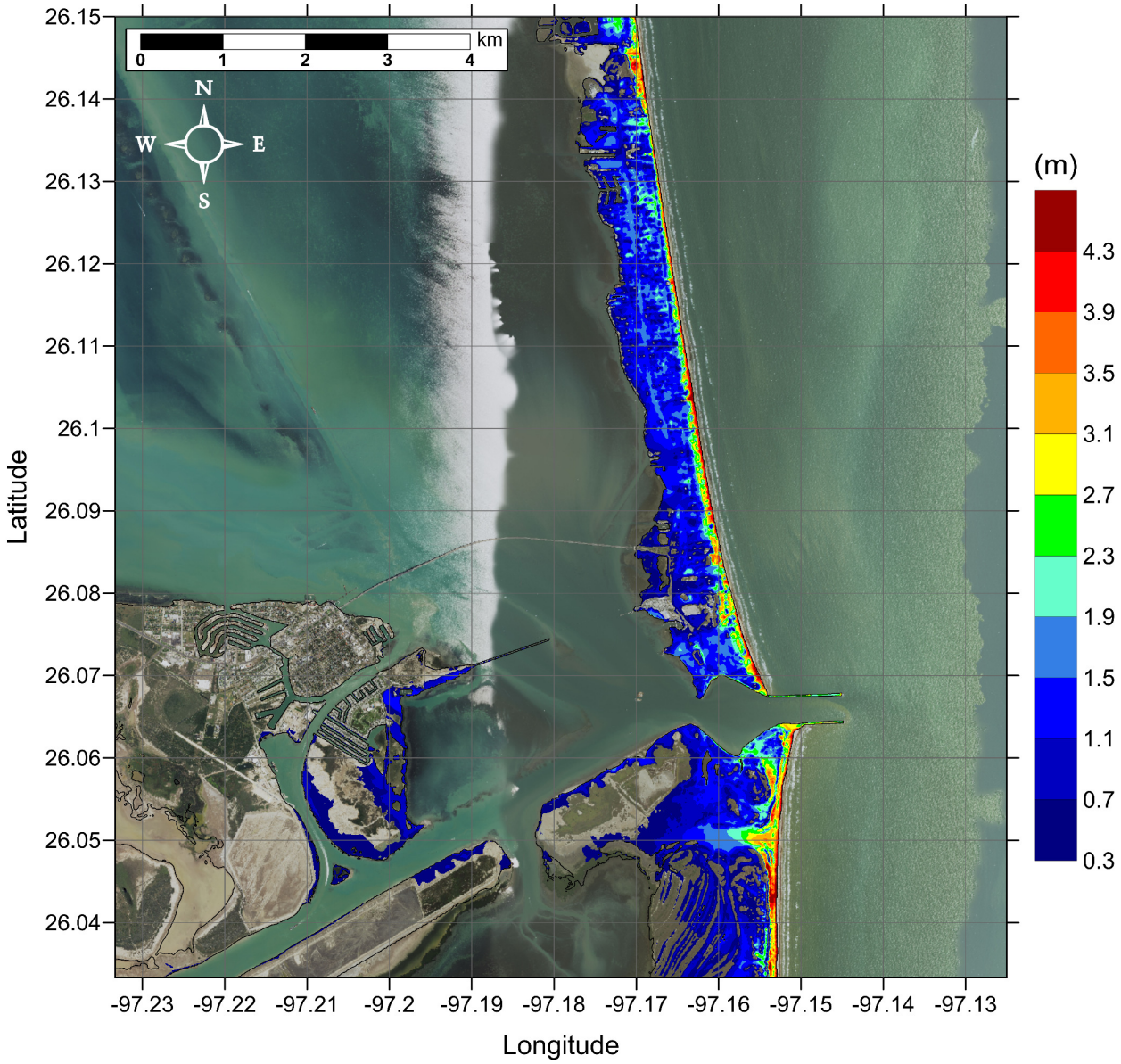

Figure 150: Inundation (in m) corresponding to an annual probability of 0.002, or a 500 year return period, in South Padre Island, TX. Contour drawn is the zero-meter contour for land elevation.

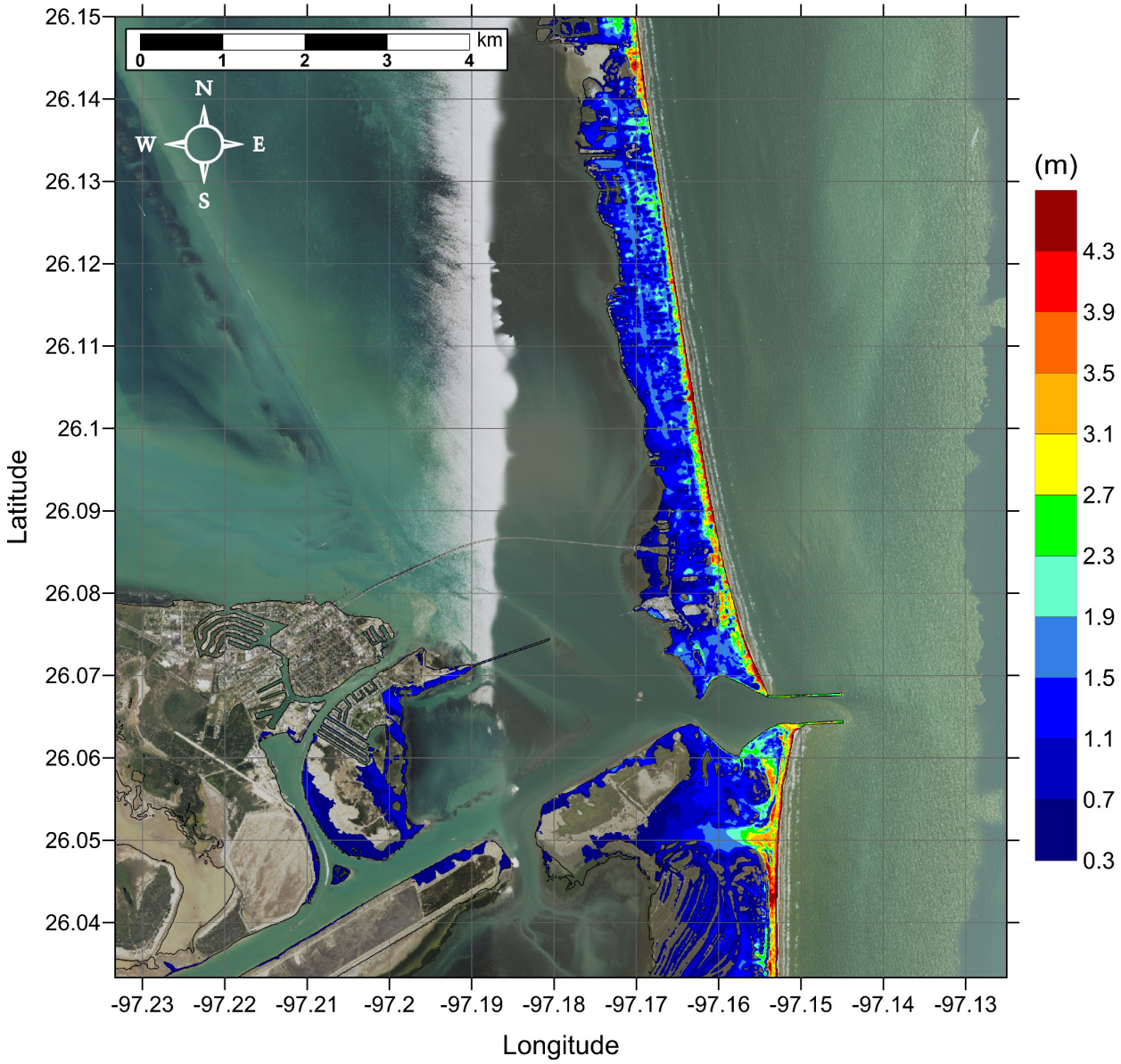

Figure 151: Inundation (in m) corresponding to an annual probability of 0.0004, or a 2500 year return period, in South Padre Island, TX. Contour drawn is the zero-meter contour for land elevation.

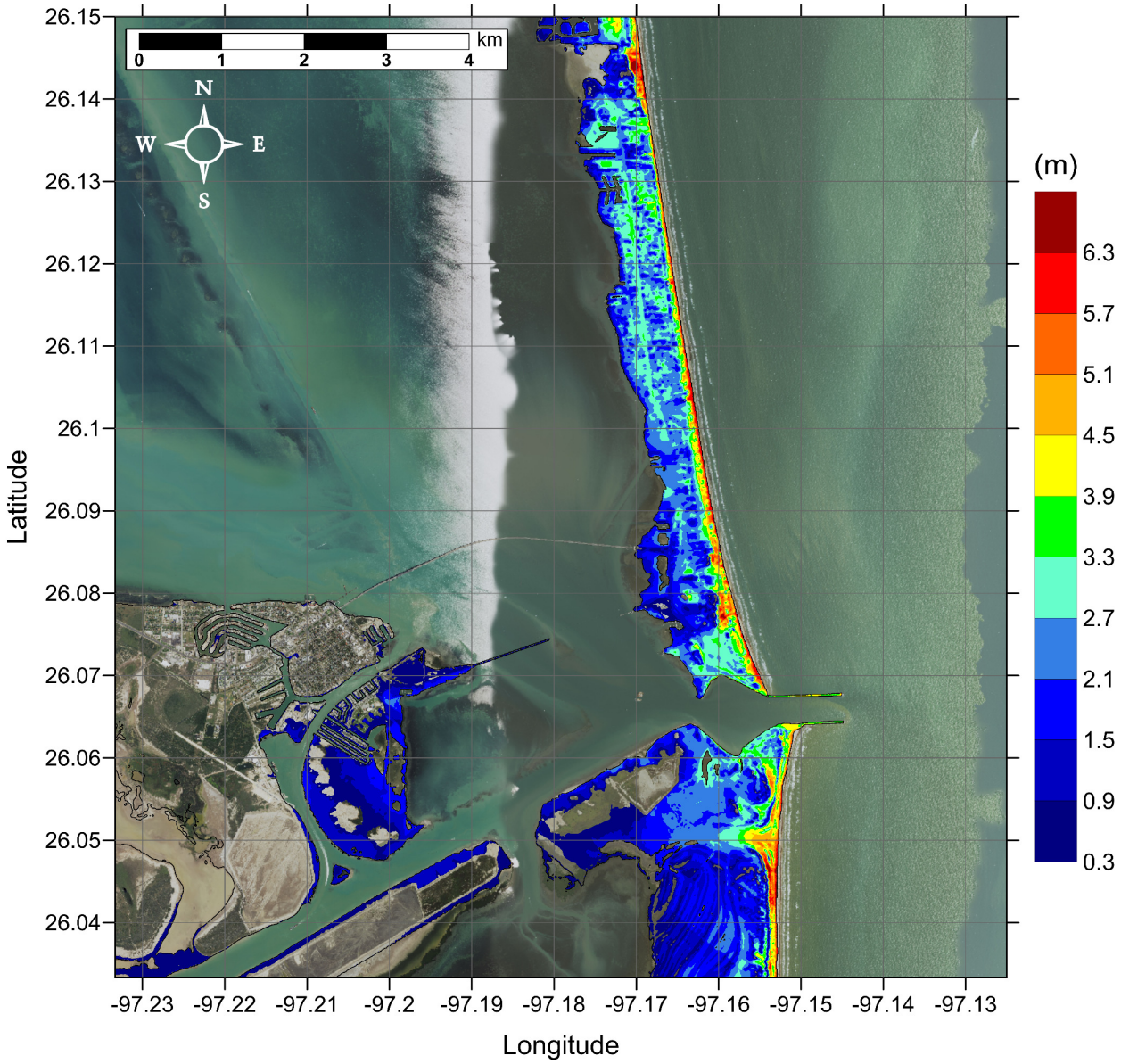

Figure 152: Inundation (in m) corresponding to an annual probability of 0.0002, or a 5000 year return period, in South Padre Island, TX. Contour drawn is the zero-meter contour for land elevation.

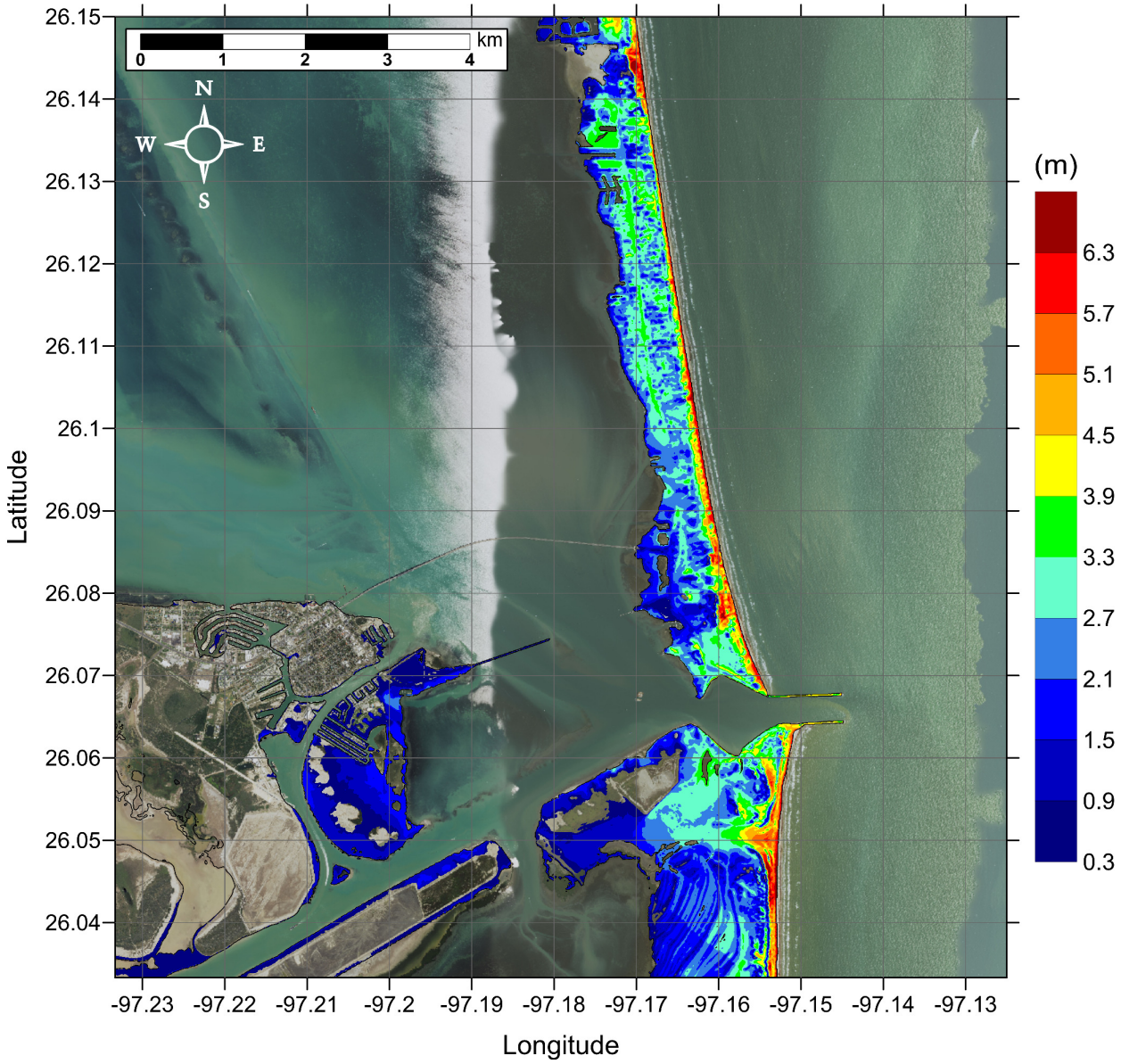

Figure 153: Inundation (in m) corresponding to an annual probability of 0.0001, or a 10,000 year return period, in South Padre Island, TX. Contour drawn is the zero-meter contour for land elevation.

Figure 154 to Figures 155-157), though it should be noted that, due to the combination of probabilities in (19), the lowest a nonzero probability can be here is 0.0001 (10,000 year return period), the lowest probability of the sources considered here. Probabilities of exceeding 2m ($\sim$6.6ft) inundation are highest along the immediate beachfront at 0.002 to 0.0025 (400-500 year return period), and mostly between 0.0002 and 0.0004 (2500-5000 year return period) across the rest of the barrier island (Figure 155). Probabilities of exceeding 4m ($\sim$13.1ft) inundation are generally between 0.0002 and 0.0004 (2500-5000 year return period) along the beachfront, with some small regions of 0.002 to 0.0025 (400-500 year return period) (Figure 156). Probabilities of exceeding 6m ($\sim$19.7ft) inundation are quite negligible, with only small areas along the beachfront seeing relatively low ($p < 0.0004$, >2500 year return period) probabilities of exceedance (Figure 157).

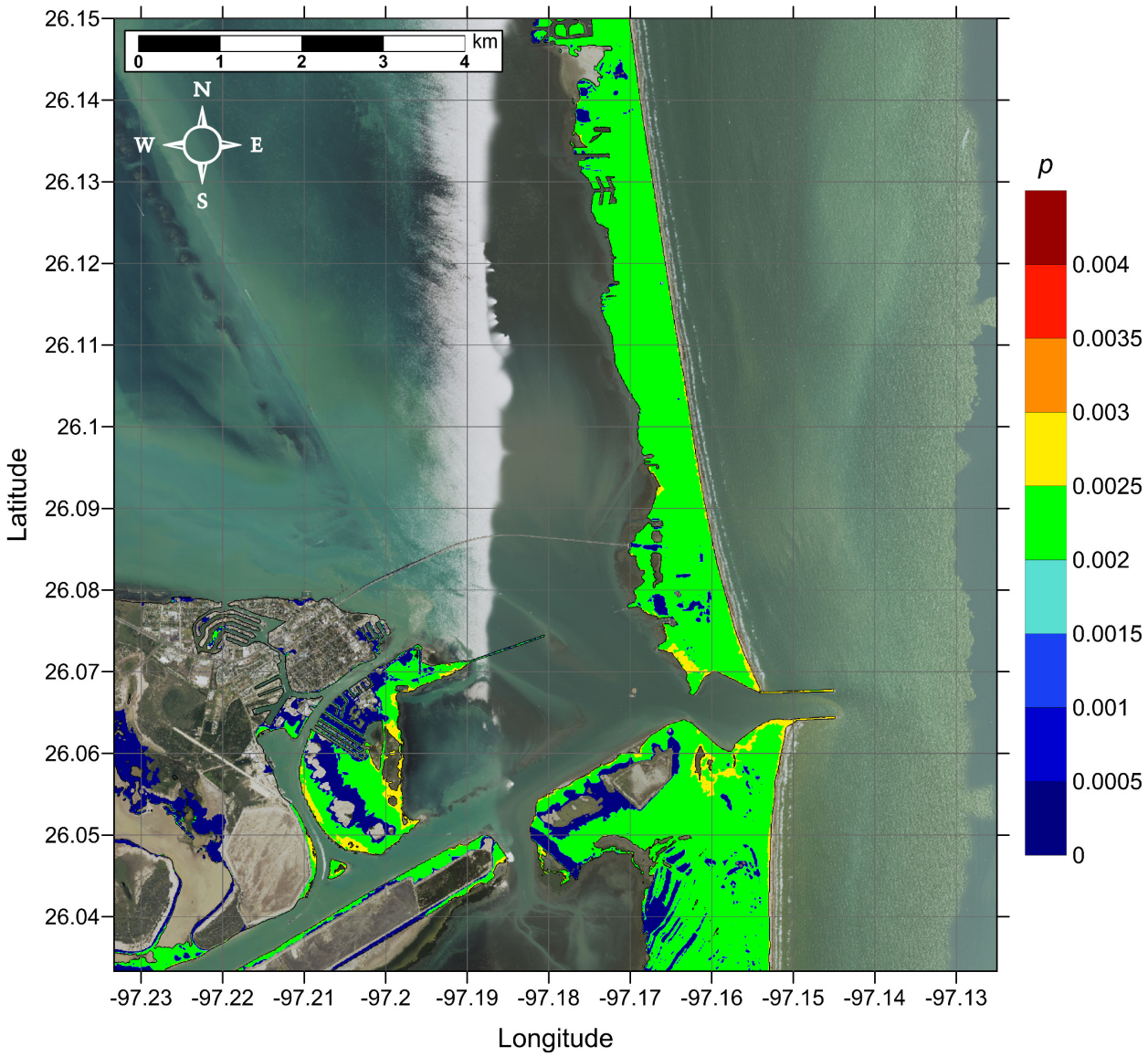

Figure 154: Probability of exceeding 0m inundation in South Padre Island, TX. Contour drawn is the zero-meter contour for land elevation.

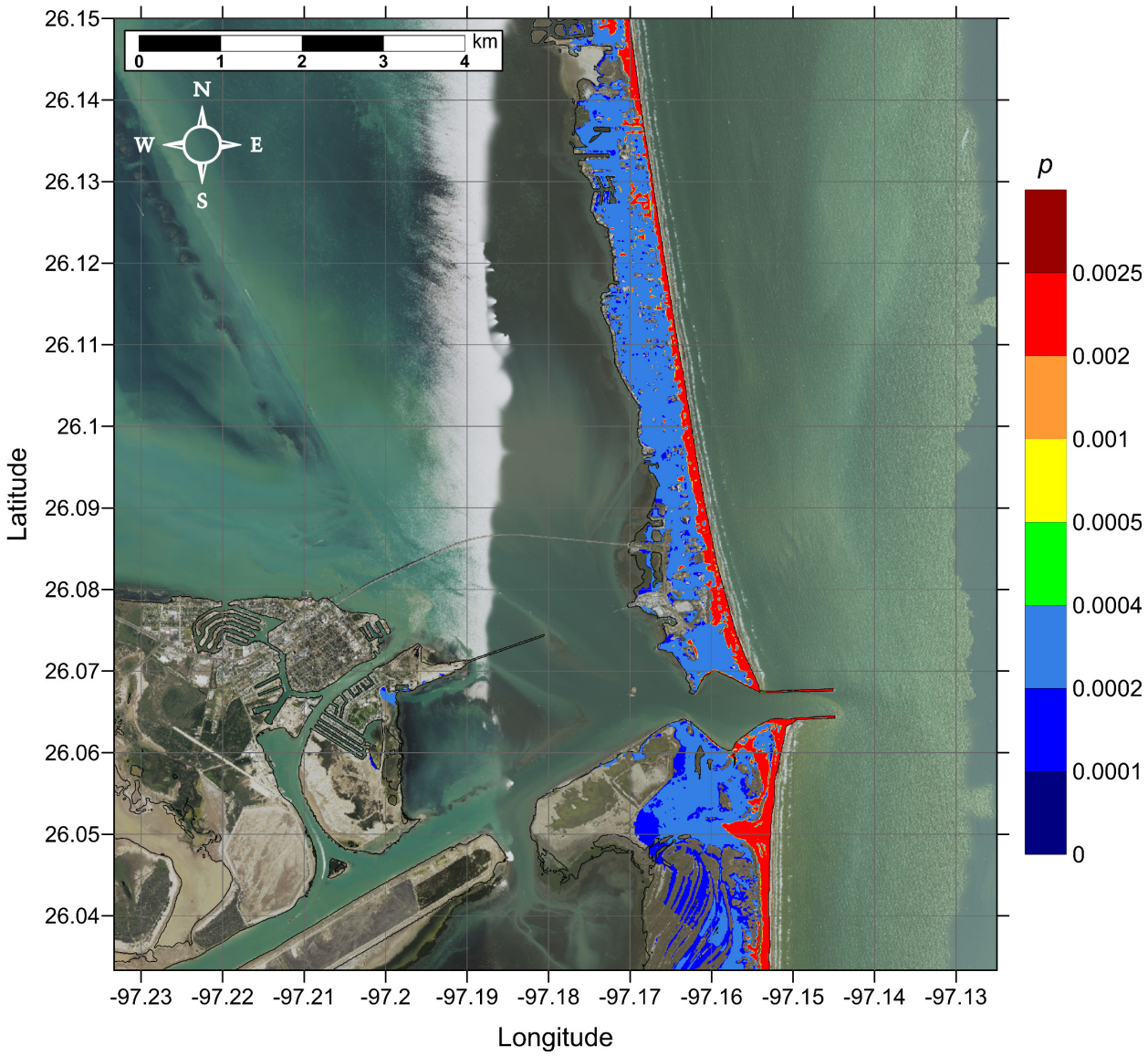

Figure 155: Probability of exceeding 2m (∼6.6ft) inundation in South Padre Island, TX. Contour drawn is the zero-meter contour for land elevation.

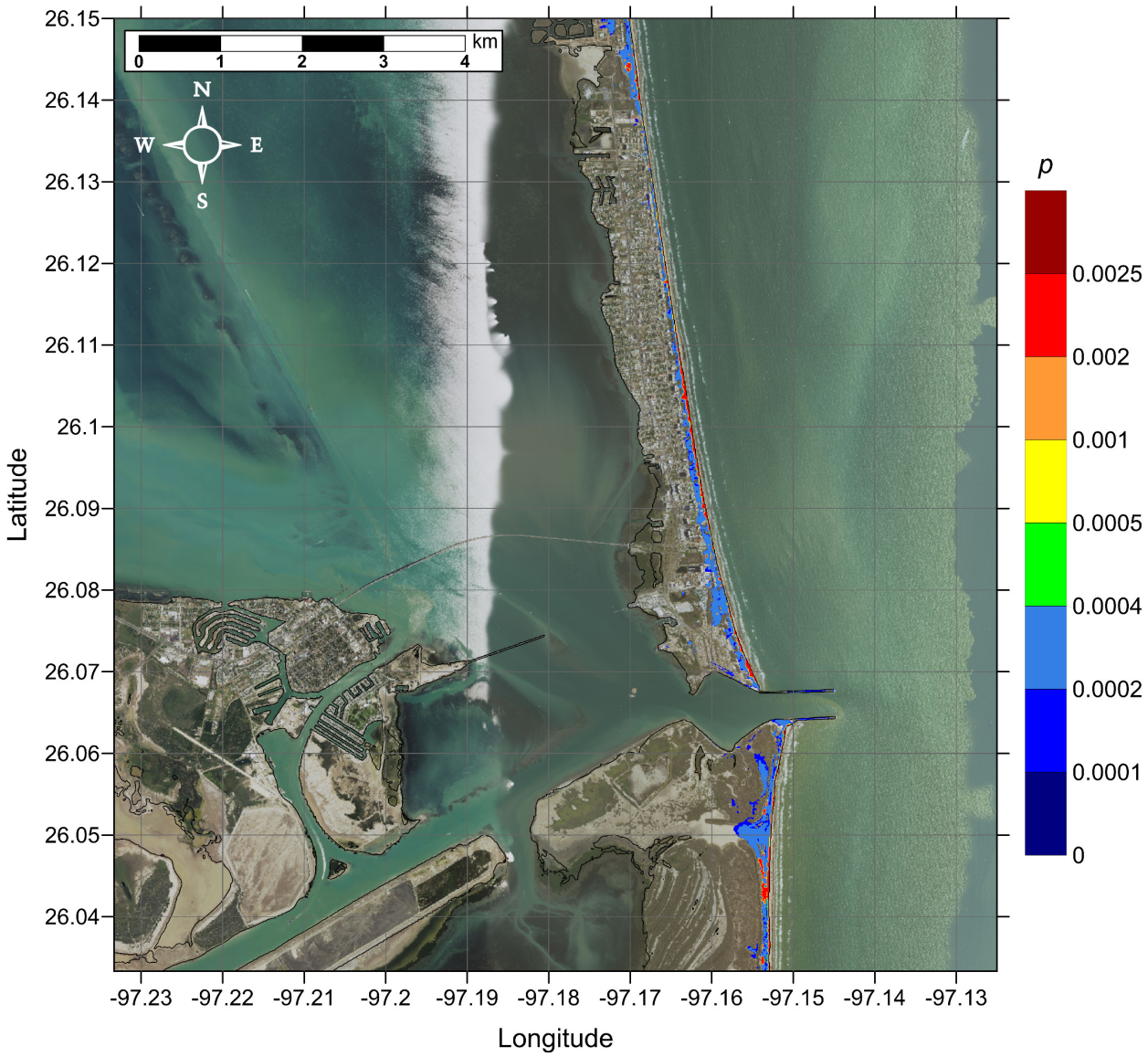

Figure 156: Probability of exceeding 4m (∼13.1ft) inundation in South Padre Island, TX. Contour drawn is the zero-meter contour for land elevation.

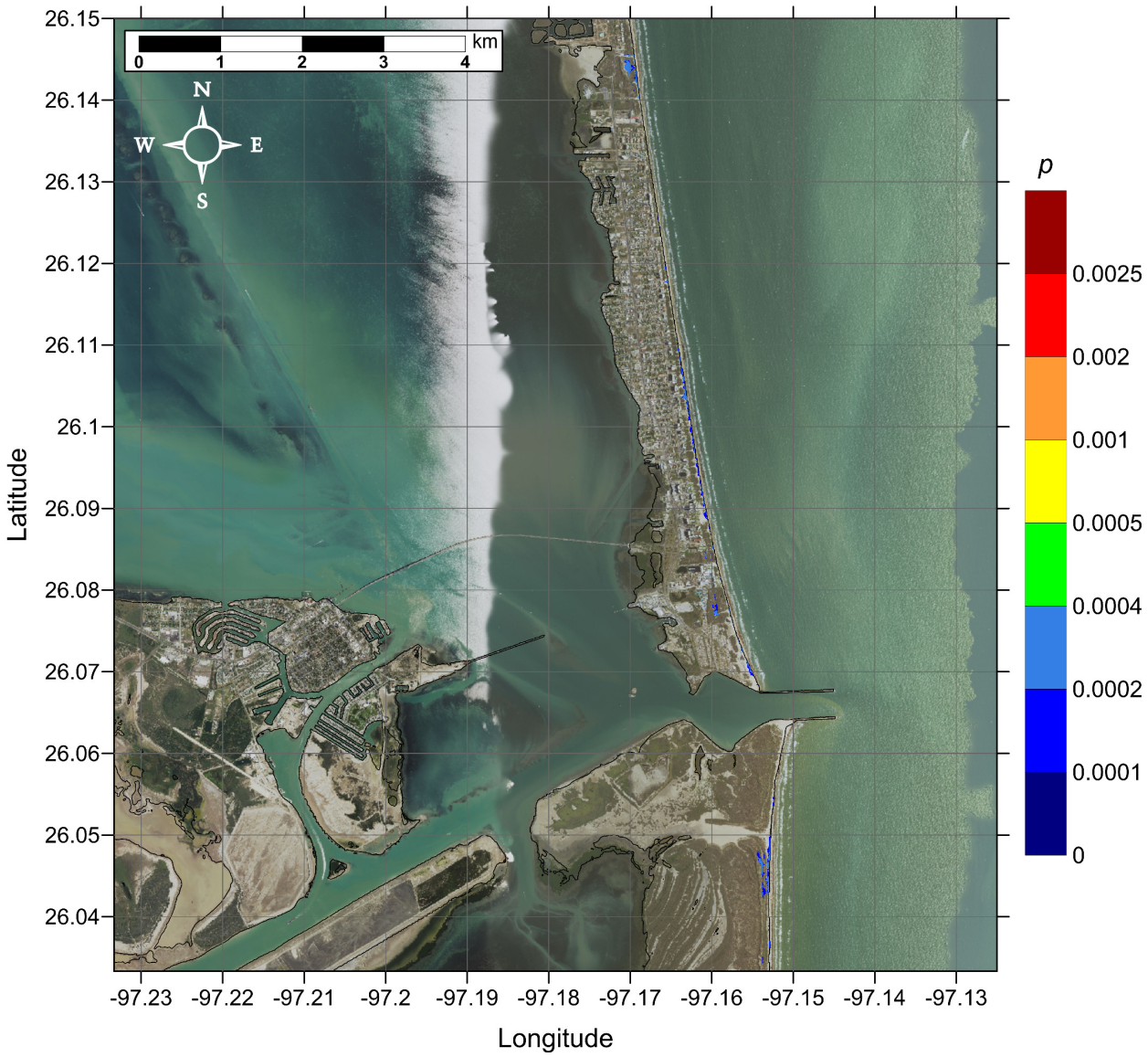

Figure 157: Probability of exceeding 6m (∼19.7ft) inundation in South Padre Island, TX. Contour drawn is the zero-meter contour for land elevation.

7 Conclusion

Tsunami inundation in five communities was modeled considering seven sources spread across the northern GOM. Using a probabilistic approach, we were able to add four additional landslide tsunami sources to the existing three massive ancient sources that have been identified. In the probabilistic approach, we implemented a MCS method based on historical data within the GOM to determine size and location parameters for potential failures. Using statistical correlations between landslide parameters which showed strong correlations in the observational data, we determined values for size and location and identified extreme events which were averaged to determine worst-case scenarios for each transect with sediment information. The probabilities of these probabilistic maximum credible landslide events indicate that, in general, return periods of $5000 - 8000$ years can be expected for large tsunamigenic submarine landslides in the northern Gulf of Mexico, though events with much higher return rates at approximately $500 - 600$ years were seen for Transect C in the northeastern GOM. This large discrepancy in return periods could be due to uncertainty in sediment data and should be viewed with some caution.

Adding the probabilistic sources allowed us to fill in the gaps between the locations of the ancient sources, providing a more continuous picture of submarine landslide tsunami hazard across the GOM. These seven sources were used in the 3D model TSUNAMI3D to model tsunami generation, and subsequently in the 2D model NEOWAVE to model tsunami propagation and inundation for the communities of South Padre Island, TX, Galveston, TX, Mobile, AL (including Dauphin Island and Gulf Highlands), Panama City, FL, and Tampa, FL.

The five communities studied here are each affected by one or more sources. South Padre Island, TX, Dauphin Isl./Gulf Highlands, AL, and Panama City, FL received the most inundation, in both depth and extent, overall, with the barrier islands of South Padre Island and Dauphin Isl./Gulf Highlands being almost completely overtopped by one or more tsunami events. We see the most widespread inundation in Panama City, with tsunami inundation of up to 1.5 m seen up to approximately 5 km inland of the beachfront caused by the Mississippi Canyon landslide. However, PSL-C is the only other source that causes any significant inundation in Panama City; this community is essentially unaffected by the other five sources. Galveston, TX is fairly well protected from inundation by most sources due to the seawall protecting the most populated part of the island, although the lower-lying areas and those not behind the seawall are at more risk. We also see inundation originating from the backside of the barrier island or inland waterways in Galveston, Panama City, and Tampa, FL. The numerous canals and waterways in Tampa provide many possible trajectories for tsunami waves to inundate the small residential islands in this community. However, most inundation is seen in northern Tampa (grid B), with southern Tampa (grid A) seeing inundation mostly along the immediate beachfront and in some small islands. Mobile, AL itself is largely protected in its position at the northern end of Mobile Bay, with only the Mississippi Canyon landslide causing minor tsunami inundation along the inland waterways.

Overall, we see that the Mississippi Canyon landslide causes maximum tsunami inundation depths and extents for all mapped locations. For South Padre Island and Galveston, along the western part of the Gulf Coast, multiple sources contribute to the maximum of max-

imums inundation depth, as seen in Figures 52 and 68. In South Padre Island, East Breaks, PSL-A, and Mississippi Canyon landslides each produce the overall maximum inundation in some places, with Mississippi Canyon dominating. In Galveston, the Mississippi Canyon landslide also causes the maximum of maximums inundation in most areas, but PSL-A, PSL-B1, and PSL-C also contribute in some places. For Mobile, Panama City, and Tampa, the inundation caused by the Mississippi Canyon landslide dominates; no other source contributes to the maximum of maximums inundation for these communities (see Figures 98, 100, 116, 146, and 148). This is most likely due to the location of the Mississippi Canyon landslide near the center of the GOM, with direction of wave propagation predominantly to the east. The large tsunami amplitude produced by the Mississippi Canyon landslide causes it to have a widespread effect also in the western communities of South Padre and Galveston Islands.

For the pilot probabilistic tsunami hazard assessment performed for South Padre Island, TX, hazard curves were constructed showing probabilities of certain inundation levels being exceeded. Inundation with a specific annual probability is similar to the maximum tsunami inundation seen for the individual landslide scenarios with similar probabilities. Additionally, we determined annual probabilities of exceeding specific threshold inundation levels. In general, probabilities are highest along the coast and decrease inland. Probabilities of having any inundation ($\zeta > 0$) is between 0.002 and 0.0025 (400-500 year return period) throughout most of the barrier island. Probabilities of exceeding 2m ($\sim$6.6ft) inundation are highest along the immediate beachfront at 0.002 to 0.0025 (400-500 year return period), and mostly between 0.0002 and 0.0004 (2500-5000 year return period) across the rest of the barrier island. Probabilities of exceeding 4m ($\sim$13.1ft) inundation are generally between 0.0002 and 0.0004 (2500-5000 year return period) along the beachfront, with some small regions of 0.002 to 0.0025 (400-500 year return period). Probabilities of exceeding 6m ($\sim$19.7ft) inundation are quite negligible, with only small areas along the beachfront seeing relatively low (< 0.0004, 2500 year return period) probabilities of exceedance. As more landslide tsunami sources are identified or constructed in the future, the hazard curves, and the resulting probabilities, will be refined.

Acknowledgments

This work was supported by the National Tsunami Hazard Mitigation Program (NTHMP) under awards NA12NWS4670014, "Construction of Five Inundation Maps in the Gulf of Mexico", and NA13NWS4670018, "A Probabilistic Methodology for Hazard Assessment Generated by Submarine Landslide in the GOM". The authors wish to thank all NTHMP modeling and Mapping Subcommittee members and GOM's emergency manager representatives for their helpful insights. High resolution inundation maps are available from `http://www.tamug.edu/tsunami/NTHMP/NTHMP.html` or by contacting corresponding author upon request.

References

Abadie, S.D., Morichon, S.D., Grilli, S., Glockner, S., 2008. VOF/Navier-Stokes numerical modeling of surface waves generated by subaerial landslides. *La Houille Blanche*, *1*, 21–26.

Abadie, S.D., Morichon, S.D., Grilli, S., Glockner, S., 2010. Numerical simulation of waves generated by landslides using a multiple-fluid Navier-Stokes model. *Coastal Engineering*, *57*, 779–794.

Abadie, S.M., Harris, J.C., Grilli, S.T., Fabre, R., 2012. Numerical modeling of tsunami waves generated by the flank collapse of the Cumbre Vieja Volcano (La Palma, Canary Islands): Tsunami source and near field effects. *J. Geophys. Res. 117*, C05030.

Angelou Economic, 2008. Galveston Island Tourism Economic Impact Analysis. (http://www.cityofgalveston.org/DocumentCenter/Home/View/215. Prepared by Angelou Economics

Art Leatherwood, 2010. PADRE ISLAND, Handbook of Texas Online. (http://www.tshaonline.org/handbook/online/articles/rrp01). Published by the Texas State Historical Association.

Ballingurd, D., 2006. It Could Happen Here. St. Petersburg Times Retrieved:October 2, 2006.

D. L. Brown, 1964. Tsunamic activity accompanying the Alaska earthquake of 27 March 1964. Technical report, U.S. Army Engineer District, U.S. Army Corps of Eng., 1964.

Casulli, V., Stelling, G.S., 1998. Numerical simulation of 3D quasihydrostatic, free-surface flows. *J. Hydr. Eng. 124*, 678–686.

Cranford, G., 2000. Tidal Wave, A List of victims and survivors, Newfoundland, 1929. *Flanker Press*, St. Johns, Newfoundland, 2000.

Dellinger, J. A., Blum, J. A., 2009. Insights into the mechanism of the Northern Gulf of Mexico MS 5.3 "Green Canyon event" of 10 February 2006. *AGU Fall Meeting Abstracts, 2009*, Abstract # S53A-1484

Dunbar, P.K., Weaver, C.S., 2008. U.S. States and Territories National Tsunami Hazard Assessment: Historic Record and Sources for Waves. *Technical Report*, Report to National Tsunami Hazard Mitigation Program. NGDC, USGS.

Dunn, R. S., 2010. HURRICANES, Handbook of Texas Online, http://www.tshaonline.org/handbook/online/articles/ybh01. Published by the Texas State Historical Association.

Geist, E. L., Chaytor, J. D., Parsons, T. , ten Brink, U., 2013. Estimation of submarine mass failure probability from a sequence of deposits with age dates. *Geosphere*, *9*(2), 287–298, doi:10.1130/GES00829.1.

González, F. I., LeVeque, R. J., Adams, L. M., 2014. Probabilistic Tsunami Hazard Assessment (PTHA) for Crescent City, CA. Final Report on Phase I, September 11, 2014.

Grilli, S.T., Watts, P., 2005. Tsunami generation by submarine mass failure part I: modeling, experimental validation, and sensitivity analyses. *J. Wtrwy. Port Coast. and Oc. Eng. ASCE 131* (6), 283–297.

Grilli, S.T., Taylor, O.-D.S., Baxter, C.D.P., Maretzki, S., 2009. A probabilistic approach for determining submarine landslide tsunami hazard along the upper east coast of the United States. *Mar. Geol. 264*, 74–97.

Hampton, M., Locat, J., 1996. Submarine landslides. *Rev. Geophys. 34*, 33–59.

Hirt, C.W., Nichols, B.D., 1981. Volume of fluid method for the dynamics of free boundaries. *J. Comp. Phys. 39*, 201–225.

Horrillo, J., 2006. Numerical Method for Tsunami calculations using Full Navier-Stokes equations and the Volume of Fluid method. Ph.D. thesis. University of Fairbanks.

Horrillo, J., Wood A., Kim, G.-B, A. Parambath A., 2013. A simplified 3-D Navier-Stokes numerical model for landslide-tsunami: Application to the Gulf of Mexico. *J. Geophys. Res. Oceans*, *118*, 6934–6950, doi:10.1002/2012JC008689.

Knight, W., 2006. Model Predictions of Gulf and Southern Atlantic Coast Tsunami Impacts from a Distribution of Sources, *Science of Tsunami Hazards*, *24*, 304-312.

Kowalik, Z., Knight, W., Logan, T., Whitmore, P, 2005. Numerical modeling of the global tsunami: Indonesian tsunami Performance Benchmarking Tsunami Models of 26 December 2004. *Science of Tsunami Hazards*, *23*, No.1, 40–56.

Locat, J., Lee, H. J., 2002. Submarine landslides: Advances and challenges. *Can. Geotech. J.*, *39*, 193–212.

López-Venegas, A.M., Horrillo, J., Pampell-Manis, A., Huerfano, V., Mercado, A., 2014. Advanced Tsunami Numerical Simulations and Energy Considerations by use of 3D 2D Coupled Models: The October 11, 1918, Mona Passage Tsunami. *Pure and Applied Geophysics*, *171*(11), 2863–3174. 10.1007/s00024-014-0988-3

Mason, D., Habitz, C., Wynn, R., Pederson, G., Lovholt, F., 2006. Submarine landslides: Processes, triggers and hazard protection. *Philos. Trans. R. Soc. A*, *364*, 2009–2039.

Maretzki, S., Grilli, S.T., Baxter, D.P., 2007. Probabilistic SMF Tsunami Hazard Assessment for the upper East Coast of the United States. In *Proc. 3rd Intl. Symp. on Submarine Mass Movements and their Consequences*, Santorini, Greece, October 2007 Lykousis, V., Sakellariou, D., Locat, J., eds), Springer, 377–386.

McAdoo, B. G., Pratson, L. F., Orange, D. L, 2000. Submarine landslide geomorphology, US continental slope. *Mar. Geol.*, *169*, 103–136.

Morgenstern, N. R., 1967. Submarine slumping and the initiation of turbidity currents, In A.F. Richards, editor, in *Marine Geotechnique*, 189–210, University of Illinois Press, Urbana, IL, 1967.

NTHMP, 2012. National Tsunami Hazard Mitigation Program, in: *Proceedings and Results of the 2011 NTHMP Model Benchmarking Workshop; NOAA Special Report*, Boulder: U.S. Department of Commerce/NOAA/NTHMP. p. 436.

Shigihara, Y., Horrillo, J., 2014. A Probabilistic Methodology for Determining Tsunami Sources Generated by Submarine Landslide - Application to the Gulf of Mexico-. *Journal of Japan Society of Civil Engineers, Ser. B2 (Coastal Engineering) 70*, I_281-I_285, (in Japanese)

Sue, L. P., Nokes, R. I., Walters, R. A., 2006. Experimental modeling of tsunami generated by underwater landslides. *Science of Tsunami Hazards*, *24*, No.4, 267–287.

Synolakis, C.E., Bernard, E.N., Titov, V.V., Kanoglu, U., Gonzalez, F.I., 2007. OAR PMEL-135 Standards, criteria, and procedures for NOAA evaluation of tsunami numerical models. *Technical Report*, NOAA Tech. Memo. OAR PMEL-135. NOAA/Pacific Marine Environmental Laboratory, Seattle, WA.

D. R. Tappin, P. Watts, S. T. Grilli, 2008. The Papua New Guinea tsunami of 17 July 1998: anatomy of a catastrophic event. *Nat. Hazards Earth Syst. Sci.*, *8*, 243–266.

ten Brink, U.S., Geist, E., Andrews, B.D., 2006. Size distribution of submarine landslides and its implication to tsunami hazard in Puerto Rico. *Geoph. Res. Lett.*, *33*, 4.

ten Brink, U., Twichel, D., Lynett, P., Geist. E., Chaytor, J., Lee. H., Buczkowski, B., Flores, C., 2009. Regional Assessment of Tsuami Potential in the Gulf of Mexico. *Open-File Report*. U.S. Geological Survey.

Thomopoulos, N. T., 2012. Essentials of Monte Carlo simulation: statistical methods for building simulation models. Springer, 2012.

Vilibić, I., Monserrat, S., Rabinovich, A.B., 2014. Meteorological tsunamis on the US East Coast and in other regions of the World Ocean. *Natural Hazard 74*, 1–9.

Waterborne Commerce Statistics, 2010. Calendar Year 2010. *Open-File Report*. United States Army Corps of Engineers.

Watts, P., Grilli, S.T., Tappin, D.R., Fryer, G.J., 2005. Tsunami generation by submarine mass failure. part II: Predictive equations and case studies. *J. Waterw. Port Coast. Ocean Eng.*, *131* (6), 298–310.

Yamazaki, Y., Kowalik, Z., Cheung, K.F., 2008. Depth-integrated, non-hydrostatic model for wave breaking and run-up. *Int. J. Numer. Meth. Fluids*, *61* (5), 473–497.